



University of Camerino
SCHOOL OF ADVANCED STUDIES

Chemical and Pharmaceutical Sciences and Biotechnologies Area

Ph.D. Curriculum in Chemical Science CHIM/01

XXXI Cycle

Doctoral Thesis

**Investigation on Next Generation Materials for Rechargeable Lithium-ion
Batteries: Alloying- and Conversion-based Materials as Viable Anode
Candidates**

Ph.D. Candidate

Gilberto Carbonari

Tutor

Dr. Francesco Nobili

A.Y. 2015/16-2017/18

Abstract

The current lithium-ion batteries (LIBs) technology has allowed the spread of portable electronic devices such as cameras, laptops, and smartphones, and at the same time has triggered the development of the electric vehicles (EVs). In order to increase LIBs mass diffusion and meet the market demands, a reduction in costs and environmental impact are required. Graphite is the conventional anodic material, but because of its relatively low specific capacity (372 mAh g^{-1}), and its implementation in the list of critical raw materials of European Union, it has to be replaced by more performant and environmentally-friendly materials. Since graphite has a capacity limitation due to its lithium storage mechanism (insertion process), the use of materials based on different lithium storage mechanisms, such as alloying and conversion materials, has been taken into consideration. Silicon is one of the most studied alloying materials because of its low cost, relatively low working potential, and high theoretical specific capacity of 3579 mAh g^{-1} (corresponding to the formation of $\text{Li}_{15}\text{Si}_4$ phase). Since the formation of the most lithiated phase is associated with a huge volume expansion ($\approx 300\%$), silicon is plagued by structural instability resulting in poor performances and safety. Thus, it is mandatory to stabilize its structure in order to have it commercialized in the future. Several strategies have been proposed such as the use of nanosize active materials, the implementation of carbonaceous and inorganic matrices, the use of tailored electrolyte and additives, and the use of more elastic and eco-friendly binders. In this thesis, different approaches have been used in combination, in order to buffer the silicon volume expansion, thus enhancing its capacity, safety and long-term performances. The performances of two silicon-based composites ($\text{Si@V}_2\text{O}_5$ and Si@TiO_2) have been evaluated by the means of structural, morphological and electrochemical characterizations. A whole chapter of this thesis will be focused on the scale-up of typical laboratory scale processes, where an in-depth study of silicon-based electrodes processing has been carried out. This study has been performed in a pre-industrial plant, starting from the electrode slurry preparation up to the electrochemical characterization of the assembled full cell. Different aspects have been taken into consideration, demonstrating that the scale-up of established laboratory-scale processes reserves important problems at an industrial level. At last, the use of a conversion material has been evaluated. These materials suffer from issues similar to those of alloying materials. Indeed, a big volume expansion associated with a low electronic conductivity and a large hysteresis in the first cycle hinder their commercialization. Fe_2O_3 nanoparticles have been synthesized using vanillin as soft template, in a cheap and very reproducible way. The electrochemical characterization showed remarkable cycling performances even at high currents.

Preface

The following doctoral thesis reports the results obtained during three years of the PhD course in Chemical Sciences at the University of Camerino (Italy), under the supervision of Dr. Francesco Nobili, and at the Zentrum für Sonnenenergie- und Wasserstoff-Forschung (ZSW) in Ulm (Germany) as a visiting PhD student, under the supervision of Dr. Michaela Memm and Dr. Margret Wohlfahrt-Mehrens.

Part of the research work reported in this thesis is the subject of the following scientific publications and conference proceedings:

Scientific Publications:

- F. Maroni, A. Birrozzi, G. Carbonari, F. Croce, S. Passerini, F. Nobili, *Graphene/V₂O₅ Cryogel Composite as a High-Energy Cathode Material for Lithium-Ion Batteries*, ChemElectroChem (2017), Vol. 4, pp. 613-619. doi:10.1002/celec.20160798.
- G. Carbonari, F. Maroni, M. Pasqualini, R. Tossici, F. Nobili, *Preparation and electrochemical Characterization of High-Stability MnO Anodes for Li-ion Batteries*, Electrochimica Acta (2017), Vol. 247, pp. 392-399. doi: 10.1016/j.electacta.2017.06.148.
- F. Maroni, G. Carbonari, F. Croce, R. Tossici, F. Nobili, *Anatase TiO₂ as a Cheap and Sustainable Buffering Filler for Silicon Nanoparticles in Lithium-Ion Battery Anodes*, ChemSusChem (2017), Vol. 10, pp. 4771-4777. doi: 10.1002/cssc.201701431.
- G. Carbonari, F. Maroni, A. Birrozzi, R. Tossici, F. Croce, F. Nobili, *Synthesis and Characterization of Si Nanoparticles wrapped by V₂O₅ Nanosheets as a Composite Anode Material for Lithium-Ion Batteries*, Electrochimica Acta (2018), Vol. 281, pp.676-683. doi: 10.1016/j.electacta.2018.05.094.

Conference Proceedings:

- G. Carbonari, F. Maroni, F. Nobili, *Sol-Gel Synthesis of Iron/Manganese Mixed Oxide as Superior and Eco-Friendly Anode for Lithium-Ion Batteries*, 5th Scientific Day of the School of Science and Technology of University of Camerino, Camerino (Italy), 08 June 2016.

- G. Carbonari, F. Maroni, F. Nobili, *Synthesis and Characterization of a Si/V₂O₅ Nanocomposite as Anode Material for Lithium-Ion Batteries*, 6th Scientific Day of the School of Science and Technology of University of Camerino, Camerino (Italy), 28 September 2018.
- G. Carbonari, F. Maroni, F. Nobili, *Vanillin-Templated Fe₂O₃ as Alternative Anode Material for Lithium-Ion Batteries*, 6th Scientific Day of the School of Science and Technology of University of Camerino, Camerino (Italy), 28 September 2018.
- G. Carbonari, F. Maroni, F. Nobili, *Synthesis and Characterization of V₂O₅-Nanosheet Buffered Si Nanoparticles as Anode Material for Lithium-Ion Batteries*, 69th ISE annual meeting, Bologna (Italy), 03-07 September 2018.
- F. Nobili, G. Carbonari, R. Tossici, F. Croce, F. Maroni, *Buffering volume changes of Si nanocomposite anodes*, POF17 Power Our Future 2017, Vitoria (Spain), 02-05 July 2017.
- G. Carbonari, F. Maroni, F. Nobili, *Optimizing the Electrode Formulation of Manganese (II) Oxide-based Anodes for Li-Ion Batteries*, Ulm Electrochemical Talk 2016 (UETC 2016), Ulm (Germany), 20-21 July 2016.

Table of Contents

Chapter 1 – Introduction	1
1.1 Fundamentals.....	2
1.2 Anode Materials	5
1.3 Cathode Materials.....	12
1.4 Electrolytes and Additives.....	16
1.5 Binders.....	18
Chapter 2 - Experimental Techniques	21
2.1 X-Ray Diffraction (XRD)	21
2.2 Scanning Electron Microscopy (SEM).....	23
2.3 Transmission Electron Microscopy (TEM).....	25
2.4 Thermogravimetric Analysis (TGA)	27
2.5 IR Spectroscopy (FT-IR).....	29
2.6 Inductively Coupled Plasm Mass Spectrometry (ICP-MS)	31
2.7 Zeta Potential measurement	33
2.8 Rheological Tests	35
2.9 Electrochemical Techniques.....	36
2.9.1 Cyclic Voltammetry (CV)	36
2.9.2 Galvanostatic Cycling with Potential Limitations (GCPL)	37
2.9.3 Electrochemical Impedance Spectroscopy (EIS).....	40
Chapter 3 – Silicon@V₂O₅ composite as anode for LIBs	45
3. 1 Introduction	45
3.2 Experimental	45
3.2.1 Si@V ₂ O ₅ synthesis	45
3.2.2 Electrodes Preparation	46

3.2.3 Cell Assembly and Cycling	47
3.3 Discussion	47
3.4 Conclusion.....	59
Chapter 4 – Silicon@TiO₂ composite as anode material for LIBs	61
4.1 Introduction	61
4.2 Experimental	61
4.2.1 Si@TiO ₂ Synthesis	61
4.2.2 Electrodes Preparation	62
4.2.3 Cell assembly and cycling	63
4.3 Discussion	63
4.4 Conclusion.....	73
Chapter 5 - Si@Graphite Composite as Industrial Relevant Anode for LIBs....	74
5.1 Introduction	74
5.1.1 LIB.DE Project	74
5.1.2 Electrodes production - Laboratory scale vs Industrial scale	76
5.2 Aqueous slurry preparation and optimization	84
5.3 Electrochemical characterization: Coin cells	101
5.3.1 Cell Assembly.....	101
5.3.2 Electrochemical characterization.....	102
5.4 Electrochemical characterization: Pouch cells	114
5.4.1 Cathode preparation and characterization	115
5.4.2 Full Cells assembly and characterization	120
5.5.1 Cell Assembly and Cycling	133
5.6 Conclusion.....	140

Chapter 6 – Vanillin-templated Fe₂O₃ nanoparticles as conversion anode material for LIBs.....	142
6.1 Introduction	142
6.2 Experimental	143
6.2.1 Synthesis	143
6.2.2 Electrodes preparation	143
6.2.3 Cell Assembly and Cycling	144
6.3 Discussion	144
6.4 Conclusion.....	156
7. References	157

Chapter 1 – Introduction

The sudden increase in energy consumption due to population growth is having a very significant impact on our planet. The daily emission of pollutants (e.g. greenhouse gases) is changing our climate resulting in unexpected natural phenomena such as storms, floods, and rising seas. Therefore, it is mandatory to reduce pollutant emissions trying to develop renewable energy sources that are accessible to everyone [1]. Solar and wind energies are the most common renewable energy sources, but since they are intermittent, the research and development of reliable Energy Storage Systems (ESS) is needed.

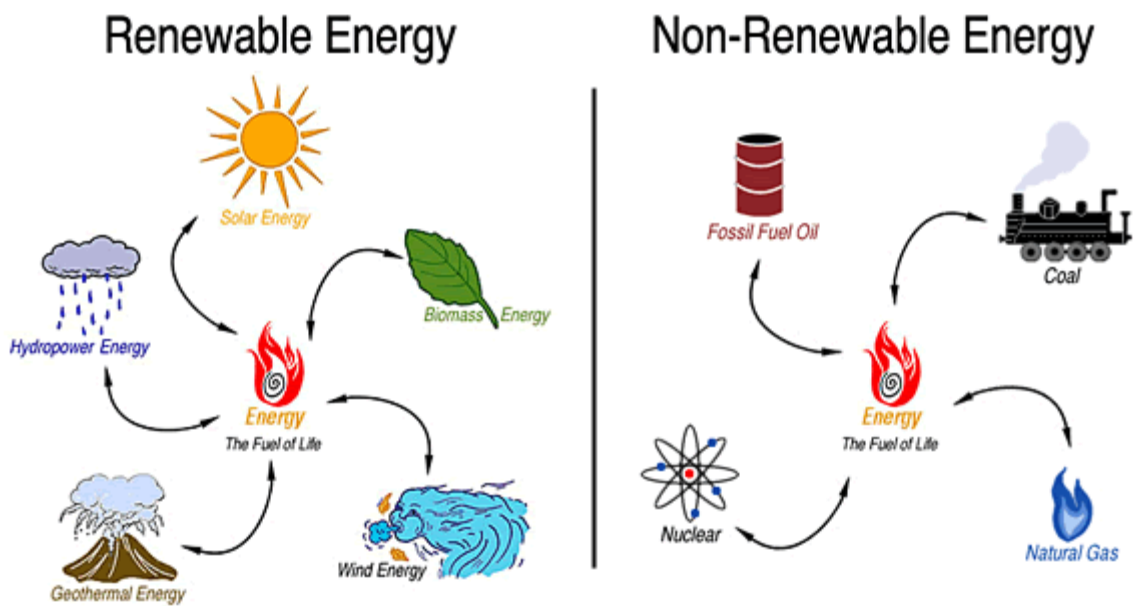


Fig. 1.1 – Renewable and non-renewable energy sources.

Lithium-Ion Batteries (LIBs) meet all the prerequisites to be considered as possible candidates, since they are characterized by high energy and power densities, but their currently high production costs make their capillary use on a large scale virtually unfeasible. However, their implementation together with electric engines in electric vehicles (EVs) could reduce the greenhouse gases emission replacing the traditional internal combustion engine.

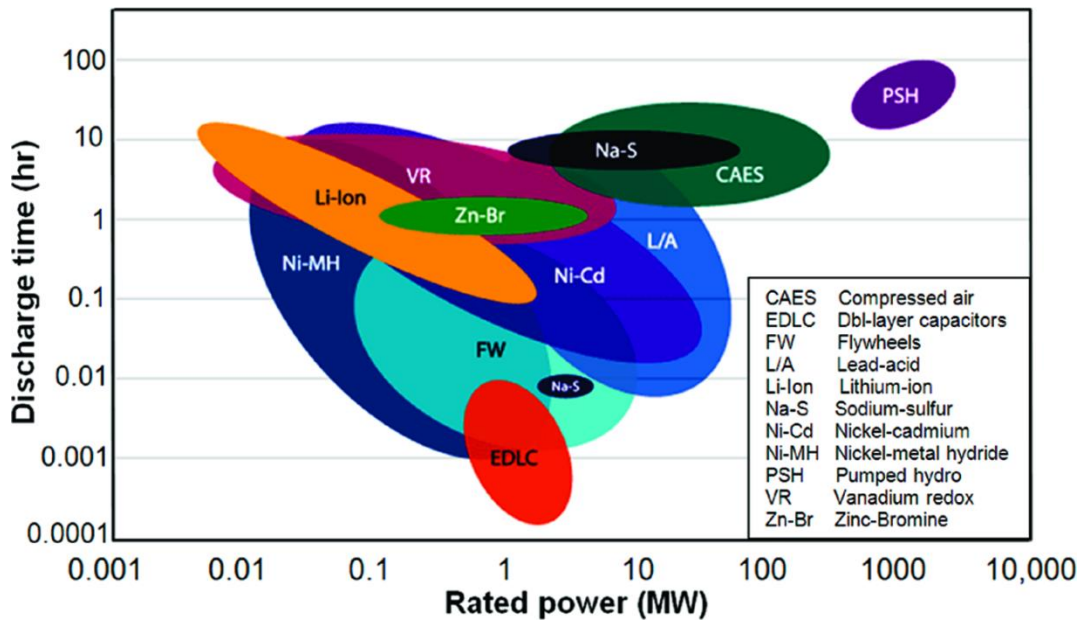


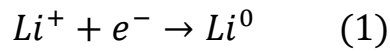
Fig. 1.2 – Discharge times and power ratings of different energy storage systems.

At the moment, EVs globally diffusion is held back by their limited range of kilometers [2], and for this reason efforts have to be done to meet consumer demands such as high energy density, high power density, low cost and safety [3,4]. A key role in obtaining this result is undoubtedly the use of more performing materials (high capacity anode and/or high-voltage cathode) to replace traditional electrode materials.

1.1 Fundamentals

Lithium-ion batteries are galvanic secondary cells that can be charged and discharged many times before being discarded. A typical LIB consists of two electrodes connected through an external circuit, separated by a microporous polymer membrane soaked in a liquid electrolyte. During the charge process, lithium ions are extracted from the cathode and inserted into the anode structure, while the opposite mechanism takes place during the discharge process. In order to balance the lithium migration, electrons flow through an external circuit causing the oxidation or the reduction of the electrode material.

A single cell is characterized by two half-reaction occurring at 2 different electrodes, namely the cathode and the anode. In order to measure the potential of a single half-reaction, a reference electrode with a fixed potential can be used. In systems where lithium is involved, it is common to refer the redox potentials to the Li^+/Li redox couple, where $E = -3.04 \text{ V vs. SHE}$ (Standard Hydrogen Electrode).



Each electrode consists of a thin layer casted onto a metal current collector such as copper for the anode and aluminum for the cathode. The use of copper at the anode side is mandatory, since lithium reacts with aluminum at the low anodic potentials [5]. The deposition of the electrodic material onto the current collector is done by preparing the slurry. It includes the active material, at least one polymeric binder to ensure electrode integrity, and a conductive agent to improve the overall electronic conductivity. A typical anode material is the graphite, which is characterized by a layered structure and a low working potential, while a typical cathode material like LiCoO_2 is a lithiated transition metal oxide characterized by a rather high working potential. The charge/discharge mechanism is shown in Fig. 1.3.

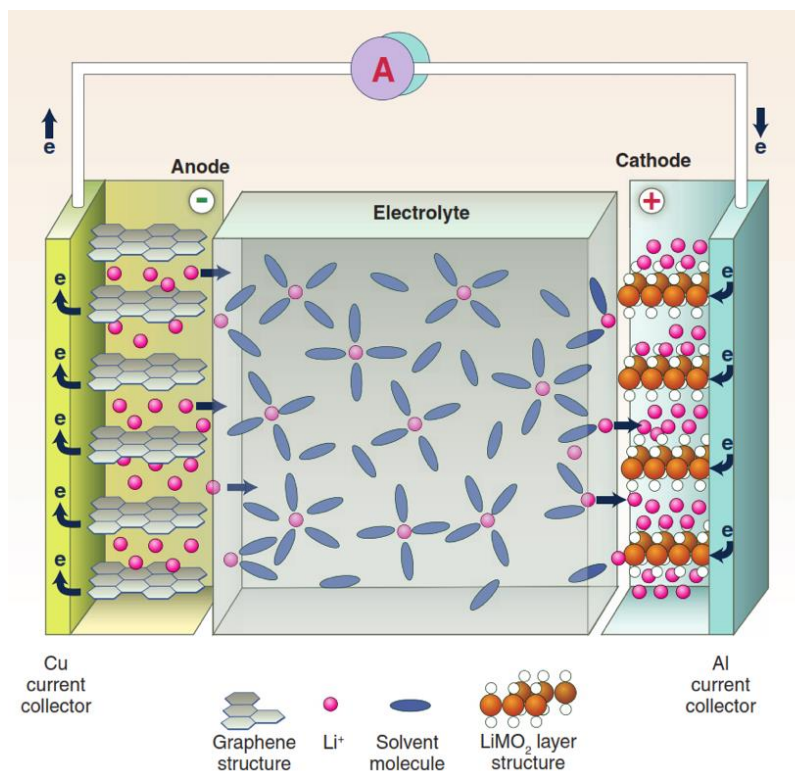


Fig. 1.3 – Schematic representation of LIBs working mechanism.

In details, the following half-reactions take place during charge using a graphite-based anode and a lithium cobalt oxide-based cathode:



In this case, the cell is assembled in a fully discharged state and needs to be charged by applying an external current. When the charged cell is connected to an external load, the current will start to flow from the anode to the cathode together with lithium ions, and the cell potential will change going toward the equilibrium.

Each active material can store a defined amount of charge defined capacity (Q). This value is expressed in Ah and can be normalized by weight, volume or mol. The theoretical gravimetric capacity (mAh g⁻¹) of a certain material can be derived by Faraday's Law:

$$Q = \frac{n \cdot F}{M_w} \cdot \left(\frac{1000}{3600} \right) \quad (4)$$

where, n is the number of exchanged electrons per mole of active material, M_w is the molecular weight, and F is the faraday constant (96485 C mol⁻¹). From the experimental charge and discharge capacity values obtained during a single charge/discharge cycle, it is possible to calculate the coulombic efficiency % related to that cycle:

$$\eta = \frac{Q_{discharge}}{Q_{charge}} \cdot 100 \quad (5)$$

Another important parameter is the charge/discharge rate (C), where a 1C-rate is the current necessary to fully charge/discharge a battery in one hour. As an example, applying a 2C-rate the battery will be fully charged/discharge within 30 minutes. Other important parameters are listed below:

- **Voltage:** It is the potential difference between the cathode and the anode, and it is expressed in volts (V);
- **State of Charge (SOC):** It is the percentage amount of charge stored in a battery relative to the total capacity;

- **State of Health (SOH):** It reflects the general condition of a battery. It can be determined taking into considerations parameters such as impedance, conductance, capacity retention etc.
- **Cycle Life:** It is the number of cycles performed by a battery under specific conditions before its performance decay below a predetermined threshold value. A battery is usually considered as depleted when the reversible capacity falls below 80% with respect to the initial value.
- **Energy:** it is related to the capacity and the voltage of the battery. It is expressed in Watt*hours (Wh) and can be normalized by mass (Wh kg⁻¹) or volume (Wh l⁻¹):

$$E = \int_0^t I \cdot V(t) dt \quad (6)$$

1.2 Anode Materials

Immediately after the first studies on the metallic lithium as an anodic material during the late 60s, it was soon realized that the use of this active material led to the growth of potentially hazardous dendrites, resulting in serious safety issues because of possible internal short-circuits triggering thermal runaway of the cells [6,7].

In order to replace this anode, intercalation compounds were proposed to overcome these problems. Anodic active materials should have the following characteristics:

- low working potential with respect to Li⁺/Li redox couple;
- low atomic number and density;
- inactivity and insolubility in electrolytes;
- fast lithiation/delithiation kinetics
- low cost and environmental impact.

Graphite is undoubtedly the most used material in the anode side, but in the early days of lithium-ion battery research it did not appear to be a feasible material, since the electrolyte used at that time (mostly propylene carbonate) [8] would result in structural degradation phenomena because of the solvent co-intercalation and its bad film-forming ability. The development of a feasible electrolyte formulation, based mostly on cyclic carbonate solvents led to the use of graphite and others carbon-based materials [9]. Graphite has a theoretical specific capacity of 372 mAh g^{-1} and an average working potential around 0.15 V , associated to step-wise lithium intercalation/deintercalation processes inside its graphene layers. The formation mechanism of the graphite intercalation compounds (GICs) are schematized in Fig. 1.4.

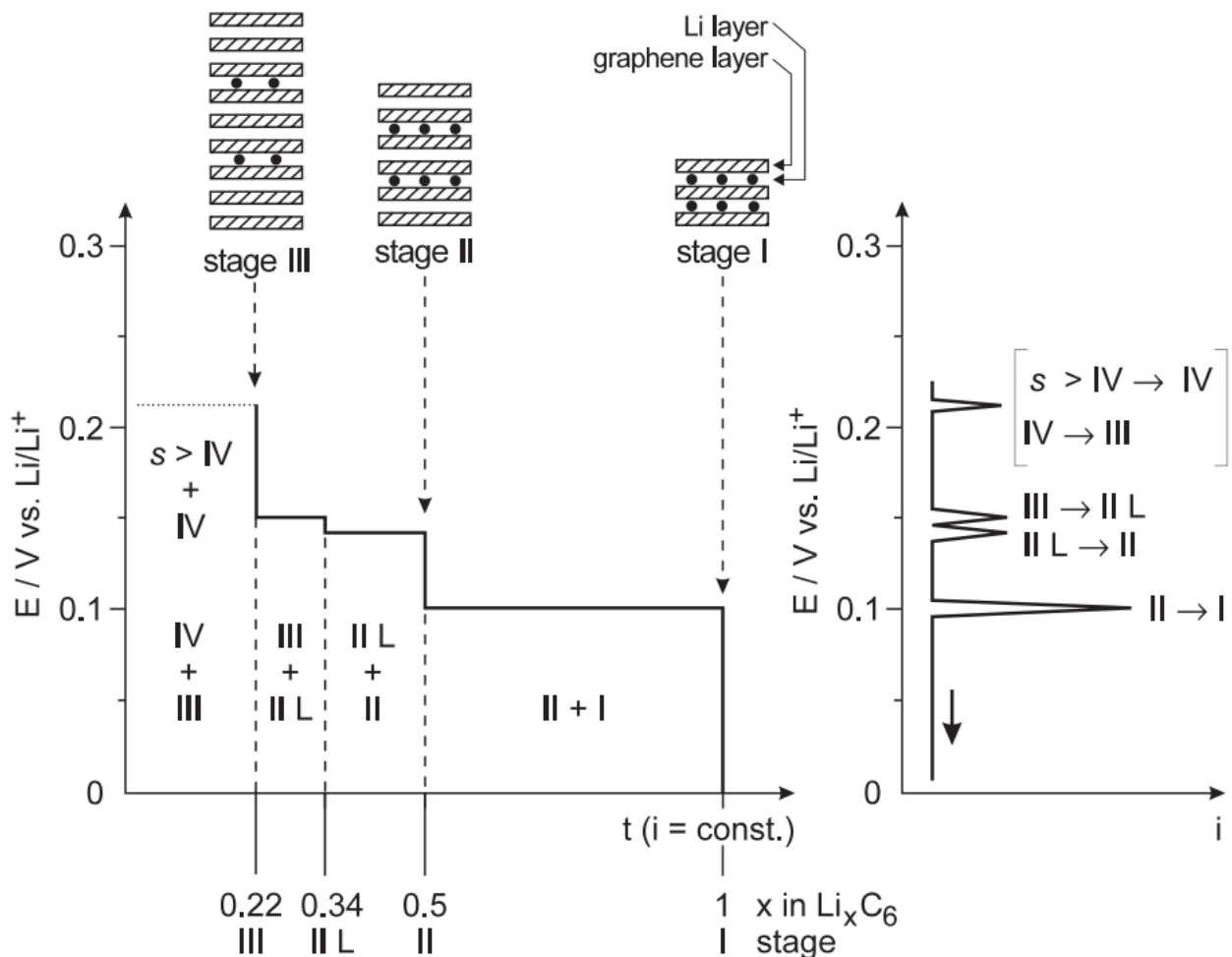


Fig. 1.4 – Graphite lithiation: galvanostatic curve (at left) and voltammetric curve (at right).

Each stage corresponds to a different GIC and a different number of lithium ions inside two adjacent graphene layers. All the plateaus correspond to two-phase regions where the Li^+ transport follows a phase boundary inside graphite structure [10]. Only during stage IV there is a one-phase region (solid-solution) where the Li^+ ions move by a solid-state diffusion process [11].

A fundamental feature of the materials that are cycled at lower potentials than the electrolyte stability window, is the formation of a passivation layer on the surface of the anode. Indeed, electrolytes are usually a mixture of aprotic organic carbonates in which a lithium salt is dissolved, where the oxidation and reduction potentials of these carbonates are respectively around 4.7 V and 1.0 V [12]. This passivation layer formed around 0.8 V vs. Li^+/Li is called Solid Electrolyte Interphase (SEI), and is electronically insulating and ionically conductive. Morphology and chemical composition of this passivation layer mainly depend on the anodic material and electrolyte formulation [13–15], which greatly influence SEI mechanical features. However, several studies have confirmed that the most frequent SEI components are Li_2O , Li_2CO_3 , LiF , and polyolefins [16,17] (Fig. 1.5).

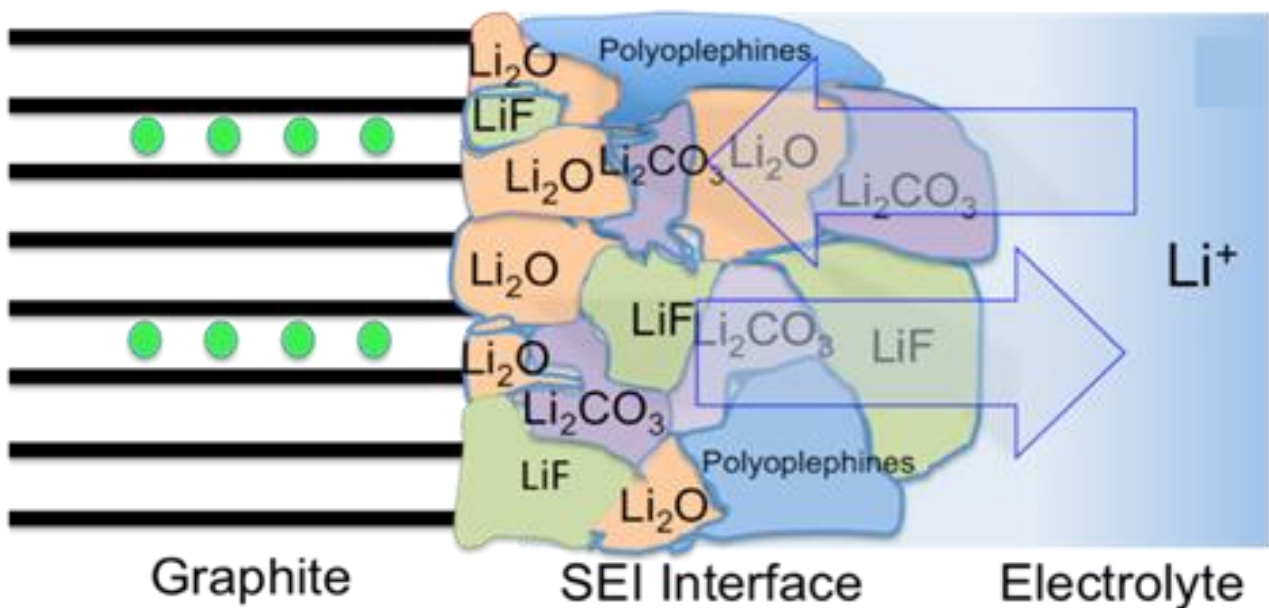


Fig. 1.5 – Solid Electrolyte Interphase (SEI) structure.

It often happens that, due to structural anode instabilities such as volume expansion upon cycling and dendrites growth (especially when metallic lithium is used as anode), the SEI becomes mechanically unstable leading to cracks. Since these cracks expose “fresh” active material to the electrolyte, the solvent decomposition reaction starts again leading to an extra Li-consumption and thus a higher irreversible capacity. Therefore, it is of paramount importance to try to stabilize this passivation layer in order to increase cycle life and cell performances.

Another class of anode materials is represented by active materials that form alloy with lithium. These alloying materials were first studied for thermally activated batteries since the heat required to melt the electrolyte would also melt lithium forming stable metal alloys at high temperatures.

For obvious reasons of application to the Li-ion batteries, the most studied elements are those able to form stable Li-alloys at room temperature such as Si, Sn, Sb, Zn, Bi, Mg, Al, Ag, and Pb [18,19]. The lithiation/delithiation mechanism of these materials generally shows high theoretical specific capacities and relatively low voltages [20]. Regrettably, they show huge volume change upon cycling and are characterized by a high initial irreversible capacity [21]. These drawbacks are the main obstacles to alloying materials commercialization on a large scale, and must be mitigated in order to replace the more traditional graphite-based anodes. Different strategies have been applied trying to reduce the initial irreversible capacity, such as anode pre-lithiation processes [22][23] and synthesis of over-lithiated cathodes [24] yielding during the first charge the excess Li at anode needed to compensate irreversibility.

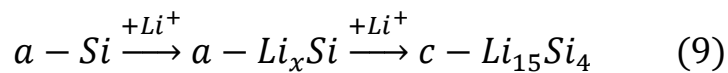
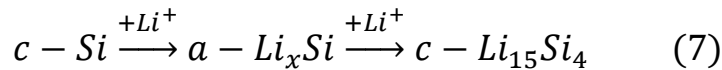
The greatest efforts were spent trying to buffer the volume expansion and stabilize the SEI layer upon cycling. Four major strategies are taken into account:

- **Size reduction:** the use of nanoparticles increases the specific capacity and the capacity retention. This could be addressed to the reduced size that shows smaller tendency to cracking [25].
- **Buffering matrices:** Carbon- [26,27] and inorganic-based matrices [28] can be used to buffer the huge volume change. Obviously, the use of an electrochemical active matrix is preferred in order to reduce the so called “dead/inactive weight” inside the composite. The application of a carbon coating is also another common strategy that helps to increase the overall conductivity of the active material [29].

- **Electrolytes:** the use of additives or co-solvents such as Vinylene Carbonate (VC) [30] or Fluoroethylene Carbonate (FEC) [31] may result in a better capacity retention and cycling performances due to the formation of a more uniform and stable SEI layer.
- **Binders:** The use of elastic binders can enhance the electrode mechanical stability avoiding delamination and active material segregation [32,33]. Water-based binders have already proven to be essential for this purpose compared to the traditional Polyvinylidene Fluoride (PVdF) [34]. In fact, the use of water as a solvent allows to replace the traditional organic solvent (e.g. NMP), thus reducing the costs related to the collection and recycling plants.

As already said, these strategies used alone or in a synergistic way have shown remarkable improvements and have paved the way for a possible battery based solely on alloying materials at the anode side.

Certainly, the most studied and used alloying material is the silicon. Its environmentally- friendliness, low cost, high theoretical specific capacity, and low charge/discharge potential, make it one of the viable candidates to replace graphite in lithium-ion batterie. Regrettably, the big volume change plaguing silicon resulted to be around 300% [35]. The gravimetric capacity of silicon is 3579 mAh g⁻¹ when Li₁₅Si₄ phase is considered as the end-member of lithiation at room temperature. Its lithiation mechanism is shown below:



During the first cycle lithiation (Eq. 7), an amorphization of the crystalline silicon (c-Si) together with the formation of Li_xSi phase take place. This is a two-phase mechanism where the two phases are separated by a reaction front. Since the Si-Si crystalline bonds require a high activation energy to be broken, a high lithium concentration at the reaction front is required for good lithiation kinetics [36]. As demonstrated by Obrovac and Christensen [37,38], this amorphous lithiated phase suddenly crystallize to $\text{Li}_{15}\text{Si}_{14}$ at potential lower than 50 mV.

At temperature below 85 °C, $\text{Li}_{15}\text{Si}_{14}$ metastable phase is formed [39] instead of the thermodynamic stable $\text{Li}_{22}\text{Si}_{15}$. Since this crystalline phase is associated to the big volume variation of about 300%, several studies have been made to limit its formation, such as capacity limitations [40] and different working potential window [41]. The subsequent de-lithiation (Eq. 8) leads to the formation of amorphous silicon. From the second cycle on, the processes described by Equations (9) - (10) are repeated upon cycling.

In Figure 1.6, it is possible to notice how the volume variation during charge/discharge cycles leads to electrode pulverization, active material isolation, and SEI breakage [42]. This means that part of silicon will become unavailable, hindering a full active material utilization and leading to a fast capacity loss.

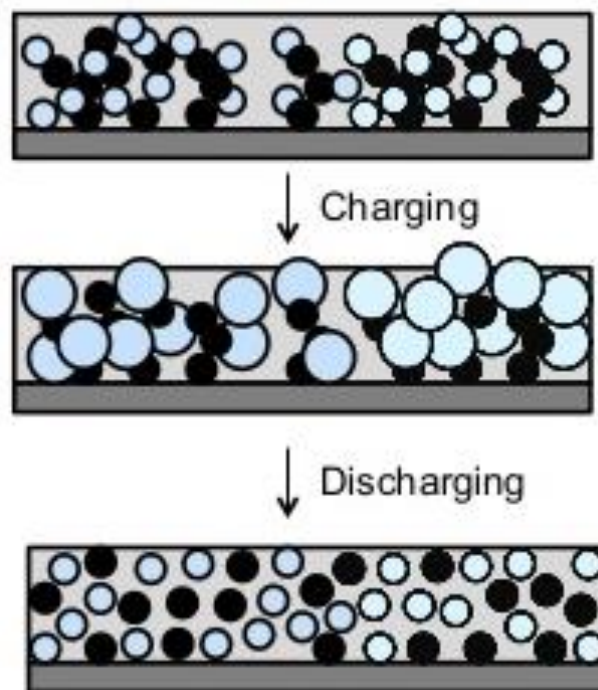
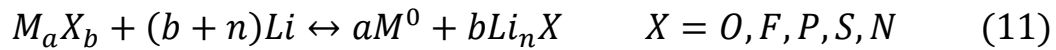


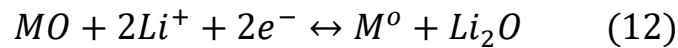
Fig. 1.6 – Silicon-based electrode pulverization mechanism.

Another important class of anode materials is represented by the conversion-based materials. This introduces a completely different reactivity concept, as regards the lithium storage ability, with respect to intercalation and alloying mechanisms. They were studied for the first time during the 80s, but because of the high reaction irreversibility, they have been abandoned.

Nevertheless, more recent studies found out that the use of nanosized materials could help to improve this reversibility [43]. The general conversion reaction is the following:



Since the most studied conversion compounds are transition metal oxides (TMOs), here we will talk only about them. Taking into consideration, as an example, a generic bivalent transition metal, the previous reaction will become:



During the first discharge the crystalline structure of pristine metal oxide is lost because of the amorphization process. At the end of the discharge, the reduced metal is dispersed inside an amorphous Li_2O inactive matrix in the form of nanoparticles [44]. In the following charge, the lithium oxide matrix is decomposed and a metal oxide is obtained again (Fig. 1.7).

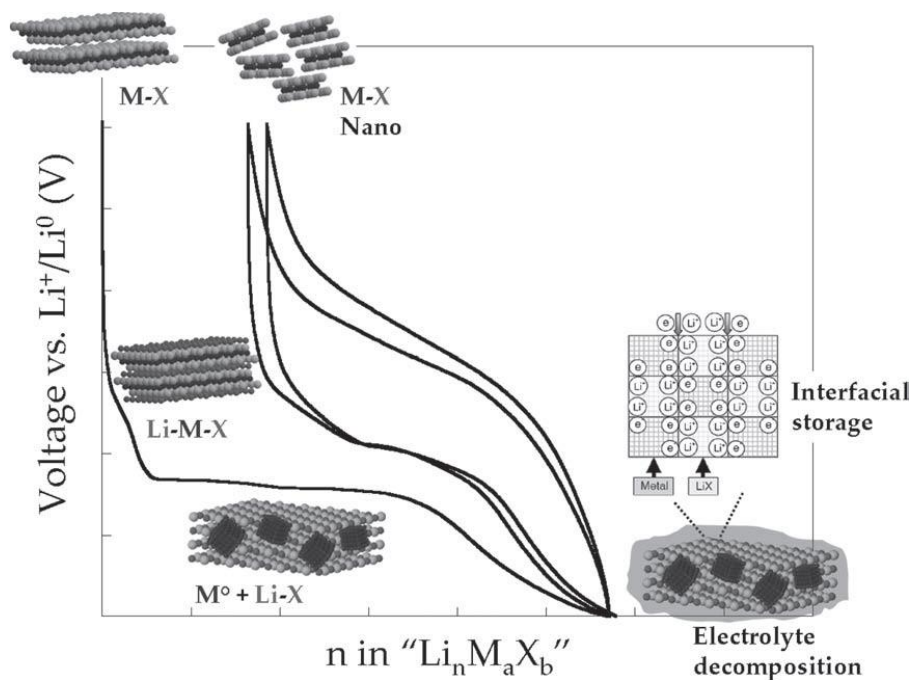


Fig. 1.7 – Voltage vs. Composition profiles of a generic conversion-based anode.

TMOs are plagued by several issues, such as a large coulombic efficiency at the first cycle, a relatively high working potential, a large voltage hysteresis, a low electronic conductivity, and a big volume change due to the structural re-organization during charge/discharge cycles [45]. Nevertheless, their high specific capacities, due to the multiple-electron reaction and the relatively low molecular weight, make them promising candidate anode materials for LIBs. Considering also that manganese and iron oxides are particularly cheap and environmentally-friendly [46–48], new strategies should be evaluated in order to minimize the aforementioned issues.

1.3 Cathode Materials

In this chapter a general overview on the cathodes is presented, with a particular attention on the lithium nickel manganese cobalt oxide-based cathodes (NMC) used in this thesis. An ideal cathode material for lithium-ion batteries should be stable, cheap and non-toxic. In addition, different properties are requested in order to obtain high stability and energy density. The main requirements are enlisted in Table 1:

Properties of an ideal cathodic material
High discharge potential
Lithiation reaction should be fast and fully reversible
High lithium diffusivity
High lithium storage capacity
Small volume variation upon cycling

Table 1a – Cathode material requirements.

Scrosati et al. developed a lithium-ion battery prototype in the 70s using TiS_2 as cathode [49]. This material has many of the characteristics listed above, but its low average working potential of 2.5 V [50], and the need to use a perchlorate-based electrolyte limited its utilization and diffusion. After 10 years, the John B. Goodenough's research group at the Oxford University developed a lithium cobalt oxide (LiCoO_2) insertion cathode [51] with a layered structure similar to that of TiS_2 . It has a rock-salt structure composed by alternating CoO_6 and LiO_6 layers.

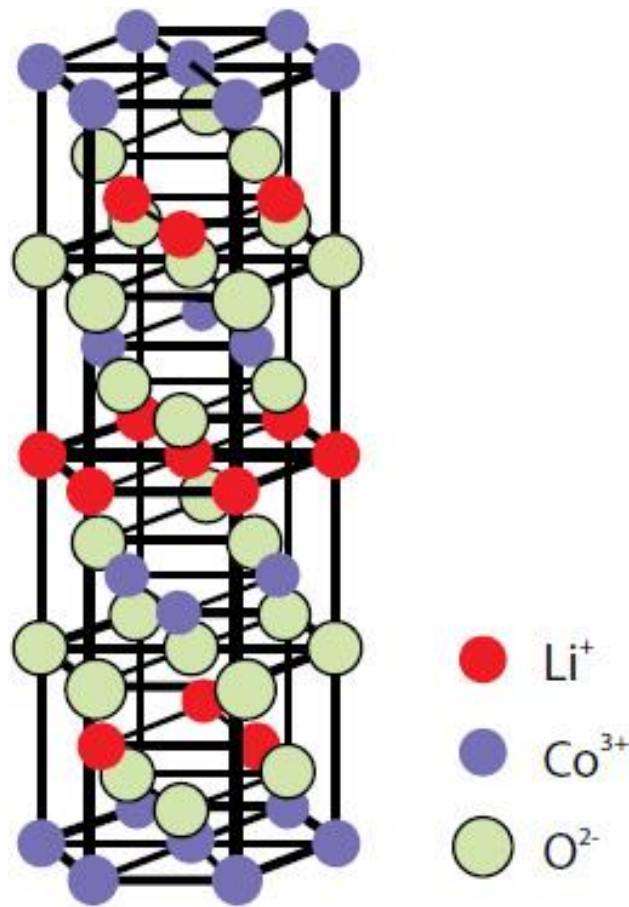


Fig. 1.8 – LiCoO_2 structure.

The lithium insertion process is highly reversible only if the material retains a lithium content x (in Li_xCoO_2) in the range $0.5 < x < 1$ resulting in a theoretical specific capacity of about 140 mAh g^{-1} . Indeed, the full lithium extraction from the structure results in high structural instability and electrochemical inactivity.



To prevent possible cathode oxidation, a cut-off potential around 4.1 V is recommended. Despite its good electrochemical performances, the presence of cobalt makes this material highly expensive and toxic. In order to solve this issue, cobalt was replaced by more environmentally friendly elements such as manganese and nickel. LiNiO_2 is a lithium cobalt oxide isostructure with a higher specific capacity of 200 mAh g^{-1} , but with a limited thermal stability leading to safety issues. Since the layered phase with manganese is not stable, LiMn_2O_4 spinel phase (Fig. 1.9) was synthesized, but despite the use of the cheap and non-toxic manganese, the resulting material is not structurally stable since manganese dissolution in the electrolyte leads to irreversible phase transition and capacity decay [52]. Recent efforts to prevent this dissolution provides for the use of metal oxides such as Al_2O_3 [53].

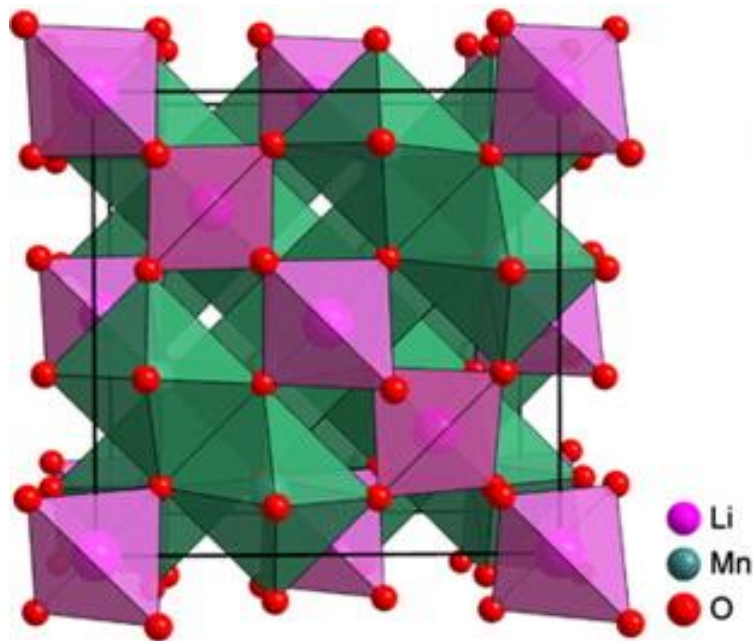
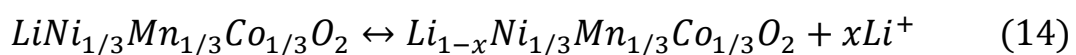


Fig. 1.9 – LiMn_2O_4 structure.

Ternary systems of lithiated mixed metal oxides have been proposed to overcome these issues. In 2001, Ohzuku and co-workers synthesized a $\text{LiNi}_{1/3}\text{Mn}_{1/3}\text{Co}_{1/3}\text{O}_2$, which was an immediate success [54]. This material shows a layered structure where nickel has an oxidation number of +2, manganese of +4, and cobalt of +3.



At lower potential, nickel is oxidized to +4 ($0 \leq x \leq 0.67$), while at higher potential cobalt is oxidized to +4 as well ($0.67 \leq x \leq 1$) [55]. The above reaction results in a specific capacity of 160 mAh g^{-1} , and an average working potential of 4.0 V. In order to reduce cobalt content, several NMC-based cathodes have been developed increasing Ni and Mn contents (see Fig 1.10). $\text{LiNi}_{0.6}\text{Mn}_{0.2}\text{Co}_{0.2}\text{O}_2$ (NMC 622) and $\text{LiNi}_{0.8}\text{Mn}_{0.1}\text{Co}_{0.1}\text{O}_2$ (NMC 811) are two of the most studied positive material [56] in order to increase the energy density of next-generation batteries together with Li-rich NMC compounds [57]. However, the higher capacities of the Ni-rich NMCs are usually accompanied by safety concerns due to their lower stability [58].

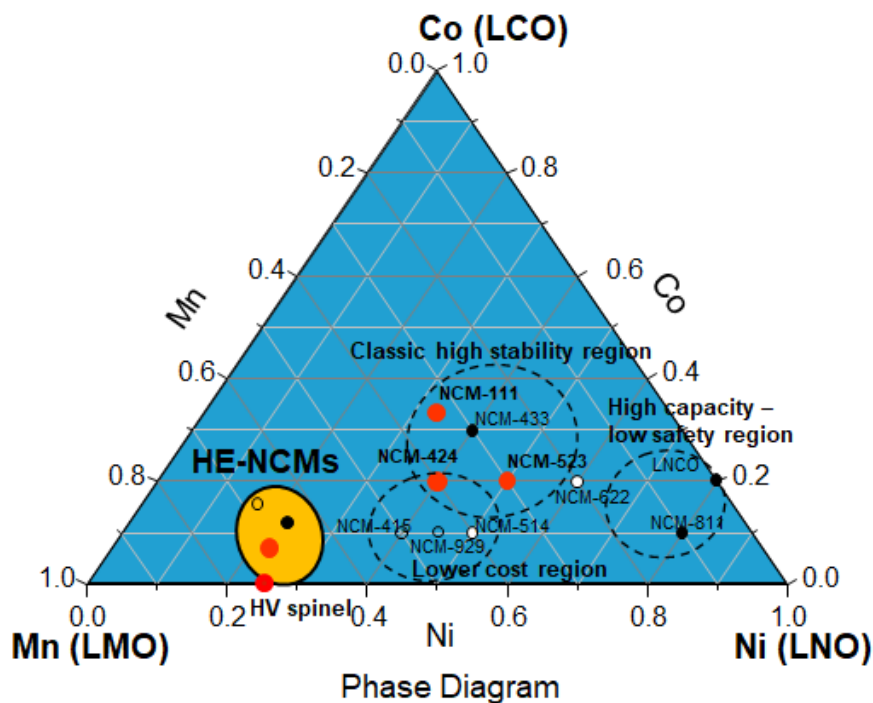


Fig. 1.10 – Triangular phase diagram of NMC materials.

Another class of cathodic materials is represented by olivine-phase materials such as lithium iron phosphate (LiFePO_4 – LFP). It is a cheap and non-toxic cathode with a specific capacity of 170 mAh g^{-1} and an average working potential of 3.5 V. Lithium insertion/deinsertion in LFP is mostly described by a very flat plateau indicating a two-phase mechanism, while sloped voltage profiles at the end and at the beginning of the lithiation describe minor extents of single-phase reaction (solid-solution). Its main drawbacks are the low electron conductivity, which can be enhanced by carbon coating [59], and the Li^+ diffusivity, which occurs preferentially along [010] channels.

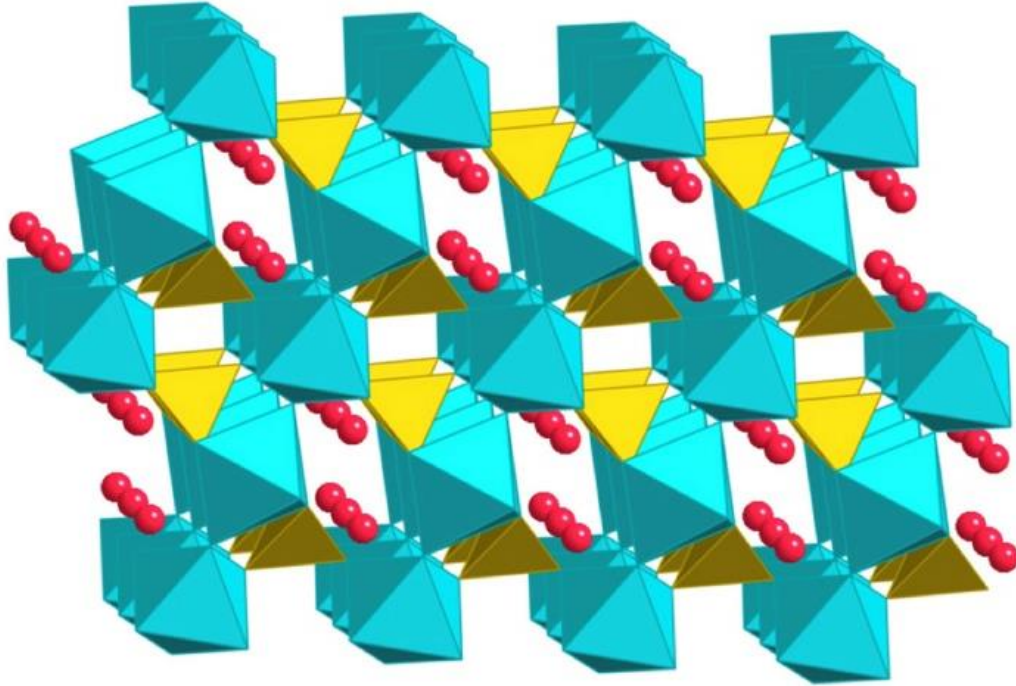


Fig. 1.11 – LiFePO₄ structure.

1.4 Electrolytes and Additives

LIBs electrolytes have the task of allowing the passage of Li⁺ ions between anode and cathode. The most common electrolytes are usually liquid, but in recent years' numerous studies have been done to replace them with safer solid electrolytes [60]. An optimal liquid electrolyte for lithium-ion batteries should be:

- cheap and non-toxic;
- thermally and electrically stable;
- inert to the others batterie components;
- good Li⁺ conductor and electronic insulator;
- stable in a wide voltage range, in order to avoid side reaction at the anode and cathode;

Commonly, the liquid version is a solution of lithium salts in a mixture of organic solvents. The lithium salts should possess the same properties listed for a general electrolyte, and of course should be completely soluble in the solvent. The most common salts are LiBF_4 , LiClO_4 , LiAsF_6 , and LiPF_6 . Historically, one of the first lithium salts used was LiClO_4 that has poor stability and react with the aluminum collector. LiBF_4 is more stable, but its low dissociation constant results in a poor ionic conductivity. LiAsF_6 instead has a very high solubility and stability, a very good SEI forming ability, but because of the As-based counter ion it is highly toxic. A good choice is represented by LiPF_6 salt, that is the right balance between performances and drawbacks [61]. For what concerns the solvents, organic carbonates are the most used (Fig. 1.12).

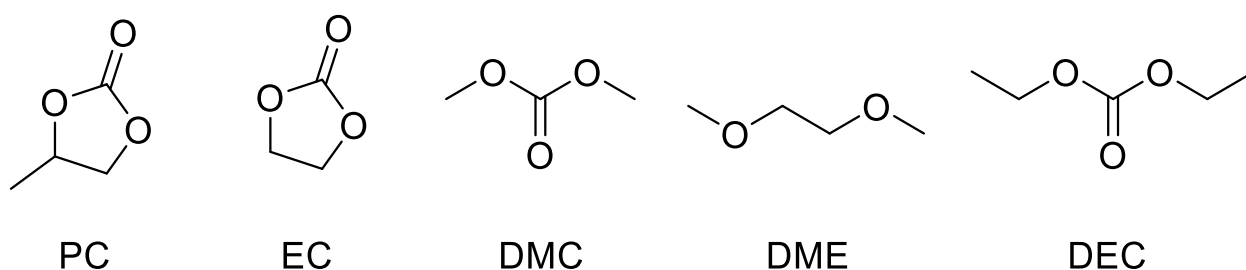


Fig. 1.12 – Common organic solvents for LIB electrolytes.

Today's electrolytes use mainly linear carbonate such as dimethyl carbonate (DMC) and diethyl carbonate (DEC) as co-solvents. Binary and ternary solvent systems are very common, because conductivity, viscosity, thermal stability, and film forming ability can be modulated. Since solvent properties directly affect the SEI formation, different solvent combinations have different film-forming ability. In order to enhance SEI properties, the use of electrolyte additives can be evaluated. Indeed, they can lead to a uniform morphology and chemical composition, enhanced thermal stability of lithium salts, avoid gas generation and also reduce irreversible capacity [62]. Among them, vinylene carbonate (VC) and fluoroethylene carbonate (FEC) are the most studied and used. Because of the presence of a carbon-carbon double bond in their structure, they are easily polymerizable under reduction forming a surface polymeric coating around 1.0 V vs. Li^+/Li redox couple [63]. While VC is used more like an additive, FEC resulted to give better results when used as a co-solvent in a concentration around 10% [31,64].

Recent studies on silicon-based anodes claim that the sudden capacity fade is attributed to a concomitant FEC consumption through cycling [64].

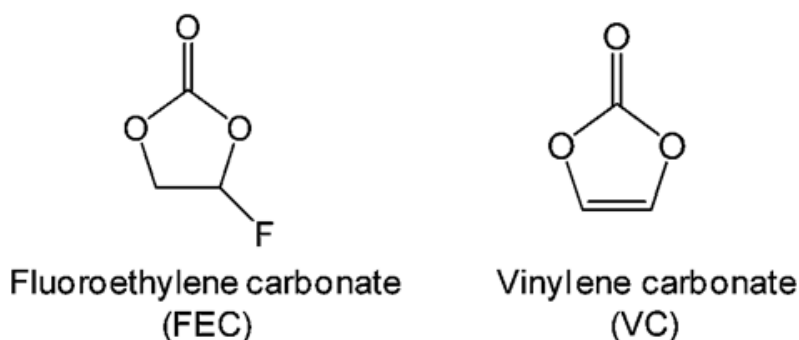


Fig. 1.13 – Fluoroethylene Carbonate (FEC) and Vinylene Carbonate (VC) structures.

1.5 Binders

Binders are polymeric materials used in the battery industry with the purpose of keeping together the active material, the conductive agent and the metallic current collector (Cu for the anodes, Al for the cathodes). An ideal binder should interact with all the electrode components, resulting in a binding mechanism like in Fig. 1.14 (a) where all the active material particles and the conductive agent are interconnected each other, and well anchored to the current collector. Binding mechanism shown in Fig 1.14 (b)-(c) would otherwise result in poor electronic conduction and low adhesion to the current collector.

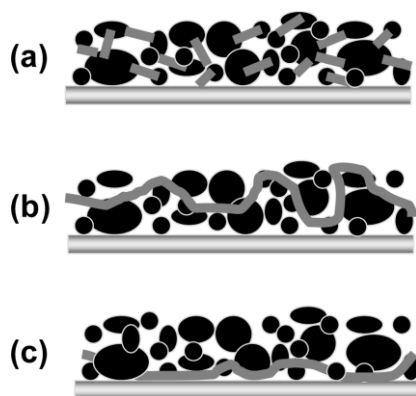


Fig. 1.14 – Binding mechanisms.

The characteristics of an optimal binder are in line with those of the other battery components, i.e. should be cheap, non-toxic, and stable in the battery environment. Stability should refer to binder/active material interaction, binder/electrolyte interaction, and binder/working potential window interaction. This means that the binder should buffer any active material volume change, it should be insoluble in the electrolyte, and that it should be not oxidized or reduced within the potential window. For what concern the binder/electrolyte interaction, it is important to say that the binder swellability in the electrolyte greatly affects the mechanical strength of the electrode [65]. The traditional binder used as industry standard is the Polyvinylidene Fluoride (PVdF), a very stable linear-type homopolymer which is widely used with graphite anodes thanks to its good mechanical properties and thermal stability. Moreover, its low HOMO energy makes it particularly stable at high voltages, and for this reason it can be used also at the cathode side [66].

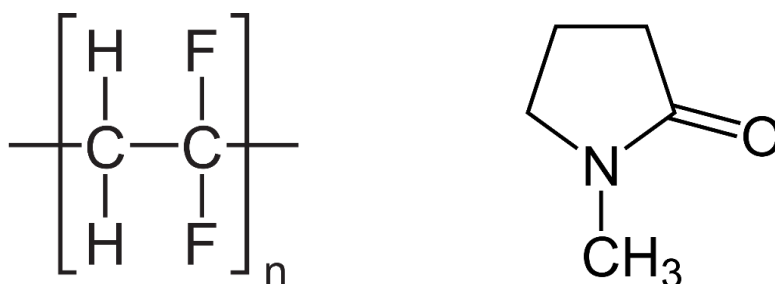


Fig. 1.15 – Polyvinylidene Fluoride (on the left) and N-methyl-2-pyrrolidone (on the right) structure.

However, PVdF is soluble in the toxic and expensive N-methyl-2-pyrrolidone (NMP), that must be treated carefully and recovered during the electrode drying [67]. Moreover, PVdF does not sustain the large volume changes of alloying and conversion materials PVdF [68], and for this reason other polymeric binders have to be investigated.

Dahn and co-workers showed that the use of Carboxymethyl Cellulose (CMC) and its sodium salt (Na-CMC) can be a viable alternative for alloying anodes [69]. CMC is a cellulose derivative, and it is cheap, non-toxic and water-soluble. Because of its brittleness it has to be used together with Styrene Butadiene Rubber (SBR), but the resulting electrodes show remarkable mechanical properties with respect to PVdF-based electrodes. Recently, it has been proposed that pH could influence the active material/CMC interaction in silicon-based anodes, enhancing their current collector adhesion and electrochemical performances [70].

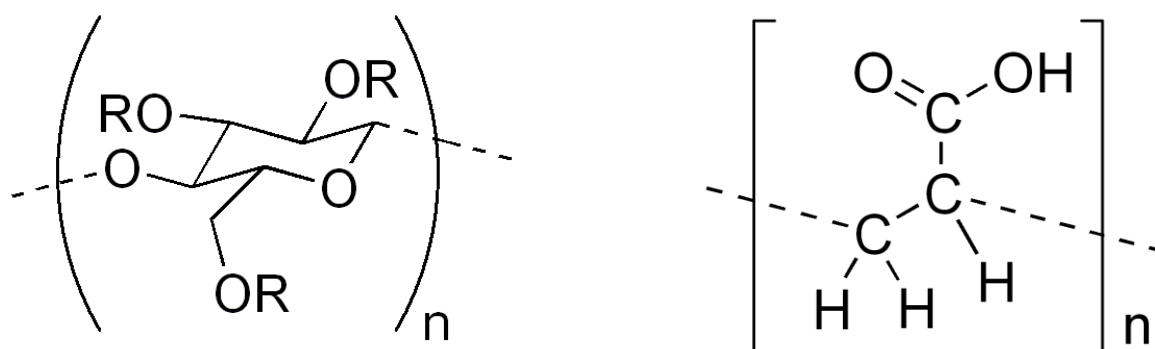


Fig. 1.16 – Carboxymethyl cellulose (on the left) ($R = H, CH_2COOH$) and Polyacrylic Acid (on the right).

Another interesting binder for alloying and conversion active materials is the Polyacrylic Acid (PAA) and its sodium and lithium salts. PAA is soluble not only in water, but also in ethanol. This flexibility is important since silicon particles can be quickly oxidized by water during slurry preparation [71]. It shows a low swellability with electrolytes and enhanced mechanical properties with respect to PVdF binder. It has been proposed that this is most likely due to the high concentration of carboxylic groups that interact with active material surface [72]. However, it has a relatively high cost with respect to CMC, and in order to obtain appreciable mechanical properties, it has to be used in higher concentrations than CMC and PVdF binders.

Other polymers have been investigated in order to replace PVdF, such as sodium alginate [73], PVA [74], self-healing binders [75], and conductive binders [76], but they will not be taken in consideration in this thesis.

Chapter 2 - Experimental Techniques

2.1 X-Ray Diffraction (XRD)

X-Ray diffraction is a powerful technique for determining the atomic/molecular structure of materials only if they are crystalline ($\approx 95\%$ of solid materials). Among the different phenomena occurring when an X-ray radiation interacts within a sample, the atoms (scattering centers), produces spherical waves. Due to a vast phenomenon of destructive interference, almost all the waves cancel each other out. However, it may happen that this interference is constructive for some specific radiation direction or angles. The “*condicio sine qua non*” for which constructive interference occurs is shown by the Bragg’s Law (Equation (15)):

$$n\lambda = 2d \sin\theta \quad (15)$$

where n is a positive integer number, λ is the wavelength of the incident X-Ray radiation, d is the spacing distance between two crystal planes, and θ is the angle of the incident and diffracted X-Ray (scattering angle).

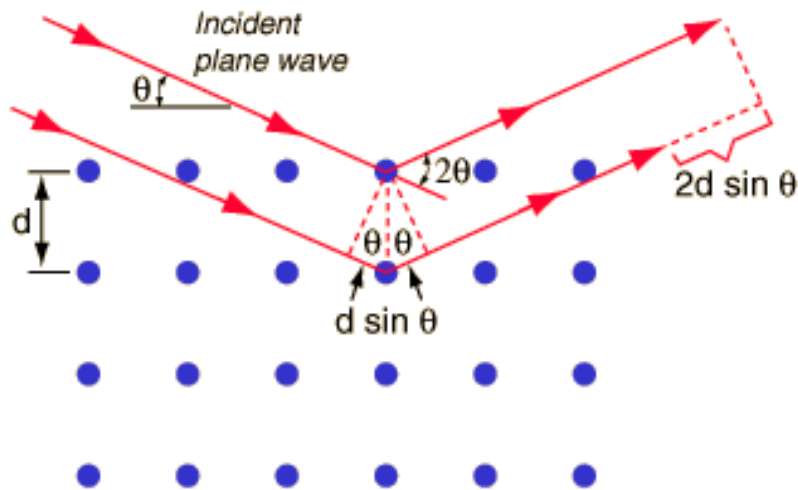


Fig. 2.1 – Graphical representation of Bragg’s Law.

In a typical diffractogram, the signal intensity is plotted against the scattering angle θ or 2θ depending on the geometrical setup of the instrument. The peak positions are characteristic of a given structure and are also dependent on the wavelength of the used source (e.g. Cu, Co, Cr etc.) of the conventional X-ray tubes.

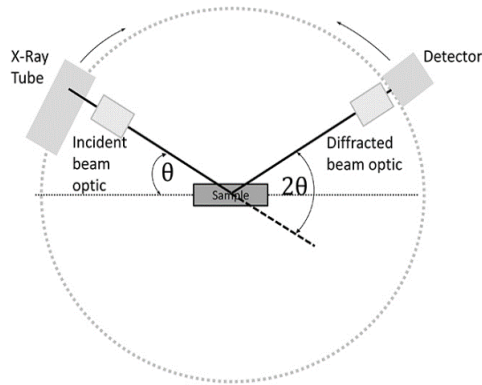


Fig. 2.2 – Schematic drawing of a diffractometer.

From the Intensity vs 2θ angle diffractogram (Fig. 2.3) is it also possible to evaluate the crystallites mean size applying the Scherrer's equation.

$$\tau = \frac{K\lambda}{\beta \cos\theta} \quad (16)$$

Where \mathbf{K} is a dimensionless shape factor (value close to 1), λ is the wavelength of the incident X-Ray radiation, β is the peak width at half the maximum intensity (FWHM), and θ is the Bragg angle.

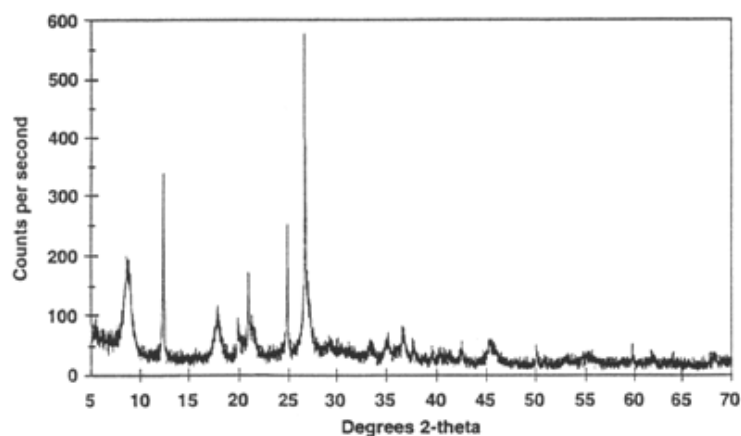


Fig. 2.3 – Example of diffractogram.

2.2 Scanning Electron Microscopy (SEM)

The Scanning Electron Microscope is a useful tool to determine the surface morphology and/or the composition of the specimen. It is based on the interaction of the sample with an accelerated electron beam (energies up to 50 KeV) originated from a stable source of electrons (Electron gun – EG). In a typical SEM, the electron beam is emitted from a LaB₆ or W tip by thermionic effect, or by field emission effect. The use of a Field Emission Gun (FEG) is fundamental in order to increase the brightness (electron current per unit area per unit solid angle) of the instrument. In this case the electrons are extracted from the Tungsten hairpin by electron tunneling and the beam spot size is of the order of nanometers. Once extracted from the EG, the electron beam is demagnified by electron lenses and projected onto the sample surface. The system operates in high vacuum condition ($\approx 10^{-4}$ Pa) since the molecules in the air would otherwise deviate the electron beam path giving a blurred image.

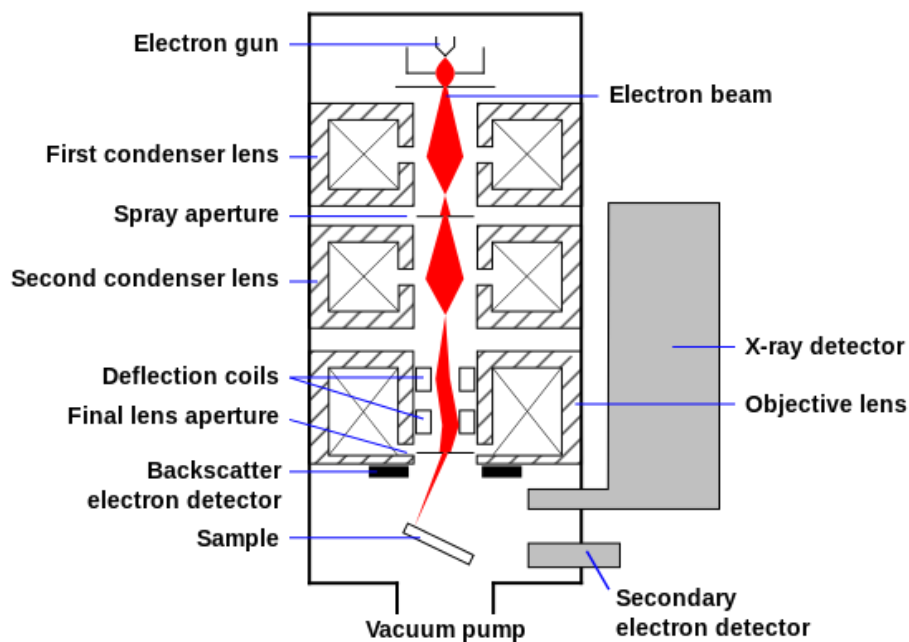


Fig. 2.4 – Schematic drawing of a Scanning Electron Microscope.

The interaction between the primary electron beam and the sample generates an interaction volume depending on beam energy, atomic number and density of the sample. From the interaction volume several signals are emitted (Fig. 2.5). Each signal carries a specific information:

- 🔦 **Secondary electrons (SE):** generated mainly by inelastic scattering (energies ≈ 50 eV). They give morphological information;
- 🔦 **Backscattered electrons (BSE):** They have higher energy than SE. Since their current depends on the atomic number Z , they give compositional information of the sample (composition map);
- 🔦 **X-Rays:** They are generated as consequence of SE emission. They are element specific and give information about the elemental composition of the sample (EPMA – Electron Probe MicroAnalysis)

The electrical conductivity of the sample is a fundamental requirement: the accumulation of electrostatic charge on sample surface gives blurred images, and for this reason the sample must be electrically grounded. In the case of insulant or poorly conductive specimen, the use of a coating applied by low vacuum sputtering (Graphite, Au, Cr, Pt, Os, W, Ir) is mandatory even if part of information of elemental composition is lost.

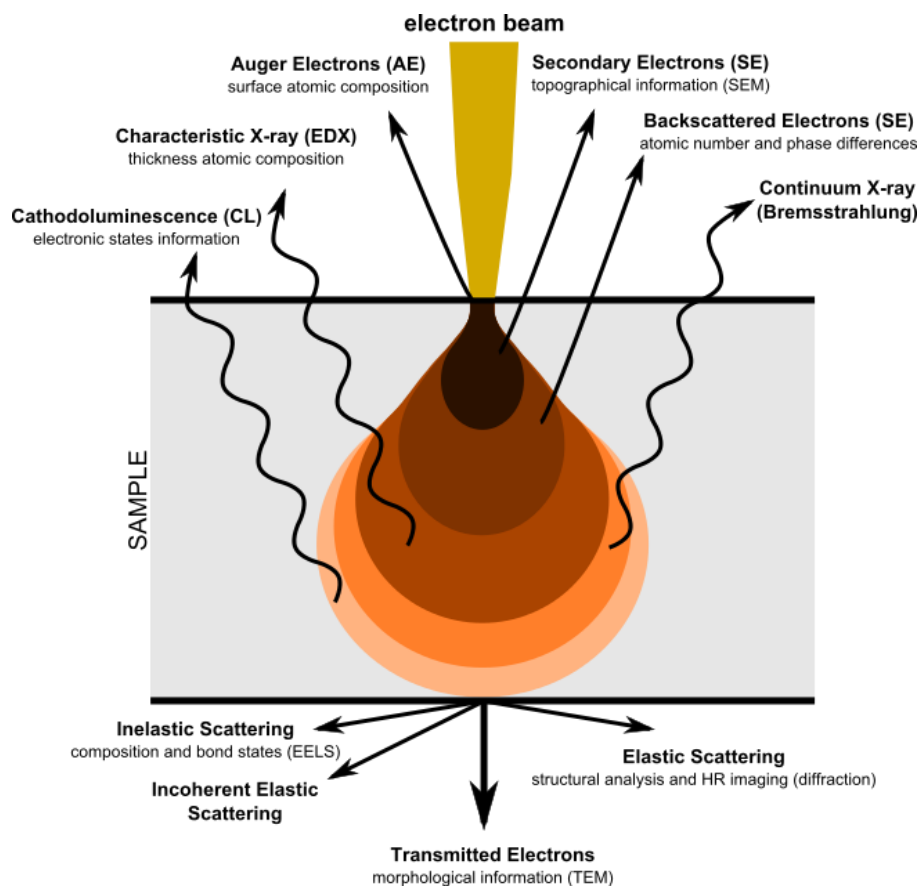


Fig. 2.5 – Interaction volume and emitted signals.

2.3 Transmission Electron Microscopy (TEM)

It is a microscopy technique like the Scanning Electron Microscopy where the electrons beam goes through the specimen. Because of the de Broglie wavelength of the electrons, the Transmission Electron Microscope (TEM) has a very high resolution compared to that of a classic light microscope. The use of a very thin specimen is a fundamental requirement for this technique since the sample has to be “electron transparent”.

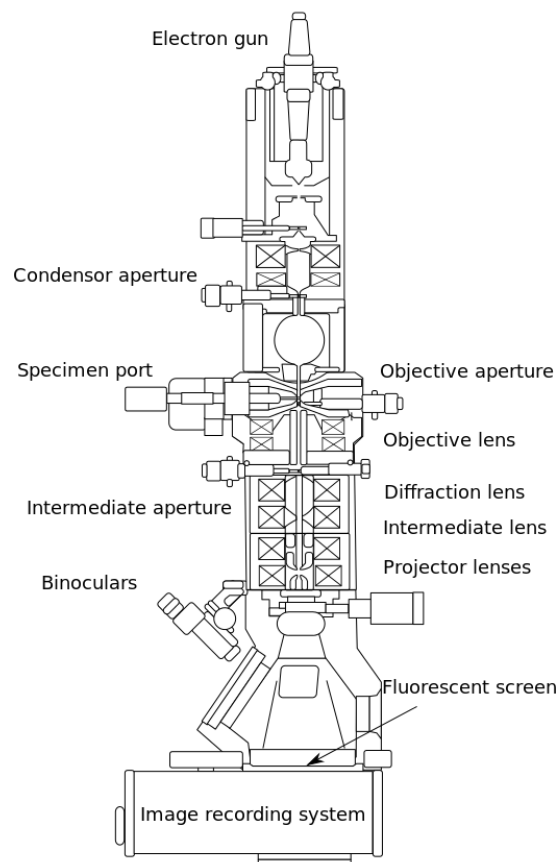


Fig. 2.6 – Schematic drawing of a Transmission Electron Microscope.

The electron beam is focused into a small beam by condenser lens and sent to the specimen. As in the Scanning Electron Microscopy, a vacuum system is essential to avoid that electrons collide with gas atoms. TEM can essentially work in two modes: Imaging and Diffraction. In imaging mode, the objective aperture is in a back focal plane where we can select among central beam (Bright Field image – BF image) or diffracted beam (Dark Field image – DF image).

The selected signal is then projected onto a detector (screen, camera etc.) and the image is obtained. When the SAD aperture is used a diffraction pattern is generated. Single crystal samples will give a pattern of dots meanwhile polycrystalline and amorphous samples will give a series of ring as a response. In both cases, it is possible to get information about the sample structure and space group symmetries.

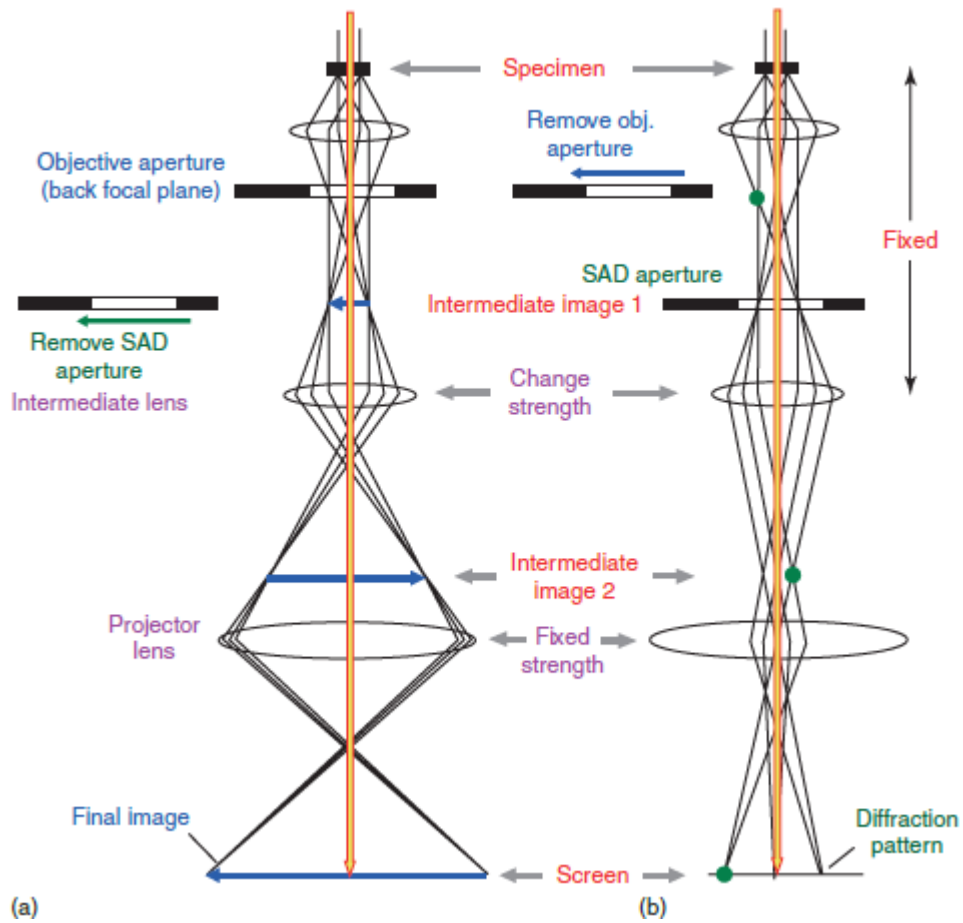


Fig. 2.7 – Imaging (a) and Diffraction (b) modes in Transmission Electron Microscopy.

2.4 Thermogravimetric Analysis (TGA)

TGA is an analytical method belonging to the thermal analysis family in which the mass of a known sample is monitored as a function of a temperature scan. The mass change of the sample is related to the absorption or release of gases at specific temperatures and controlled atmosphere. The instrumentation is composed by a precision electronic balance coupled with a furnace.

The sample holder is a crucible that can be made of Al_2O_3 , Sapphire or Platinum, depending on the operating temperature and reactivity with the sample (e.g. Platinum can easily react with organic substances).

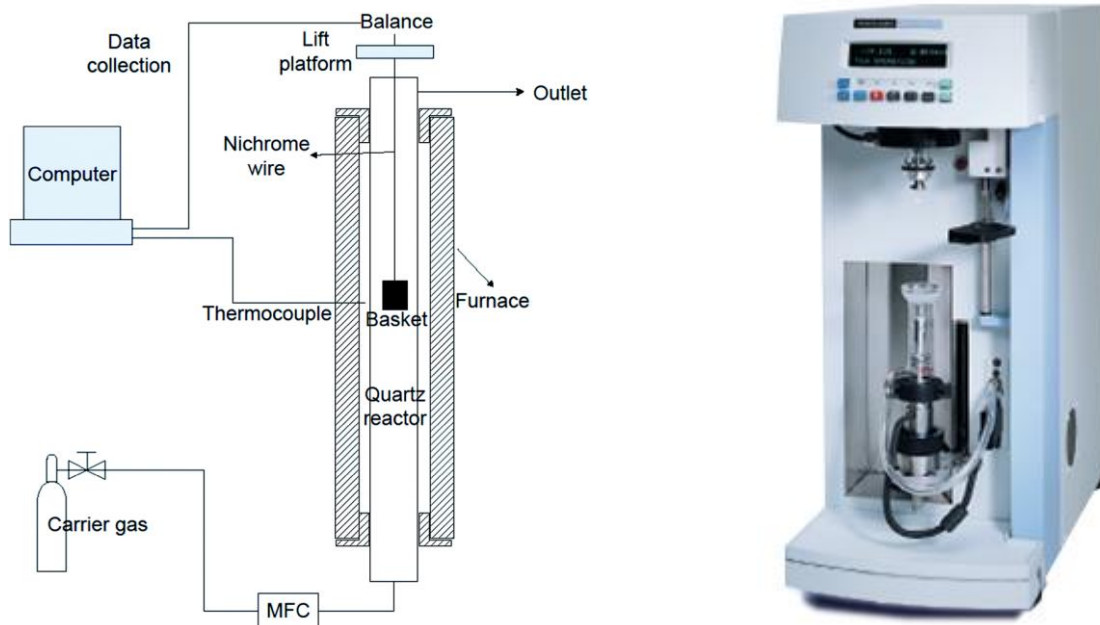


Fig. 2.8 – TGA: Schematic drawing (a) and instrument (at right).

The crucible is connected with the high precision balance and located inside the furnace. The atmosphere of this closed system can be easily controlled by software. The possibility to use reducing (Ar/H_2 mixture), oxidant (air or O_2) or inert (N_2 or Ar) atmosphere allows us to associate specific weight change based on the relative atmosphere. The use of a purge gas helps to increase the instrument's life since any corrosive or harmful gas is carried away from the furnace.

As well as the atmosphere, even the heating mode can be modulated since we can choose between a linear temperature variation (one or more step) or an isothermal measurement where the temperature is kept constant over a specific amount of time.

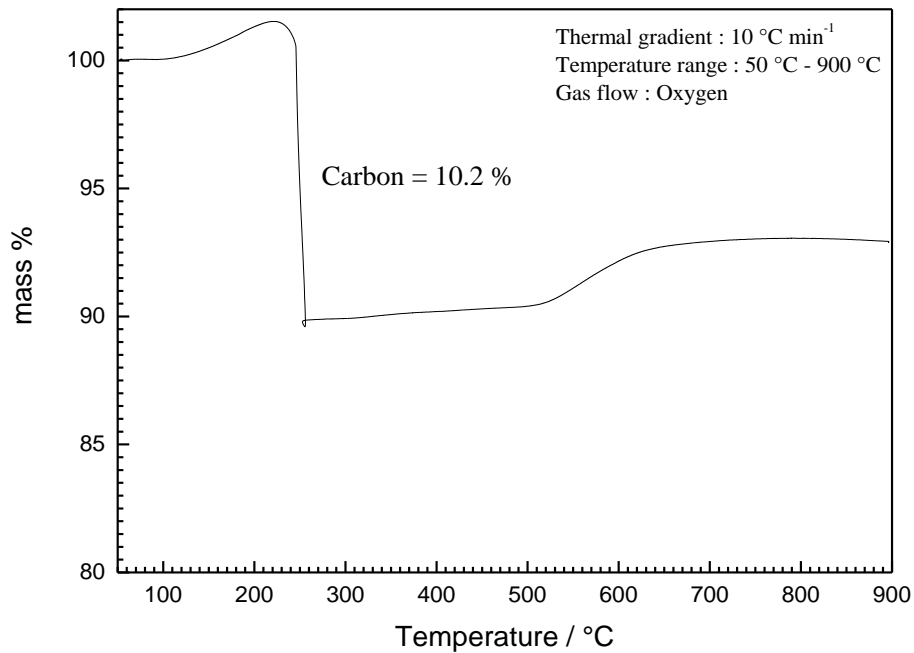


Fig. 2.9 – Example of Mass % vs. Temperature thermogram.

The results obtained from these measurements are plotted in a graph called Thermogram, where the mass variation or mass percentage (y-axis) is plotted versus temperature or time (x-axis).

In Figure 2.9, TGA analysis in oxidant atmosphere is shown for a carbon coated metal oxide. The sudden weight loss around 250 °C is attributable to the $C + O_2 \rightarrow CO_2$ reaction. The weight increase after 500 °C is mainly due to metal oxidation in air/oxygen atmosphere. Other frequent phenomena are the humidity evaporation, volatile solvent evaporation, desorption of crystallization water or thermal decomposition of the sample (pyrolysis).

2.5 IR Spectroscopy (FT-IR)

IR spectroscopy involves molecular vibrational transitions due to the interaction between matter and the infrared radiation with wavelength between 0.78 μm and 1000 μm . This technique based on absorption spectroscopy allows to detect functional groups in a molecule, and the information is mainly of a qualitative nature. The IR radiation absorption is due to the interaction of the oscillating electromagnetic field with the molecular chemical bonds.

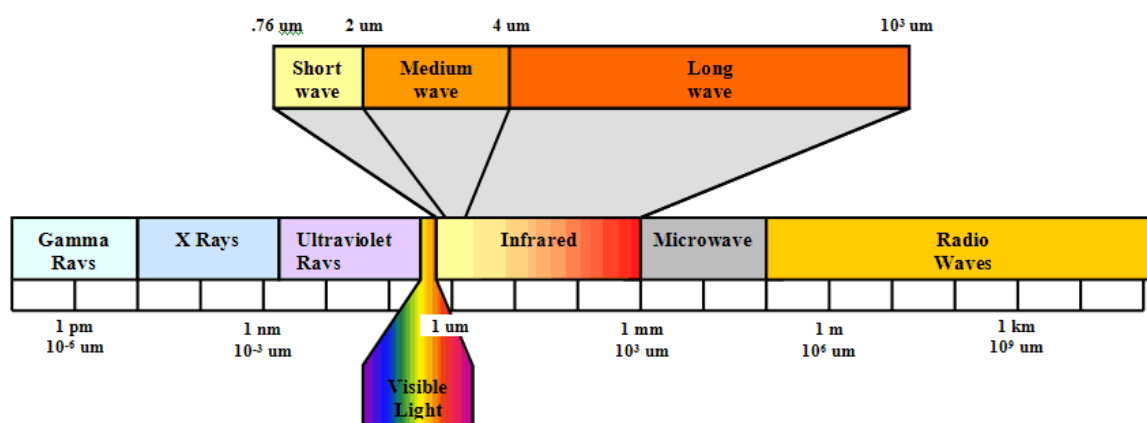


Fig. 2.10 – IR wavelength range.

These chemical bonds can be considered as harmonic oscillators and from a derivation of Hooke's law it is possible to obtain the equation governing this phenomenon:

$$\bar{\nu} = \frac{1}{2\pi c} \sqrt{\frac{k}{\mu}} \quad (17)$$

where $\bar{\nu}$ is the oscillation wavenumber (cm^{-1}), c is the speed of light (m/s), k is the spring constant for the bond (corresponding to the strength of the bond), and μ is the reduced mass calculated as follow:

$$\mu = \frac{m_A \cdot m_B}{m_A + m_B} \quad (18)$$

where m_A and m_B are the atomic masses of the bonded atoms A and B.

The fundamental condition for the IR radiation absorption is a dipolar momentum variation that can exchange energy with the radiation producing an oscillating electric field. IR spectra are usually reported in a graph with the IR light absorbance (or transmittance) on the y-axis versus wavenumber on the x-axis. Different functional groups show different absorption bands in the graph, whereas the zone from 400 cm^{-1} to 1000 cm^{-1} is known as fingerprint region, which is specific of the analyzed molecule.

Bond type	Functional group	Wavenumber range (cm^{-1})
C-H	Alkanes	2850-2960
		1350-1470
C-H	Alkenes	3020-3080
		675-1000
C-H	Aromatic rings	3000-3100
		675-680
C=C	Alkenes	1640-1680
C=C	Aromatic rings	1500-1600
C-O	Alcohols, Carboxylic acids, Esters, Ethers	1080-1030
C=O	Aldehydes, Ketones, Carboxylic acids, Esters	1690-1760
O-H	Alcohols, Phenols, Carboxylic acids	3610-3640
		2500-3000

Table 2a – IR absorptions table.

The recent application of the Fourier-transform to the Infrared Spectroscopy allowed to have faster results with a higher signal-to-noise (S/N) ratio.

2.6 Inductively Coupled Plasma Mass Spectrometry (ICP-MS)

It is an atomic emission spectroscopy technique where the detector is a mass spectrometer. This technique allows to detect elements at concentration in the order of ppq (part per quadrillion – $1/10^{15}$) with higher speed, precision and sensitivity than by Atomic Absorption Spectroscopy (AAS).



Fig. 2.11 – ICP-MS instrument.

This particular type of Atomic Emission Spectroscopy (AES) exploits the high temperature of plasma sources (6000 - 10000 K) to ionize and excite the sample aerosol localized in the plasma toroidal fireball. The subsequent cooling at 6000-7000 K returns the sample to the ground state emitting spectral lines. Because of the plasma fireball, ICP analysis has many advantages compared to the other spectroscopic techniques:

- 🔦 The plasma toroidal shape increases the sample permanence in the plasma increasing the sensibility of the measurement;
- 🔦 The temperature homogeneity is higher in the plasma than in the traditional flame
- 🔦 The high operating temperature of plasma allows a more complete ionization. Besides, the absence of a flame avoids the presence of oxides and hydroxides;
- 🔦 The total absence of electric circuits gives a negligible background;

The ions ejected from the ICP are analyzed simultaneously by a Mass Spectrometer (MS) and separated according to their mass/charge ratio (m/z) thanks to a quadrupole mass analyzer (QMA).

Typical causes of error are:

- 🔦 Isobaric interference, different element with same m/z ratio (e.g. Ca, Ar have $m/z = 40$)
- 🔦 Polyatomic interference, molecular species or ions with double charge (e.g. $^{40}\text{Ar}^{16}\text{O}^+$ and $^{56}\text{Fe}^{2+}$)
- 🔦 Matrix effect, due to salts or non-volatile solids.

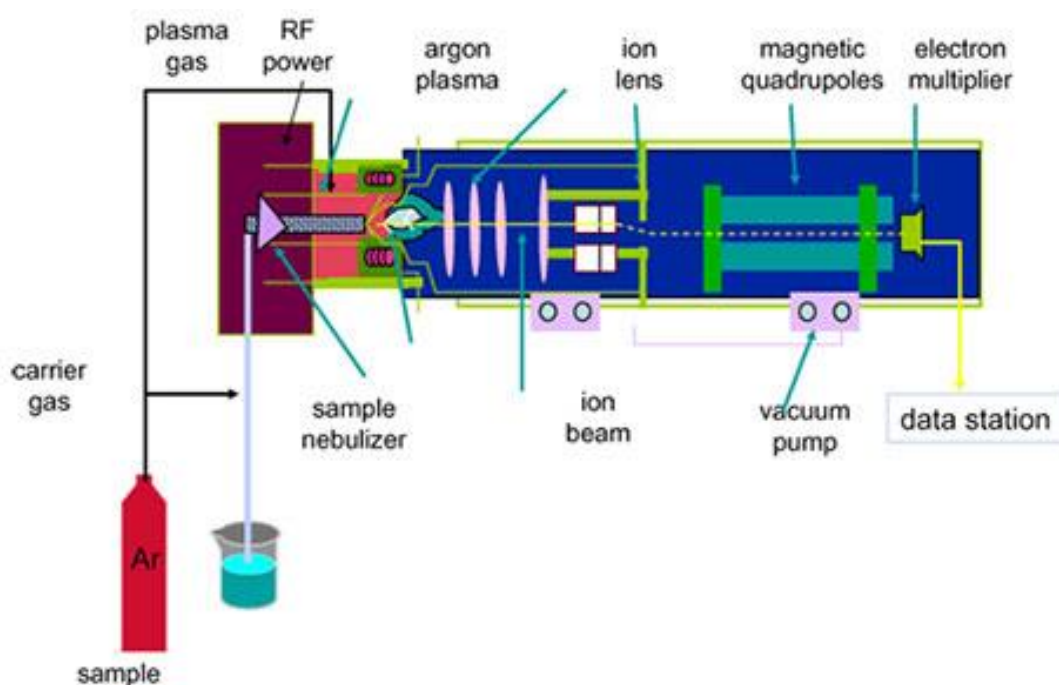


Fig 2.12 – Schematic drawing of a ICP-MS.

A crucial factor is interfacing between CP and MS. This is possible through the use of a skimmer, where the ions are subjected to a step by step dispersion, sent to the QMA, analyzed based on their m/z ratio, and revealed by a detector that translates their signal in amplified electric current.

2.7 Zeta Potential measurement

The Z-potential (ZP) also known as electrokinetic potential is the measure of the attractive/repulsive electrostatic forces between particles in colloidal dispersion (insoluble particles dispersed in another substance, e.g. slurry). It is usually denoted with the Greek letter zeta (ζ) and measured in millivolts (mV). The ZP is an indicator of the colloidal stability. High ZP values (negative or positive) mean great electrostatic repulsion between adjacent particles in a colloidal dispersion. When ZP values are low (negative or positive), the attractive forces between particles are predominant, therefore the particles tend to coagulate/flocculate.

Every object exposed to a fluid has an electrical double layer (EDL) that refers to the two ion layers surrounding the object surface. The first layer is usually connected to the object through chemical interactions whereas the second (diffuse layer) is loosely connected via coulombic forces. The study of this layer is really important since it affects the electrokinetic characteristics of these materials. This EDL has a specific differential capacitance (C) which is one of the parameters to characterize this phenomenon. The differential capacitance is the ratio between the surface charge of the object and its electric surface area [C (farad) = charge (coulomb) / potential (volt)].

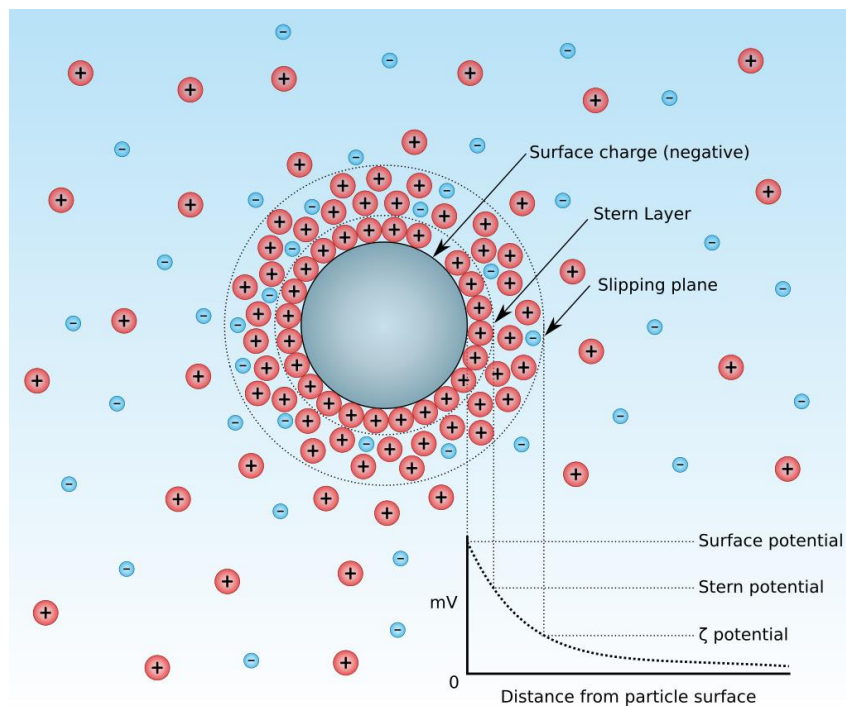


Fig. 2.13 – Potential vs. Distance graph for a charged particle in a dispersion medium.

Several models have been proposed during years to determine the potential dependence (Helmholtz, Gouy-Chapman, Stern). In the case of ζ potential, the electric potential taken in consideration is in proximity of the slipping plane (Fig. 2.12) which is a conventional layer that separates the mobile fluid from the fixed fluid attached to the object surface. This technique has been used to determine the slurry stability since agglomeration has to be avoided. Using the same dilution, it is possible to compare different slurries in order to have an idea of possible improvements due to the recipe or slurry formulation. Typical ZP values are listed in the table below [77,78].

Zeta potential [mV]	Stability behavior
from 0 to ± 5	Rapid coagulation/flocculation
from ± 10 to from ± 30	Incipient stability
from ± 30 to from ± 40	Moderate stability
from ± 40 to from ± 60	Good stability
more than ± 61	Excellent stability

Table 2b – Zeta potential ranges table.



Fig. 2.14 – Instrument for Zeta potential measurement.

2.8 Rheological Tests

Rheology is a branch of physics which deals with the deformation and flow of liquid or solid materials when a force is applied. It is of paramount importance in battery production, since the slurry rheological properties greatly influences the coating process and thus the electrode performances. The rheological characterization of the slurries has been carried out by the means of a steady state flow experiment. Slurries are non-Newtonian fluid where the viscosity is dependent on the shear rate and the relationship between viscosity and shear-rate is the following:

$$\eta = K \cdot \gamma^{n-1} \quad (19)$$

where η is the viscosity (Pa s^{-1}), K is a constant, γ is the shear rate (s^{-1}), and n the flow behaviour index.

In pseudo-elastic materials ($n < 1$) the viscosity decreases with increasing shear rate, whereas in dilatant fluids ($n > 1$) the viscosity increases with the shear rate [79]. In order to have a comparison and meaningful values between the different slurries, in our tests, we took into account the viscosity values at a shear rate of $1 \text{ Pa}\cdot\text{s}$.



Fig. 2.15 – Rheometer.

2.9 Electrochemical Techniques

2.9.1 Cyclic Voltammetry (CV)

CV is an electrochemical technique used to get quantitative and qualitative information from an electrochemical reaction. In cyclic voltammetry, a potential window is set and scanned linearly in cyclic phases by a linear voltage scan ($V s^{-1}$). This will result in a triangular profile of the potential wave (Fig. 2.16, left). When a charge-transfer reaction (CT) occurs, an increase of current will appear at a specific voltage.

During the analysis, the potential is controlled between reference and working electrodes, while the current is measured between the working and the counter electrodes. This means that the cell setup for this analysis is a three-electrode setup. A typical voltammogram the current response (y-axis) is plotted versus the applied potential (x-axis) resulting in characteristics peaks of each redox reaction (Fig. 2.16, right).

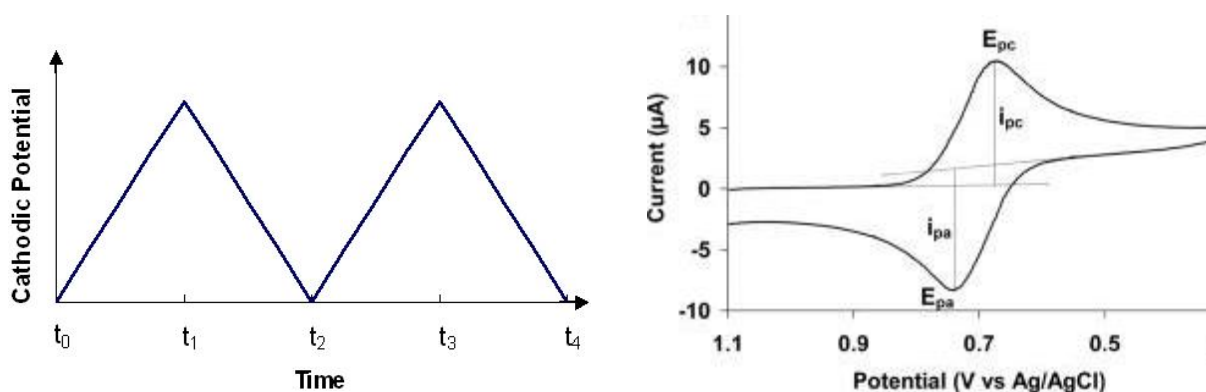


Fig. 2.16 – Potential vs. Time graph (on the left) and Current vs. Potential graph (on the right).

When the electrochemical process is governed by diffusion processes (semi-infinite linear diffusion) the peak current values are affected by the concentration gradients and governed by the Randles-Sevcik equation:

$$i_p = 0.4463nFAC_0 \left(\frac{nF}{RT} \right)^{1/2} (v)^{1/2} (D)^{1/2} \quad (20)$$

where i_p is the peak current (A), n is the number of electrons involved in the redox process, F is the Faraday constant ($C\ mol^{-1}$), A is the electrode surface area (cm^2), C_0^* is the analyte concentration ($mol\ cm^{-3}$), R is the gas constant ($8.311\ J\ mol^{-1}\ K^{-1}$), T is the temperature (K), v is the scan rate ($V\ s^{-1}$), and D is the diffusion coefficient ($cm^2\ s^{-1}$).

Using equation 20, it is possible to determine the diffusion coefficient value plotting the peak current (i_p) against $v^{1/2}$. When the diffusion coefficient is known, the slope of the line in the graph gives information about the stoichiometry of the redox process.

In case of reversible process at 25 °C, the anodic and cathodic peak currents have the same absolute value ($|i_{pa}|=|i_{pc}|$) and their potential difference (ΔE_p) is given by the following equation:

$$\Delta E_p = |E_{pa} - E_{pc}| = \frac{0,058}{n} \quad (21)$$

where n is the number of electrons transferred in the process.

Since many redox processes are not reversible, it can happen that the potential difference between the two redox peaks increases. In order to determine the formal redox potential, it is possible to calculate the half-wave potential ($E_{1/2}$):

$$E_{1/2} = \frac{(E_{pa} + E_{pc})}{2} \quad (22)$$

2.9.2 Galvanostatic Cycling with Potential Limitations (GCPL)

The galvanostatic cycling with potential limitation (GCPL) is a galvanostatic technique where the electrochemical cell is charged and discharged under a controlled current within an established potential window. The GCPL is very useful to determine the charge/discharge behavior and the cycle life of a battery under one or more applied current values. The applied current is controlled between working (WE) and counter (CE) electrodes, meanwhile the potential is recorded, between WE and a third, reference electrode (RE) for three-electrode cells, or between WE and CE for two-electrode cells.

The use of a three-electrode setup is required when a more precise monitoring of electrodic potential is needed, since the measurement is not affected by iR drop. This technique is based on Nernst equation (Equation (23)), which expresses the equilibrium potential assumed by an electrode in a given system.

$$E = E^0 + \left(\frac{RT}{nF}\right) \ln\left(\frac{[Ox]}{[Red]}\right) \quad (23)$$

where E^0 is the standard potential, R is the universal gas constant ($8.311 \text{ J mol}^{-1} \text{ K}^{-1}$), T is the temperature (K), n is the number of exchanged electrons, F is the Faraday constant (C mol^{-1}), and $[Ox]/[Red]$ are molar concentrations of the oxidized and reduced species in solution.

Figure 2.16 shows the current profile for a galvanostatic cycle: the applied current can be positive or negative respectively for the charge and the discharge cycles. The current is applied until the potential limit set for the analysis is reached.

The typical graph obtained from this analysis is an electrode potential vs. time (or amount of charge) graph (galvanostatic profiles). Depending on the redox process, the potential (E) vs time (t) curve can have different shape. If a single-phase reaction (solid-solution) takes place, the potential changes continuously the redox process, whereas in a two-phase reaction the potential remains quite stable during the phase transition resulting in a plateau.

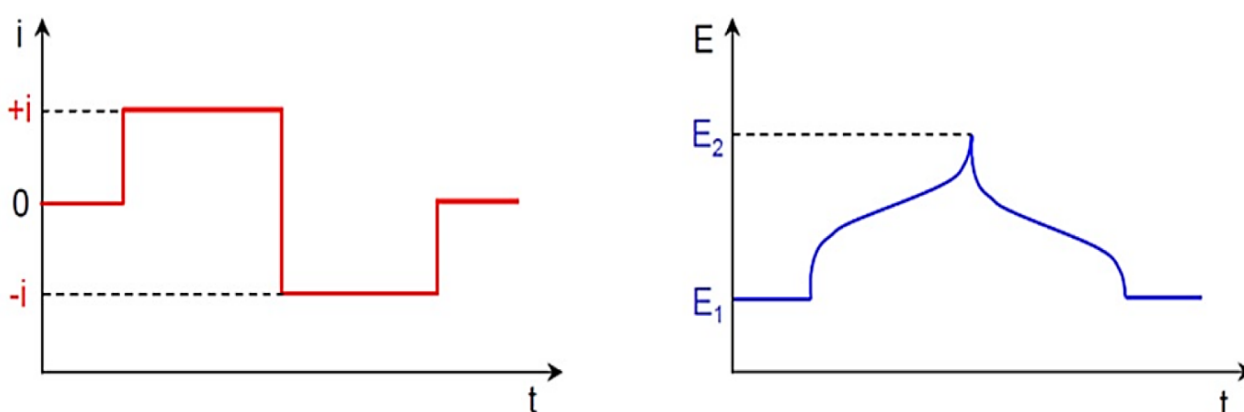


Fig. 2.17 – Current vs Time graph (on the left) and Potential vs. Time graph (on the right).

The differential analysis of the galvanostatic profiles (Fig. 2.18) allows to study the electrode redox processes: each peak has a specific potential and area that helps to understand the charge/discharge mechanism and the involved exchange of charge.

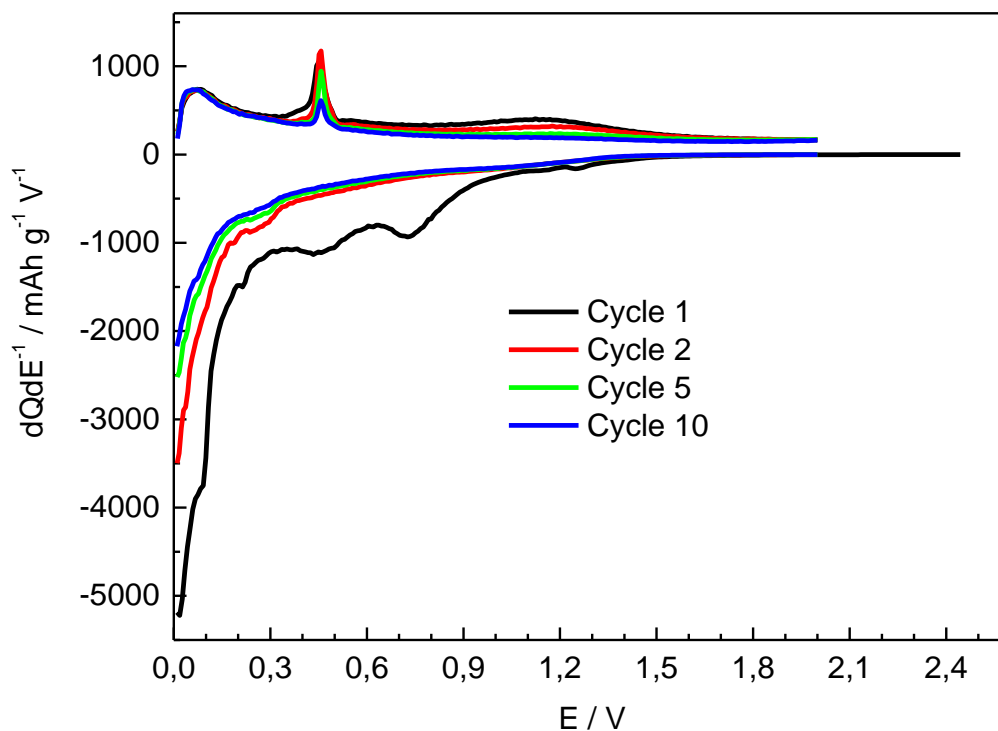


Fig. 2.18 – dQ/dE vs. Potential graph.

The most common way to define the rate at which a battery can be charged and/or discharged is the C-Rate (C/h, where h is the number of hours necessary to fully charge/discharge the battery). From the galvanostatic cycling other parameters can be evaluated:

- 🔋 **Practical Specific Capacity**, is the weight-normalized capacity value of the material. It is usually different from the theoretical specific capacity and it is measured in mAh g^{-1} .
- 🔋 **Coulombic efficiency (CE)**, is the ratio between the discharge capacity ($Q_{\text{discharge}}$) and the charge capacity (Q_{charge}). It is an index of the reversibility of the redox process ($\text{CE} = 1 \rightarrow$ process fully reversible, but only from the charge point of view; for the energy-related reversibility also the potentials at which charge and discharge take place have to be considered).

- 🔦 **Rate capability**, is very useful to determine the electrode response to different current. By varying the applied C-rate, it is possible to evaluate the capacity response at different current and identify possible electrode polarization phenomena.
- 🔦 **Cycling life**, is the life of the cell before it becomes unusable under given testing conditions. The threshold value for the cell usability is commonly set at 80% of its initial capacity. The main key factors influencing the cycling life are time, temperature, storing conditions and number of charge/discharge cycles.

2.9.3 Electrochemical Impedance Spectroscopy (EIS)

The electrochemical impedance spectroscopy (EIS) is one of the best tools to unravel the interfacial kinetics of electrode material and the resistive elements in electric devices. The main processes occurring at electrodes interface are charge-transfer reaction, ohmic conduction, interfacial charging and mass transfer phenomena. During this analysis, a small sinusoidal AC potential perturbation with frequency ν is applied to the electrochemical system. The response is a sinusoidal current with the same frequency but shifted in phase. The wave shift (θ) is specific of the circuital elements corresponding to the polarization processes involved in the studied system.

$$E(t) = E_0 \sin(\omega t) \quad (24)$$

where $E(t)$ is the potential at time t , E_0 is the signal amplitude, and ω (radian/second) is the angular frequency related to the AC perturbation frequency (Hertz) by the following relationship:

$$\nu = \frac{\omega}{2\pi} \quad (25)$$

In order to obtain a linear response, a very small AC perturbation frequency is mandatory, and as already said, the current response will have a different value and will be shifted in phase (θ). For sufficiently low currents, the impedance depends only on the AC perturbation frequency.

$$I(t) = I_0 \sin(\omega t + \theta) \quad (26)$$

Since the impedance takes in account the resistance concept in AC circuits, the impedance calculation can be obtained from the Ohm's law:

$$Z = \frac{E(t)}{I(t)} = \frac{E_0 \sin(\omega t)}{I_0 \sin(\omega t + \theta)} = Z_0 \frac{\sin(\omega t)}{\sin(\omega t + \theta)} \quad (27)$$

where Z_0 is the impedance value, and θ its phase shift.

Using the complex number notation, the equation (27) can be written as follow:

$$Z(\omega) = Z e^{-j\theta} = Z_0(\cos \theta - j \sin \theta) = Z_{real} - jZ_{im} \quad (28)$$

where j is the imaginary unit ($j = \sqrt{-1}$).

Plotting the impedance imaginary part ($-\text{Im}(Z)$) versus the real part ($\text{Re}(Z)$), results in a Nyquist plot, whereas the length of the $|Z|$ vector correspond to the absolute impedance value.

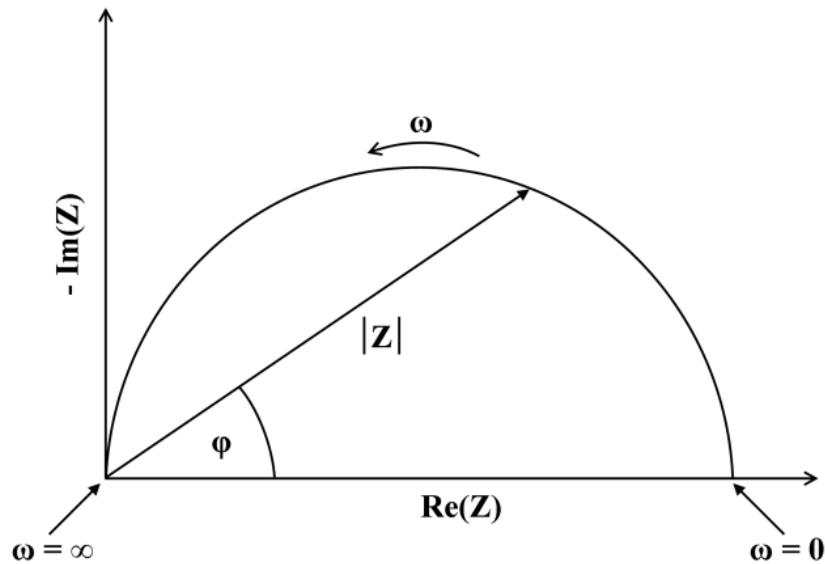


Fig. 2.19 – Nyquist plot.

EIS can be fitted by relating the electrode behavior to the electrical response of a so-called “equivalent circuit” model, in which the processes taking place are described by using common circuit elements such as those listed in the table:

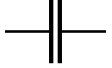
Component	Symbol	Current vs. Voltage	Impedance
Resistor		$V = I \cdot R$	$Z = R$
Capacitor		$I = C \frac{dV}{dt}$	$Z = \frac{1}{j\omega C}$
Inductor		$V = L \frac{dI}{dt}$	$Z = j\omega L$

Table 2c – Circuit elements.

From the previous table it is possible to see how the resistor impedance is not dependent on frequency and has not imaginary part, the capacitor impedance increases as frequency decreases, and the inductor impedance increases as frequency increases. These circuit elements often behave in a non-ideal way, and thus they can be approximated with a “Circuit Phase Element” (CPE). The CPE value is defined by the following equation:

$$Z = A(j\omega)^{-\alpha} \quad (29)$$

where **A** and **α** are system parameters, and **α** can range from 1 to -1:

- 🔋 If $\alpha = 0$, then $Z = R$ and CPE behaves as a resistor;
- 🔋 If $\alpha = 1$, then $Z = 1/j\omega C$ and CPE behaves as a capacitor;
- 🔋 If $\alpha = -1$, then $Z = j\omega L$ and CPE behaves as an inductor;
- 🔋 If $\alpha = 0.5$, then $A = R_D (1/\tau^{1/2})$ where R_D is the diffusion resistance, τ the time of diffusion process, and CPE is called Warburg Impedance (W).

Each interface in the electrochemical system reacts in a different way to the sinusoidal excitation. The typical chemical and physical processes that result in an impedance in a Lithium-ion battery are:

🔦 **Electrolyte resistance (R_e):** It is due to the electrolyte, and is usually influenced by temperature, electrolyte ionic concentration, ions type and cell geometry. This resistance is defined as:

$$R = \rho \frac{l}{A} \quad (30)$$

where ρ is the resistivity of the electrolyte ($\Omega \cdot \text{cm}$), l is the length (cm), and A is the electrode surface area (cm^2).

🔦 **Charge-transfer resistance (R_{ct}):** due to the electrons transfer at the electrolyte/electrode interface. The rate of this electron transfer process depends on temperature, potential, type of reaction and concentration of reaction products. The potential and the current in a charge-transfer process are related by Butler-Volmer equation.

$$i = i_0 \left(\exp \left(\alpha \frac{nF}{RT} \eta \right) - \exp \left(-(1 - \alpha) \frac{nF}{RT} \eta \right) \right) \quad (31)$$

Where i is the electrode current density (A m^{-2}), i_0 is the exchange current density (A m^{-2}), α is the anodic charge transfer coefficient (dimensionless), n the number of electrons involved in the reaction, F is the Faraday constant (96485 C mol^{-1}), η is the activation overpotential, R is the universal gas constant ($8,31 \text{ J K}^{-1} \text{ mol}^{-1}$), and T is the absolute temperature (K).

When the electrochemical system is at equilibrium and the overpotential (η) is small, the charge-transfer resistance can be calculated from:

$$R_{ct} = \frac{RT}{nFi_0} \quad (32)$$

🔦 **Double layer capacitance (C_{dl}):** It is due to the charge accumulation at electrode/electrolyte interface and it is influenced by potential, temperature, ionic concentrations, ions type, electrode roughness, impurity etc. Since this results in an electrical double layer, this element will behave like a capacitor;

- 🔦 **SEI capacitance (C_{SEI}) and resistance (R_{SEI}):** they are due to accumulation at the surface of and to migration through the electrode passivation layer. C_{SEI} capacitance is due to the SEI geometry at the electrode/electrolyte interface;
- 🔦 **Warburg Impedance (W):** it is due to the ion diffusion and depends on the AC sinusoidal frequency. On a Nyquist plot, it usually appears as a diagonal line with a 45° slope.

When a real system is investigated, the impedance response is the sum of these different elements connected in series and/or in parallel. It is important to recall that the impedance of element in series is the sum of the single element, meanwhile the impedance of elements in parallels is the reciprocal of the sum of the reciprocal impedances.

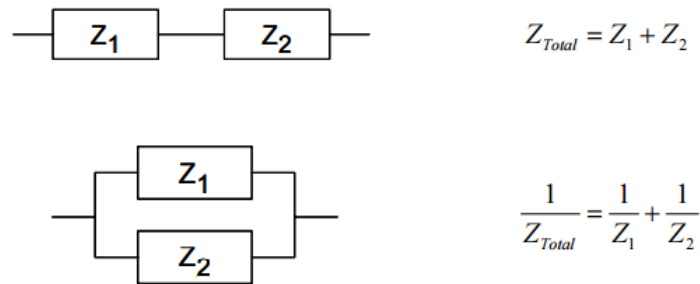


Fig. 2.20 – Impedance values of element in series and in parallel.

The EIS data are usually fitted in terms of an equivalent circuit. The fitting procedure is usually performed by software (e.g. Boukamp's software [80]) where the experimental data are processed to obtain the equivalent circuit parameters. The parameter estimation is performed by applying a non-linear least squares fitting algorithm (NLLS), usually starting from a graphical fit of the Nyquist plots.

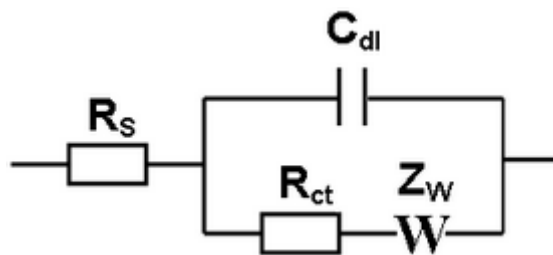


Fig. 2.21 – Randles equivalent circuit.

Chapter 3 – Silicon@V₂O₅ composite as anode for LIBs

3.1 Introduction

The search for increasingly efficient and safe energy storage systems has led to the attempt to replace traditional battery materials with new lithium storage chemistries. The demand for greater energy density is leading to replace the graphite-based anodes with the more abundant, cheap, performant, and environmentally-friendly silicon. Although the high specific capacity (3579 mAh g⁻¹ corresponding to Li₁₅Si₄ phase), the electrochemical performances fade drastically upon cycling, because of the huge volume changes experienced by this active material. Several attempts have been made to buffer this volume expansion, and the most common is the use of silicon nanoparticles dispersed in a buffering matrix such as graphite or the more performing graphene. Because of the high cost and instability of the graphene, the use of a cheaper and more stable inorganic matrix has been evaluated. Amorphous vanadium pentoxide (a-V₂O₅) is here proposed as buffering matrix because of its layered structure that mimics that of graphene.

3.2 Experimental

3.2.1 Si@V₂O₅ synthesis

Crystalline o-V₂O₅ was dispersed in 50 mL of ultrapure water, and 50 mL of hydrogen peroxide (H₂O₂ 50% w/w solution) were added slowly. To avoid excessive foaming and bubbling, an ice bath was used to control and lower the temperature of this very exothermic reaction. A previously sonicated silicon nanoparticles aqueous solution was added when the solution color turned clear orange and the O₂ bubbling stopped. After 3 days of aging, the resulting gelled solution was washed several times with acetone and oven-dried overnight at T = 60 °C. Eventually, the obtained powder was subjected to a final thermal treatment in a tubular furnace under air atmosphere (T = 220 °C, 24h, 2 °C min⁻¹). For sake of comparison, bare V₂O₅ was synthesized with the same procedure without the silicon addition step.

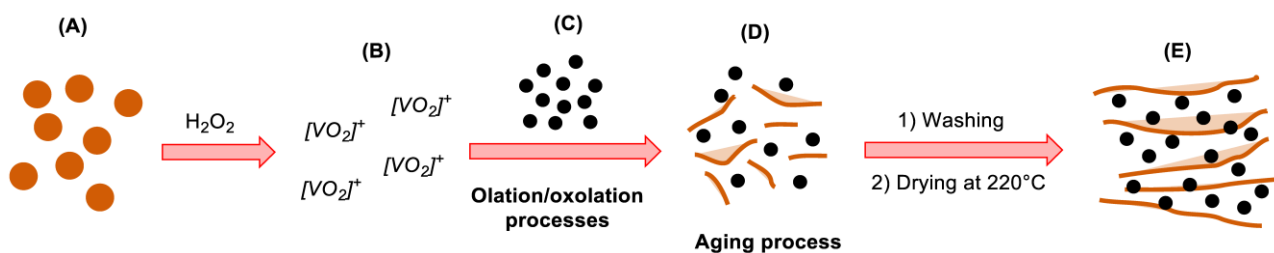


Fig 3.1 – Synthetic route of Si@V₂O₅ nanocomposite. (A) Crystalline o- V₂O₅; (B) [VO₂]⁺ ions which give olation and oxolation processes; (C) Si nanoparticles; (D) Intermediate Si@ V₂O₅ nanocomposite; (E) Final Si@ V₂O₅ nanocomposite.

3.2.2 Electrodes Preparation

Electrode slurries have been prepared in a glass vial using a magnetic stirrer overnight. The mass ratios are summarized in the table below.

	Si@V ₂ O ₅ -PAA_#1		V ₂ O ₅ -PAA_#1	
Active Material:	Si@V ₂ O ₅	70 %	V ₂ O ₅	70 %
Binder:	Poly(acrylic acid) - PAA (M _w ≈ 450000)	10 %	Poly(acrylic acid) - PAA (M _w ≈ 450000)	10 %
Conductive Agent:	Super C65	20%	Super C65	20%
Solvent:	Ethanol	---	Ethanol	---

Table 3a – Electrode formulations of Si@V₂O₅-PAA_#1 and V₂O₅-PAA_#1 coatings.

The resulting slurry has been spread onto a 10 μm thick copper foil using the “Doctor Blade technique” and dried on a heating plate for 2h at 70 °C. 9mm-diameter circular electrodes have been cut and calendared at 7 tons cm⁻¹ using a hydraulic press. The average active material loading was ≈ 1 mg cm⁻².

3.2.3 Cell Assembly and Cycling

Three electrode Swagelok-type polypropylene cell were assembled in an Ar-filled glovebox, using metallic lithium as counter and reference electrodes, and 12 mm-diameter glass fiber disks (Whatman GF/A) as separators. A mixture of Ethylene Carbonate:Dimethyl Carbonate (EC:DMC) 1:1 v/v (Solvionic, France) + LiPF₆ 1M solution has been used as “baseline” electrolyte. The use of different amounts of vinylene carbonate (VC) as electrolyte additive has been evaluated.

The cells have been cycled using a VMP-2Z multi-channel electrochemical workstation (Biologic, France) in a 0.01 < E (V) < 1.5 potential window, using specific current ranging from 100 mA g⁻¹ to 4000 mA g⁻¹. All the cells have been kept 12h at open circuit voltage (OCV) to enable a full wetting of separator and electrodes. All the measurements have been recorded at room temperature. All potentials are given vs. Li⁺/Li redox couple.

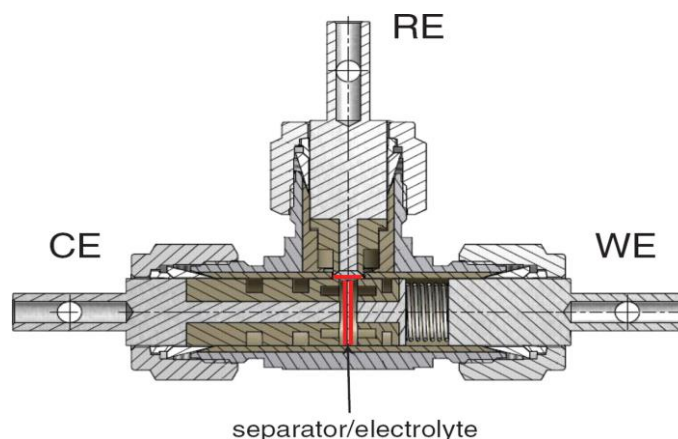
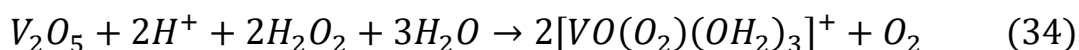
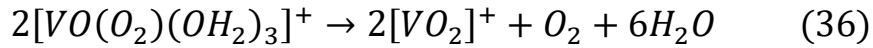
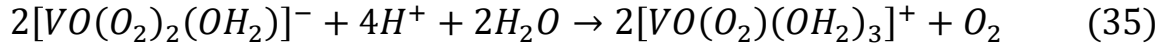


Fig 3.2 – Scheme of a Three electrode Swagelok-type polypropylene cell.

3.3 Discussion

When the crystalline vanadium pentoxide reacts with the hydrogen peroxide solution, peroxy- and diperoxy-vanadium species are formed, which eventually lead to [VO₂]⁺ ions as already discussed by Livage et al. (Eqns. 33-36) [81,82].





Eventually, $[VO_2]^+$ species gives V_2O_5 amorphous fibers ($V_2O_5 \cdot nH_2O$) by olation and oxolation reactions. The addition of the silicon nanoparticles allows the vanadium pentoxide gel to grow around them providing an optimal silicon dispersion in the resulting composite. The final thermal treatment at 220 °C allows to remove part of the characteristic hydration water trapped in the amorphous vanadium pentoxide structure [83], and obtain a partial crystallinity of the V_2O_5 structure, since its crystallization start at 216 °C [84]. The diffraction pattern of the $Si@V_2O_5$ nanocomposite is shown in Fig. 3.3. Panel (A) shows all the bare V_2O_5 diffraction peaks (panel (B)), together with the principal crystalline silicon diffraction peaks (JCPDS 27-1402) corresponding to [111], [220], and [311] reflection planes.

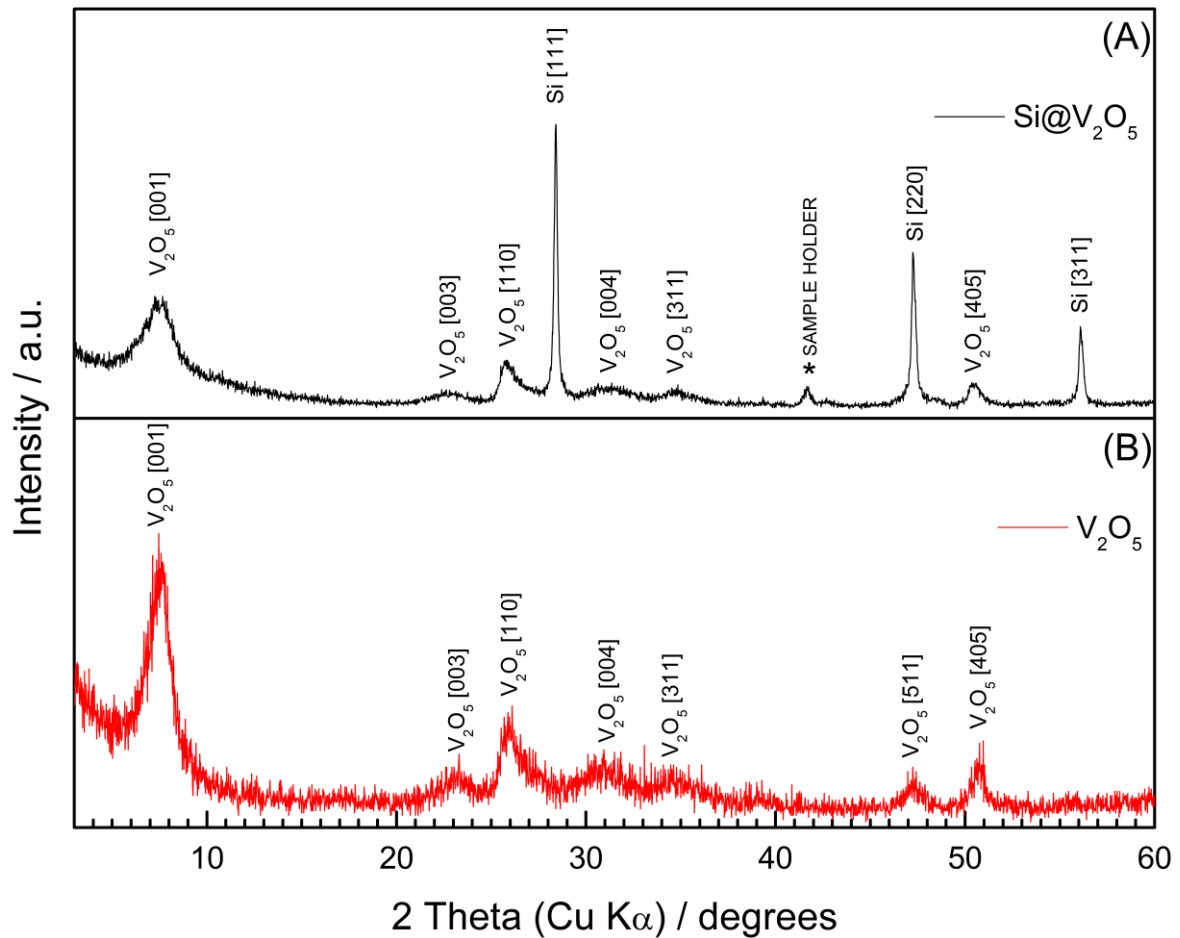


Fig 3.3 – XRD pattern of: (A) $Si@V_2O_5$ nanocomposite; (B) V_2O_5 .

The extra peak labelled with an asterisk (*) is due to the instrument sample holder. The presence of broadened peaks is typical of materials lacking a long-range order, furtherly confirming that this material has a “lower crystalline domain” of ill-crystalline structure [85,86]. According to Scherrer’s equation [87], an average silicon crystallite size of about 75 nm has been estimated from the peak related to the [111] reflection plane. The average silicon crystallite size around 70 nm and their dispersion in the vanadium pentoxide nanosheet is confirmed by TEM images (Fig. 3.4 a-b). This morphology is furtherly confirmed by SEM micrographs (Fig. 3.4 c-d). The same nanosheet morphology is present in the bare V_2O_5 (Fig. 3.4 e-f), suggesting a good reproducibility for the synthesis of this inorganic matrix. The reported morphology is consistent with literature findings [88].

$Si@V_2O_5$ microstructure has been explored using Raman spectroscopy. The silicon crystallinity is revealed by the main band around 500 cm^{-1} and confirmed by the presence of two bands at 295 cm^{-1} and 921 cm^{-1} respectively [89]. The vanadium pentoxide contribution is partially masked by the higher intensity of silicon bands, but still traceable by the presence of two bands at 147 cm^{-1} and 422 cm^{-1} [85,86,88]. The Si:V weight ratio in the nanocomposite was revealed by OCP-MS analysis. The silicon content of 39% w/w is in a 30% ~ 40% range known as an optimal compromise between high specific capacity and matrix buffer ability [90].

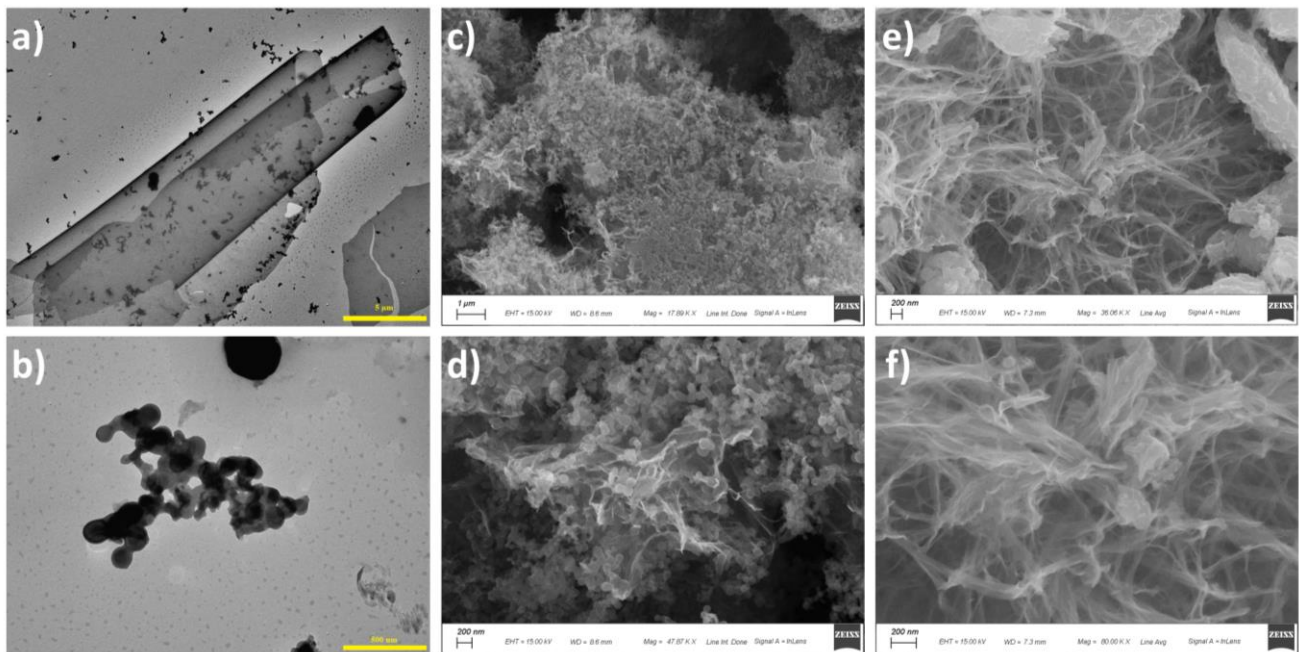


Fig 3.4 – Morphological and structural characterization of $Si@V_2O_5$ and V_2O_5 : (a) – (b) TEM micrographs of $Si@V_2O_5$; (c) – (d) SEM micrographs of $Si@V_2O_5$; (e) – (f) SEM micrographs of V_2O_5 .

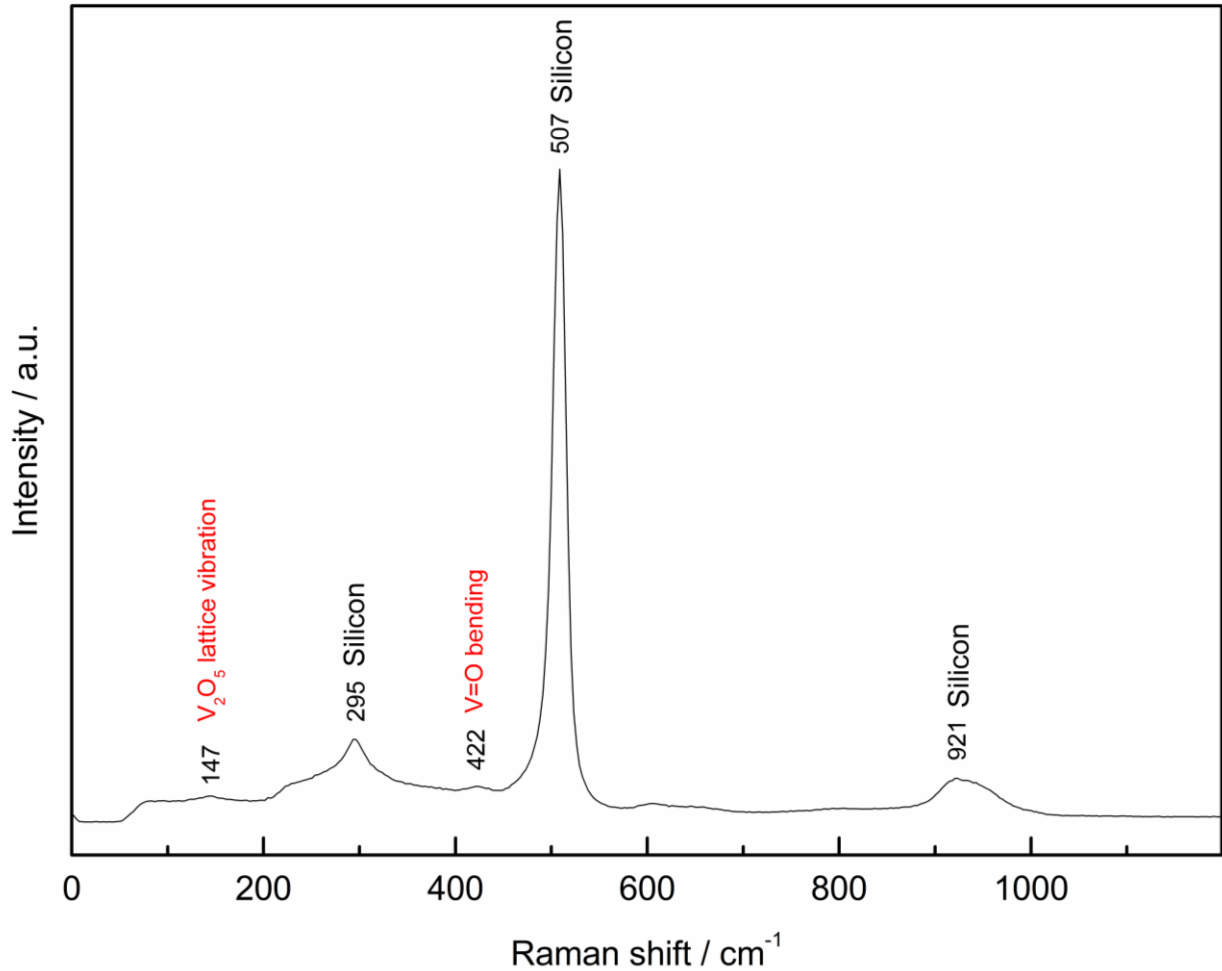


Fig 3.5 – Raman spectra of Si@V₂O₅ nanocomposite.

Several electrochemical tests were carried out to investigate the redox behavior and the lithium storage ability of the Si@V₂O₅ nanocomposite. Fig. 3.6 shows the Si@V₂O₅ voltammetric curves carried out in the 0.01 < E (V) < 1.5 potential range at a 0.1 mV sec⁻¹ scan rate. Peak (A) is a typical first-cycle process of the silicon-based anodes: the crystalline silicon is lithiated forming an amorphous a-Li_xSi_y phase [91]. Since the lower cut-off value is lower than 50 mV, the formation of a crystalline Li₁₅Si₄ phase results in the peak (G), which in the first cycle is masked by the prominent peak (A). During dealloying, the disappearance of a-Li_xSi_y and c- Li₁₅Si₄ phases, to form a-Si, results in peak (B) and (C) respectively. From the second cycle on, the a-Si alloying processes (E) and (F) are coupled with peaks (B) and (D) during the dealloying of a-Li_xSi_y phases.

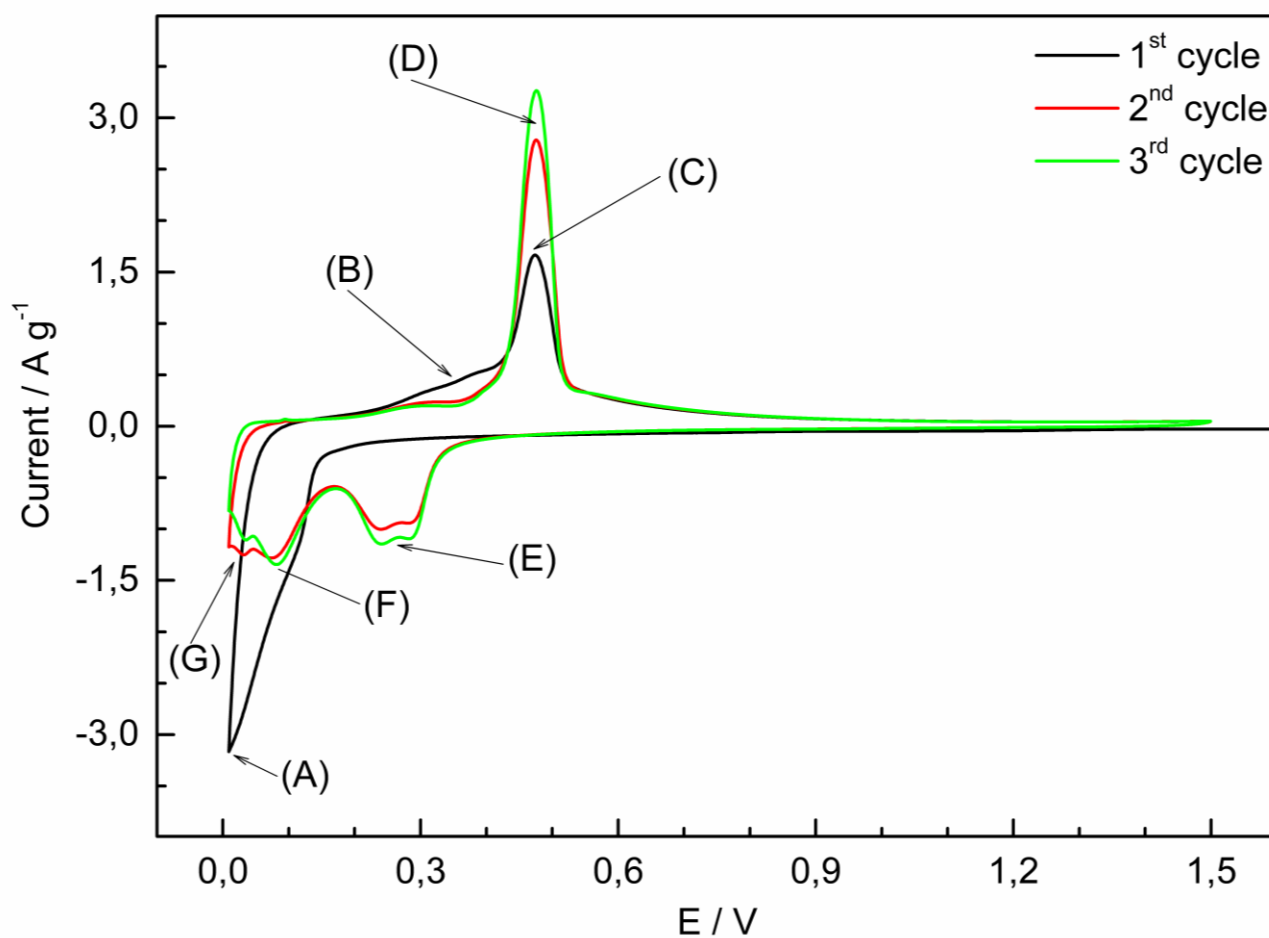


Fig 3.6 – Cyclic voltammogram of Si@V₂O₅ nanocomposite. 0.01 < E (V) < 1.5 potential range. Scan rate = 0.1 mV sec⁻¹. Electrolyte: LiPF₆ 1M in EC:DMC 1:1.

Peak	Potential	Description
(A)	0.015 V	1 st cycle alloying : c-Si → a-Li _x Si _y
(B)	0.35 V	Dealloying : a-Li _x Si _y → a-Si
(C) - (D)	0.47 V	Dealloying : c-Li ₁₅ Si ₄ → a-Si
(E) - (F)	0.26 V – 0.08 V	Alloying : a-Si → a-Li _x Si _y
(G)	0.04 V	Formation of c-Li ₁₅ Si ₄ phase

Table 3b – Peaks description of the Si@V₂O₅ cyclic voltammetry (Fig. 3.6).

In the studied potential range, V_2O_5 electrochemical activity is not evidenced. Nevertheless, low-potential lithium intercalation by vanadium pentoxide has been reported in literature [92], and from the bare V_2O_5 cyclic voltammetry (Fig. 3.7) it is possible to confirm a minor contribution to redox processes.

In order to estimate the charge/discharge ability of the $Si@V_2O_5$ and the possible contribution of bare V_2O_5 to the electrochemical activity, electrodes based on both materials have been subjected to galvanostatic cyclations. Figure 3.7a shows the capacity values comparison between the composite and the bare vanadium pentoxide in the $0.01 < E \text{ (V)} < 1.5$ potential range, at a specific current $I = 500 \text{ mA g}^{-1}$.

The $Si@V_2O_5$ electrode shows an initial specific capacity of 1840 mAh g^{-1} , then a reversible capacity around 1150 mAh g^{-1} with a capacity retention of 43% at 50th cycle. After an initial specific capacity of 645 mAh g^{-1} , the V_2O_5 electrode shows a reversible capacity around 100 mAh g^{-1} . In both cases, the high initial irreversible capacity is most likely due to the SEI formation on the anode surface, and in the case of the $Si@V_2O_5$ electrode to the silicon amorphization in the first cycle. This confirms that the capacities of the V_2O_5 nanosheets and of the conductive agent are only a minor contribution of the total nanocomposite capacity. Part of the vanadium pentoxide electrochemical activity in the nanocomposite is evidenced in figure 3.7b. A sloping plateau is visible around $E = 2.5 \text{ V}$ probably due to the Li^+ insertion inside the V_2O_5 nanosheets. Eventually, a long sloping plateau is visible from 0.1 V to the lower cut off potential, due to the amorphization of the c-Si nanoparticles to a- Li_xSi_y phase.

The dQ/dE^{-1} vs. E plot in figure 3.7c are consistent with the behavior observed in the cyclic voltammetry of $Si@V_2O_5$ (Fig. 3.6).

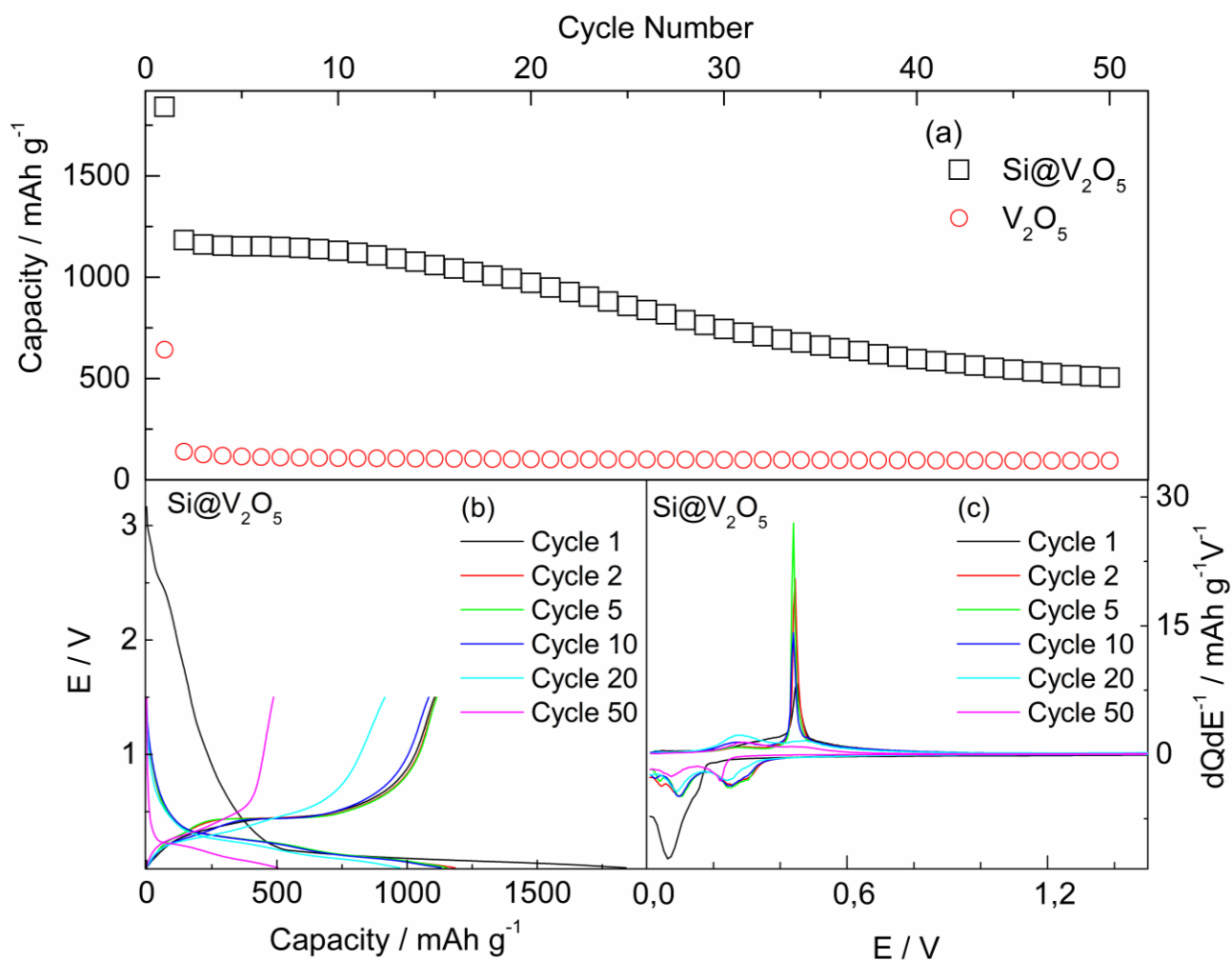


Fig. 3.7 – (a) Discharge capacity values of Si@V₂O₅ and V₂O₅ electrodes. (b) Galvanostatic E vs. Q profiles of Si@V₂O₅ electrode. (c) Differential profiles dQ/dE^{-1} vs. E of Si@V₂O₅ electrode. $I = 500 \text{ mA g}^{-1}$. $0.01 < E$ (V) < 1.5 potential range.

For the sake of comparison, Fig. 3.8 reports the E vs. Q profiles at 500 mA g^{-1} specific current (b) and the corresponding differential dQ/dE^{-1} vs. E plot (c) of the bare V₂O₅ electrode. This confirms that this inorganic matrix can contribute to the initial irreversible capacity, meanwhile its contribution to the reversible capacity is negligible. We should say that the capacity fade of the Si@V₂O₅ nanocomposite could be ascribed to a poor interfacial stability of the composite.

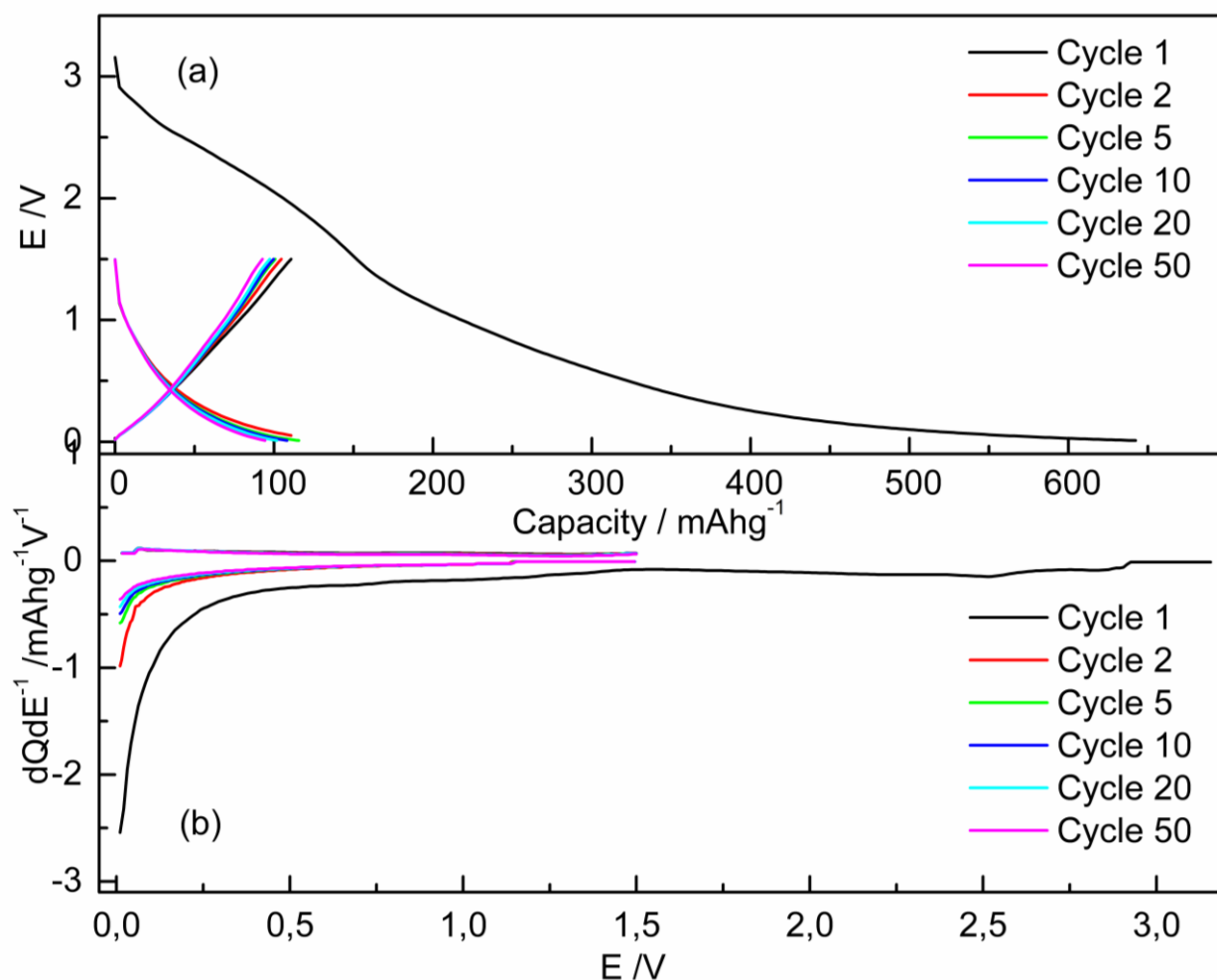


Fig. 3.8 – (b) E vs. Q and (c) differential $dQ dE^{-1}$ vs. E profiles of V_2O_5 -PAA anode. $0.01 < E (V) < 1.5$ potential range. $I = 500 \text{ mA g}^{-1}$.

When the electrode/electrolyte interface is not optimized, the stability of the solid electrolyte interphase can be affected resulting in breakage and re-formation processes during cycling. For this reason, a more stable and uniform passivation layer is fundamental to increase cycle efficiency and capacity retention. The use of electrolyte additives is one of the most used and common method to this aim. The addition of different amount of vinylene carbonate (VC) to the standard LiPF_6 1M in EC:DMC 1:1 electrolyte has been evaluated. Vinylene carbonate is a cyclic alkyl carbonate with a polymerizable double bond. It is known as a reduction-type additive [93] since its higher reduction potential than the standard electrolyte component [94] allows the pre-formation of a smoother and stable passivation layer. VC has already shown to be effective in improving the SEI stability on silicon-based anodes [30,95,96].

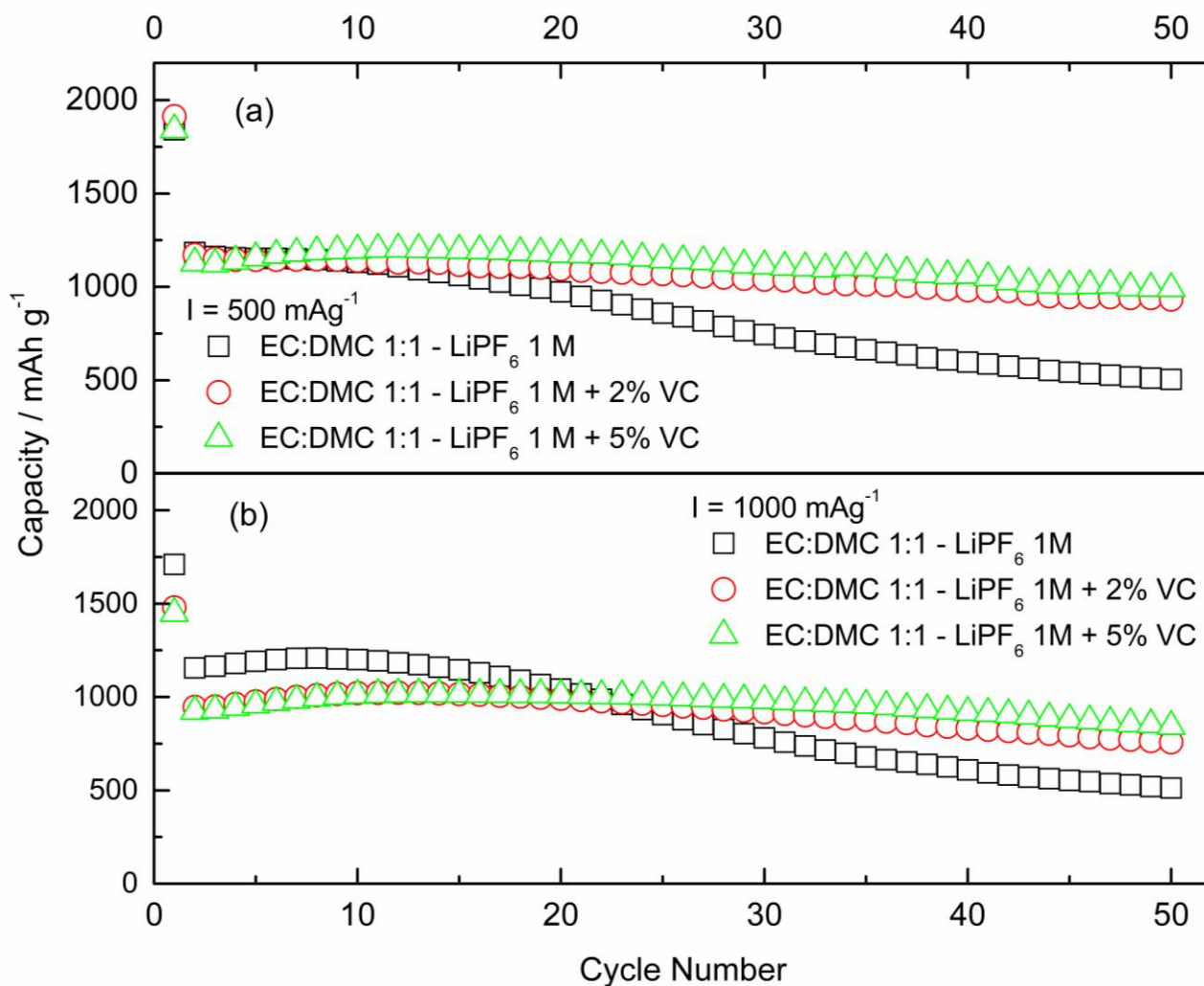


Fig. 3.9 – Discharge capacity values of Si@V₂O₅ electrode in LiPF₆ 1M in EC:DMC 1:1, LiPF₆ 1M in EC:DMC 1:1 + 2% VC, LiPF₆ 1M in EC:DMC 1:1 + 5% VC. 0.01 < E (V) < 1.5 potential range. (a) I = 500 mA g⁻¹; (b) I = 1000 mA g⁻¹.

The discharge capacity values at 500 mA g⁻¹ and 1000 mA g⁻¹ for the three different electrolyte formulations are shown in Figure 3.9 and listed in the Table 3b. At both applied currents, the addition of VC results in better capacity retention values than the standard electrolyte. This confirms that the use of VC in silicon-based electrodes can help mitigating the performance decay thanks to the improved electrode/electrolyte interface. Fig. 3.10 shows the rate capability test result of Si@V₂O₅ anode for the three different electrolyte formulations. When the applied current is in the 100 mA g⁻¹ to 500 mA g⁻¹ range, the specific capacity values are comparable to the galvanostatic cycles in figure 3.9. The use of the two VC-based electrolyte results in similar behaviors and provides better results than standard electrolyte.

When the current is in the 1000 mA g⁻¹ to 4000 mA g⁻¹ range, the 2% VC formulations shows slightly better results than the 5% VC formulation. This is most likely due to the higher VC amount which forms a thicker SEI passivation layer resulting in a higher cell polarization at higher current. Nevertheless, both VC-based formulations contribute in SEI stabilization giving reversible capacities of about 850 mAh g⁻¹ and 770 mAh g⁻¹, respectively for 2% VC and 5% VC formulation at 4000 mA g⁻¹ current. It is worth noting that restoring the specific current of 500 mA g⁻¹, both electrodes cycled in the VC-based formulations show a good capacity recovery.

Electrolyte	Charge/Discharge current	Discharge Capacity at 50th cycle	Capacity retention
LiPF ₆ 1M in EC:DMC 1:1	500 mA g ⁻¹	504 mAh g ⁻¹	42.5%
LiPF ₆ 1M in EC:DMC 1:1 + 2% VC	500 mA g ⁻¹	932 mAh g ⁻¹	79.5%
LiPF ₆ 1M in EC:DMC 1:1 + 5% VC	500 mA g ⁻¹	991 mAh g ⁻¹	87.9%
LiPF ₆ 1M in EC:DMC 1:1	1000 mA g ⁻¹	512 mAh g ⁻¹	44.3%
LiPF ₆ 1M in EC:DMC 1:1 + 2% VC	1000 mA g ⁻¹	759 mAh g ⁻¹	80%
LiPF ₆ 1M in EC:DMC 1:1 + 5% VC	1000 mA g ⁻¹	842 mAh g ⁻¹	91%

Table 3c – Specific discharge capacity values for galvanostatic cycling in electrolytes with 0%, 2%, 5% w/w VC contents. I = 500 mA g⁻¹; 1000 mA g⁻¹. Capacity retention values are calculated with respect to the reversible capacity obtained at 2nd cycle.

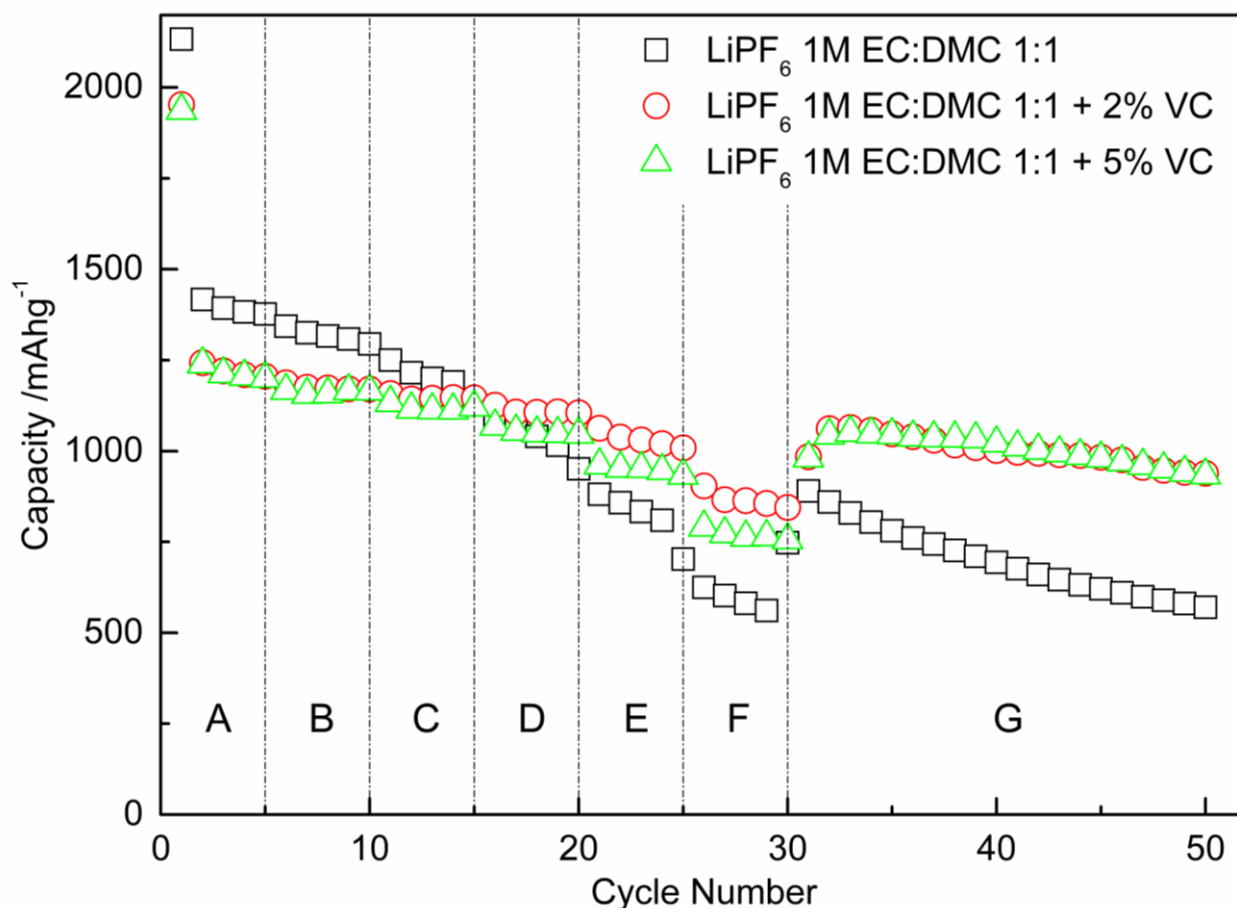


Fig. 3.10 – Rate capability behaviour of $\text{Si@V}_2\text{O}_5$ anode in electrolyte formulations at different VC % contents. $0.01 < E \text{ (V)} < 1.5$ potential range. (A) $I = 100 \text{ mA g}^{-1}$; (B) $I = 200 \text{ mA g}^{-1}$; (C) $I = 500 \text{ mA g}^{-1}$; (D) $I = 1000 \text{ mA g}^{-1}$; (E) $I = 2000 \text{ mA g}^{-1}$; (F) $I = 4000 \text{ mA g}^{-1}$; (G) $I = 500 \text{ mA g}^{-1}$.

This behavior is confirmed by E vs. Q profiles of selected cycles (3rd cycle at 200, 500, and 1000 mA g^{-1}) for the $\text{Si@V}_2\text{O}_5$ electrodes in the three electrolyte systems. In Figure 3.11, all the Li-Si alloying/dealloying features are practically overlapped, highlighting that the differences in rate capability behavior do not arise from different redox processes. Considering the capacity values at low currents, the presence of a thicker SEI could increase the anode polarization and result into lower capacity values. Nevertheless, at higher currents the VC stabilizing effect becomes more relevant. The electrode cycled in the standard electrolyte shows a more pronounced capacity fade, most likely associated with electrode pulverization and electrical isolation of active material. The electrode cycled in the 2% VC-modified electrolyte appears to be the best trade-off between low polarization and cycling stability.

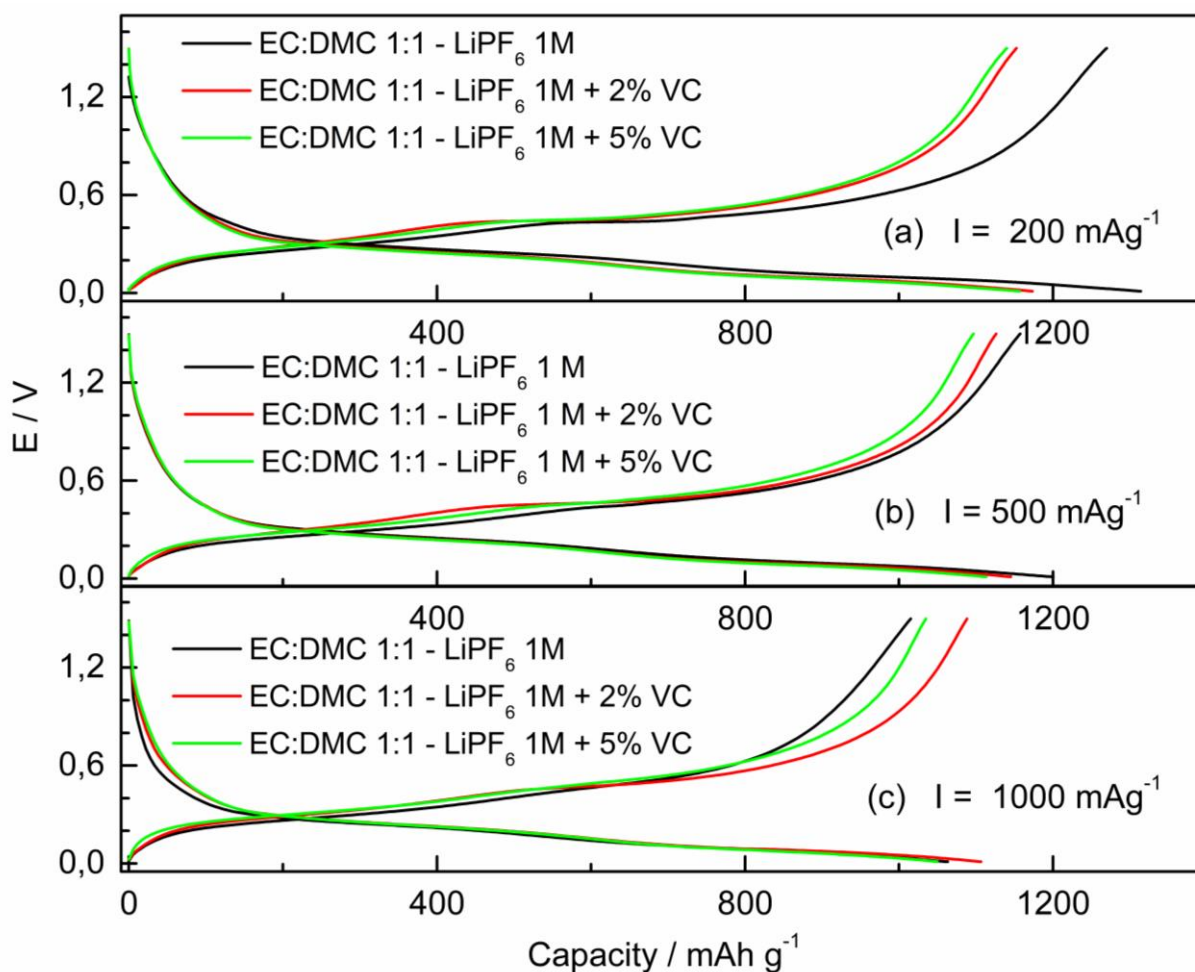


Fig. 3.11 - Selected E vs. Q profiles of $\text{Si@V}_2\text{O}_5$ anode. $0.010 < E$ (V) < 1.500 . (a) $I = 200 \text{ mA g}^{-1}$; (b) $I = 500 \text{ mA g}^{-1}$; (c) $I = 1000 \text{ mA g}^{-1}$.

The different electrode/electrolyte interfacial behaviors of the $\text{Si@V}_2\text{O}_5$ composite in the three electrolyte formulations have been examined as well by the use of post-mortem scanning electron microscopy. Fully discharged electrodes, that underwent 50 galvanostatic cycles in the three different electrolyte formulations, have been disassembled in an Ar-filled glovebox and washed repeatedly with pure dimethyl carbonate (DMC). Fig. 3.12 shows the post mortem SEM micrographs of these three electrodes compared to a pristine electrode. The morphology of the pristine electrode (Fig. 3.12a) is characterized by a compact surface with a relevant number of pores in line with the PAA/ethanol slurry processing [72]. The post mortem SEM of the $\text{Si@V}_2\text{O}_5$ electrode cycled in the VC-free electrolyte (Fig. 3.12b) shows a high degree of grain agglomeration together with deep cracks, a clear signature of the mechanical stress due to the silicon volume expansion.

However, electrodes cycled in 2% VC- and 5% VC-modified electrolyte (Fig. 3.12 c-d) show a much lower aggregation degree and less cracking. Particularly, the electrode cycled in the 2% VC-modified electrolyte shows a lower degree of clustered particles on its surface, confirming the great impact of the VC on the morphology of the electrode surface.

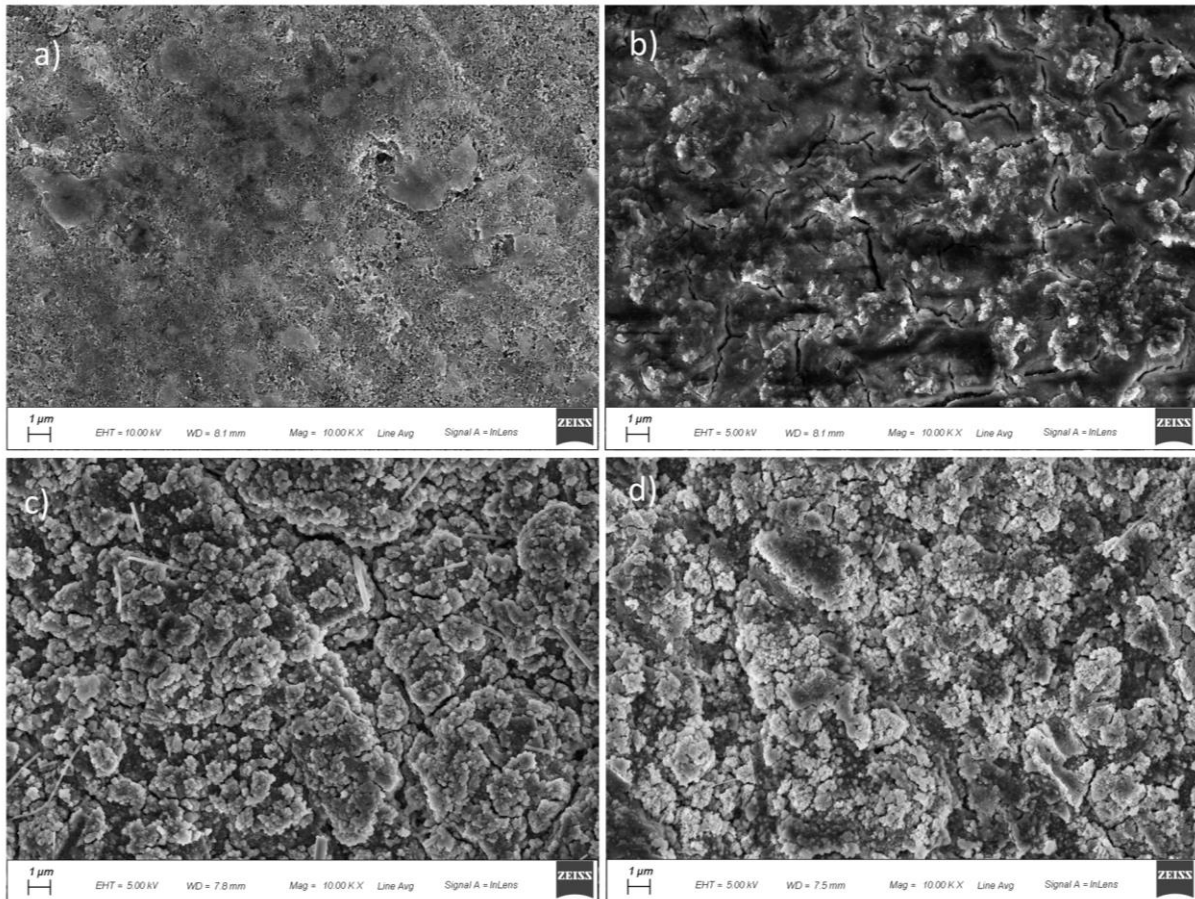


Fig. 3.12 – Scanning electron microscopy of Si@V₂O₅ electrodes. (a) Pristine electrode; (b) electrode cycled in LiPF₆ 1M in EC:DMC 1:1; (c) electrode cycled in LiPF₆ 1M in EC:DMC 1:1 + 2% VC; (d) electrode cycled in LiPF₆ 1M in EC:DMC 1:1 + 5% VC.

3.4 Conclusion

A reproducible and easy synthetic route for the wrapping of silicon nanoparticles inside an amorphous V₂O₅ nanosheets matrix has been presented. The Si@V₂O₅ nanocomposite has been structurally and morphologically characterized, and the electrodes have been prepared following an optimized and low-impact procedure based on Polyacrylic Acid and ethanol. The addition of VC-modified electrolyte resulted in a greater cycling stability respect the VC-free electrolyte.

This optimized system delivered capacity values higher than 900 mAh g^{-1} through 50 cycles at 500 mA g^{-1} current. Also, an outstanding rate capability was obtained in the 100 mA g^{-1} to 4000 mA g^{-1} range. Electrochemical and post-mortem SEM characterizations confirmed that the best $\text{Si@V}_2\text{O}_5$ electrode performances can be obtained adding a 2% VC to LiPF_6 1M in EC:DMC 1:1 electrolyte. These preliminary results, together with the possibility of future improvements, make the $\text{Si@V}_2\text{O}_5$ nanocomposite a good candidate for high-energy anode materials for Li-ion batteries, and pave the way to the use of alternative and inexpensive inorganic buffering matrixes for alloying anodes.

Chapter 4 – Silicon@TiO₂ composite as anode material for LIBs

4.1 Introduction

In order to avoid the typical issues and improve electrode performance of silicon-based anodes, several strategies have been adopted to overcome their main problems, such as the volume expansion which can cause cracking, pulverization, loss of contact with the current collector and, ultimately, cell failure. The stabilization of the silicon morphology upon cycling is mandatory for a longer cycle life, and the use of inorganic buffering matrices has been already discussed in chapter 3. Anatase TiO₂ has been largely studied as anode material in lithium-ion batteries and it is a cheap, easily synthesizable, and environmentally friendly material. For this reason, the use of anatase TiO₂ as buffering filler for silicon anodes has been proposed. To our knowledge, there are no reports of the use of TiO₂ nanoparticles as a buffering filler in Si anodes.

4.2 Experimental

4.2.1 Si@TiO₂ Synthesis

Commercial Si nanoparticles (Alfa Aesar, average diameter ~ 100nm) were weighted and dispersed in isopropanol via magnetic and ultrasonic stirring (40 W power; continuous mode). Triton X-100 was used as dispersant and added to the suspension. After 2h of stirring, Titanium (IV) Isopropoxide was added setting the heating plate temperature at 80 °C. After the addition of aqueous ammonia solution (30% w/w) and ultrapure water, the formation of a pale grey precipitate was observed. In order to remove the remaining solvent, the residues were dried overnight at 70 °C. The resulting powder was heated in a tubular furnace in Ar atmosphere (600 °C, 4h, 5 °C min⁻¹ heating ramp)

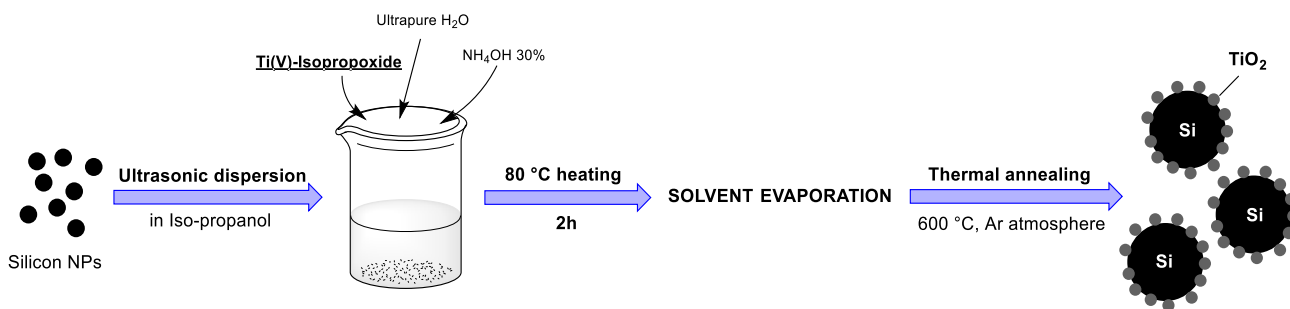


Fig. 4.1 – Synthetic route of Si@TiO₂.

4.2.2 Electrodes Preparation

The active material and the conductive agent were finely ground in an agate mortar, added in a glass vial containing the binder solution and magnetically stirred overnight. The mass ratios are summarized in the table below.

	Si@TiO₂-PAA	
Active Material:	Si@TiO ₂	70 %
Binder:	PAA (M _w ≈ 450000)	10 %
Conductive Agent:	Super C65	20%
Solvent:	Ethanol	---

Table 4a – Electrode formulation of Si@TiO₂-PAA coating.

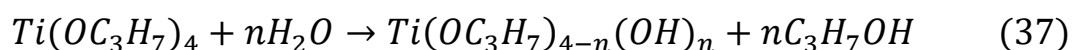
The slurry was casted over a copper foil using the “Doctor Blade” technique (thickness of wet coating = 100 μm), dried at 70 °C for 2 h. 9mm-diameter circular electrode have been cut and calendared at 5 tons cm⁻¹ using a hydraulic press. The average active material loading was ≈ 1 mg cm⁻².

4.2.3 Cell assembly and cycling

Three-electrode Swagelok-type polypropylene cells were assembled using metallic lithium (Aldrich) disks as counter and reference electrodes, glass fiber Whatman GF/A separators and 1M LiPF₆ in EC:DMC (1:1 v/v) + 2% vinylene carbonate (VC) additive as electrolyte (Solvionic). The cells have been cycled using a VMP-2Z multi-channel electrochemical workstation (Biologic, France) in a 0.01 < E (V) < 1.0 potential window, using specific current ranging from 100 mA g⁻¹ to 5000 mA g⁻¹. All the cells have been kept 12 h open circuit voltage (OCV) to enable a full wetting of separator and electrodes. Electrochemical impedance spectroscopy (EIS) has been carried out every tenth cycle in the 101 kHz - 9 mHz frequency range, by applying a bias potential of E = 1.0 V and a sinusoidal amplitude ΔE = ±5 mV. All the measurements have been recorded at room temperature. All potentials are given vs. Li⁺/Li redox couple.

4.3 Discussion

The active material was prepared dispersing the silicon nanoparticles in isopropanol thanks to the help of the ultrasound treatment and the addition of Triton X-100 as surfactant. The subsequent addition of Titanium (IV) isopropoxide, ammonia solution and ultrapure water starts the base-catalyzed hydrolytic-reaction [97] shown in equation (37):



After the thermal annealing, the precursor is transformed into anatase titanium dioxide (TiO₂) that acts like a buffering filler for the dispersed silicon nanoparticles. The XRD pattern of the Si@TiO₂ powder is shown in Fig. 4.2, together with the reference diffraction patterns of anatase TiO₂ (Fig. 4.2b) and crystalline silicon (Fig. 4.2c). The silicon-related peaks are located at 28°, 47°, and 56° and are in good agreement with the 27-1402 JCPDS card.

The main anatase peaks located at 25.3°, 38.0°, 48.2° are broadened thanks to the very small size of the TiO₂ crystallites; the peaks between 53° and 55° are partially overlapped with other peaks owing to line broadening.

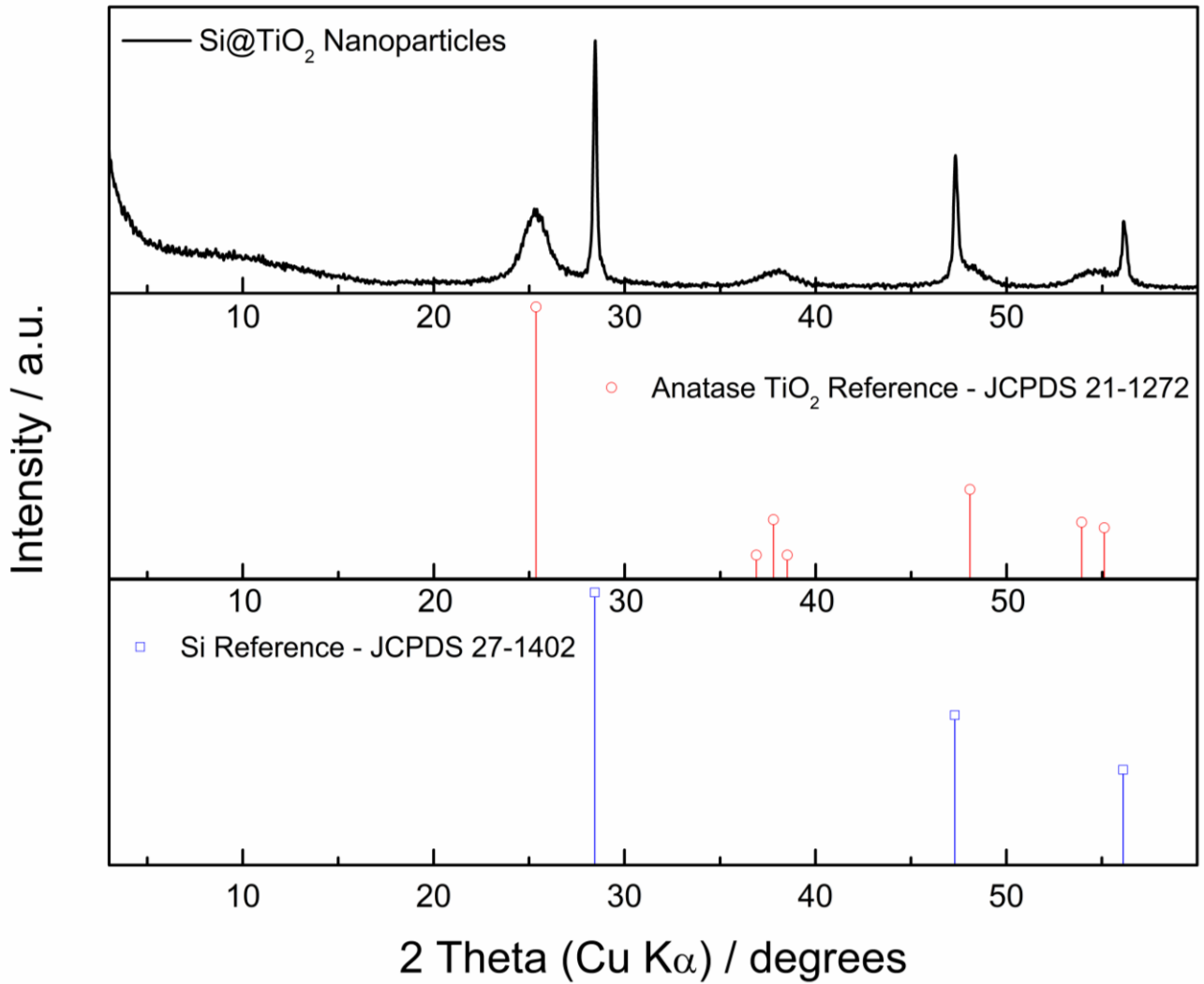


Fig 4.2 – XRD analysis of Si@TiO₂ material: a) Experimental Si@TiO₂ diffraction pattern; b) anatase-TiO₂ diffraction data from JCPDS 21-1272; c) Crystalline Si diffraction data from 27-1402.

Scherrer equation [87] for TiO₂ revealed an average crystallite size of 5.5 nm (peak at 25.3°), which is in good agreement with the TEM image shown in Figure 4.3 a-b. SEM images in Fig. 4.3 c-d indicates that TiO₂ crystallites are uniformly distributed on the Si nanoparticles, confirming again the results obtained with the TEM analysis.

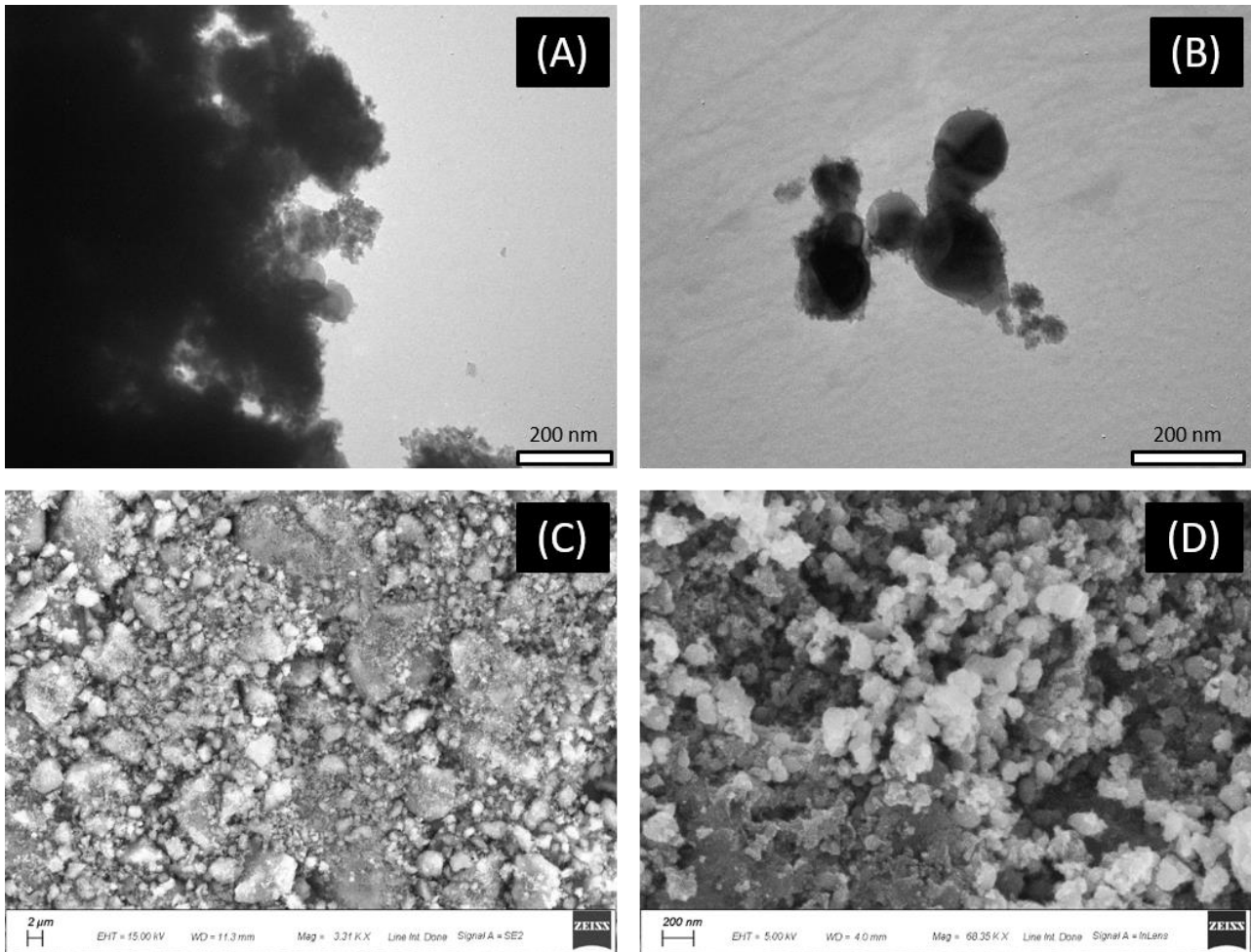


Fig. 4.3 – Morphological characterization of Si@TiO₂ active material. (A)-(B) Transmission electron microscopy micrograph of Si@TiO₂ powder; (C)-(D) Scanning electron micrographs of Si@TiO₂ powder.

Further structural information about Si@TiO₂ composite has been obtained using the Raman spectroscopy (632 nm laser). Several bands are clearly visible in Fig. 4.4, with the TiO₂ bond vibration modes located at 151 cm⁻¹ (Eg), 425 cm⁻¹ (B1g), and 611 cm⁻¹ (Eg). Silicon bands are visible at 511 cm⁻¹ and at 926 cm⁻¹. The slight shift of TiO₂ bands with respect to literature findings is most likely due to nanometric nature of its particles [98,99]. A similar behavior has been proposed for the silicon nanoparticles: the higher surface area strengthens the scattering as a combination of bulk and size distribution effects [100].

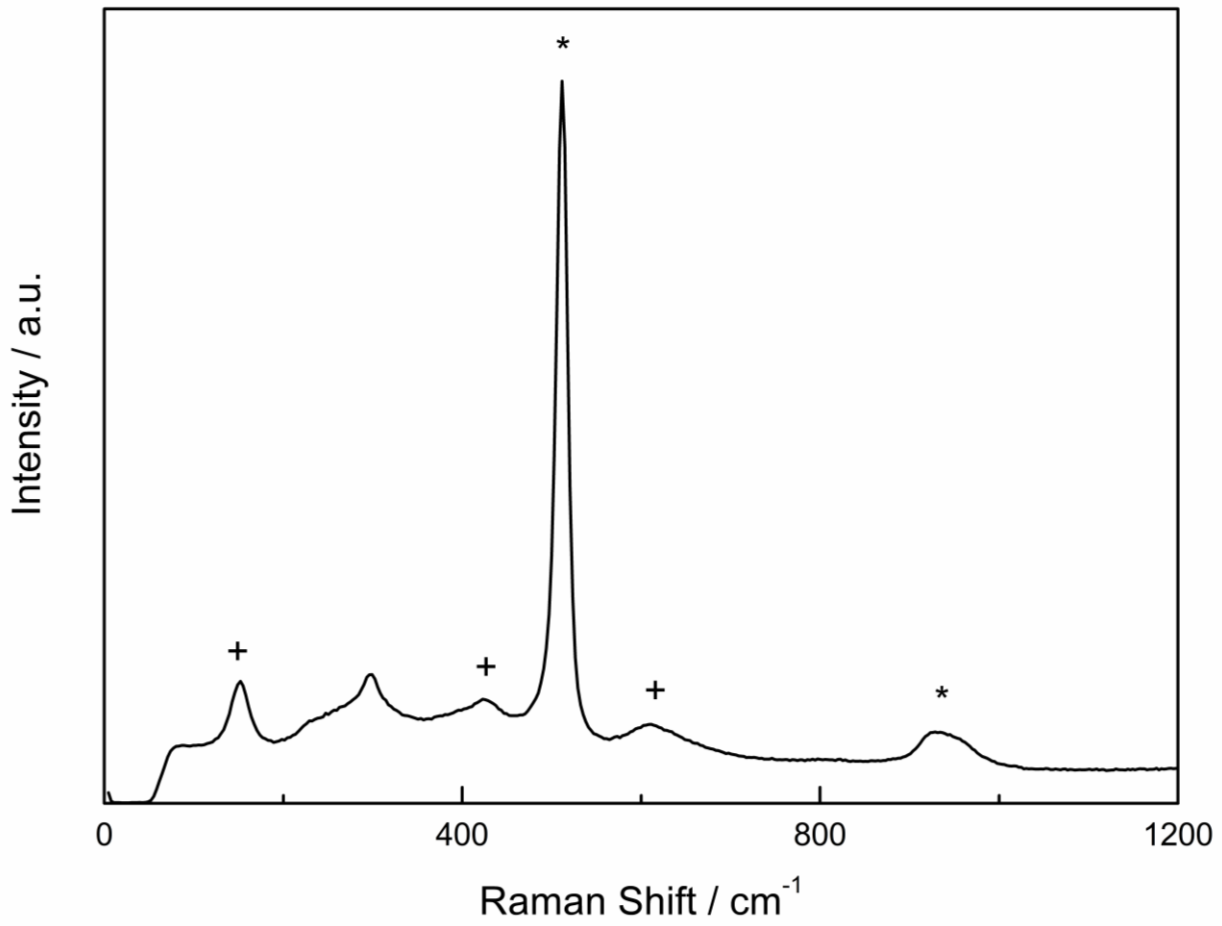
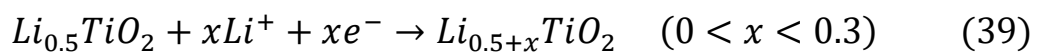
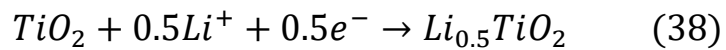


Fig. 4.4 – Si@TiO₂ Raman spectrum (* refers to Si bands, and + refers to TiO₂ bands).

Several electrochemical tests have been carried out to assess the electrochemical performances of Si@TiO₂ composite as anodic material for lithium-ion batteries. Fig. 4.5 shows the cyclic voltammogram of a Si@TiO₂-PAA electrode. Peak (A) at 1.72 V can be assigned to the Li⁺ insertion in the TiO₂ structure [98].



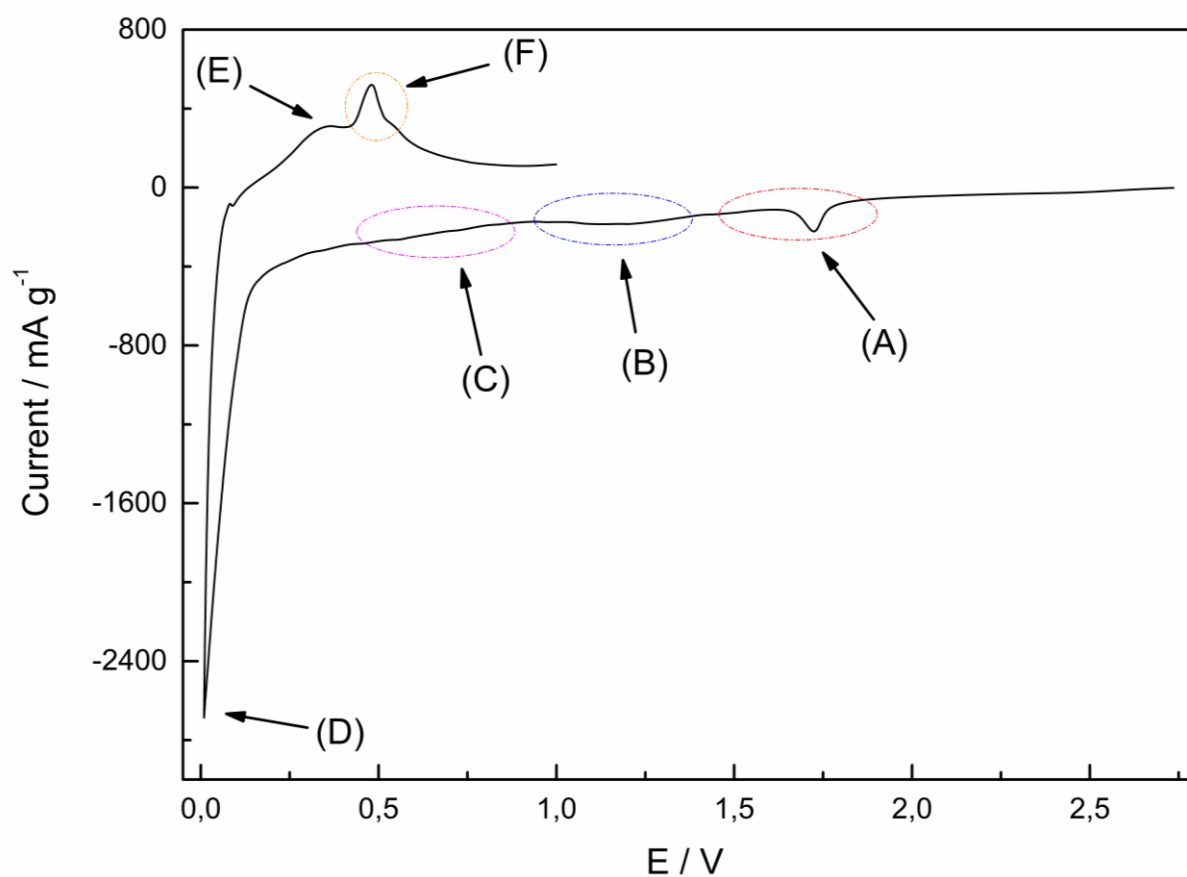


Fig. 4.5 – Cyclic voltammery scan of the first cycle of a fresh Si@TiO₂-PAA electrode.; Scan rate = 0.1 mV sec⁻¹; 0.01 < E (V) < 1.0 potential range

Peak	Potential	Description
(A)	1.72 V	Li ⁺ insertion in TiO ₂ structure
(B)	1.15 V	VC decomposition
(C)	0.69 V	SEI formation
(D)	0.01 V	1 st cycle alloying : c-Si → a-Li _x Si _y
(E)	0.34 V	Dealloying : a-Li _x Si _y → a-Si
(F)	0.48 V	Dealloying : c-Li ₁₅ Si ₄ → a-Si

Table 4b - Peaks description of the Si@TiO₂ cyclic voltammery (Fig. 4.5).

Equations (38) and (39) are related to the first lithium insertion within TiO_2 , which induces an irreversible structural conversion from a tetragonal to an orthorhombic structure. Region (B) and (C) can be assigned respectively to vinylene carbonate reduction [101] and SEI formation. The peak (D) located in proximity of the lower cut-off potential was attributed to the amorphization of crystalline silicon during the first cycle. The peak related to the $\text{Li}_{15}\text{Si}_4$ formation is not visible being overlapped by the (D) peak. In the reverse scan, the presence of (E) and (F) peaks, respectively at 0.34 V and 0.48 V are due to the dealloying process of $\alpha\text{-Li}_x\text{Si}_y$ and $\text{c-Li}_{15}\text{Si}_4$. In order to investigate the cycling behavior of Si@TiO_2 -based electrodes, galvanostatic tests have been carried out at several specific currents. Fig. 4.6a shows the cycling behavior at 500 mA g^{-1} specific current. The first-cycle lithiation capacity was 1822 mAh g^{-1} with a coulombic efficiency of 37%. This is mostly due to TiO_2 lithiation together with irreversible processes such as SEI formation and VC decomposition. After the second cycle, the capacity was 785 mAh g^{-1} with a capacity retention of 83.4% after 100 cycles. E vs. Q galvanostatic profiles confirm the features observed in the cyclic voltammetry.

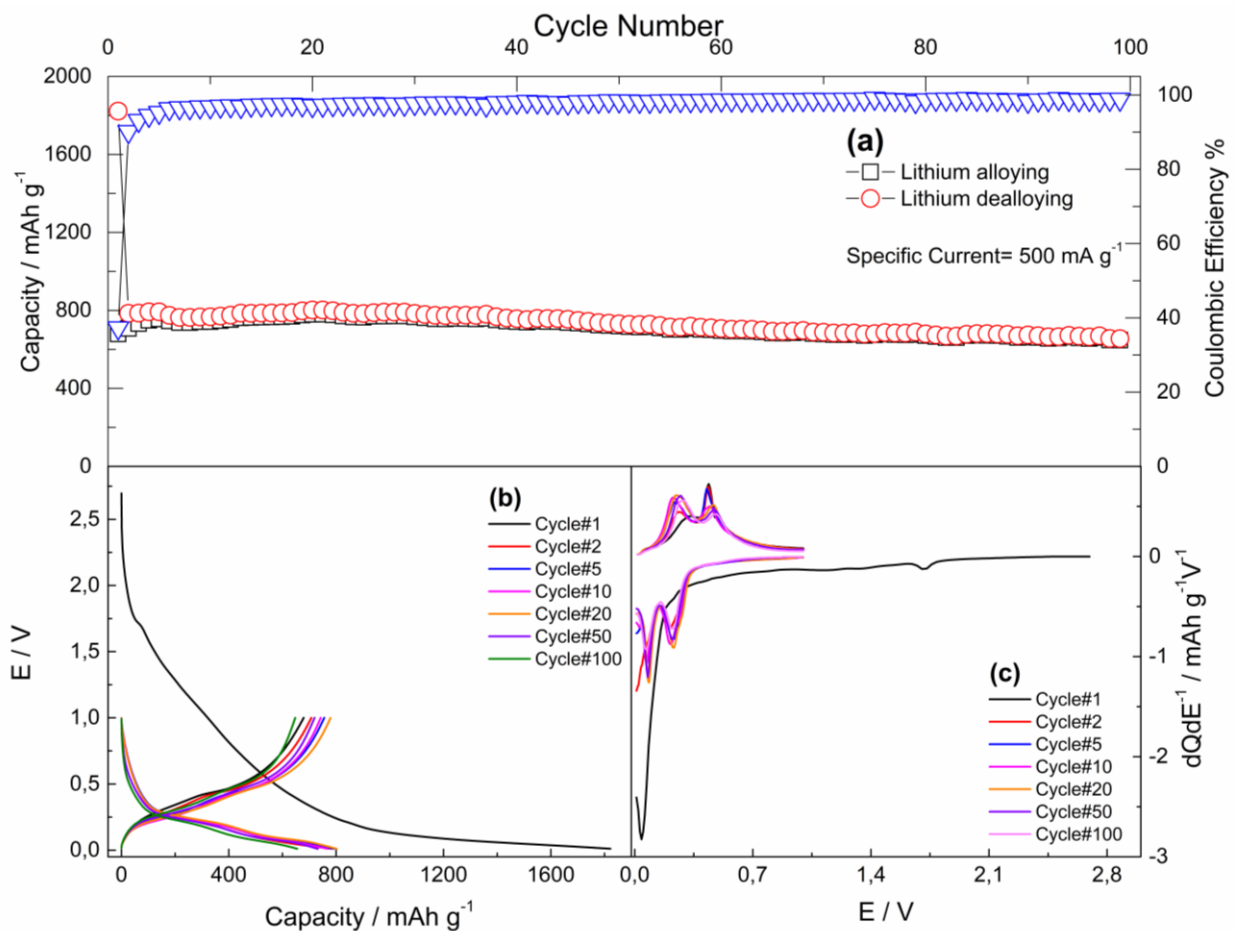


Fig. 4.6 – Si@TiO_2 galvanostatic cycling. $0.01 < E \text{ (V)} < 1.0$ potential range; $I = 500 \text{ mA g}^{-1}$.

In the first discharge profile, a short sloping plateau at 1.7 V is consistent with the peak attributed to the TiO_2 lithiation. A sloping line until 0.15 V confirms the decomposition phenomena described in the CV experiment. Eventually, a long sloping plateau until 0.01 V indicates the Si amorphization, and finally the possible formation of $\text{c-Li}_{15}\text{Si}_4$. The presence of a high amount of conductive agent (20%) should enable the storage of Li^+ via intercalation and surface adsorption as well. These phenomena could give a capacity contribution that cannot be excluded. Figure 4.6c shows the dQ/dE^{-1} vs. E plot for selected cycles where the peak positions are consistent with the CV results. Moreover, the presence of a small peak at $E = 0.027$ V could be assigned to the formation of $\text{c-Li}_{15}\text{Si}_4$ phase, which become less relevant upon cycling. In the anodic scan two broad signals at $E = 0.25$ V and $E = 0.45$ V are assigned to the dealloying processes, where the latter is specifically assigned to the $\text{Li}_{15}\text{Si}_4$ crystalline phase dissolution. The electrode response at different polarization levels was evaluated by the means of rate capability tests.

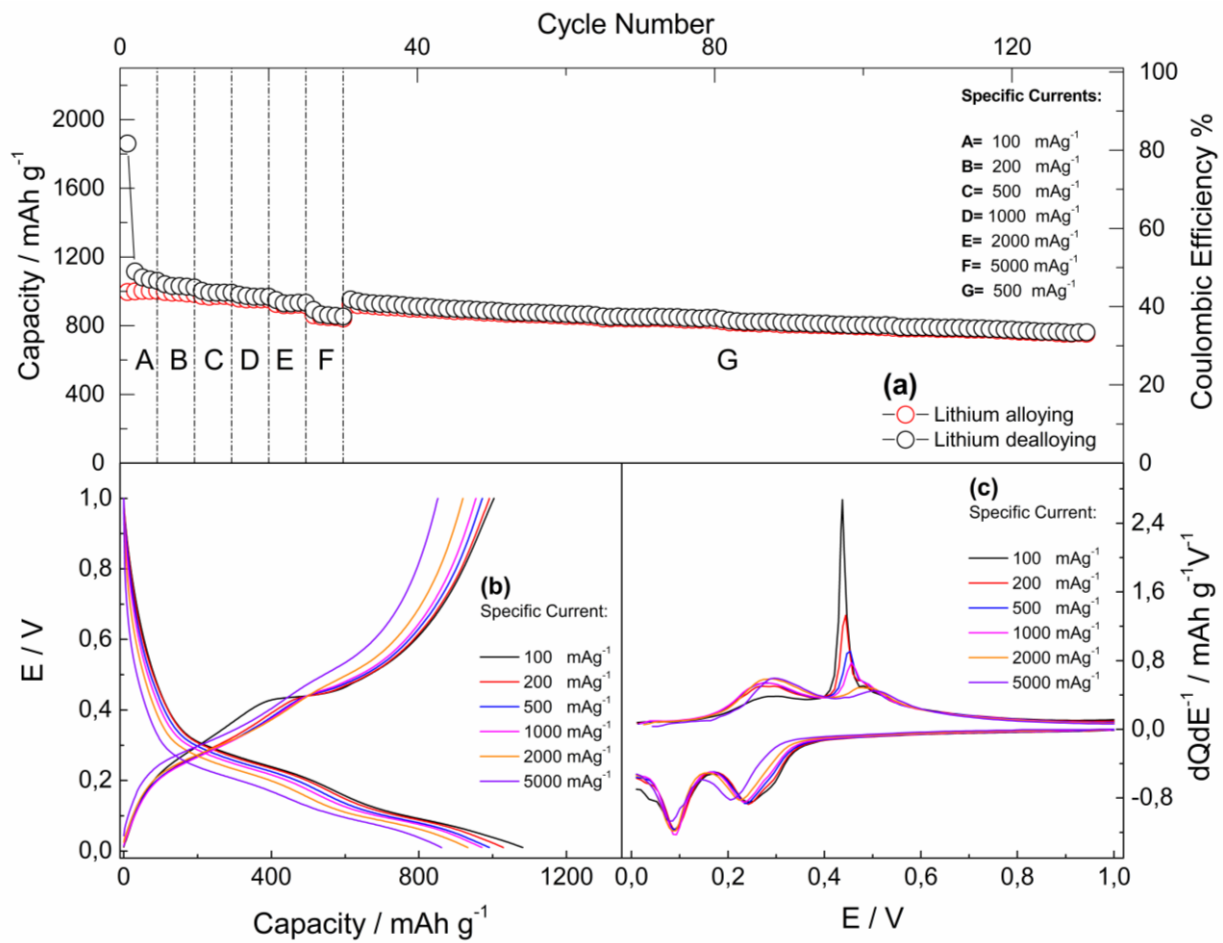


Fig. 4.7 – Si@TiO_2 rate capability. $0.01 < E$ (V) < 1.0 potential range; $100 < I$ (mA g^{-1}) < 5000 specific currents.

The tests were carried out with specific currents ranging from 100 mA g⁻¹ to 4000 mA g⁻¹. Then, the current was restored at 500 mA g⁻¹ to assess the Si@TiO₂ capacity recovery and long-term cycling performances. The results reported in Table 4c show a very good tolerance to the increasing currents and specific capacity values. The capacity values at 500 mA g⁻¹ are higher than the capacity values shown in Figure 4.6a at the same specific current. This is most likely due to the low-current steps applied before 500 mA g⁻¹, that could kinetically favor the initial lithium storage in a slower and more reversible way, rather than lithium irreversible uptake by interfacial storage and SEI formation.

Plot label	Specific current	Specific capacity	Coulombic efficiency
(A)	100 mA g ⁻¹	1080 mAh g ⁻¹	92.8 %
(B)	200 mA g ⁻¹	1030 mAh g ⁻¹	96.2 %
(C)	500 mA g ⁻¹	990 mAh g ⁻¹	97.6 %
(D)	1000 mA g ⁻¹	970 mAh g ⁻¹	98.4 %
(E)	2000 mA g ⁻¹	930 mAh g ⁻¹	98.7 %
(F)	5000 mA g ⁻¹	860 mAh g ⁻¹	98.6 %

Table 4c – Rate capability test specific capacity values in the 0.01 < E (V) < 1.0 potential range. The coulombic efficiency is extrapolated by the charge and discharge capacity values of the third cycle at every applied rate.

Figure 4.7 b-c shows respectively E vs. Q galvanostatic profiles and dQ dE⁻¹ vs. E differential plots of selected cycles, where all the processes related to Li-Si alloying/dealloying remain well defined at different currents. This polarization tolerance can be related to the stabilizing effect of TiO₂ crystallites and to the electrode morphology. From TEM images, very small TiO₂ crystallites (≈ 5 nm) uniformly surround the Si nanoparticles.

Their presence could enhance the electrolyte wetting of silicon nanoparticles, ensuring higher Li^+ concentration at electrode surface and thus avoiding diffusion limitations. This could result in electrode kinetics enhancement with a minimization of concentration overpotential. Moreover, the porous electrode morphology derived by PAA/ethanol processing [102,103] could help ensuring structural stability and avoid pulverization phenomena. The electrode/electrolyte interfacial processes have been investigated by electrochemical impedance spectroscopy (EIS).

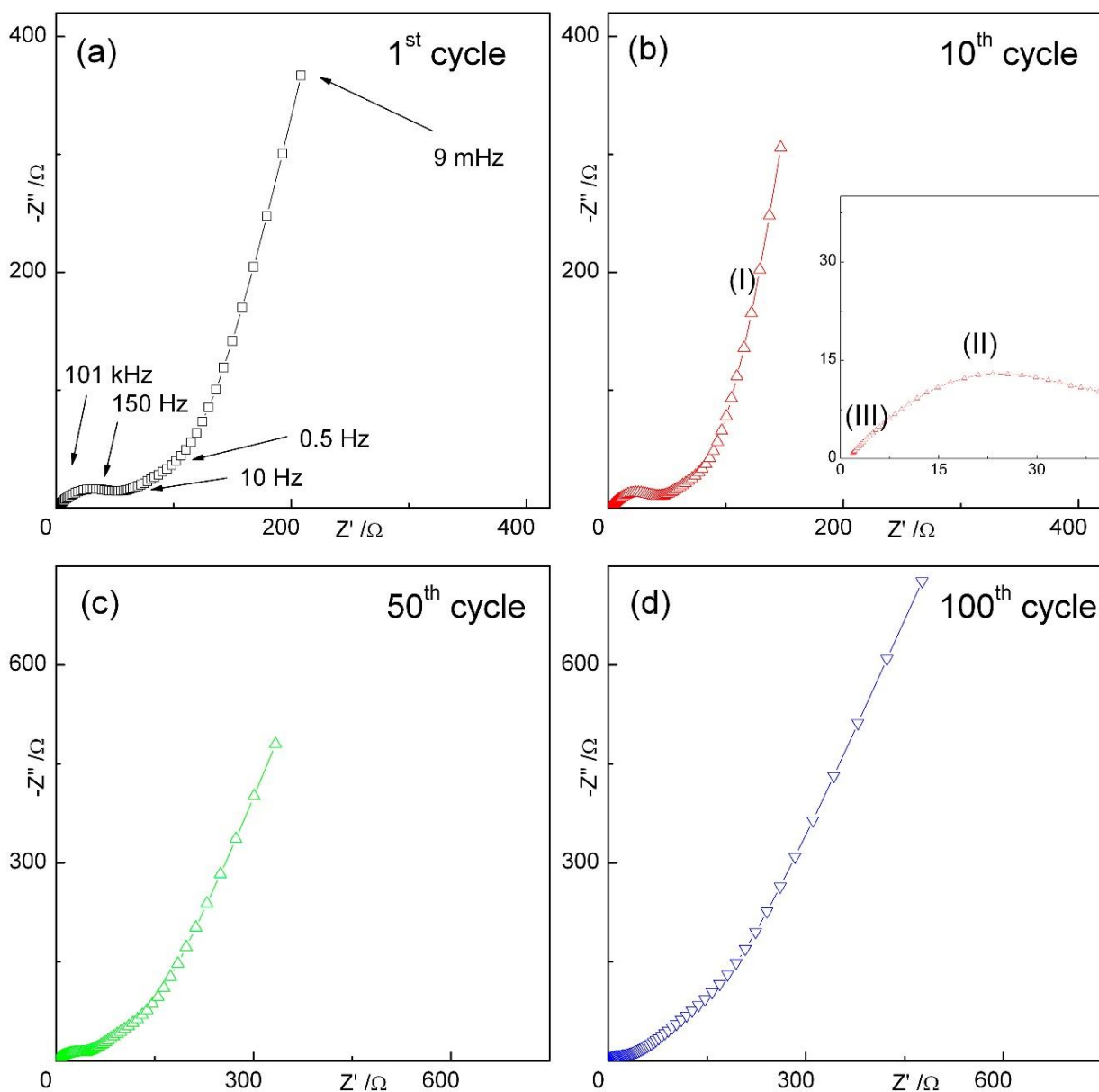


Fig. 4.8 – Nyquist plots of Si@TiO_2 nanoparticles at the 1st, 10th, 50th, and 100th cycle. The inset in panel (b) shows the enlargement of the high-frequency region.

Figure 4.8 shows the Nyquist plot recorded at $E = 1.0$ V at selected cycles. The plots show common features from high-frequency to low-frequency region: a sloping line at low-frequencies (I in Fig. 4.8b), a large semicircle (II in Fig. 4.8b), and a smaller semicircle overlapped to the previous one (III in Fig. 4.8b). These features can be ascribed to diffusion to a blocking electrode (I), a resistance due to the charge transfer process and formation of an electrical double layer (II), and polarization due to the passivation layer formation (III). The intercept on the x -axis is assigned to the electrolyte resistance. These features result in an equivalent circuit such as $R_{el}(R_{SEI}C_{SEI})(R_{ct}C_{dl})WC_i$ in Boukamp's notation [80,104]. The equivalent circuit elements correspond to the electrolyte resistance (R_{el}), SEI resistance (R_{SEI}), SEI capacitance (C_{SEI}), charge-transfer resistance (R_{ct}), electric double-layer capacitance (C_{dl}), Warburg resistance (W) and differential intercalation capacity (C_i), where the latter two describe the diffusion to a blocking electrode. A thorough analysis of the impedance spectra is beyond the aims of these studies, but from the Nyquist plots it is possible to observe a change in the slope of the diffusive part. Upon cycling, this almost vertical line, typical of blocking behavior, tend to 45° slope, typical of pure diffusive behavior. This transition can be tentatively related to the presence of lithiated TiO_2 crystallites that act as a "lithium reservoir" toward silicon. The higher Li^+ availability, could enhance their migration toward the silicon nanoparticles reducing the diffusion-related processes. The increase of impedance in the medium-to-low frequency region upon cycling can be assigned to Si nanoparticles aggregation and/or possible cracks on electrode surface. The morphology deterioration exposes "fresh" active material to the electrolyte, worsening the charge-transfer kinetics, because of fresh surface portions lacking TiO_2 coverage TiO_2 buffering ability.

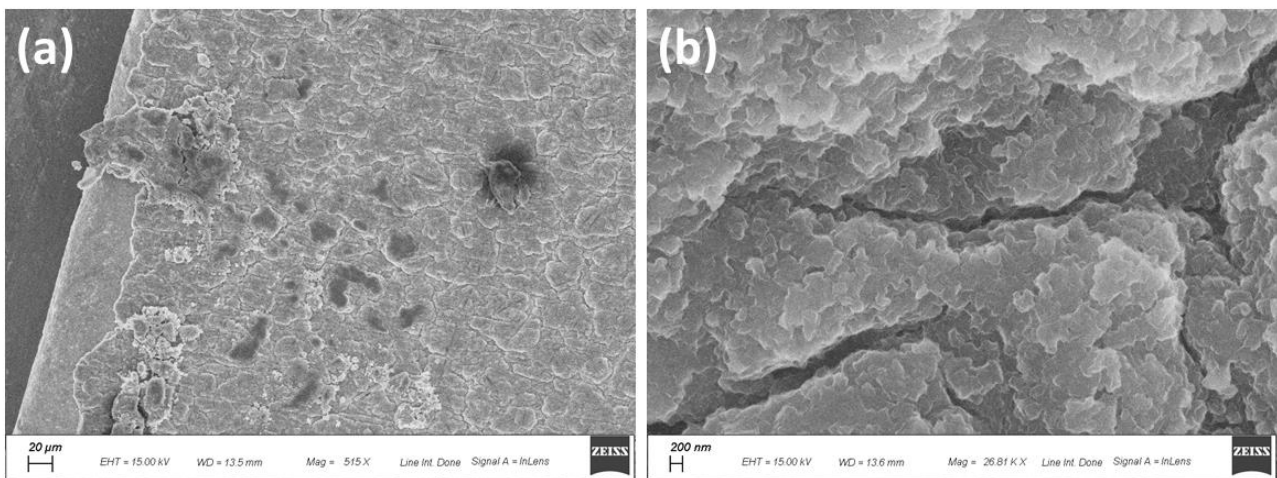


Fig. 4.9 – Post-mortem SEM micrographs of the $Si@TiO_2$ electrode at different magnification level.

Post-mortem SEM micrographs show the electrode surface after 100 cycles at 500 mA g⁻¹ specific current. At low magnification (Fig 4.9a), the electrode surface shows no peculiar morphological features. When the magnification is increased (Fig 4.9b) a good integrity is still maintained and only few cracks are visible.

4.4 Conclusion

A simple, cheap and environmentally-friendly synthesis has been proposed for the Si@TiO₂ material as anode material for lithium-ion batteries. The synthesis provides an optimal distribution of TiO₂ nanocrystallites around silicon nanoparticles confirmed by SEM and TEM analysis. The use of an optimized PAA-based electrode processing and the use of Vinylene Carbonate as electrolyte additive enabled the resulting electrodes to give very good capacity values and capacity retention at different specific currents. EIS measurements revealed a moderate worsening of charge-transfer kinetics upon cycling due to possible structural problems. At the same time, a reduction of the concentration polarization by TiO₂ was suggested. The obtained results suggest that Si@TiO₂ could be an innovative and sustainable candidate for the next-generation anode material for LIBs.

Chapter 5 - Si@Graphite Composite as Industrial Relevant Anode for LIBs

5.1 Introduction

This chapter describes the research activity carried out in the Zentrum für Sonnenenergie- und Wasserstoff-Forschung, Baden-Württemberg (ZSW) within the German project LIB.DE (**L**ithium-**I**onen-**B**atterie aus **D**eutscher Wertschöpfung), funded by the Federal Ministry for Economic Affairs and Energy. LIB.DE is a consortium of five industrial partners (BASF SE, BMW AG, SGL Carbon GmbH, Wacker Chemie AG and ZSW) coordinated by the Zentrum für Sonnenenergie- und Wasserstoff-Forschung, Baden-Württemberg (ZSW).

5.1.1 LIB.DE Project

The vast majority of Lithium-ion cells are produced in Asia and the expertise for their production is hardly available in Germany and other European countries. In addition to this, many electrode materials are produced in Asia: it is assumed that 70-80% of the world's natural graphite is extracted in China. Natural Graphite is included in the list of the Critical Raw Material drawn up by the European Union (EU) because of its high price, delivery risks, and at last but not least, the poor working conditions of workers in this area of competence. Therefore, it is mandatory to replace these materials with synthetic derivatives in order to reduce or stop the European dependence on Asia.

The current state-of-the-art on LIB anodes involve the use of graphite as active material due to its low cost, good kinetics, high availability and stability. Because of graphite limited theoretical capacity (372 mAh g^{-1}) [105] together with the recent progress on the cathode capacity, the anode is becoming the capacity bottleneck of the future batteries. A viable alternative to graphite and carbonaceous materials seems to be given by elements like Sn, Si or Al, which can store higher amount of lithium by forming alloys. Among them, silicon has the highest theoretical specific capacity of 3579 mAh g^{-1} (Fig. 5.1) corresponding to the formation of $\text{Li}_{15}\text{Si}_4$ lithiated stage [106].

The aim of this project is to improve the technical scalability and economical implementation of processes, in order to produce prototype series in the standardized PHEV1 format under serial conditions. The key points addressed by this project are:

- 🔋 Next generation materials with better energy density and specific capacity, by the use of Nickel-rich NMC materials (NMC 622 and 811) as cathode active materials, and Si-based composites as an anode active materials;
- 🔋 A greater use of cost saving and environmentally-friendly battery material by reducing the use of critical raw material as Cobalt;
- 🔋 Reduction of dependency on Asian suppliers for natural graphite;
- 🔋 Development of a scalable industrial process for a future cells production based in Germany;
- 🔋 Replacement of the traditional PVdF/NMP system with a water-based binder;
- 🔋 Use of electrolyte additives optimized to the active materials.

The presence of a Research Production Line (FPL) at the ZSW allows the study and optimization a possible scalability and the possibility to industrialize the cells production process.

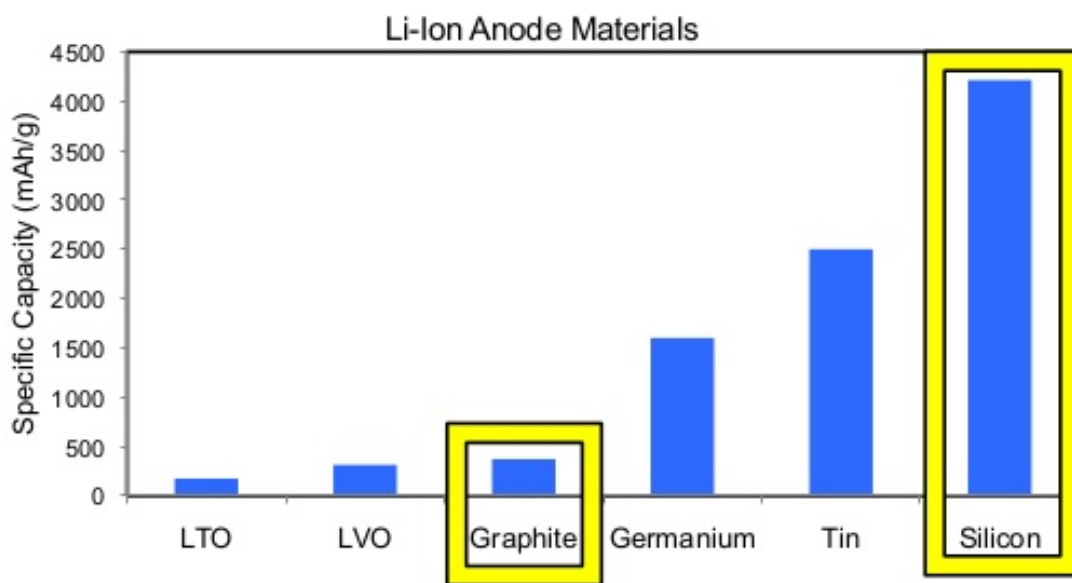


Fig 5.1 – Gravimetric capacities of Li-ion anode materials.

The use of silicon or silicon-based composites, often results in volume expansion issues. Since the breaking and the formation of new chemical bonds result in huge volume change during charge/discharge cycles (up to 300%), we must deal with the problems arising from this expansion.

- 1) **Electrochemical grinding:** Micrometric silicon particles cannot withstand the stress due to the volume change, resulting in silicon particles isolation and loss of capacity [107]. The use of nanoscale silicon can be a solution to this issue [108].
- 2) **Electrode damage:** Since graphitic anodes experience relatively small volume variations, a viable approach to use silicon in LIBs is to use a porous carbonaceous matrix with dispersed silicon nanoparticles in order to reduce the mechanical stress in the electrode structure [90]. The use of aqueous binders and the optimization of slurry recipe can also help to buffer the volume change [66].
- 3) **Irreversible capacity due to SEI effects:** Because of silicon expansion, the Solid Electrolyte Interphase (SEI) that covers the anode surface is subject to sudden breakages [109]. The use of well-known electrolyte additives such as Vinylidene Carbonate (VC) and Fluoroethylene Carbonate (FEC) can improve the SEI-forming ability of the electrolyte, resulting in reversible capacity gain [30,110].

5.1.2 Electrodes production - Laboratory scale vs Industrial scale

One of the fundamental requirements for the industrialization and production of lithium-ion cells is the scalability between laboratory and industrial scale. As it is easy to imagine, producing LIB electrodes on an industrial level presents totally different and new issues compared to the laboratory scale.

A generalized electrodes process chain provides for some basic steps listed below:



Dry and/or Wet Mixing: The most common strategies for industrial mixing process are the dry and the wet mixing. While the dry mixing is often an optional step where the solid components are blend together in a dry state, the wet mixing is a mandatory step where the optimal dispersion is achieved by mixing in the presence of a suitable solvent. In a typical laboratory approach, the slurry is in many cases prepared by magnetic stirring. This method usually does not provide a good dispersion of the components that will result in a low coating homogeneity and then poor and not reproducible electrochemical performance. Depending on the available amount of active material the laboratory scale preparation can also be carried out by the application of a dissolver mixer or a planetary mixer. Because of the quantity and quality required by the industry, an optimized mixing process is mandatory. In this regard, the industry mainly uses mixing systems such as planetary mixers that allow a complete homogenization of the slurry components. Further rheological analyses allow a precise adjusting of slurry parameters such as viscosity, rheological yield point, stability over storage etc. All of them are influenced by active material, solvent and binder type, mixing parameters (time, mixing speed, sequences order etc.) and slurry formulation.

The main characteristics of the dissolver mixing are listed below:

DISSOLVER MIXER
Slurries from 50 ml to 3 l
<i>Low viscosity mixing</i>
The mixing process starts from solvent or <i>binder solution</i>. Eventually the addition of active material and conductive agent takes place. The target viscosity is reached by addition of proper solvent.
The presence of <i>Doughnut Effect</i> (see Fig 5.2 central image) assess a good operating condition.

Table 5a – Dissolver Mixer characteristics.

Dissolver mixing is mainly used for laboratory scale preparations usually involving low viscosity slurries. To optimize the dispersion effect and removal of aggregates under these conditions, the rotation speed and the position of the dissolver disk are two important parameters. When they are set correctly, the so-called Doughnut Effect appears. This phenomenon is due to circular movement of the slurry inside the mixing vessel and, if adjusted correctly, the maximum mechanical power and shear force is transferred to the particles of the slurry, leading to a thorough de-agglomeration thereof. Too high solid matter content leads to only partial movement of the mixture, too low solid matter content is ineffective due to a too low particle-particle contact.



Fig 5.2 –Dissolver mixer (left image); Doughnut effect (central image); Slurry flow during mixing (right image).

Planetary mixing is the method of choice for pilot and industrial scale slurry preparation of aqueous anodes, since it is suitable for the preparation of high viscosity slurries with higher solid content. In the initial step, the dry components are mixed together and subsequently the addition of solvent or binder solution takes place. At the beginning, the slurry is kept in a dough-like state with a very high viscosity. This favors the efficiency of the kneading phase, which is the most important step of the preparation process, since in this phase the de-agglomeration of the hydrophobic carbonaceous components in the aqueous medium takes place. Subsequent slurry sampling during preparation allows to monitor its rheological properties and to adjust them according to the requirements of the final electrode. At the end of process, a degassing step is applied: the removal of free gas by vacuum provides a stable and homogeneous slurry ready to be coated.

This method has several advantages with respect to the dissolver mixing:

- 🔧 Possibility to process large quantities of slurries at once.
- 🔧 In order to be effective, planetary mixing requires less time than dissolver mixing.
- 🔧 Since the applied stirring force is dissipated more effectively when the particles are in intense contact and shear vs. each other, the energy input in a planetary mixer results in a lower extent of particle destruction and less local stress on particles which are in direct contact to the stirring tool compared to a dissolver mixer.

PLANETARY MIXER
Slurries from 1.5 l to 10 l
<i>High viscosity mixing</i>
The mixing process starts from the dry mixing of solid components.
More effective energy dispersion
Faster process than dissolver mixing

Table 5b – Planetary mixer characteristics.

In both mixing techniques, we must be careful about the mechanical stability of the components. The mixer rotation speed is related to the energy transferred to the particles, therefore delicate and fragile compounds (e.g. **SBR** – **S**tyrene-**b**utadiene **r**ubber) have to be treated in a mild manner or added during the last steps of the process where usually the rotation speed is decreased.



Fig 5.3 – Planetary mixer.

Coating/Drying: Once the slurry rheological properties match the required coating parameters, the coating step can start. One of the most used coating technique in laboratory scale is the Doctor Blade technique. The film applications can be manual or automatic (see Fig. 5.4).

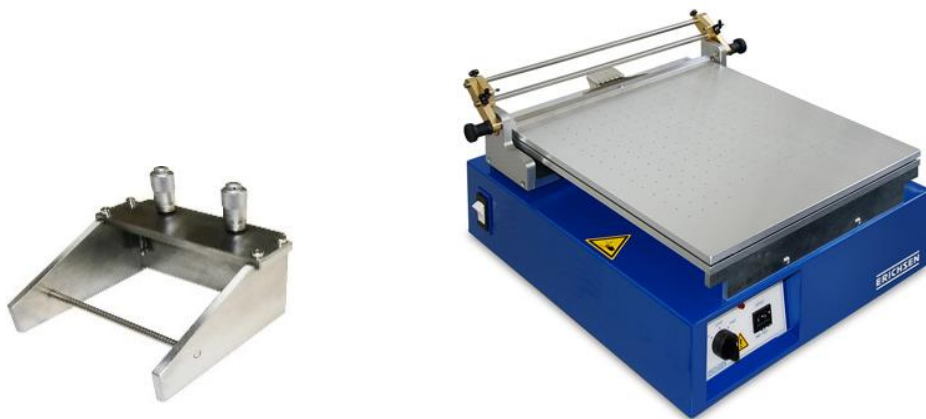


Fig 5.4 – Manual film applicator (left image); Automatic film applicator equipped with a heating plate (right image).

Using an automatic film applicator, you can set specific coating speed, wet film thickness, drying temperature and drying time. For pre-industrial and/or industrial use, a coating machine is required. This device combines coating and drying in one machine and allows to vary many parameters in order to optimise the processes and to adapt them to the specific slurry properties and the targeted electrode parameters. Once properly adjusted, a homogeneous mass loading throughout the coating avoiding wrinkle, streaks, holes and cracks is feasible. Since inhomogenities in electrodes are the primary drivers of failure, an efficient control of these parameters is fundamental. The stored and degassed slurry is feeded to the coater through a pulsation pump connected to a filtering system. The two main application systems are the Commabar and the Slot Die System. Their typical features are listed in the table below.

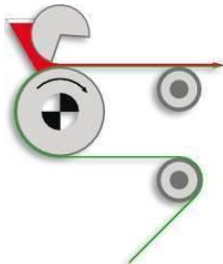
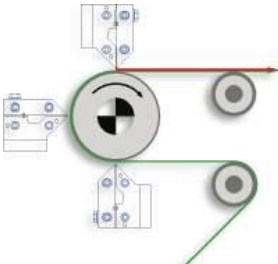
<p style="text-align: center;">COMMABAR SYSTEM</p> 	<p style="text-align: center;">SLOT DIE SYSTEM</p> 
<p style="text-align: center;">Combination of knife and roller applications</p>	<p style="text-align: center;">Coating loading defined by pump flow</p>
<p style="text-align: center;">Universally applicable</p>	<p style="text-align: center;">Each slurry requires different settings</p>
<p style="text-align: center;">Problematic slurries can be processed</p>	<p style="text-align: center;">Very precise only with optimized design</p>
<p style="text-align: center;">No intermediate coating</p>	<p style="text-align: center;">Possibility of intermittent coating</p>
<p style="text-align: center;">High mechanical stress</p>	<p style="text-align: center;">Coating without mechanical contact</p>

Table 5c – Main features of Commabar and Slot die coating systems.

Every coater is usually coupled to a drying zone which is usually composed of several hot air ovens or infrared (IR) oven segments. The presence of different oven segments helps to precisely adjust the drying procedure since each oven can have a different drying temperature. A not optimized drying process can lead to binder migration, coating defects, low homogeneity and curled current collectors due to a fast drying rate.



Fig 5.5 – Pre-industrial automatic coater equipped with a mass load scanner.

Calendering: The manufactured electrode is compressed in a calender machine in order to yield a specific coating density, porosity and adhesion and to increase electronic conductivity, by intensifying the particle-particle contact.

Electrode Cutting: The calendered coating is slit to a specific width and length according to the cell format to be assembled.

Final Drying: The electrodes can undergo an additional and final drying step to adjust the moisture ($H_2O < 500$ ppm) since high water content in the cell can negatively affect the cell lifetime and performance.

PARAMETER	PILOT SCALE PREPARATION	LABORATORY SCALE PREPARATION
Mixing technique	Planetary mixing	Dissolver Mixing
Final solid content aqueous [wt%]	35-50	20-45
Final solid content organic preparation [wt%]	65-75	50-75
Final viscosity range aqueous preparation [Pa·s @ 1 s⁻¹]	1-20	20-80
Final viscosity range organic preparation [Pa·s @ 1 s⁻¹]	15-30	30-60
Drying technique	Air flow	Hot Plate
Drying temperature [°C]	50-110	40-80

Table 5d – Comparative table: Pilot scale vs. Laboratory scale.

5.2 Aqueous slurry preparation and optimization

The work done at ZSW was mainly focused on the preparation and optimization of aqueous slurries using silicon/graphite composites.

One of the materials chosen for this project was a Silicon/Graphite composite (Si@Gr) synthesized and provided by a project partner. The relatively small amount of silicon in the composite should be a right balance between high specific capacity and graphite buffering ability [111,112]. The use of graphite as buffering matrix has the advantages of using a highly conductive material, which also contributes to the total specific capacity of the composite. The absence of inactive materials will help to increase the energy density of the cell.

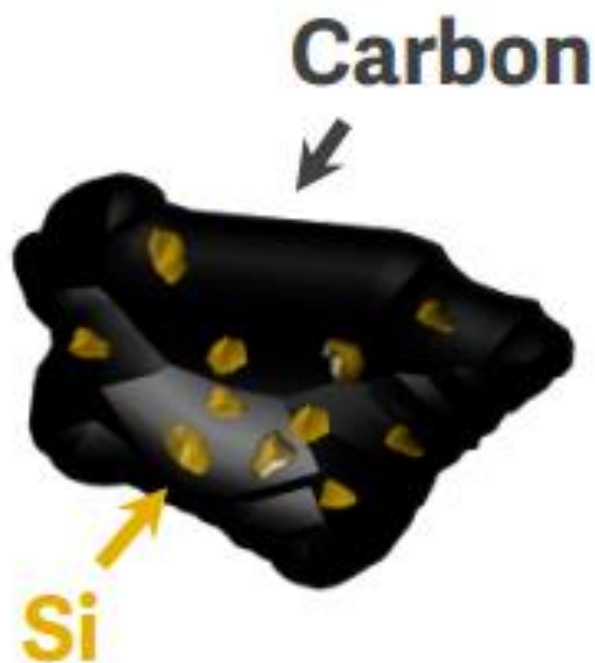


Fig 5.6 – Si@Gr schematized morphological structure.

The most important features of this composite are listed in the table below.

PARTICLE SIZE	<i>D50</i>	15 μm
SPECIFIC SURFACE	<i>BET</i>	11 m ² g ⁻¹
SILICON CONTENT	-----	8%
SPECIFIC CAPACITY (@C/10 rate)	<i>3rd cycle</i>	575 mAh g ⁻¹
SPECIFIC CAPACITY (@1C rate)	<i>5th cycle</i>	550 mAh g ⁻¹
FORMATION EFFICIENCY	<i>1st cycle</i>	91%

Table 5e – Si@Gr main characteristics.

Further information about its synthesis are protected by industrial secrecy and will be not discussed in this chapter.

In the attempt of replacing the organic solvent and go toward a more environmental-friendly approach, the use of aqueous binder for anode preparation has been proposed in the LIB.DE project. Since the battery energy density and calendar life are two of the most important parameters for a battery, it is desirable to minimize the binder amount and at the same time maintain electrode stability and conductivity [113]. A mixture of Carboxymethyl Cellulose and Styrene Butadiene Rubber (Na-CMC/SBR) dissolved in water (H₂O) have already shown good stability and performances together with a good processability [33,114]. In addition to this, Na-CMC shows the presence of polar groups and a not polar carbonaceous backbone in its structure, which make this amphiphilic polymer a sort of surfactant [115] that helps to disperse uniformly the different slurry components.

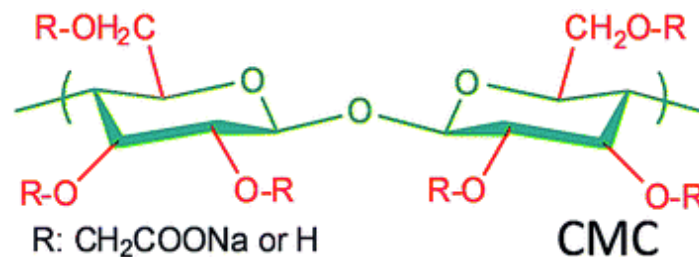


Fig 5.7 – Sodium Carboxymethyl Cellulose (Na-CMC) chemical structure.

The final addition of SBR block co-polymer increases the flexibility, the adhesion, and heat resistance of the final coating.

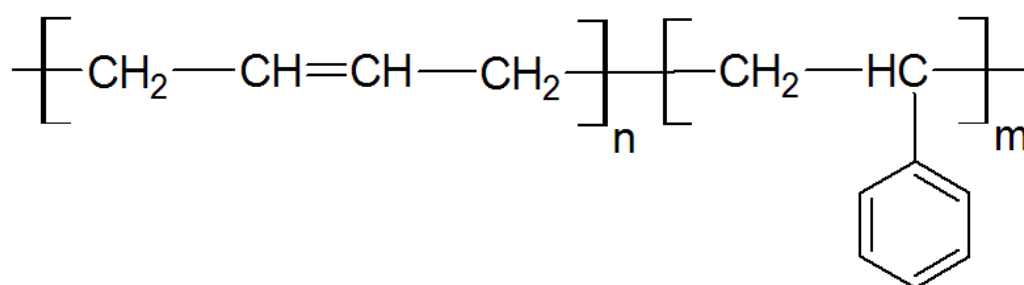


Fig 5.8 – Styrene Butadiene Rubber (SBR) chemical structure.

All the slurry preparations have been made using a planetary mixer or a dissolver mixer. Regarding the coating/drying step, an automatic tabletop coater and a pilot scale coater have been used depending on the purpose. All the preparations have been realized and designed in order to transfer the process knowledge to the production line (FPL).

As a starting point the anode slurry was manufactured with a standard formulation (*Formulation A*) in a planetary mixer. The dry components were first thoroughly mixed at low speed and after the subsequent addition of small quantities of solvent the kneading phase was initiated. After a specific kneading time, further solvent addition has been taken out to achieve a specific slurry viscosity. After reducing the rotation speed of the mixer, finally SBR was added at the end of the process. This is important, because the initial high mixing rate of the process could have damaged its structure and function. In the last step, the mixer was evacuated to remove air bubbles. The zeta potential and density measurements were taken out at the end of this process.

FORMULATION A			
<i>Si@Gr</i>	<i>Super C65</i>	<i>Na-CMC</i>	<i>SBR</i>
94%	2%	2%	2%

Table 5f – Weight percentage of Formulation A components.

Optimizing the recipe of a slurry is the starting point for obtaining excellent electrodes, and therefore better performances. For this reason, several attempts have been made to improve this fundamental part of the electrode-making process. Changing the mixing process, using additives, or using different percentages of slurry components can help to achieve better results such as:

- 🔪 A more homogeneous active material and conductive agent distribution in the slurry. This results in a superior electrical conductivity and electrochemical performances;
- 🔪 An increased mechanical stability of the coating, which ensures a homogeneous coating concerning the mass loading as well as the composition of the coating. Moreover, the fine tuning of binder concentration could increase the adhesion of the coating to the current collector, which also improves the electrode performances;

Obtaining a coating without imperfections such as agglomerations, streaks, holes, and cracks was one of the main objectives for the success of the project, since inhomogeneities in batteries are the primary drivers of failure [116].

High-surface carbon-based materials are commonly employed as conductive additives in lithium ion batteries. Their size, morphology, amount and dispersion can heavily influence the charge/discharge behaviour of LIBs. The tendency of carbonaceous materials to agglomerate in polar solvents (e.g. water, ethanol, etc.) is given by the apolar C-C bond. This results in their hydrophobicity that does not allow for a homogeneous dispersion leading to poor electrochemical performances and safety. The addition of additives such as surfactants is a possible strategy for obtaining a good dispersion of slurry components.

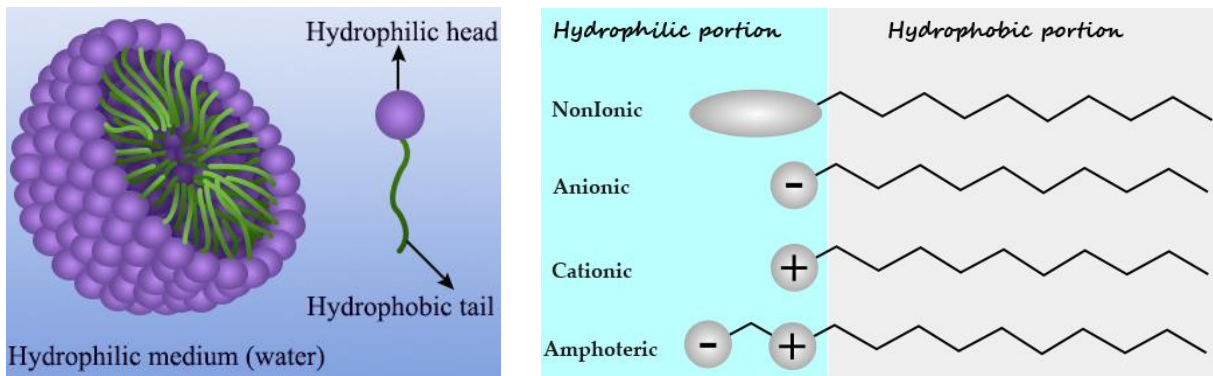


Fig 5.9 – Surfactant and Micelle structure (left image); most common surfactants type (right image).

Surfactants (short for surface-active-agent) are compounds formed by a polar head (hydrophilic) linked to a non-polar tail (hydrophobic). In a polar solvent, several surfactant molecules surround the hydrophobic particles (e.g. graphite) exposing the hydrophilic heads to the polar environment. This particular structure called micelle helps to avoid agglomeration and flocculation phenomena. According to their use they can be classified as emulsifiers, foaming agents, detergents and dispersant. Surfactants can be classified according to the composition of their head that can be non-ionic (e.g. Triton X-100), anionic (e.g. Sodium Dodecyl Sulfate, SDS), cationic (e.g. Cetyltrimethylammonium Bromide, CTAB), and amphoteric (e.g. Imino acetates).

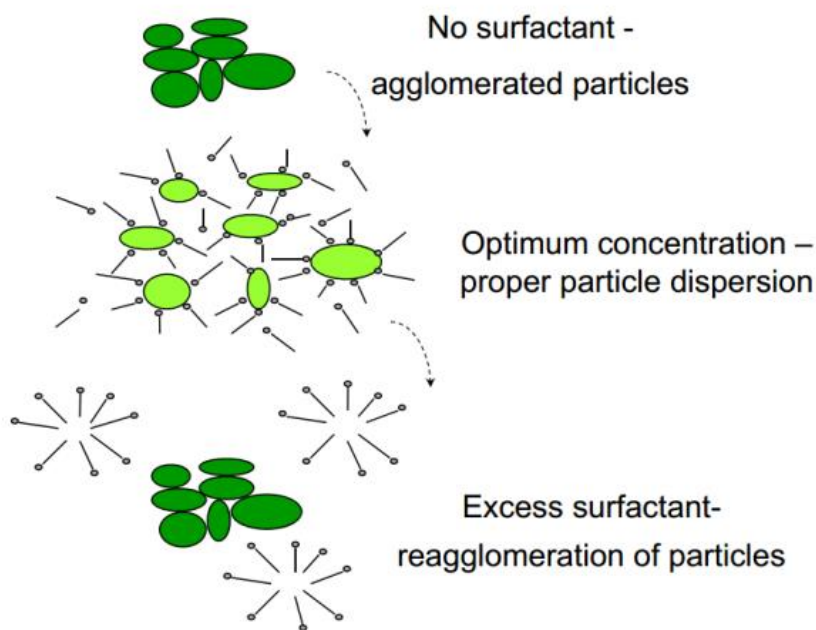


Fig 5.10 – Effect of surfactant concentration on particles dispersion.

The dispersive ability could become less effective due to too high concentrations of surfactant: if the surfactant concentration is higher than a threshold value called Critical Micelle Concentration (CMC), the repulsive forces between micelles can again lead to agglomerates (see Fig. 5.10).

The nature of surfactant stabilization can be electrostatic or steric. Since the steric stabilization is predominant in concentrated solution, two high-molecular weight dispersants have been chosen as slurry additives. Polyvinylpyrrolidone (PVP) and Polyvinyl Alcohol (PVA) are water-soluble polymer used also as binders [74,117]. In Formulations B and C, they were used in a 1% concentrations reducing the amount of SBR rubber.

FORMULATION B				
<i>Si@Gr</i>	<i>Super C65</i>	<i>Na-CMC</i>	<i>SBR</i>	<i>PVP</i>
94%	2%	2%	1%	1%

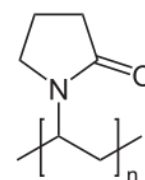


Table 5g - Weight percentage of Formulation B components.

FORMULATION C				
<i>Si@Gr</i>	<i>Super C65</i>	<i>Na-CMC</i>	<i>SBR</i>	<i>PVA</i>
94%	2%	2%	1%	1%

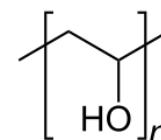


Table 5h – Weight percentage of Formulation C components.

The binder/active material interaction can strongly influence the electrode charge/discharge behaviour. During cycling, our active material (Si@Gr) is subjected to the typical volume expansion of silicon, despite the graphitic matrix is supposed to buffer the expansion of a small percentage of silicon (8%). When Na-CMC is used as binder at neutral pH (pH = 7), the carboxyl groups in its structure bind to the hydroxyl group on silicon surface, since it is naturally coated by a thin layer of silicon oxides (SiO_x) [66].

In presence of very small amount of water, the resulting hydrogen bond can exhibit a self-healing behaviour during cycling, helping with the reconstruction of electrical network [118]. Several groups have tried to lower the natural pH of the CMC solution using acids [119] or buffer solution [120]. While the former resulted in poor performances due to an inaccurate pH control, the use of buffer solutions has been shown to promote an esterification reaction between Na-CMC and Si. At pH = 3, carboxylic and hydroxyl groups are both fully protonated, and after drying a covalent bond is formed. This stronger bond seems to better support the volume expansion resulting in a more efficient collector/coating adhesion and longer cyclability [40]. The use of a citrate buffer as solvent has been evaluated in Formulation D to assess the impact of slurry pH on the final electrode.

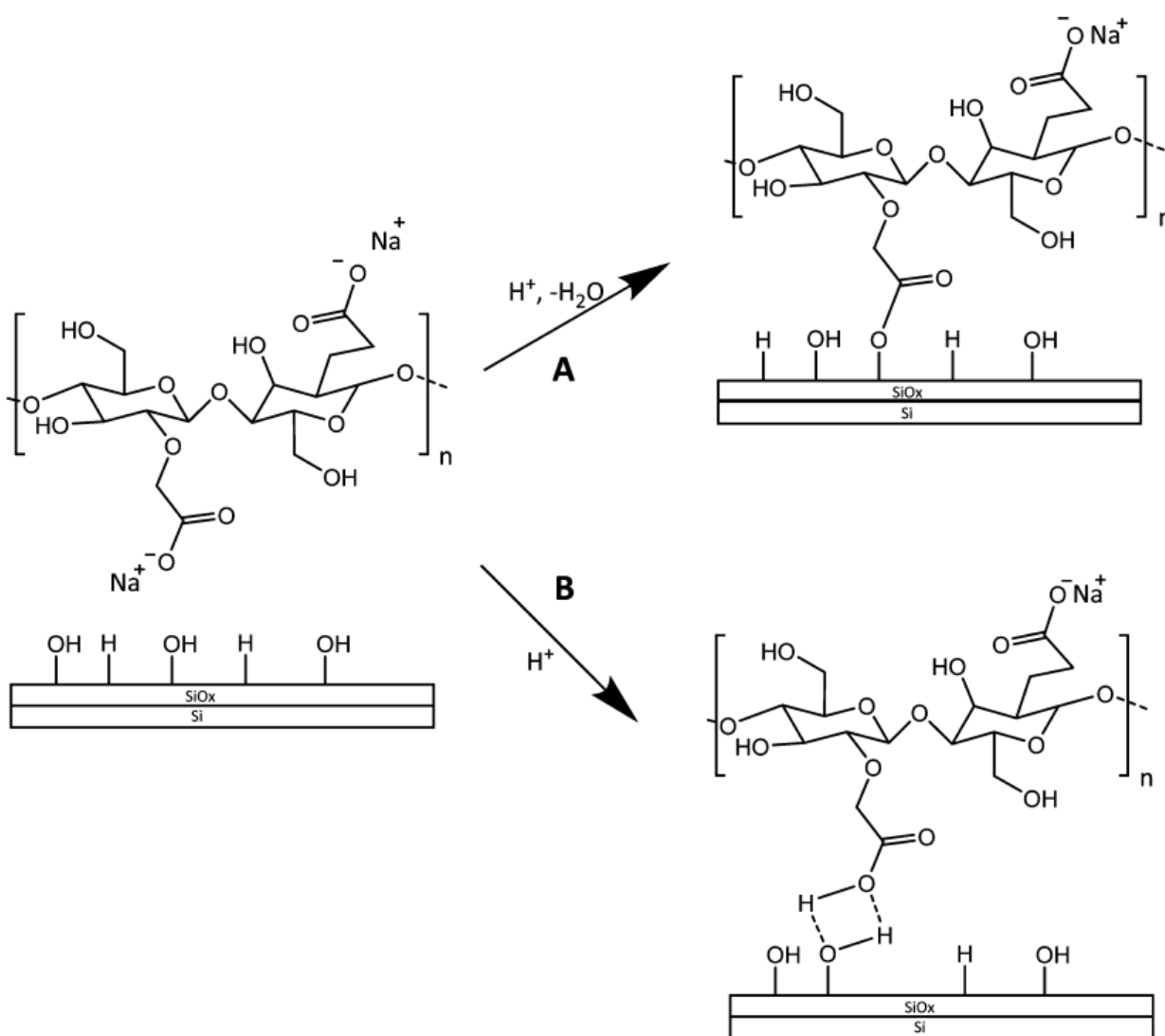
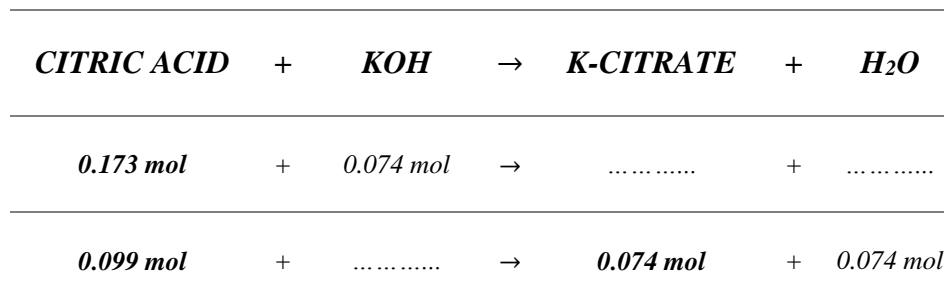


Fig 5.11 – Interaction of Silicon and Na-CMC at different pH levels.

A citrate buffer has been prepared dissolving citric acid and potassium hydroxide in ultrapure water. The reaction is shown below:



With the Henderson-Hasselbalch equation (Eq. 40) it is now possible to calculate the pH:

$$pH = pK_a + \log_{10} \frac{[A^-]}{[HA]} = 3.1 + \log_{10} \frac{0.074}{0.099} = 2.97 \quad (40)$$

The buffer solution pH has been adjusted to 3 with a NaOH 1M solution monitoring the pH with a Mettler-Toledo SevenGo pHmeter. The use of a buffer solution introduced also citric acid and potassium citrate in the slurry. From calculations 12.53 g of salts has been introduced resulting in a high percentage of inactive and insulant material in the final coating. The final composition of Formulation D is shown in table 5i:

FORMULATION D				
<i>Si@Gr</i>	<i>Super C65</i>	<i>Na-CMC</i>	<i>SBR</i>	<i>Salts</i>
90%	2%	2%	2%	4%

Table 5i - Weight percentage of Formulation D components.

This salts percentage is not negligible, and together with the resultant lower amount of active material will not make this approach attractive for large-scale production.

Since the mixing process and the sequence of steps can greatly influence the success of the slurry, for a further experiment the mixing order was inverted. For this purpose, a dissolver mixer has been used, since starting with the binder solution leads to relatively low initial viscosities. In **Formulations E and F**, first a binder solution from Na-CMC and water was prepared. After the addition of the conductive agent, the mixture was stirred for 6 h to ensure a thorough de-agglomeration. Eventually the active material was added in small batches in order to improve the homogeneity of the slurry and the dispersion of the particles. Except for the use of a dissolver mixer, and except for the final solid matter content, Formulation E (Table 5j) is identical with *Formulation A*.

Additionally, in order to evaluate the impact of the amount of binder on the dispersion of components and on the slurry stability, another slurry was prepared based on Formulation E and increasing the amount of binder to 7 wt% at the expense of the active material content, while not using SBR (Formulation F, see Table 5k).

FORMULATION E			
<i>Si@Gr</i>	<i>Super C65</i>	<i>Na-CMC</i>	<i>SBR</i>
94%	2%	2%	2%

Table 5j - Weight percentage of Formulation E components.

FORMULATION F		
<i>Si@Gr</i>	<i>Super C65</i>	<i>Na-CMC</i>
91%	2%	7%

Table 5k - Weight percentage of Formulation F components.

All these formulations and the respective slurries have been coated with a laboratory scale automatic coater using the doctor blade technique. Based on the solid content and the slurry density values, it is possible to calculate the wet film thickness for a given loading:

$$\text{Wet film thickness } (\mu\text{m}) = \frac{\text{Loading } (\text{mg cm}^{-2})}{\left(\frac{\text{Slurry density } (\text{g cm}^{-3})}{\text{Solid content } \% * 1000} \right)} \quad (41)$$

The coatings obtained from these formulations have been made by trying to obtain an areal capacity range around 2 to 4 mAh cm⁻².

All the specification of these slurry formulations are enlisted in the following table:

Table 5I – Summary table: Formulations and their components.

Name	Mixing Method	Active Material	Binder 1	Binder 2	Conductive agent	Additive	Percentages
A	Planetary mixer	Si@Gr	Na-CMC	SBR	Super C65	-----	94/2/2/2
B	Planetary mixer	Si@Gr	Na-CMC	SBR	Super C65	PVP	94/2/1/2/1
C	Planetary mixer	Si@Gr	Na-CMC	SBR	Super C65	PVA	94/2/1/2/1
D	Planetary Mixer	Si@Gr	Na-CMC	SBR	Super C65	Buffer sol.	90/2/2/2/4
E	Dissolver mixer	Si@Gr	Na-CMC	SBR	Super C65	-----	94/2/2/2
F	Dissolver Mixer	Si@Gr	Na-CMC	-----	Super C65	-----	91/7/2
G	Planetary mixer	Si@Gr	Na-CMC	SBR	Super C65	-----	94/2/2/2

The final step in optimizing slurry formulation has been the use of a pilot scale coater. The scale-up of this process was of fundamental importance, because it was necessary to confirm the feasibility and transferability of the coating processes. *Formulation G* was applied to realize a slurry in the planetary mixer. There have been some small modifications to the process, such as a higher molecular weight Na-CMC and a slower approach to a more energetic kneading phase. For the application of the slurry onto the current collector a Commabar system was used. The drying procedure was realized by running the coated electrode through 4 separate drying zones, as depicted in figure 5.5. Humidity and drying temperature controls allow to avoid latex and binder migration toward the coating surface [121,122] and to ensure a homogeneous coating. Scientific evidences have shown that the edge drying rate is higher than the central area drying rate resulting in a current collector curling. The humidity control can help reducing this effect: 1~2% of residual water content in the coating improves its processability and handling. Thus, it was possible to obtain a very homogeneous longitudinal and transverse mass loading and the achievement of the desired thicknesses. The application of a mass load scanner equipped with a Kr-85 source ensured the monitoring of the mass loading of the electrode. Figure 5.12 depicts the evaluated mass loading data:

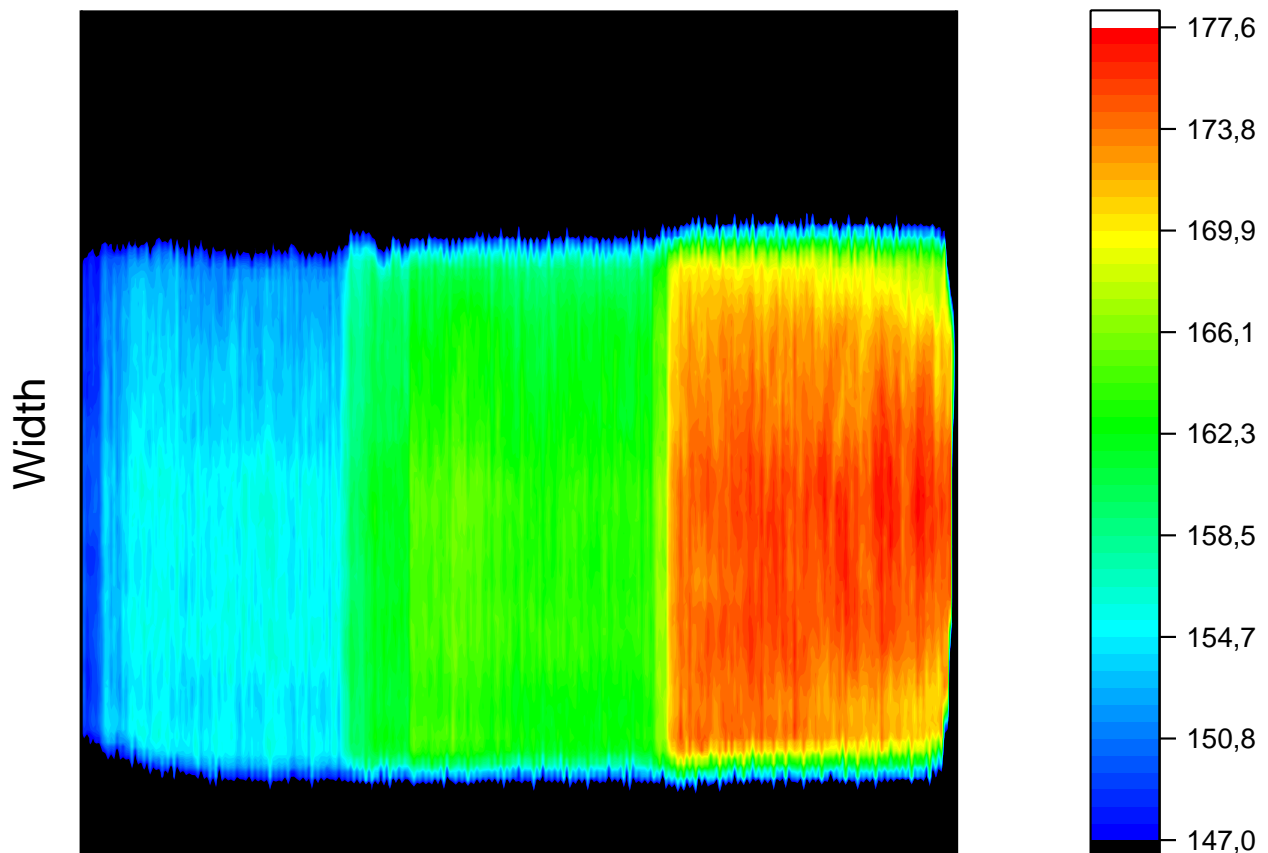


Fig 5.12 – Mass load scanner results of *Formulation G* with legend expressed in $g\ m^{-2}$.

3 different loading zones have been obtained from the slurry with Formulation G:

Zone	Loading [mg cm⁻²]	Loading Name	Active Material Loading [mg cm⁻²]	Capacity [mAh cm⁻²]
Blue	5.99	L1	5.63	3.25
Green	6.87	L2	6.46	3.83
Red	7.94	L3	7.46	4.26

Table 5m – Formulation G: target loadings and their main features.

All the coatings made from formulations (A → G) have been calendered to a target density ($\approx 1.3 \text{ mg cm}^{-2}$) in order to increase the particle/particle contact and increase the adherence to the current collector.

Figure 5.13 shows the results of the viscosity measurements of the slurry manufactured in this work. During measurement, an increasing shear rate is applied to the slurry and the corresponding viscosity is recorded. Depending on the studied system, it is possible to choose different shear rate values to evaluate a meaningful viscosity value. In this case the shear rate that equals to 1 s^{-1} at $25 \text{ }^\circ\text{C}$ was chosen as a reference value for all slurries. Depending on the coating system, the viscosity is adjusted to a specific range. For the Doctor Blade coating, a higher value is used (20 – 60 Pa·s), since the slurry would otherwise creep away beneath the blade. For the pilot coater, a lower viscosity is technically preferred (2 – 15 Pa·s), since the slurry would otherwise dry too fast. Viscosity values are shown in Table 5n together with other slurry parameters.

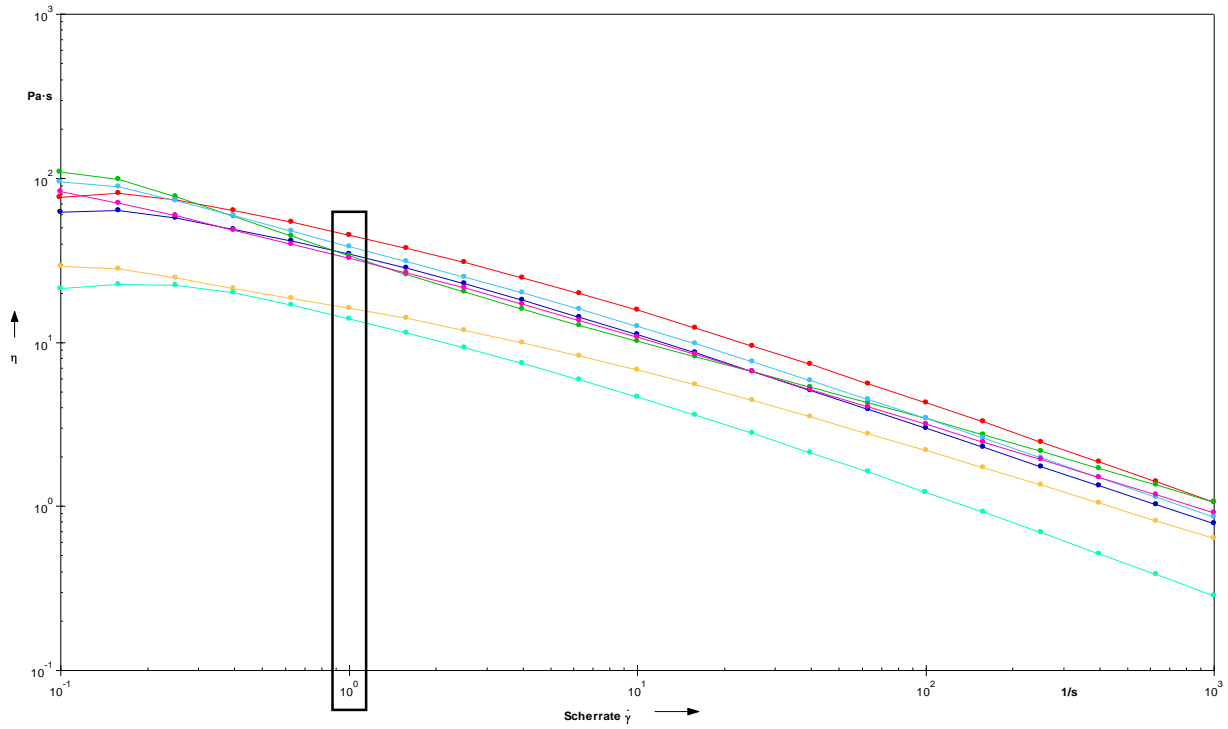


Fig. 5.13 – Viscosity curves of the anode slurries (Shear rate vs. Viscosity): formulation A (purple); formulation B (red); formulation C (blue); formulation D (green); formulation E (yellow); formulation F (light blue).

Formulation	Mixing method	Viscosity [Shear rate 1 s^{-1} at 25 °C]
A	Planetary mixer	36 Pa·s
B	Planetary mixer	45 Pa·s
C	Planetary mixer	36 Pa·s
D	Planetary mixer	33.5 Pa·s
E	Dissolver mixer	16 Pa·s
F	Dissolver mixer	14 Pa·s

Table 5n – Viscosity values of different slurries as a function of shear rate ($T = 25 \text{ °C}$).

After drying and calendering, the electrodes have been subjected to peeling tests in order to measure the adhesion strength on the coating/current collector interface. The results are shown in Fig. 5.14.

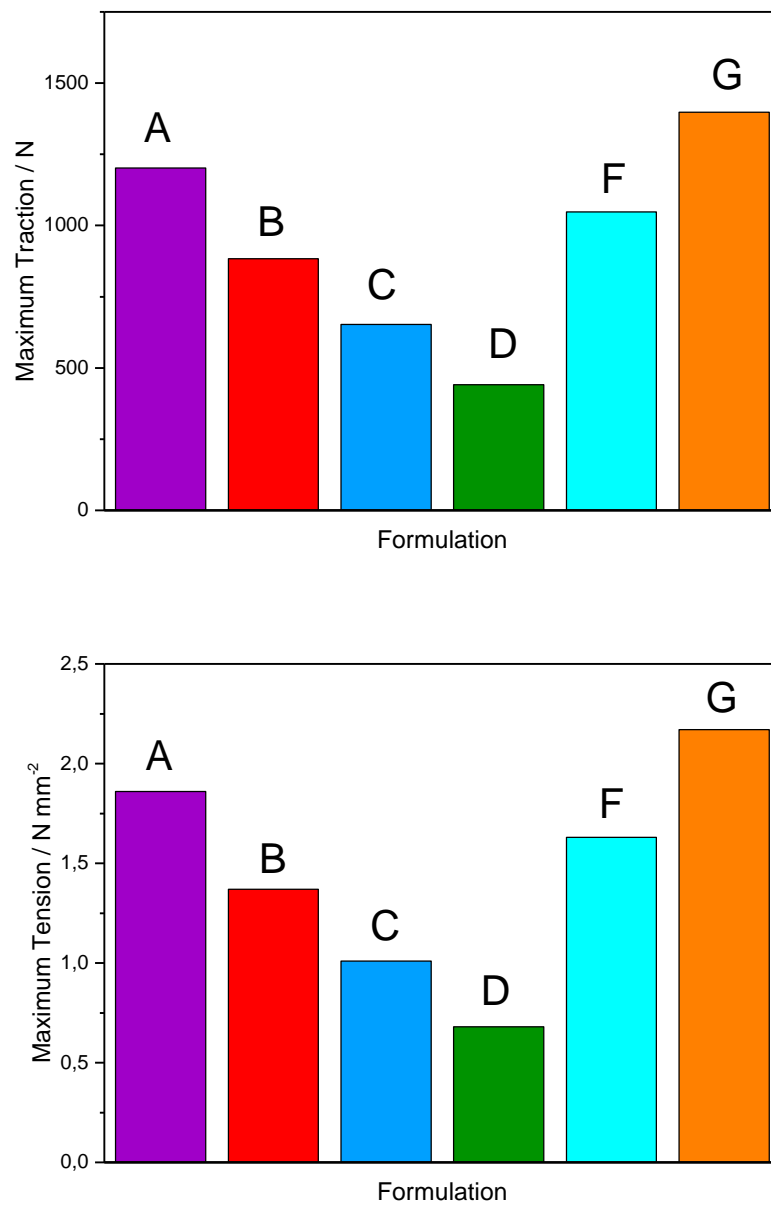


Fig 5.14 – Peeling test results in term of max. traction (upper panel) and max. tension (lower panel).

The obtained results show that the coating obtained from *Formulation A and G* have the strongest adhesion. Although they have the same slurry formulation and mixing method, formulation G shows better results, which are most likely due to the drying process and the use of different Na-CMC with a higher molecular weight. The use of surfactants (*Formulation B and C*) seems to weaken the coating adhesion, as it appears also in the case of the use of a buffer solution (*Formulation D*). From the direct comparison of two different mixing methods with the same recipe (Formulation A and F), it is possible to conclude that in this case, the mixing method do not greatly affect the adhesion values of the different coatings.

Table 5o – Summary table: Slurries and their main characteristics. The name of the slurry corresponds to the name of the formulation.

Slurry Name	Solid Content %	Density [g cm ⁻³]	Viscosity [shear rate 1 at 25 °C]	Zeta Potential [mV]
A	47.5	1.347	36	-67
B	48.7	1.359	45	-76.5
C	47.1	1.355	36	-65.1
D	53.5	1.402	33.5	-27.6
E	46.9	1.330	16	-65.6
F	20.4	1.12	14	-70.9
G	53.3	1.4	35	-70.2

5.3 Electrochemical characterization: Coin cells

5.3.1 Cell Assembly

In order to investigate the electrochemical performances of the Si@Gr negative electrodes, CR 2016- and CR 2032-format coin cells (Hohsen Corporation) have been assembled in an argon-filled glovebox (M-Braun), using metallic lithium disks (\varnothing 16mm) as counter electrode, two glass fiber separators (Whatman GF/A, \varnothing 16mm), and a LiPF_6 1M solution in EC:DEC (3:7) + 10% FEC (BASF). 12-mm diameter (1.131 cm^2 area) working electrodes have been cut and dried at $130 \text{ }^\circ\text{C}$ overnight. Coin cells were cycled using a VMP-3 multichannel electrochemical workstation (Biologic, France) in a $0.02 < E \text{ (V)} < 1.5$ potential range. The main difference between CR 2016 and the CR 2032-coin cell formats is the position of the stainless steel spacer and the presence of a disk spring in the CR 2032 format.

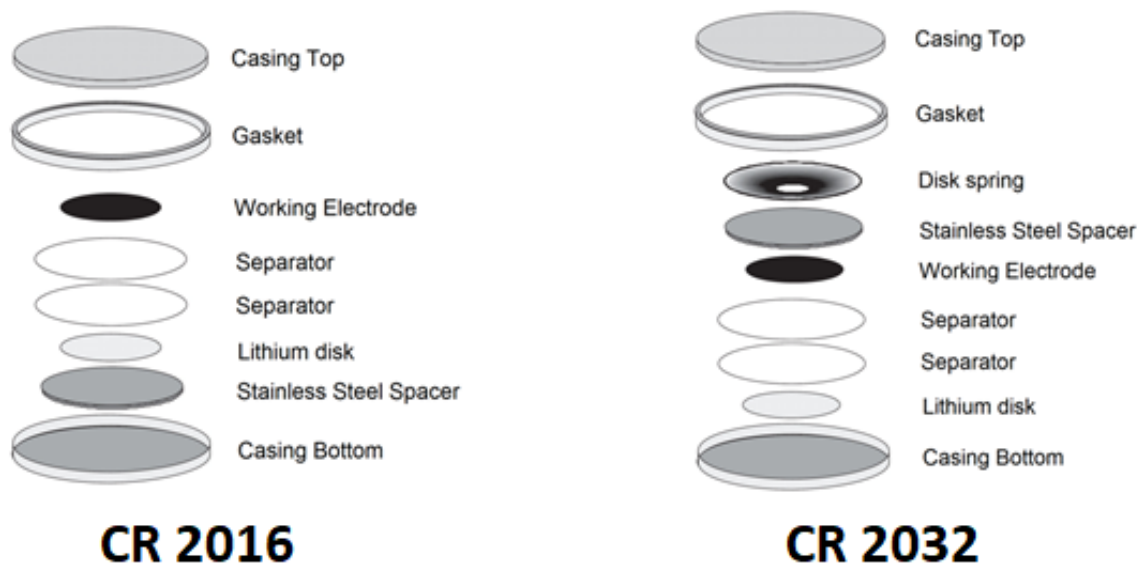


Fig 5.15 – Coin cell setup: CR 2016 (left); CR 2032 (right).

Two electrochemical tests were applied:

- 🔦 **ANODE LONG-TERM PROTOCOL:** 3 formation cycles at C/10 rate with a potential step (CC-CV mode) at the end of the anode lithiation until current reaches C/20 rate. After formation, 100 cycles are performed using a C/2 rate during lithiation (CC-CV mode until current is lower than C/20) and 1C during delithiation (CC mode); The current rate is referred to the Si@Gr composite.
- 🔦 **ANODE RATE CAPABILITY PROTOCOL:** 3 formation cycles at C/10 rate with a potential step (CC-CV mode) at the end of the anode lithiation until current reaches C/20 rate. After formation, 5 cycles at C/5, 5 cycle at C/2, 5 cycles at 1C, 5 cycles at 2C, 5 cycles at 3C, 5 cycles at 5C, and again 5 cycles at C/5 are applied during delithiation. Finally, a C/5 rate lithiation (CC-CV mode until current is lower than C/20) is applied. The current rate is referred to the Si@Gr composite.

5.3.2 Electrochemical characterization

Figure 5.16 shows the long-term protocol delithiation results of selected electrodes in terms of gravimetric (mAh g^{-1} ; upper graph) and areal (mAh cm^{-2} ; lower graph) capacities. Table 5p furthermore supplies the most important electrode parameters.

From the capacity plots, it is clearly visible that, from about 50th cycle, during the delithiation step the capacity starts to scatter. Because of the large areal capacity of the anode, a relatively high delithiation current is applied at 1C. Due to the lower active surface of the lithium disk compared to the anode, a (local) polarization of the counter electrode can occur, which leads to an incomplete delithiation process of the anode. After a specific amount of cycles this can cause dendritic growing from the anode to the Li-disk, generating micro-short-circuits, which affect the lithiation- and delithiation processes and lead to the scattering of the recorded capacities. The capacity scattering is observable for all the tested electrodes depicted in graph 5.16 and can be traced back to this phenomenon.

Formulation	Active Material mg/1.131 cm ²	Active Material mg/cm ²	Capacity @0.1C mAh/1.131 cm ²	Coating Density mg/cm ³	Capacity mAh/cm ²
A	4.69	4.15	2.71	1.26	2.40
B	4.55	4.02	2.63	1.25	2.33
D	4.41	3.90	2.55	1.34	2.56
F	3.15	2.79	1.82	1.09	1.61

Table 5p – Characteristics of some selected coatings.

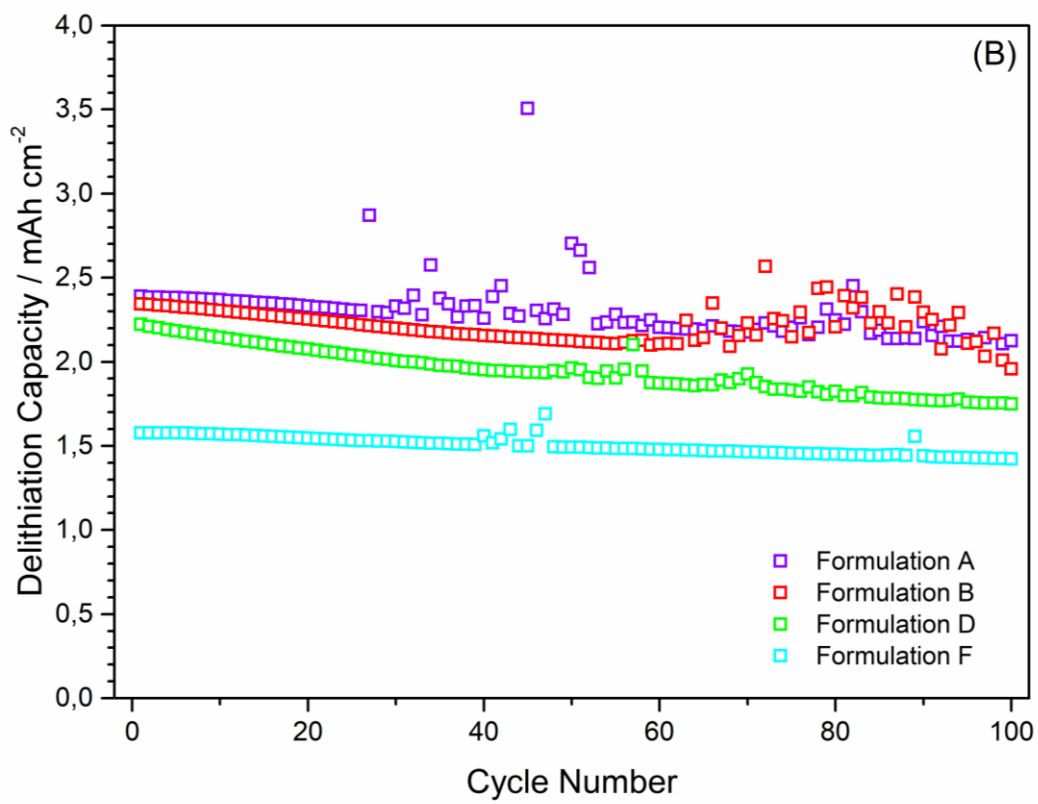
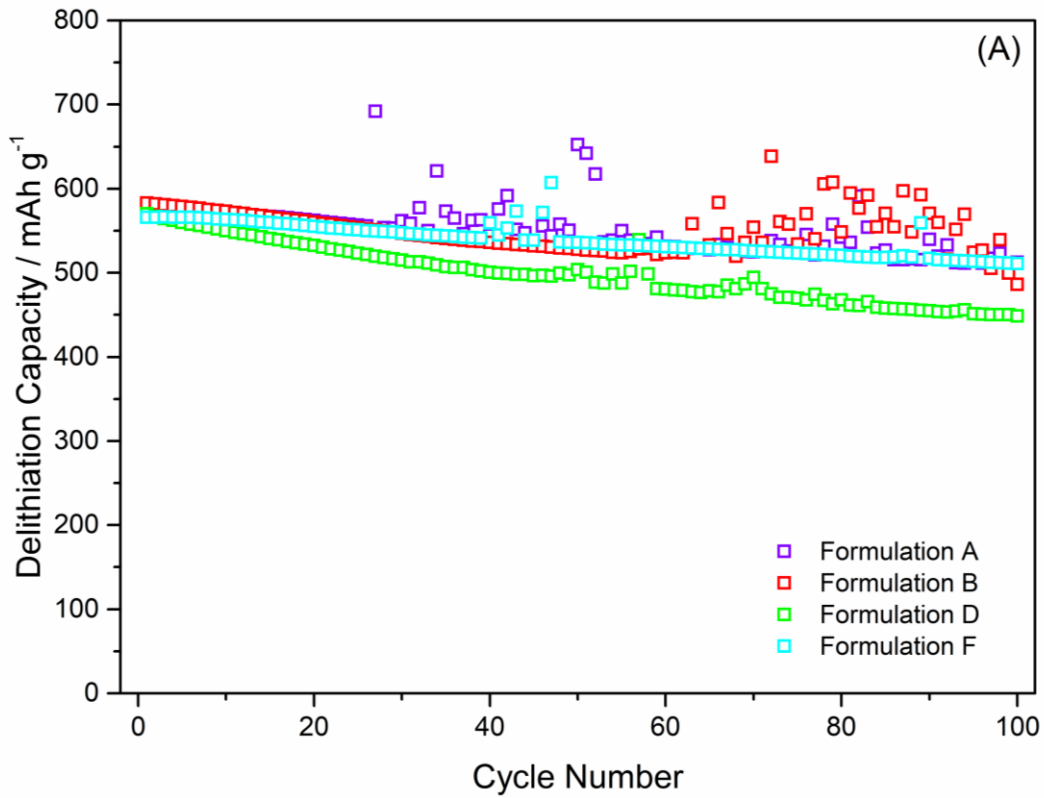


Fig 5.16 – Gravimetric and areal capacities of some selected coatings (CR 2016-coin cell format).

The dQ/dE^{-1} vs. E plot of a Si@Gr electrode (*Formulation A*) is shown in Figure 5.17 and compared to the dQ/dE^{-1} vs. E potential plot of a graphite-based electrode. Both plots have the characteristic graphite peaks shown by the dotted curve, and all those peaks correspond to the graphite lithiation/delithiation processes [11]. The silicon electrochemical reactivity is highlighted by the presence of only two fundamental peaks (E and I), since the others are most likely overlapped by those of the graphite. As already confirmed by Obrovac et al., whenever the potential drops below 0.05 V, there is the formation of the $Li_{15}Si_4$ crystalline phase [37]. The presence of peak E at 0.04 V is a confirmation of this phenomenon together with the respective delithiation peak at 0.45 V.

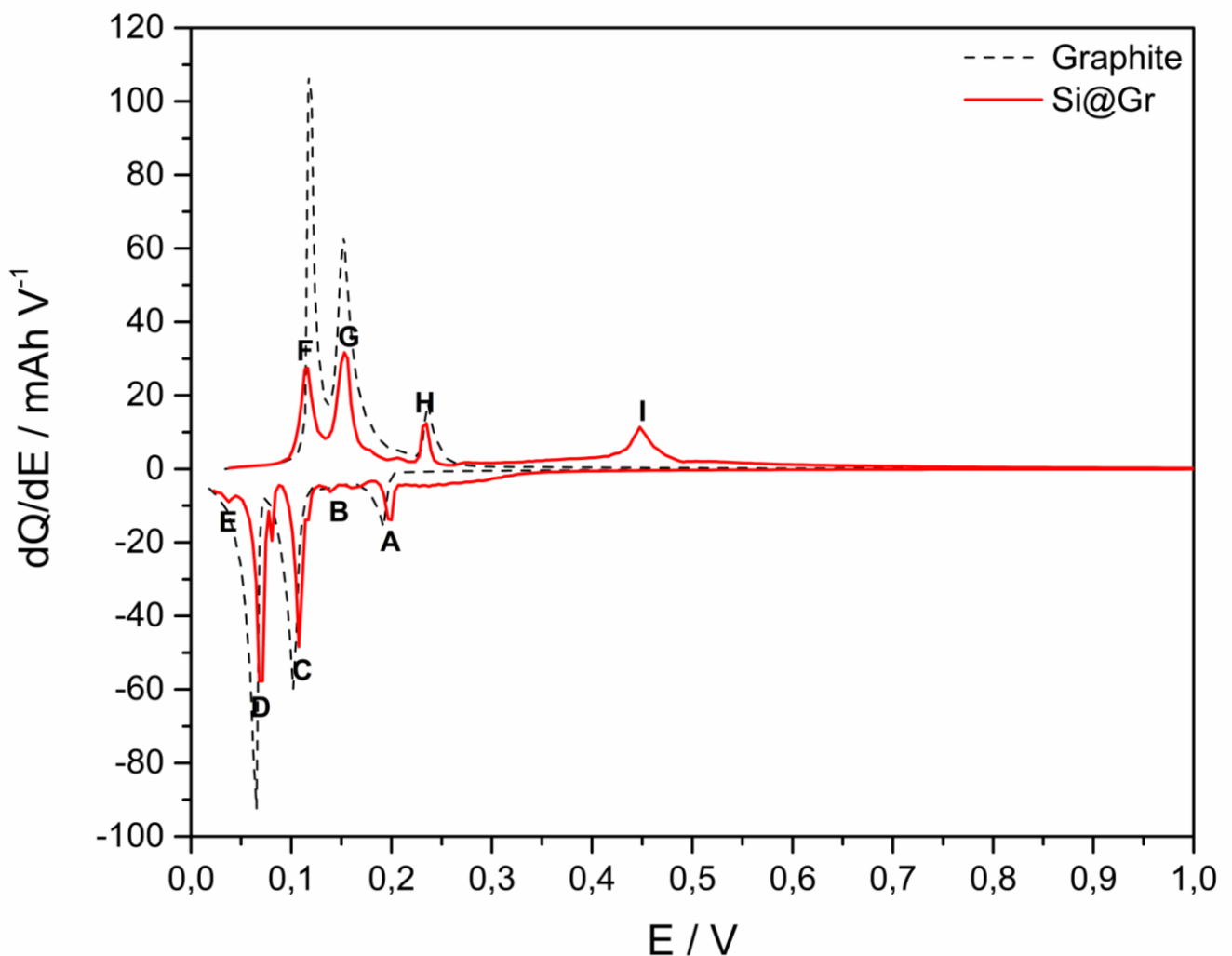


Fig 5.17 – dQ/dE^{-1} vs. E plot of *Formulation A* electrode (CR 2016-coin cell format).

Peak	Potential	Description
A	0.20 V	Graphite Lithiation: $\text{LiC}_{72} + \text{Li} \rightarrow 2 \text{LiC}_{36}$
B	0.14 V	Graphite Lithiation: $3 \text{LiC}_{36} + \text{Li} \rightarrow 4 \text{LiC}_{27}$
C	0.11 V	Graphite Lithiation: $4 \text{LiC}_{27} + 5 \text{Li} \rightarrow 9 \text{LiC}_{12}$
D	0.07 V	Graphite Lithiation: $\text{LiC}_{12} + \text{Li} \rightarrow 2 \text{LiC}_6$
E	0.04 V	Silicon lithiation: $a\text{-Li}_x\text{Si} \rightarrow \text{Li}_{15}\text{Si}_4$
F	0.12 V	Graphite Delithiation
G	0.15 V	Graphite Delithiation
H	0.23 V	Graphite Delithiation
I	0.45 V	Silicon Delithiation: $\text{Li}_{15}\text{Si}_4 \rightarrow 4 \text{Si} + 15 \text{Li}$ (two-phase region)

Table 5q – Summary of the main features evidenced by dQ/dE^{-1} vs. E plot in Fig 5.17.

The rate-capability protocol of some selected formulations are shown in Figure 5.18. Up to a current rate of 2C the performance is quite comparable. Applying a 5C current, a clear gap in capacity occurs indicating that *Formulation A* has the highest capacity retention at high currents. The low capacity at 5C current of *Formulation D* is most likely due to the presence of the 4% of insulating salts arising from the buffer solution. Their presence could hinder a complete utilization of the active material since some areas could be electrically isolated. The capacity scattering observed after ≈ 40 cycles in the long-term protocol is not present here, suggesting that the limited amount of cycles is not enough to detect this phenomenon.

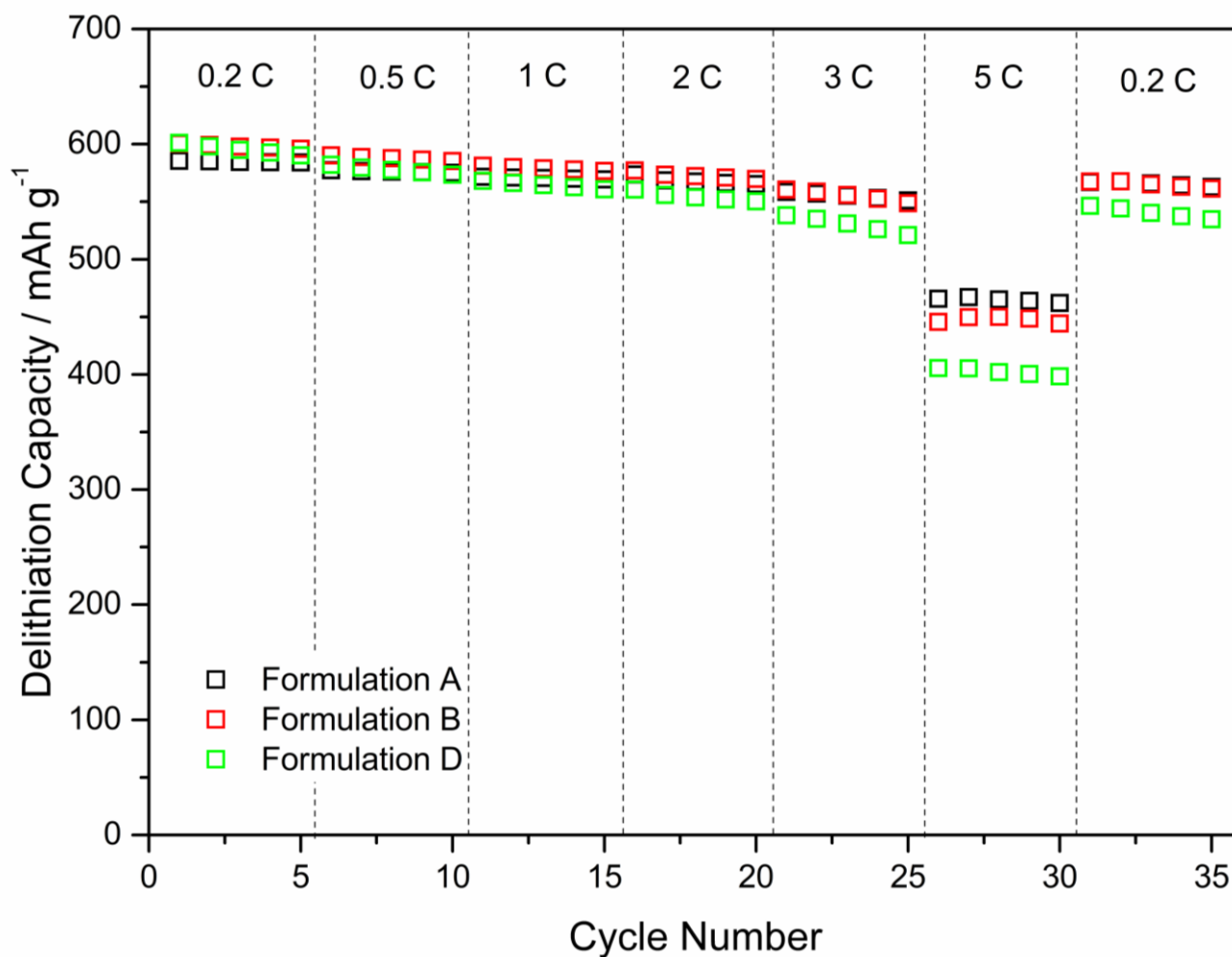


Fig 5.18 – Rate capability behaviour of some selected coatings (CR 2016-coin cell format).

For these reasons *Formulation A* was chosen as the definitive recipe for our slurry, and later optimized to obtain *Formulation G*. Considering the capacity scattering, further studies have been carried out to understand the origin of this phenomenon. The so far used CR 2016-coin cells have been replaced by CR 2032-coin cells to investigate the application of a different coin cell format and trying to find the solution for that problem.

CR 2016 and CR 2032-coin cell setup has the same width but different height. This means that in the case of CR 2016-coin cell, the working electrode is subject to a higher internal pressure. Taking a closer look at a close CR 2016-coin cell, a slight curvature of the cap (casing top) near the outer circumference of the coin cell is visible. This could lead to an uneven pressure distribution on the working electrode, which could affect the cell kinetics.

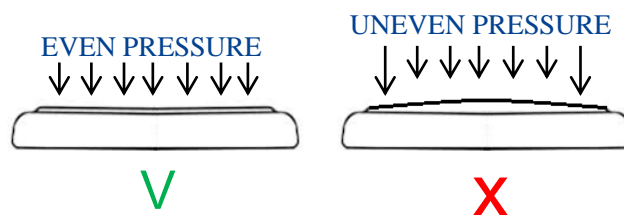


Fig 5.19 – Pressure distribution on the working electrode in the CR 2016-coin cell format.

First, the spacer position in the CR 2016-coin cell setup has been evaluated, then with the use of a CR 2032-coin cell format, we tried to understand the effect of the pressure applied on the working electrode. As a proof of concept, coin cells have been assembled replacing the working electrode with a pressure-sensitive paper. The red marks that appear on the surface of the paper identify the areas subject to a greater pressure. The post-mortem disassembly of selected CR 2016-coin cells (Fig 5.21) shows how the coin cell format together with other variables (glove-box contamination, lithium purity etc.) can affect the electrochemical performances. As we can see from the Figure 5.21, the capacity scattering seems to be related to the presence of lithium dendrites grown through the separators. The absence of capacity scattering and lithium dendrites on the CR 2032 format seems to confirm the hypotheses. The higher pressure on the external part of the working electrode decreases the counter/working electrode distance resulting in a lower resistance and thus a higher local current density that starts the Li dendrites growth. The spacer position can also help to avoid these Li dendrites. Using a pressure-sensitive paper, it is possible to see how the spacer adjacent to the working electrode (Fig. 5.20 (B)) redistributes the pressure homogeneously across the electrode. Without the metallic spacer near the working electrode, it experiences a higher pressure on the circular external part near the cap, resulting in the appearance of red marks, see figure 5.20 (A).

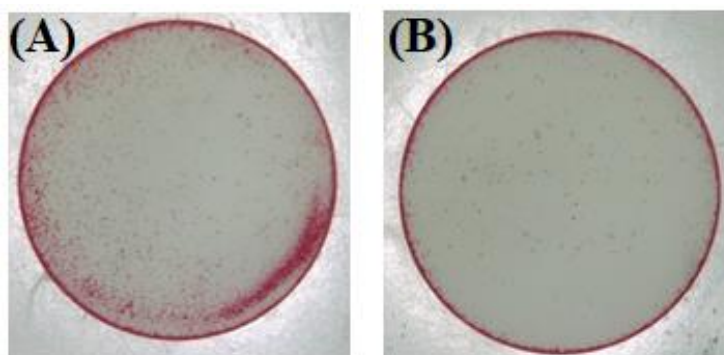
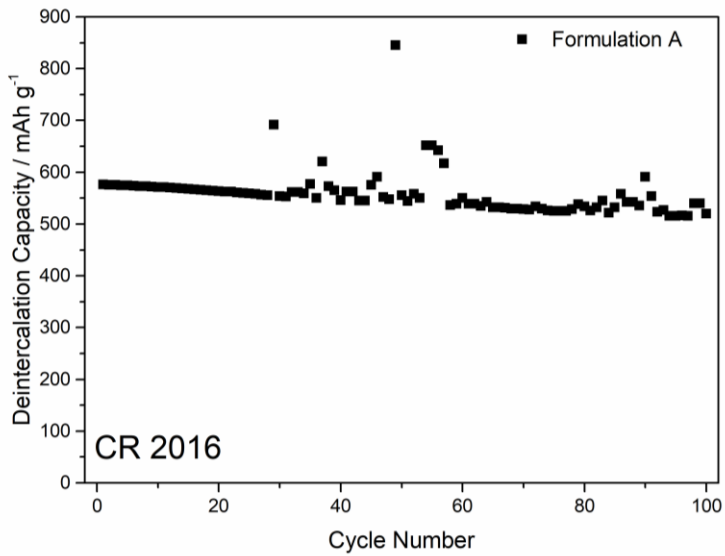
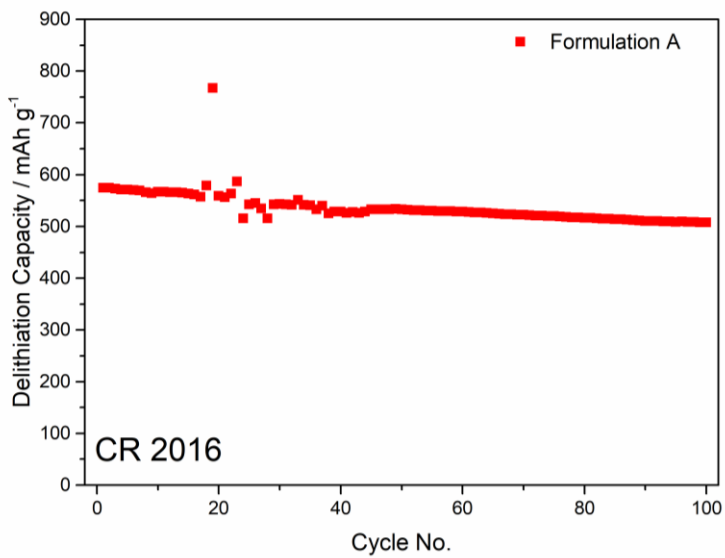


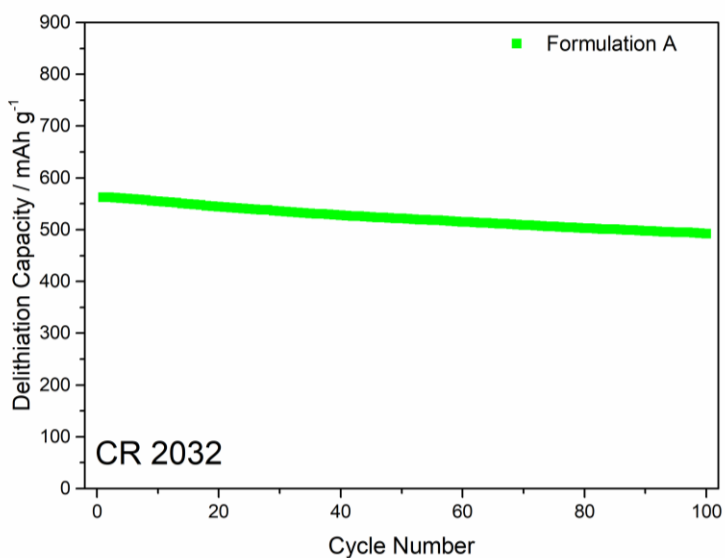
Fig 5.20 – Pressure-sensitive paper results in the CR 2016-coin cell format.



- Black Circle (Li dendrites)
- Huge Capacity scattering



- Few black spots (Li dendrites)
- Lower Capacity scattering



- No Li dendrites
- No capacity scattering

Fig 5.21 – Correlation between used coin cell format and Li dendrites growth.

The absence of Li dendrites and the more stable capacities of CR 2032-coin cells made them the format of choice for our 2-electrodes electrochemical measurements.

The long-term protocol results of the CR 2032-coin cells are shown in figure 5.22.

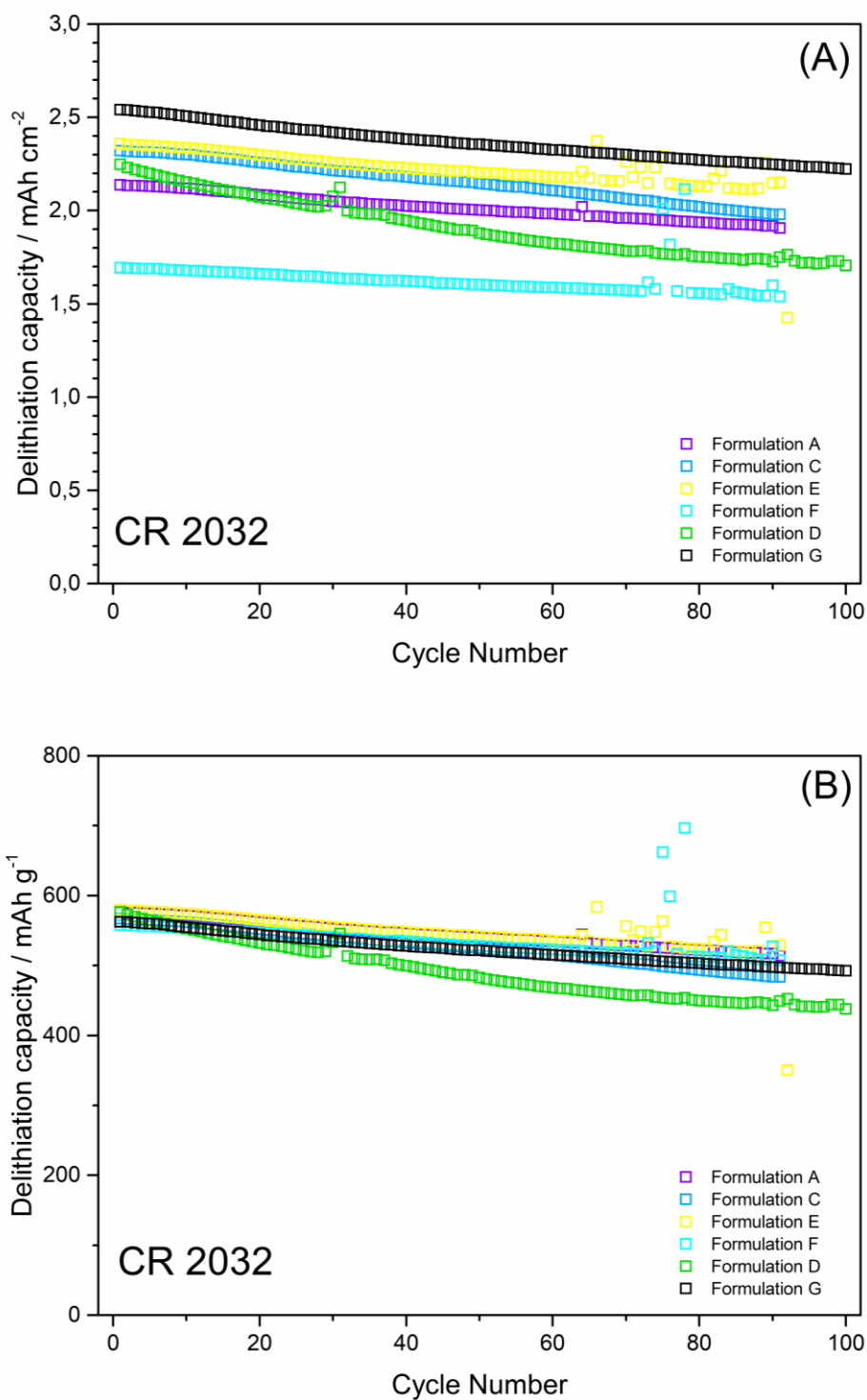


Fig 5.22 – Long-term behaviour of some selected coating (CR 2032-coin cell format): areal (A) and gravimetric (B) capacities.

Formulation A shows very good results in terms of capacity and stability through cycling compared to other formulations with similar density and active material loading. *Formulation G*, which is the optimized version of *Formulation A*, show the best stability and capacity, which can be referred to the optimized coating and drying process. Figure 5.23 shows the delithiation capacities (in terms of mAh cm^{-2} and mAh g^{-1}) of *Formulation G* electrodes with different loadings ranging from 5.63 to 7.46 mg cm^{-2} of active material.

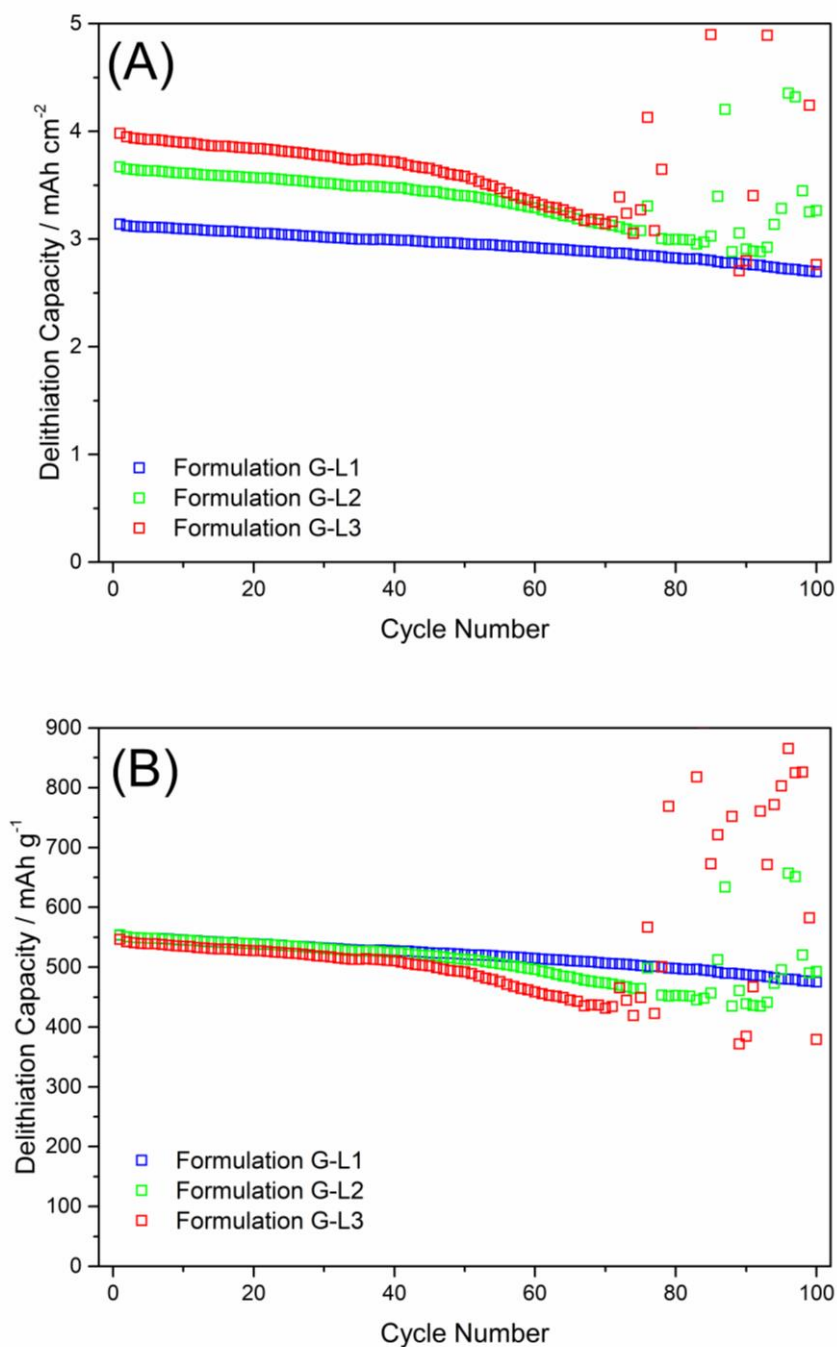


Fig 5.23 – Long-term behaviour of *Formulation G*'s loadings (CR 2032-coin cell format): areal (A) and gravimetric (B) capacities.

The three electrodes have different areal capacities according to their different loadings, (Fig. 5.23A) whereas L2 and L3 are subjected to capacity fade and scattering after 70 cycles. These phenomena are also observable when plotting the gravimetric capacity (Fig. 5.23B). As aforementioned, the polarization of the lithium counter electrode becomes crucial at higher current densities, which might be the reason that, among the three tested electrodes, only the one with the lowest areal capacity, L1 shows very good stability.

Rate capability tests (Fig 5.24) confirm the long-term protocol results. Anyway, they all show good capacity retention at different C-rates with the L1 revealing the highest rate capability (Fig 5.25).

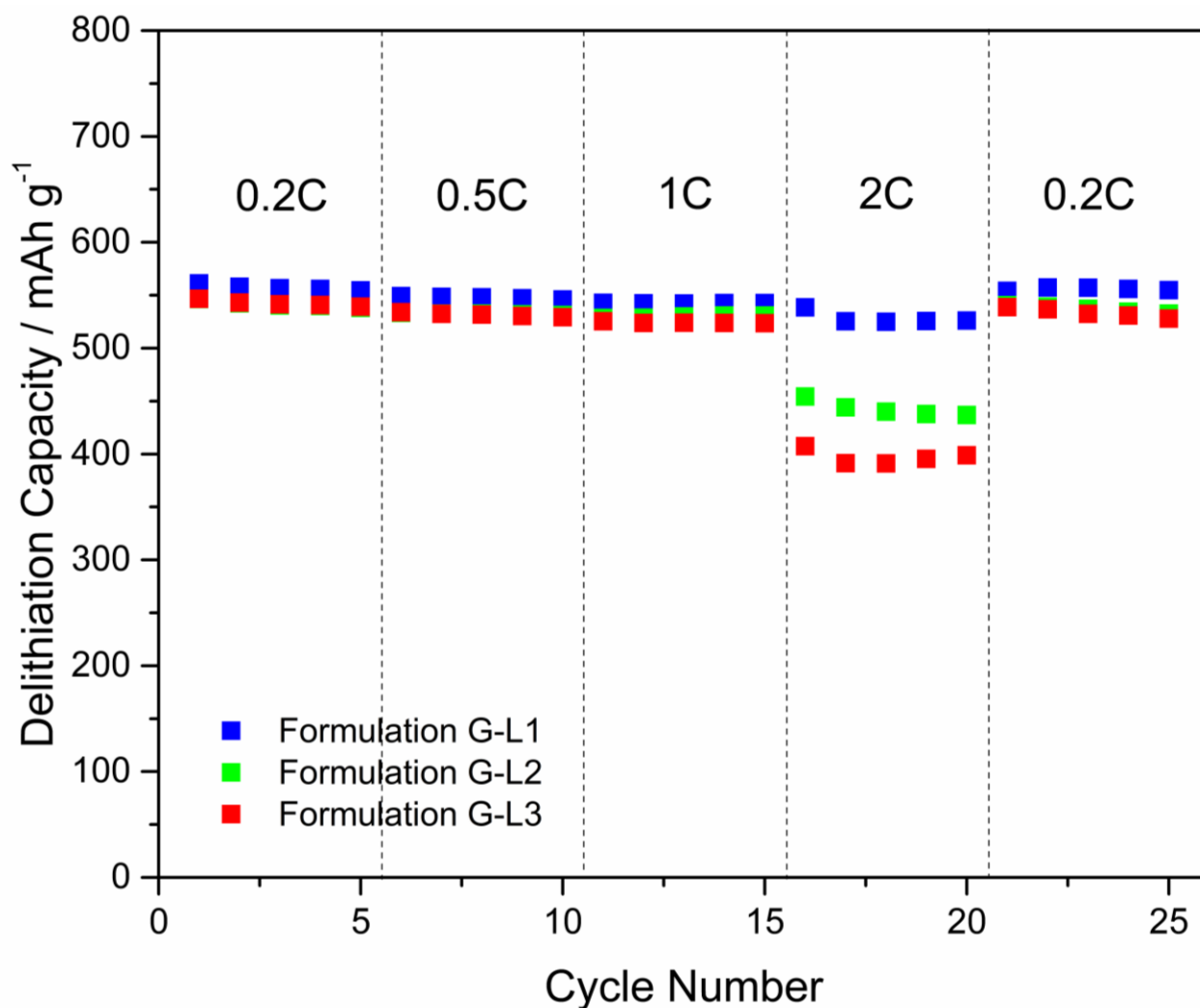


Fig 5.24 – Rate capability behaviour of Formulation G's loadings (CR 2032-coin cell format).

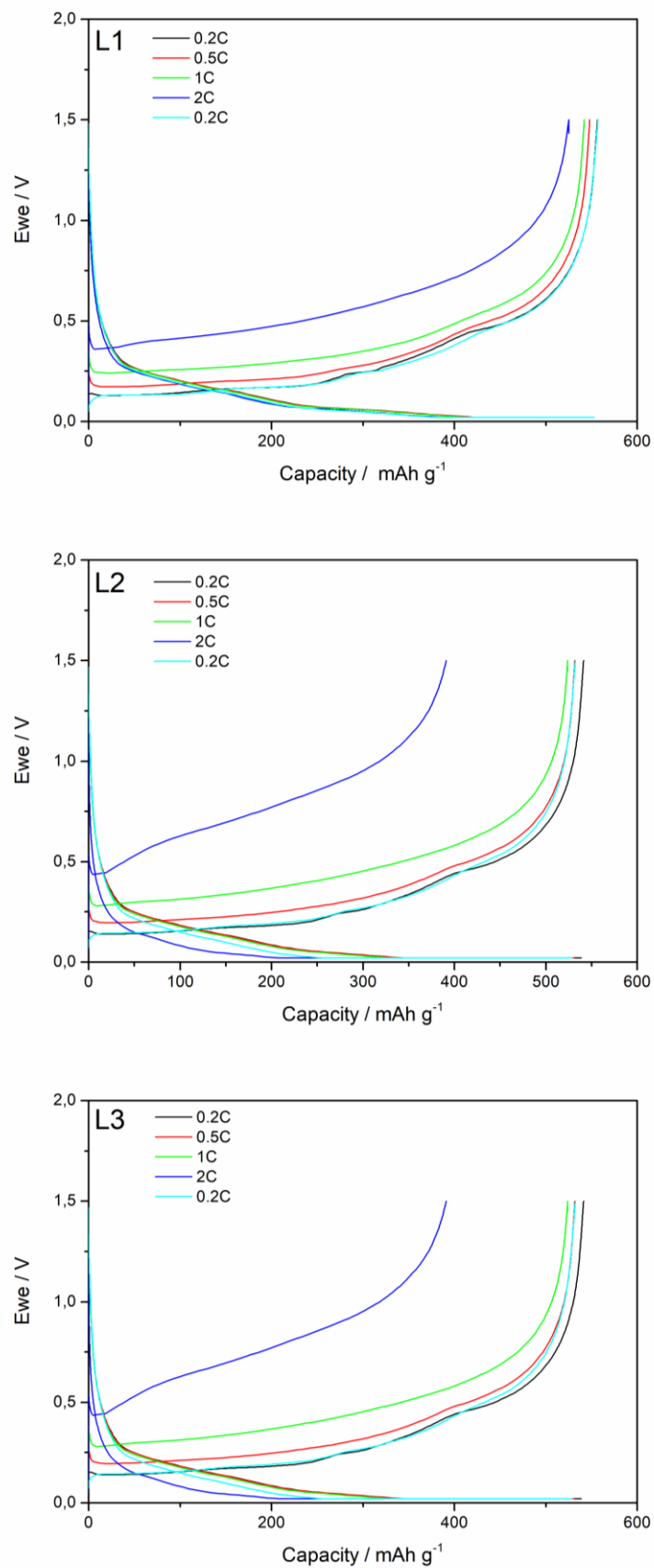


Fig 5.25 – Galvanostatic profiles of formulation G electrodes: L1 (upper panel), L2 (central panel), and L3 (lower panel) loadings.

5.4 Electrochemical characterization: Pouch cells

The first milestone of this project was the assembly of a single-layer pouch cell with the generation II materials (Si@Gr // NMC 811), whereas the energy density of this cell (Wh l^{-1}) should be 10% higher than its generation I analogue (reference cell), i.e. approximately 550 Wh l^{-1} . (Fig. 5.26).

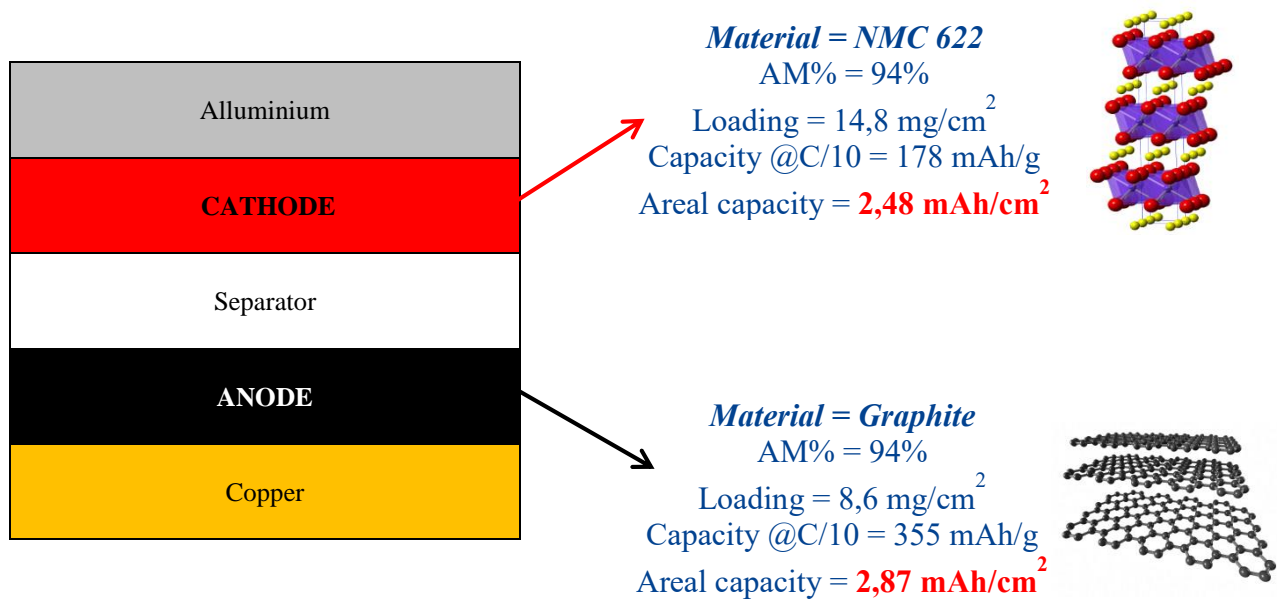


Fig 5.26 – Generation I single-layer pouch cell used as reference.

This reference single-layer pouch cell has a Graphite-based anode and an NMC 622-based cathode. Its parameters are listed in the table below:

Nominal Voltage	Balancing	Stack volume	Capacity @C/10	Energy	Energy density
3.65 V	+ 13,7 %	0,413 ml	56.6 mAh	0.207 Wh	$500,41 \text{ Wh l}^{-1}$

Table 5r - Generation I single-layer pouch cell electrochemical features.

5.4.1 Cathode preparation and characterization

Because of the lower Cobalt content and the higher specific capacity and energy density, NMC 811 replaced NMC 622 as next generation cathode material [123]. The cathode formulation (*Formulation H*) is shown in Table 5s. For the preparation, a dissolver mixer (3 liters) was used. The electrode was coated and dried with the pilot coater. Three different loading have been obtained for balancing experiments (B1, B2 and B3, see Table 5t).

FORMULATION H			
<i>NMC 811</i>	<i>Super C65</i>	<i>PVdF</i>	<i>Graphite</i>
94%	2%	2%	2%

Table 5s - Weight percentage of Formulation H components.

Loading [mg cm⁻²]	Loading Name	Active Material Loading [mg cm⁻²]	Capacity [mAh cm⁻²]
12,95	B1	12,17	2,37
14,01	B2	13,17	2,57
15,47	B3	14,51	2,83

Table 5t - Formulation H: target loadings and their main features.

CR 2032-coin cells were assembled to evaluate the cycling performances and stability of the cathodes. The cells were cycled using a VMP-3 multichannel electrochemical workstation (Biologic, France) in a $3.0 < E \text{ (V)} < 4.3$ potential range, while the applied long-term protocol is described below:

 **CATHODE LONG-TERM PROTOCOL:** 2 formation cycles at C/10 rate with a potential step (CC-CV mode) at the end of the anode lithiation until current reach C/20 rate. Using the current value after formation, 100 cycles have been performed using a C/2 rate during delithiation (CC-CV mode until current is lower than C/20) and 1C during lithiation (CC mode).

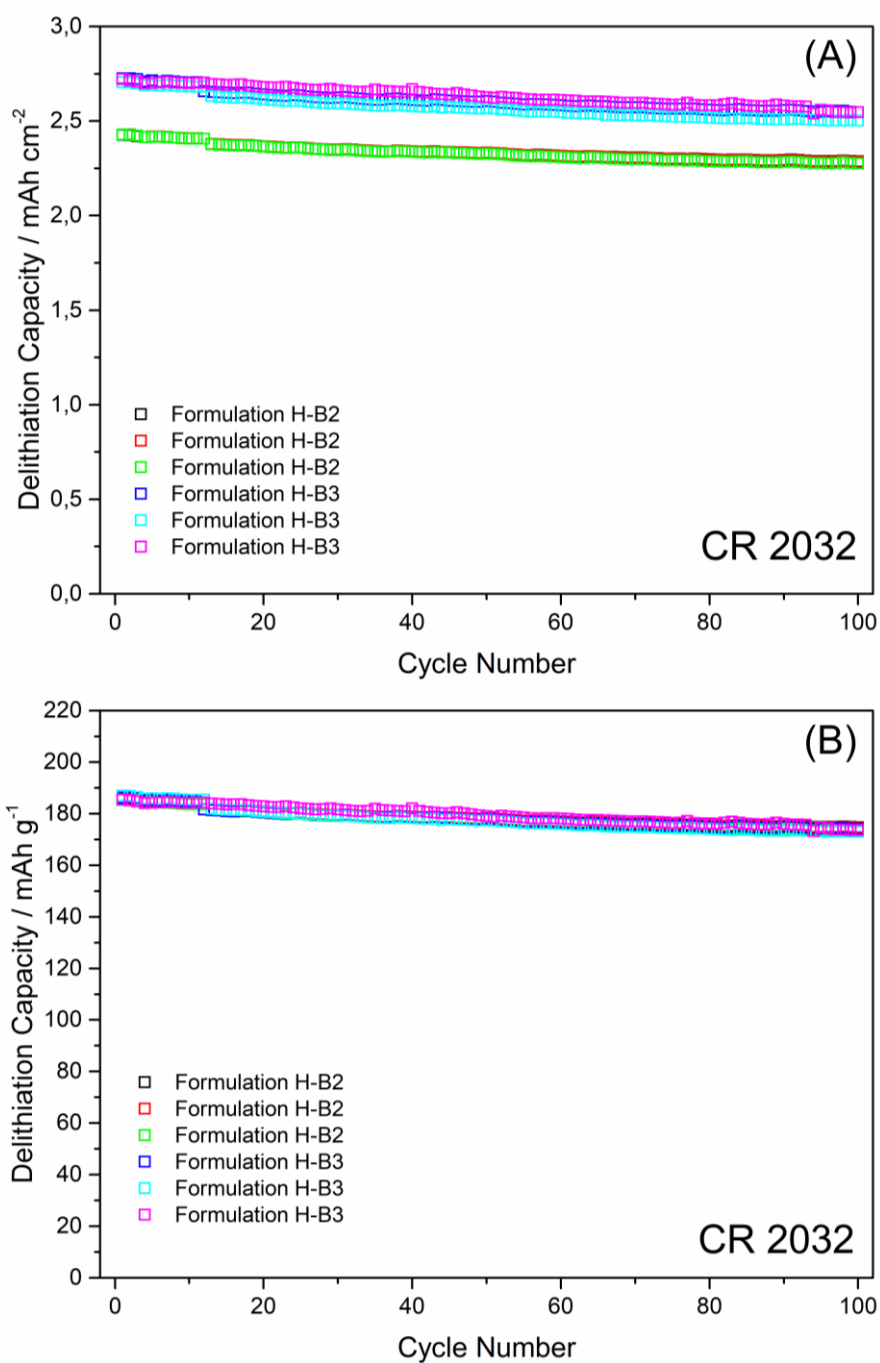


Fig 5.27 - Long-term behaviour of Formulation H loadings (CR 2032-coin cell format): areal (A) and gravimetric (B) capacities.

Long-term cycling results of 2 different *Formulation H* loadings are reported in Fig. 5.27. All of them have a good stability and capacity retention upon cycling, with loadings B2 and B3 having 94% and 93.2% of capacity retention after 100 cycles, respectively. $dQ dE^{-1}$ vs. E plot of a NMC 811-based cathode is shown below (Fig. 5.28).

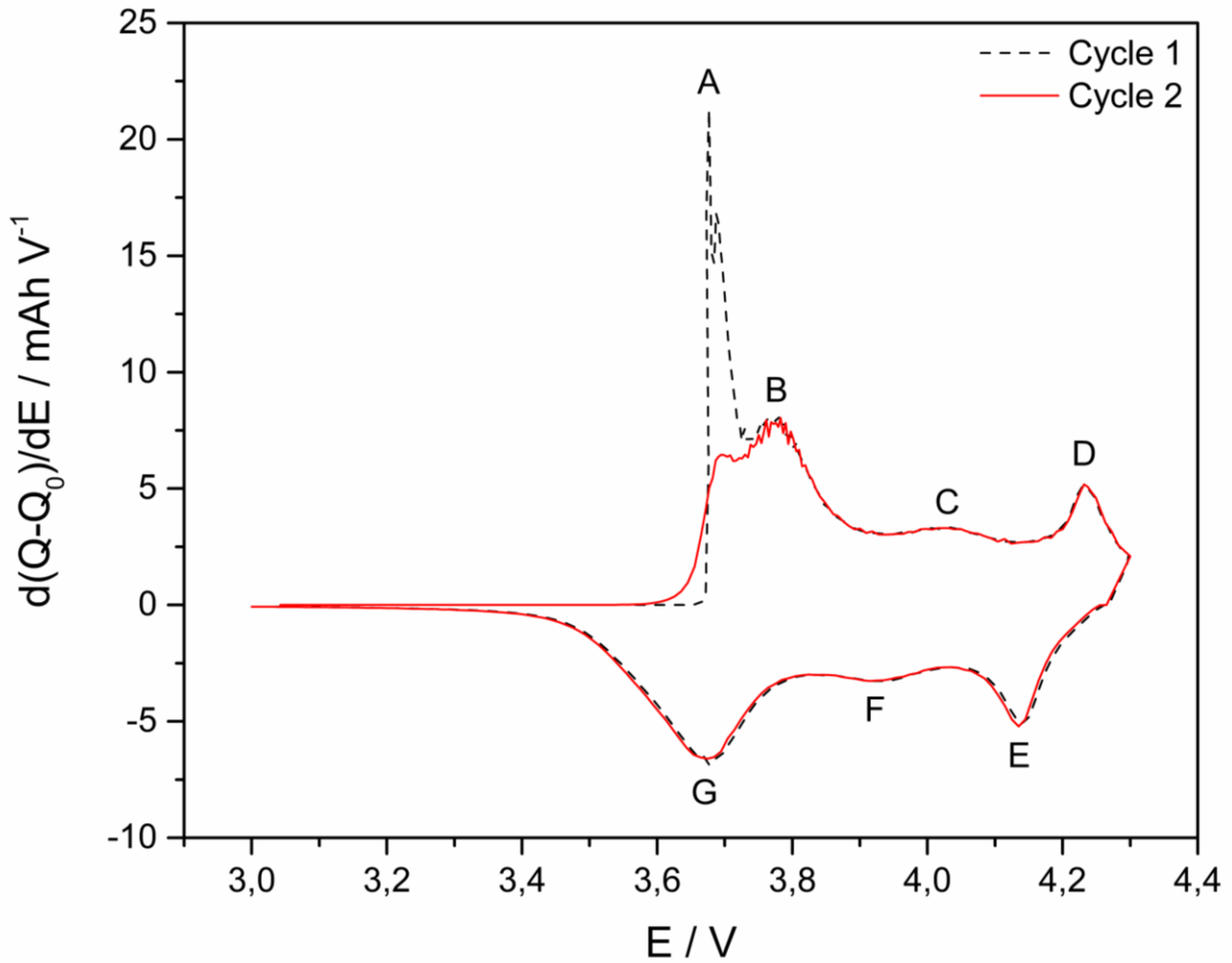


Fig 5.28 – dQ/dE vs. E plot of Formulation H electrode (CR 2032-coin cell format).

During delithiation, the cell shows a sharp peak (A) and three secondary peaks (B, C, D) attributable to a multiphase transition already reported in literature by Dahn et al [124]. From the second cycle on, the sharp peak A becomes smaller but the oxidation peaks positions are perfectly overlapped as well as the corresponding reduction peaks (E, F, G). As in the case of LiNiO_2 -based materials, the peaks correspond to three different phase transitions: hexagonal to monoclinic ($\text{H}_1 \rightarrow \text{M}$; Peak B), monoclinic to hexagonal ($\text{M} \rightarrow \text{H}_2$; Peak C) and hexagonal to hexagonal ($\text{H}_2 \rightarrow \text{H}_3$; Peak D) [125][126]. The peak maxima are listed in Table 5u.

<i>Formulation H [dQ dE⁻¹ vs. E plot]</i>							
Peak	A	B	C	D	E	F	G
Potential	3.68 V	3.77 V	4.03 V	4.23 V	4.13 V	3.92 V	3.67 V

Table 5u – Summary of the main features evidenced by dQ dE⁻¹ vs. E plot in Fig 5.28

5.4.2 Full Cells assembly and characterization

For this purpose, single-layer pouch cells have been assembled in a battery dry room ($T = 21\text{ }^{\circ}\text{C}$, dew point $< -62\text{ }^{\circ}\text{C}$) using different combination of *Formulation G* anodes (L1 - L2 - L3) and Lithium Nickel Cobalt Manganese Oxides (NMC 811 – $\text{LiNi}_{0.8}\text{Mn}_{0.1}\text{Co}_{0.1}\text{O}_2$ and NMC 622 - $\text{LiNi}_{0.6}\text{Mn}_{0.2}\text{Co}_{0.2}\text{O}_2$) cathodes. The steps of the cell assembly are shown in Fig. 5.28. A trilayer polypropylene-polyethylene-polypropylene membrane (Celgard 2325) was used as separator. 900 μl of LiPF_6 1M solution in EC:DEC (3:7) + 10% FEC (BASF) was applied as electrolyte. Anode and cathode areas were respectively 26 cm^2 and 23.94 cm^2 in order to help electrodes alignment during assembly (Fig. 5.29), and avoid lithium plating due to the higher electromagnetic field nearby the anode edges [127]. Before assembly, anode and cathode were selectively dried in a vacuum oven at 130 $^{\circ}\text{C}$. After assembly, the pouch cell was again dried in a glove-box oven. Before the final welding, the pouch was filled with the electrolyte under vacuum. In order to check if the anode is negatively polarized respect to the metallic lithium electrode, a custom reference electrode has been inserted in the anode side of the pouch bag. This helps to evaluate the maximum charging rate for an optimized test plan without causing Li deposition. Single-layer pouch cells were cycled using a VMP-3 multichannel electrochemical workstation (Biologic, France) in a $2.7 < E\text{ (V)} < 4.2$ potential range. The effect of a pouch cell holder during cycling was also a topic of investigation.

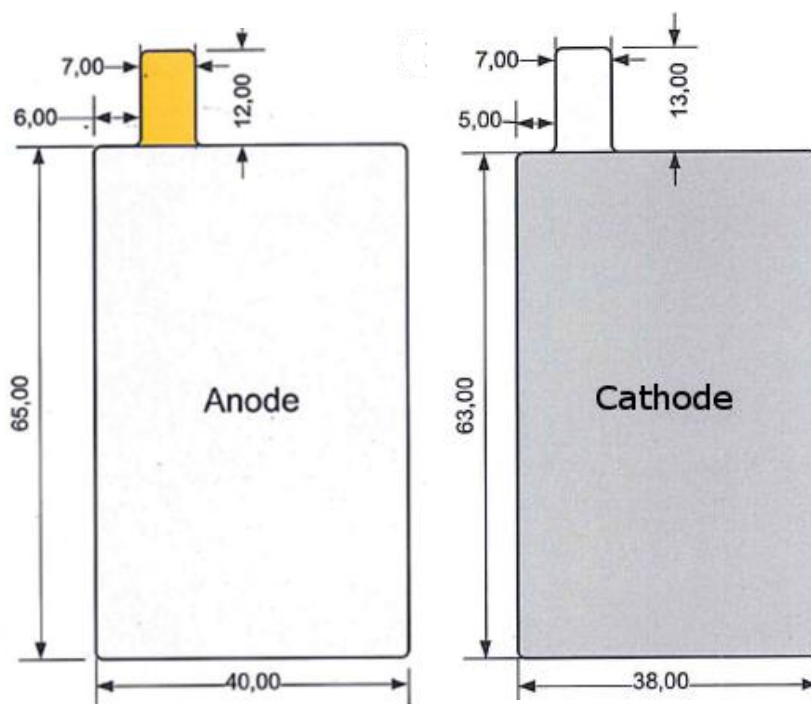


Fig. 5.29 – Schematized single-layer pouch cell electrodes.

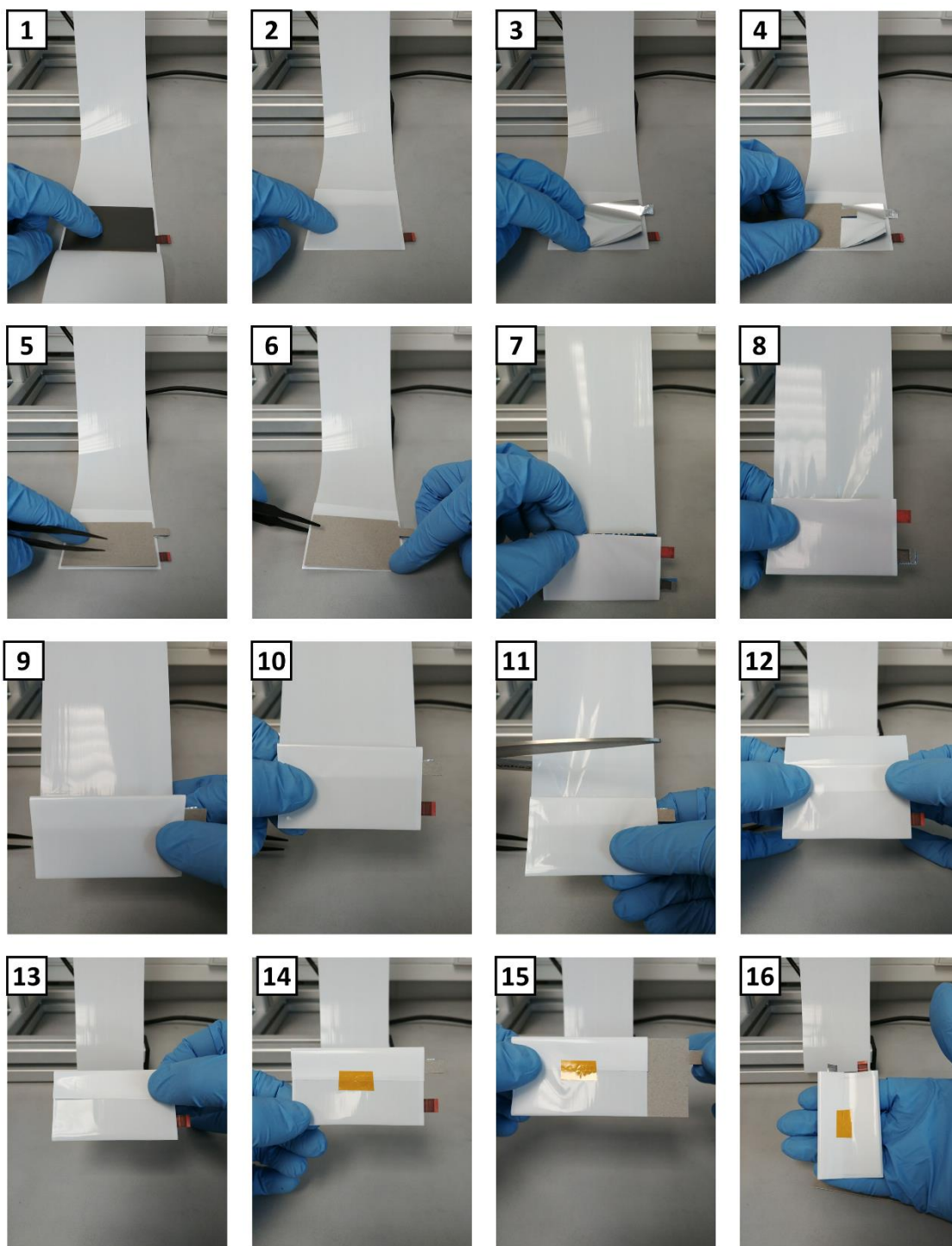


Fig 5.30 – Assembly procedure of single-layer pouch cell stack.

In order to finely monitor the electrodes potential during cycling, EL-CELL ECC-Ref full cells have been assembled using some of the previous anode/cathode combinations. In this case, 400 μl of the above-mentioned electrolyte were applied.

The separator was a 1.5 mm thick glass fiber membrane (\varnothing 18mm) which separated the anode (\varnothing 16mm) from the cathode (\varnothing 15mm). The cells were cycled using a VMP-3 multichannel electrochemical workstation (Biologic, France) in a $2.7 < E \text{ (V)} < 4.2$ potential range.

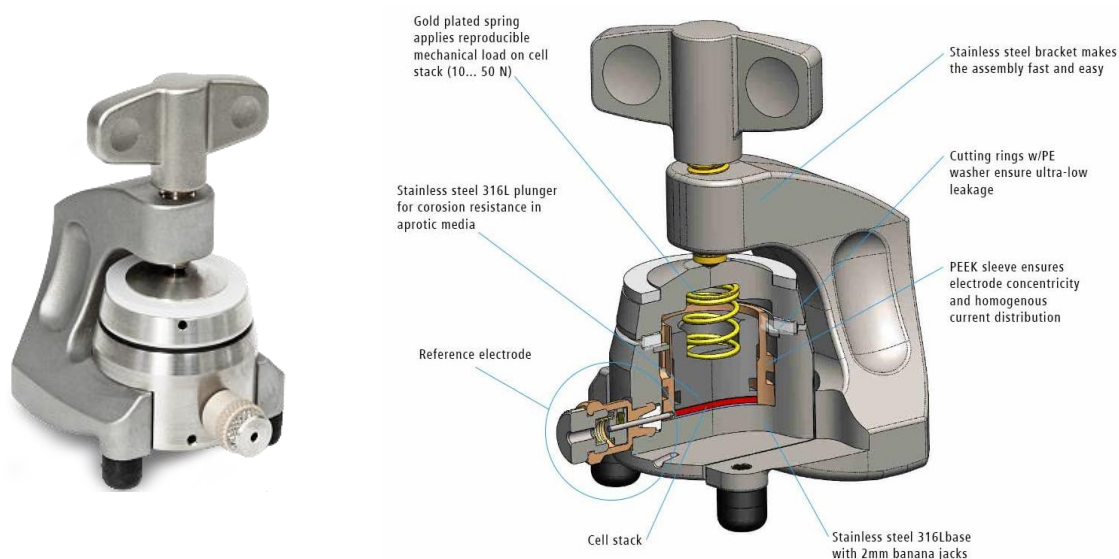


Fig 5.31 – EL-CELL ECC-Ref cell.

The test plans for the single-layer pouch cells and EL-CELL ECC-Ref full cells are stated below:

- 🔦 **FULL CELL LONG-TERM PROTOCOL:** 3 formation cycles at $C/10$ rate with a constant voltage step (CC-CV mode) at the end of the anode lithiation until current reach $C/20$ rate. Using the current value after formation, 100 cycles have been performed using a $C/2$ rate during lithiation (CC-CV mode until current is lower than $C/20$) and 1C during delithiation (CC mode)

- 🔦 **FULL CELL RATE CAPABILITY PROTOCOL:** 3 formation cycles at $C/10$ rate with a potential step (CC-CV mode) at the end of the anode lithiation until current reach $C/20$ rate. Using the current value after formation, 3 cycles at 0.1C, 3 cycle at 0.33C, 3 cycles at 0.5C, 3 cycles at 0.7C, 3 cycles at 1C were applied during delithiation (CC-CV mode until current is lower than $C/20$). A 1C rate delithiation (CC mode) was applied.

For the sake of clarity, the full cells results will be shown referring the gravimetric capacity (mAh g^{-1}) to the cathode active material. All the single-layer pouch cells have been tested using a tailored pouch cell holder.

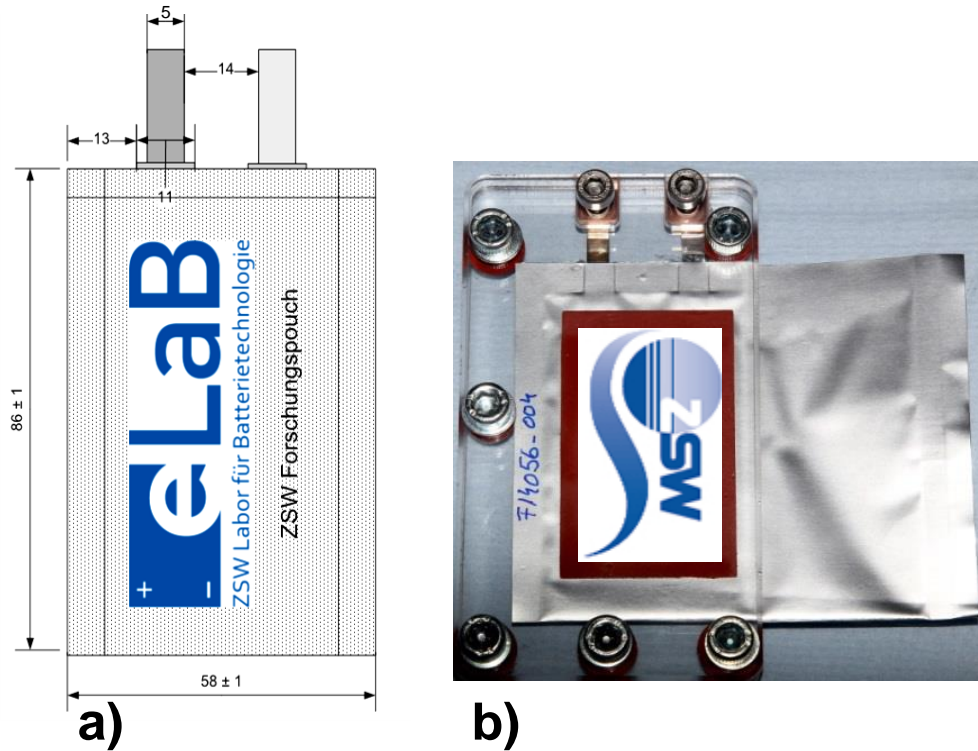


Fig 5.32 – Single-layer pouch cell: cell configuration (a), and the plexiglass holder used for the cycling (b).

Once the anode (*Formulation G*) and the cathode (*Formulation H*) have been analyzed and characterized, single-layer pouch cells have been assembled according to different loading combinations (Table 5v). In order to improve cell safety and reduce lithium plating, an oversizing of anode capacity respect the cathode capacity is mandatory. Adjusting the negative electrode to positive electrode reversible capacity ratio is called balancing, and it can be expressed as N/P ratio or as anode percentage excess.

$$\text{Anode Excess \%} = \frac{q_{\text{anode}} - q_{\text{cathode}}}{q_{\text{anode}}} * 100 \quad (42)$$

where q_{anode} and q_{cathode} are respectively the anode and cathode areal capacities expressed in mAh cm^{-2} .

Since oversizing leads to an increase of active material mass, and thus to a decrease of the cell energy density, an optimal trade-off between safety and performance is required. Since the kinetics of stage I are very sluggish compared to II and III, the increasing overpotential would lead to a fast drop into lower or even negative potentials, if areal capacities of cathode and anode were identical. This would mean either Li deposition or at least incomplete charging process, if the cell reaches a certain cut-off. Otherwise, if anode \gg cathode, a lot of capacity is lost during SEI formation.

Combination	Anode (Formulation G)		Cathode (Formulation H)		Balancing
	Loading	Capacity / mAh cm^{-2}	Loading	Capacity / mAh cm^{-2}	
#1	L1	3.25	B2	2.57	+ 21%
#2	L2	3.83	B3	2.83	+ 26%
#3	L3	4.26	B2	2.57	+ 40%
#4	L1	3.25	B3	2.83	+ 13 %

Table 5v – Anode and cathode combinations and their respective balancing.

The first results of combinations #1, #2, #3, and #4 (Fig. 5.33) show a counterintuitive behaviour. The increase of the cell balancing should provide a better stability since could avoid possible plating phenomena. Figure 5.32 shows a random correlation between balancing and stability, revealing the presence of other variables that could influence the cell behaviour. In addition to the poor stability, it is possible to observe a rapid capacity fading for all combinations.

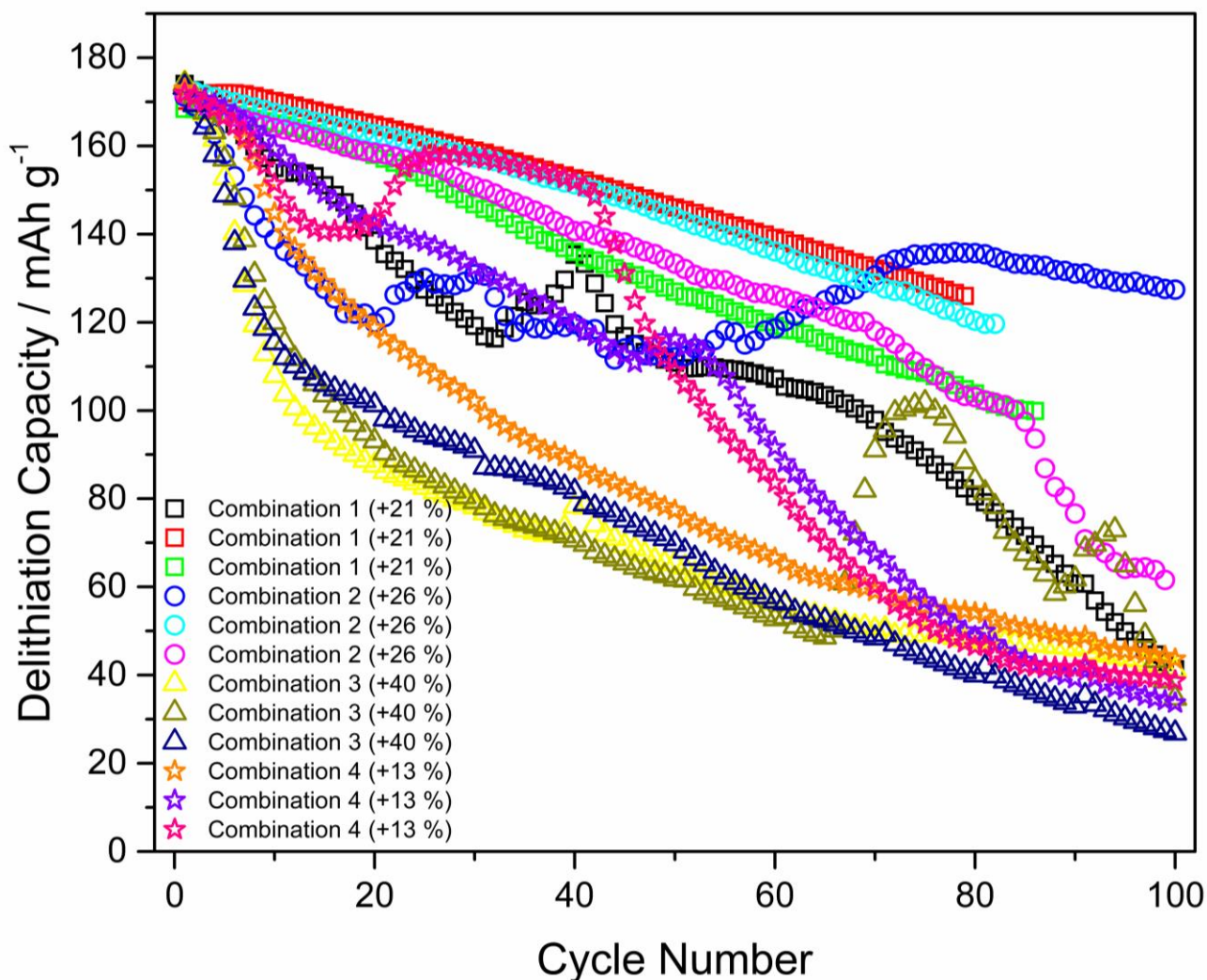


Fig 5.33 – Balancing influence of the single-layer pouch cells on the electrochemical stability.

The cycling of these pouch cells is carried out with the use of a plexiglass-made holder, which should ensure the electrodes stack contact and optimal working condition. Since the screws fixing force is difficult to adjust, often it ends up having different pressures that act on the pouch cells.

For this reasons, the measurements are not very reproducible, especially in the case of single-layer pouch cells where the pressure has a greater impact than regular stacked pouch cells. Too low pressure results in a bad contact, and thus in poor electrochemical performances. On the other hand, too high pressures could initiate plating phenomena. Since this silicon-based composite proved to be very sensitive to pressure compared to traditional graphite, an optimal pressure management is therefore required for a correct and reproducible electrochemical characterization of these cells.

In the attempt to investigate the reasons of such unpredictable performance variability, the electrodes water content has been evaluated by the means of a Karl-Fisher titration. Indeed, a high water amount in the electrodes can negatively affect the pouch cell performances reacting with electrolyte, lithium, and other cell components. Taking into account the combination #1, it is possible to see how the drying of the only anode or the drying of both anode and cathode do not greatly affect the resulting single-layer pouch cell performances (Fig. 5.34). The uncertainty of the results is most likely due to assembly process and to the operator.

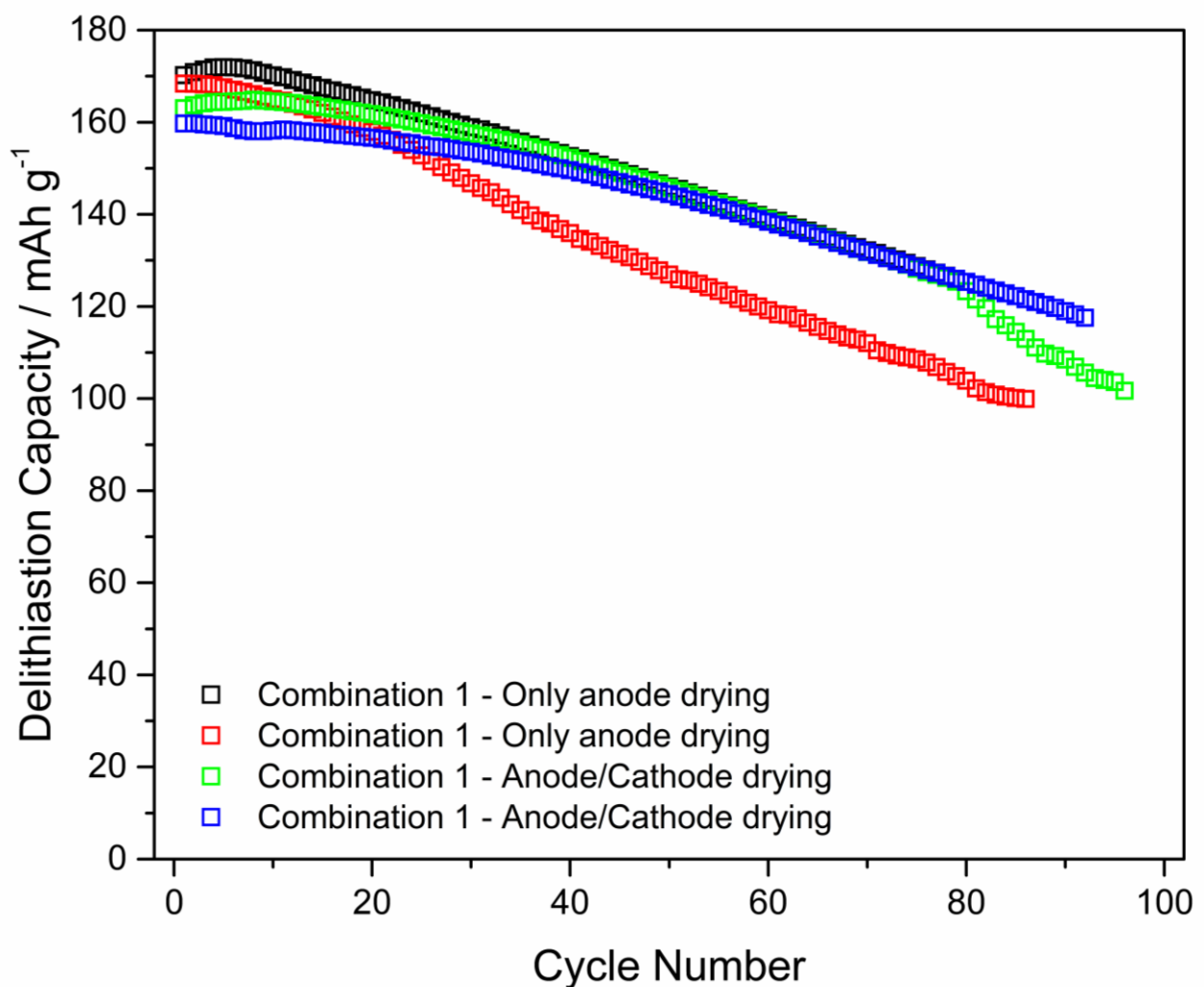


Fig 5.34 – Anode/cathode drying influence of the single-layer pouch cells on the electrochemical stability.

To confirm the obtained results, Karl Fisher titrations have been made on the assembled electrodes. The results are listed in the Table 5w.

	Name	Active Material	H₂O content
ANODE	Formulation G	Si@Gr	47.7 ppm
CATHODE	Formulation H	NCM 811	257.7 ppm

Table 5w – Karl Fisher titration results.

From the commercial point of view, cells should have a water content lower than 500 ppm, thus these moisture levels could be considered average, and should not negatively affect performances.

In order to further investigate this source of instability and poor performances, post-mortem disassembly of fully charged single-layer pouch cells have been carried out. Figure 5.35 revealed how many of them show localized lithium plating on the anode side.



Fig 5.35 – Post-mortem disassembly of a fully charged single layer pouch cell.

Without any kind of pattern, disassembled anodes shows lithium plating in proximity of the current tab, whereas the current density is higher. The assembly of three-electrode pouch cells allowed to check the anode potential during cycling.

Fig. 5.36(A) shows that combination #1 and #2 have a good capacity retention at different C-rate ranging from 0.1 to 1C, but a lower gravimetric capacity (respect the cells shown in Fig. 5.33) probably due to the presence of the reference electrode in the stack. Fig 5.36(B) shows instead the anode potential vs. time plot, where it is shown that anode potentials reach values lower than zero at the end of lithiation. These values are most likely influenced by the pouch cell format.

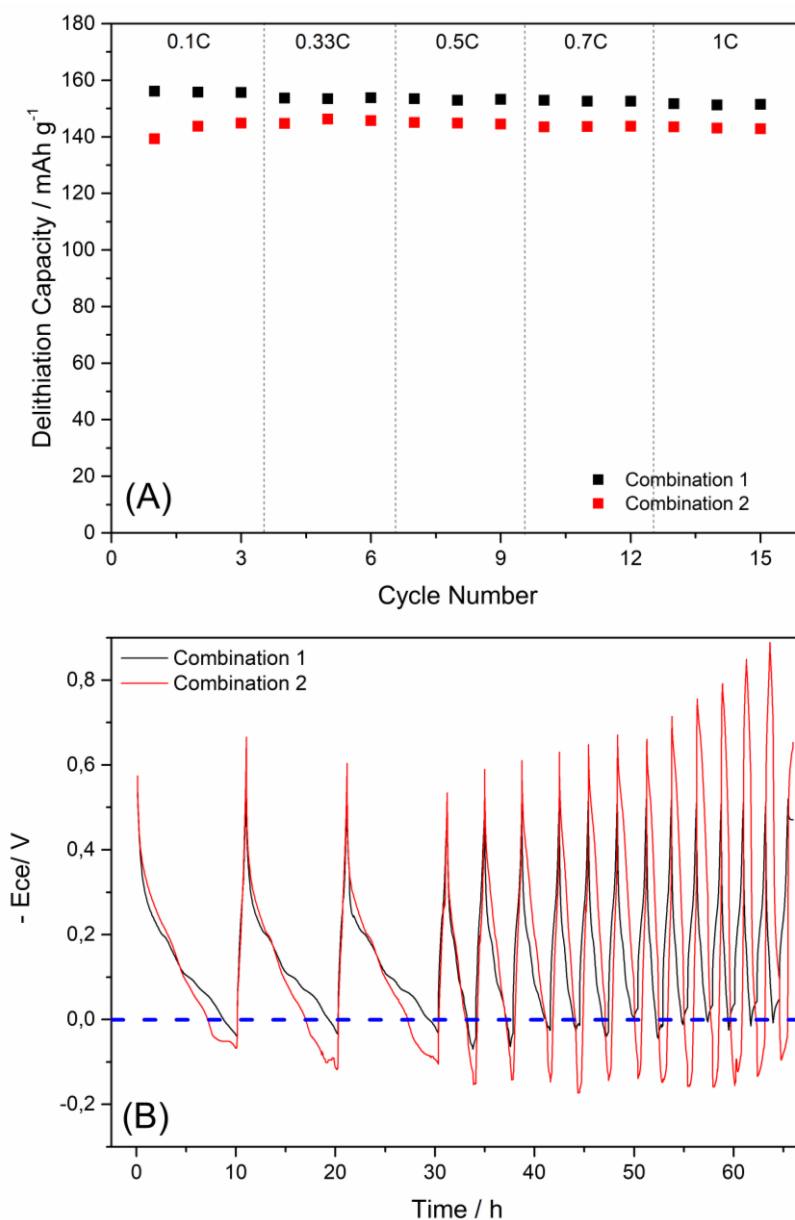


Fig 5.36 – Rate capability behaviour of single-layer pouch cells (combinations #1 and #2): gravimetric capacities (A) and their galvanostatic profiles (B).

The presence of a lithium reference electrode can greatly affect the system under consideration. Since the lithium RE is placed near the anode side, this could result in a higher lithium activity at the anode surface resulting in lithium deposition especially at the critical spots. For the sake of clarity, it is important to say that Li deposition might also be reversible during charge/discharge cycles, and part of lithium can react with the electrolyte too. If the potential goes below 0 Volts, one should notice the presence of a plateau due to the lithium plating. Since we do not detect such plateau, the idea was that the potential curve was just shifted below zero because of the increased lithium activity in proximity of the reference electrode.

In order to find out the cell setup influence, the same combination has been studied in an EL-CELL ECC-Ref cell. It is important to say that the absence of a reference electrode between anode and cathode should exclude the setup influence, giving information about the studied combination. But, because of the local lithium activities, a full cell with a reference electrode placed outside the electrodes stack will experience a different potential.

The use of a thick glass fiber separator allows the use of a lithium-covered metallic pin as reference electrode directly inside the separator (Fig. 5.37). This should not disturb the electrode kinetics between anode and cathode.

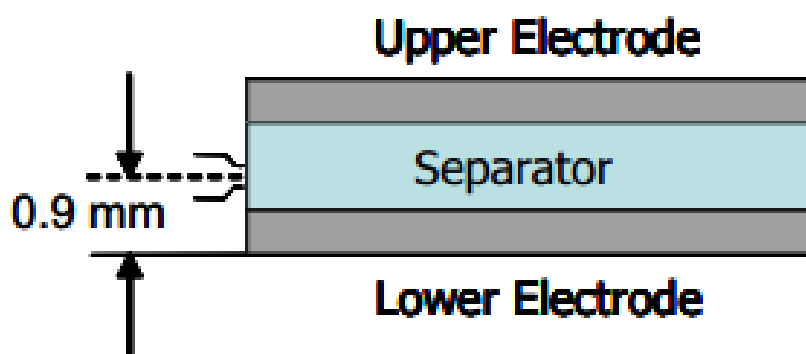


Fig 5.37 – Electrodes stack in the EL-CELL ECC-Ref cell.

From the EL-CELL results (Fig 5.38) it is possible to observe that the anode potential never reaches 0 V. This could confirm that the potential is influenced by the lithium activity of reference electrode.

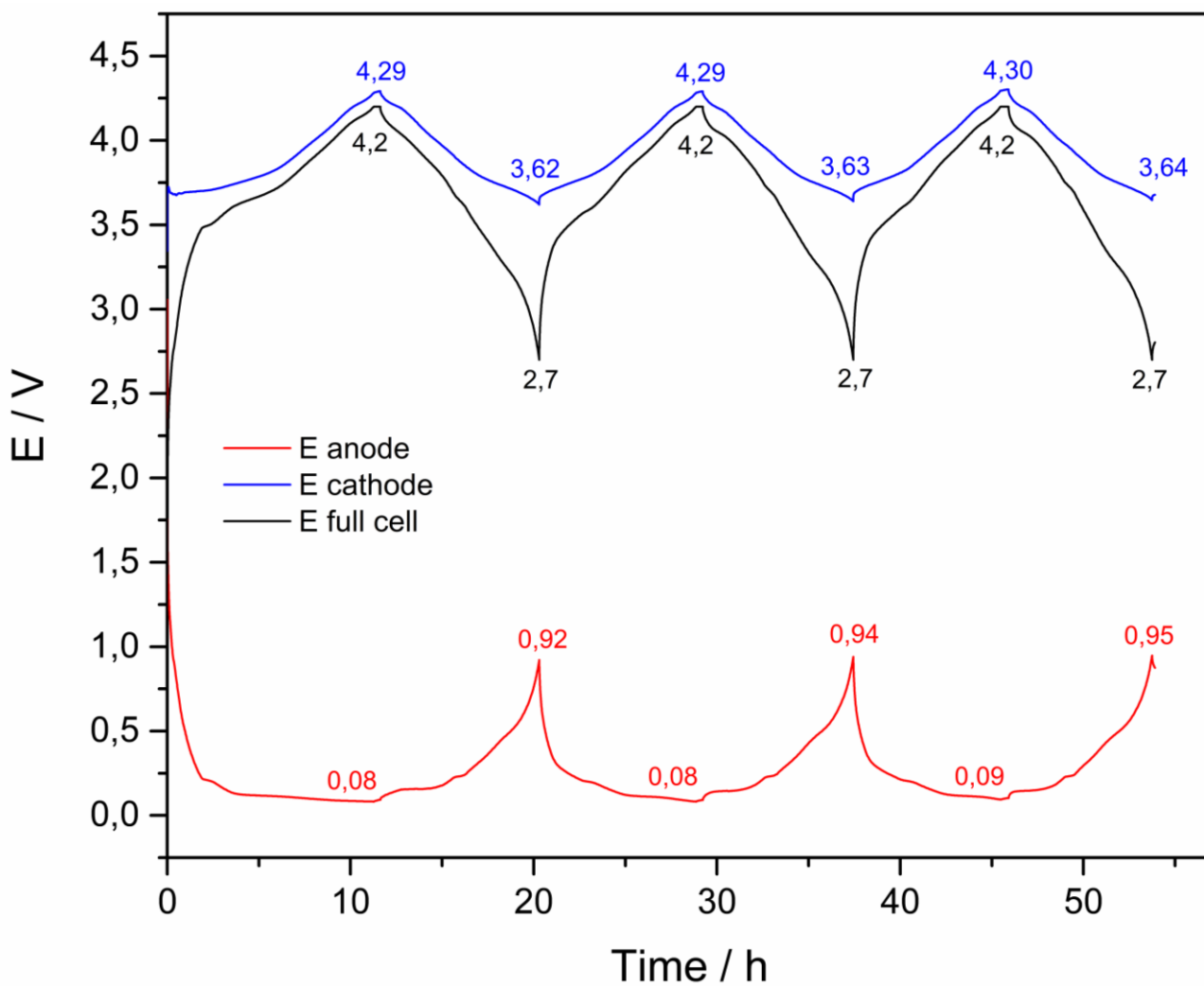


Fig 5.38 – Galvanostatic profiles of the EL-CELL ECC-Ref cell (Combination #1).

In order to compare the obtained results with another cell format, the 4 different combinations assembled in the single-layer pouch cells have been assembled on CR 2032-coin cell too. The assembly specifications are the same described in 5.3.1 chapter, while WE and CE were electrodes from Formulation G and Formulation H respectively. These full coin cells have been tested using the single-layer pouch cell long-term protocol described above.

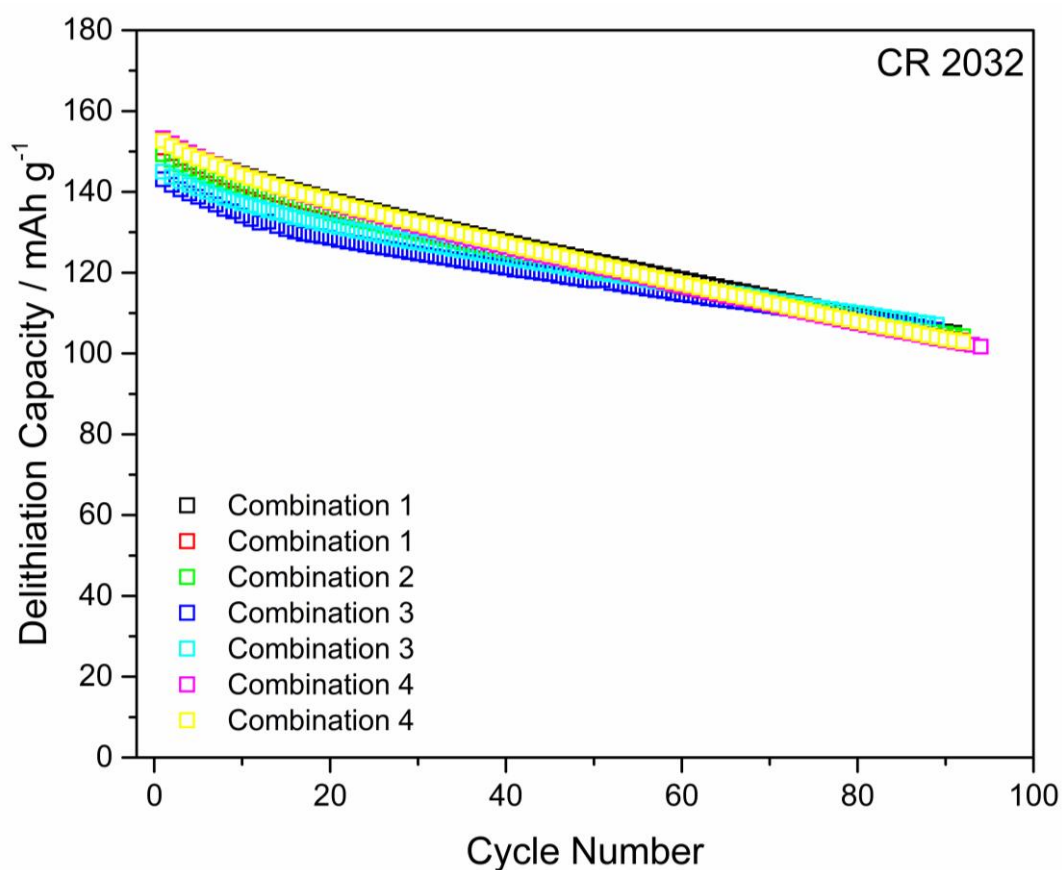


Fig 5.39 – Comparison between gravimetric capacities of the different anode/cathode combinations (CR 2032-coin cell format).

In Figure 5.39 it is possible to notice an interesting detail. Besides the already discussed capacity fading always present in the tested pouch cells, it is possible to observe how the use of coin cells gives a good results reproducibility. Any abnormal behaviour, such as capacity scattering, is not present, most likely due to the more reproducible cell assembly and the more controlled and constant pressure inside the cells. As in the single-layer pouch cells, the initial capacities are much lower than expected while the stability is the same. The conclusion that anode material may be the cause of this behaviour can be proven by evaluating the role of the cathode.

NMC 811 and NMC 622 have been used as cathodes in order to find out the cathode role in the single-layer pouch cells results. Applying the same settings and components, different pouch-cells have been assembled and cycled, using a graphite-based and a Si@Gr-based formulations. The use of NMC 811 as cathode ensure higher capacity than NMC 622 (Fig 5.39A), thus higher energy density can be reached in the full cell. Regardless the used cathode, full cells using a reference graphite-based anode shows remarkable cycling stability and very good capacity retention values.

When instead Si@Gr composite is used as anode, it is possible to notice a fast capacity fade that reaches capacity retention values lower than 80% after about 60 cycles. This could confirm that the problem could reside on the anode side. Si@Gr composite could have compatibility problems with NMC-based cathodes, in additions to the problems discussed above.

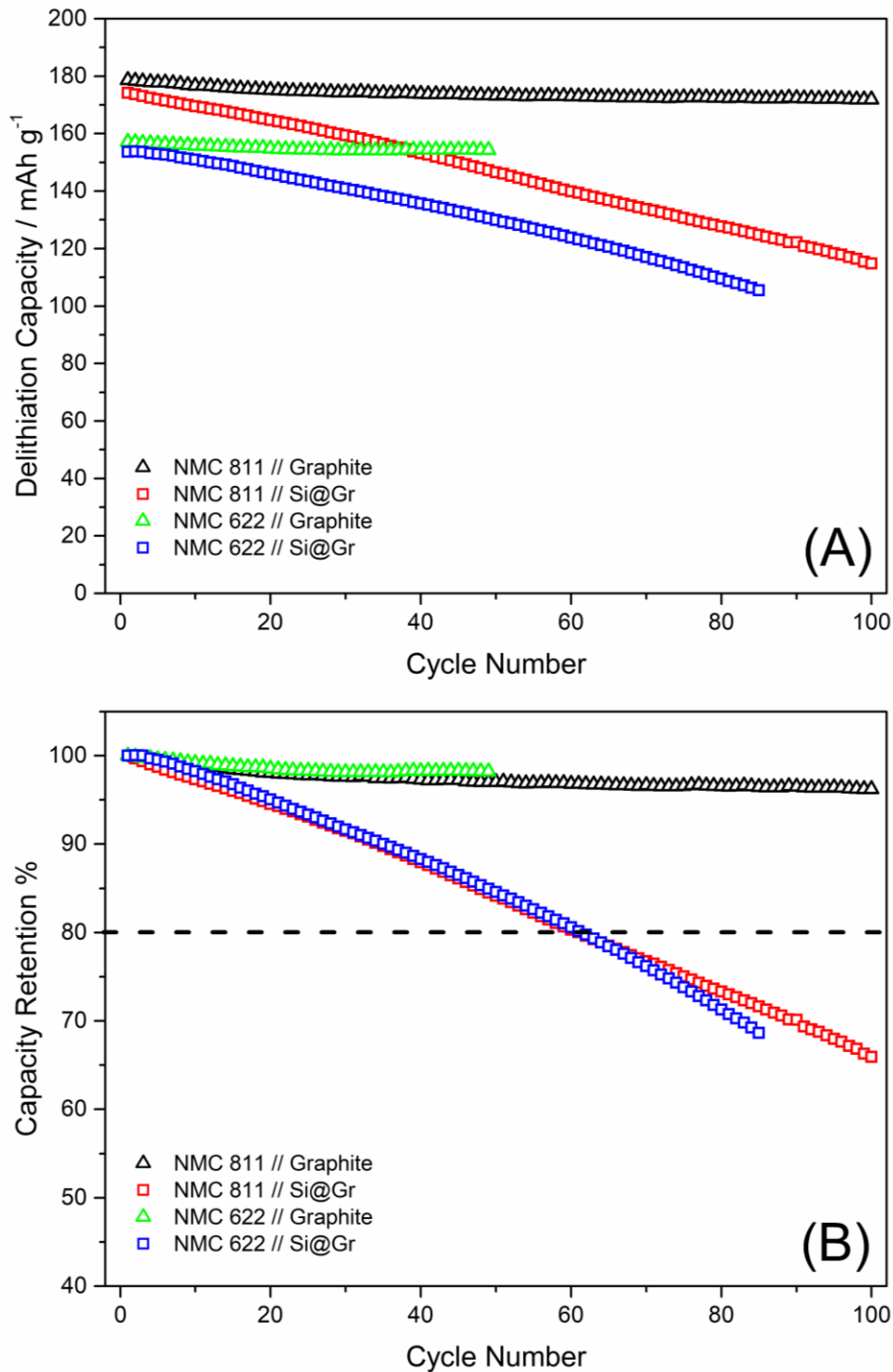


Fig 5.40 – Evaluation of the cathode material role in the single-layer pouch cell format: gravimetric capacities (A), and capacity retention values (B). The dotted line in graph (B) represents the 80% SOH.

5.5 Dilatometric Tests

In-situ electrochemical dilatometry was used to determine the macroscopic expansion of Si@Gr-based anodes (*Formulation G-LI*) during lithiation/delithiation processes. The thickness change can be recorded simultaneously with electrode potential, current, temperature, and time. In the past it was mainly used to determine the thickness change due to Li⁺ insertion process, or assess the thickness change due to the solvated lithium intercalation in graphite-based electrodes [128][129][129]. The silicon has a theoretical volume expansion of 311% during the $4\text{Si} + 15\text{Li}^+ + 15\text{e}^- \rightarrow \text{Li}_{15}\text{Si}_4$ reaction [130]. This volume change, in addition to the previously described problems (electrode pulverization, loss of electrical contact, etc.) can also affect the cell energy density and safety. For this reason, the study of the volume change is of paramount importance, since the quantification of the anode volume change is a starting point to determine the full battery volume change.

5.5.1 Cell Assembly and Cycling

An EL-CELL ECD-3-nano cell (Fig 5.41A-B) was assembled using a Ø 17mm-diameter lithium disk as counter electrode, metallic lithium as reference electrode, and Ø 8mm-diameter Si@Gr-based anodes as working electrode. 2 ml of LiPF₆ 1M solution in EC:DEC (3:7) + 10% FEC (BASF) was used as electrolyte, and 3 layers of Whatman GF/A glass fiber (Ø 20mm) serve as separator/electrolyte reservoir. These cells were cycled using a Verstat 3F/Ametek (Princeton Applied Research) (Fig. 5.41C) in a constant climate chamber in a $0.02 < E \text{ (V)} < 1.5$ potential range. The dilatometric test has been performed by cycling the cells with the following protocol:

- 🔋 12h of open circuit voltage period (OCV);
- 🔋 3 cycles at C/10 rate with a potential step (CC-CV mode) at the end of the anode lithiation until current reach C/20 rate, and C/10 rate delithiation until 1.5 V.

The thickness change % (Δh %) has been calculated by using the following equation:

$$\Delta h \% = \frac{h(t) - h_i}{h_i} \cdot 100 \quad (43)$$

where $h(t)$ is the electrode thickness at the time t , and h_i is the initial electrode thickness. The thickness values taken into account here correspond to the coating height, whereas the collector foil is not included.

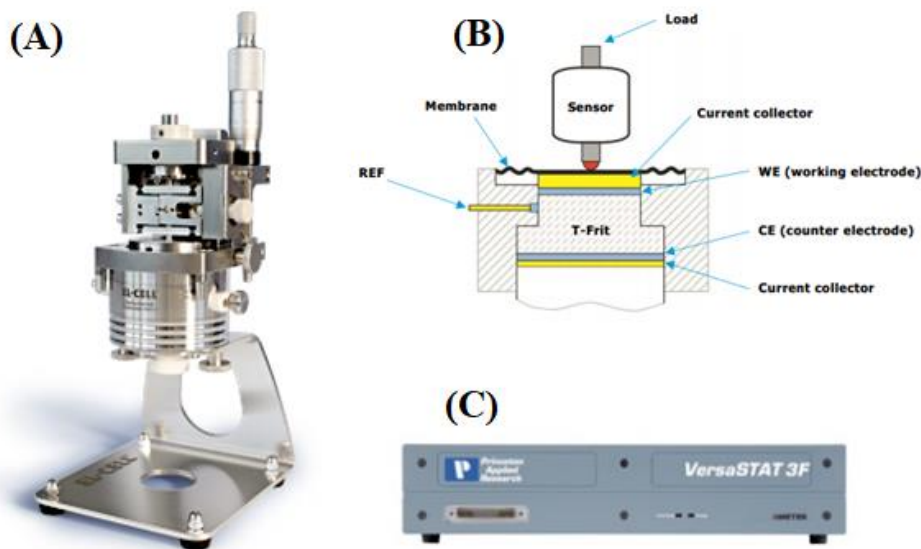


Fig 5.41 – (A) EL-CELL ECD-3-nano cell; (B) Cell setup; (C) Verstat 3F/Ametek (Princeton Applied Research).

The characteristics of the two tested electrodes are listed in the Table 5y. Electrodes coming from the same coating and with similar densities have been chosen to have comparable results.

#	Formulation	Coating	Thickness [μm]	Density [g cm^{-3}]	Capacity [mAh cm^{-2}]
1	G	L1	60	1.23	3.29
2	G	L1	60	1.26	3.37

Table 5y – Characteristics of the tested electrodes.

Figure 5.42 shows the results of the electrode #1, where the maximum thickness is reached during the silicon alloying reaction with lithium as confirmed by previous studies [131].

The anode potential may vary slightly from literature values, since the three separators and the glass frit can increase the ohmic resistance. The greater thickness change occurs during the first cycle, and then decreases through cycling. This behaviour has been evidenced by other studies regarding silicon and graphite-silicon composites [130]. The large swelling during the initial OCV phase is, however, an unexpected observation.

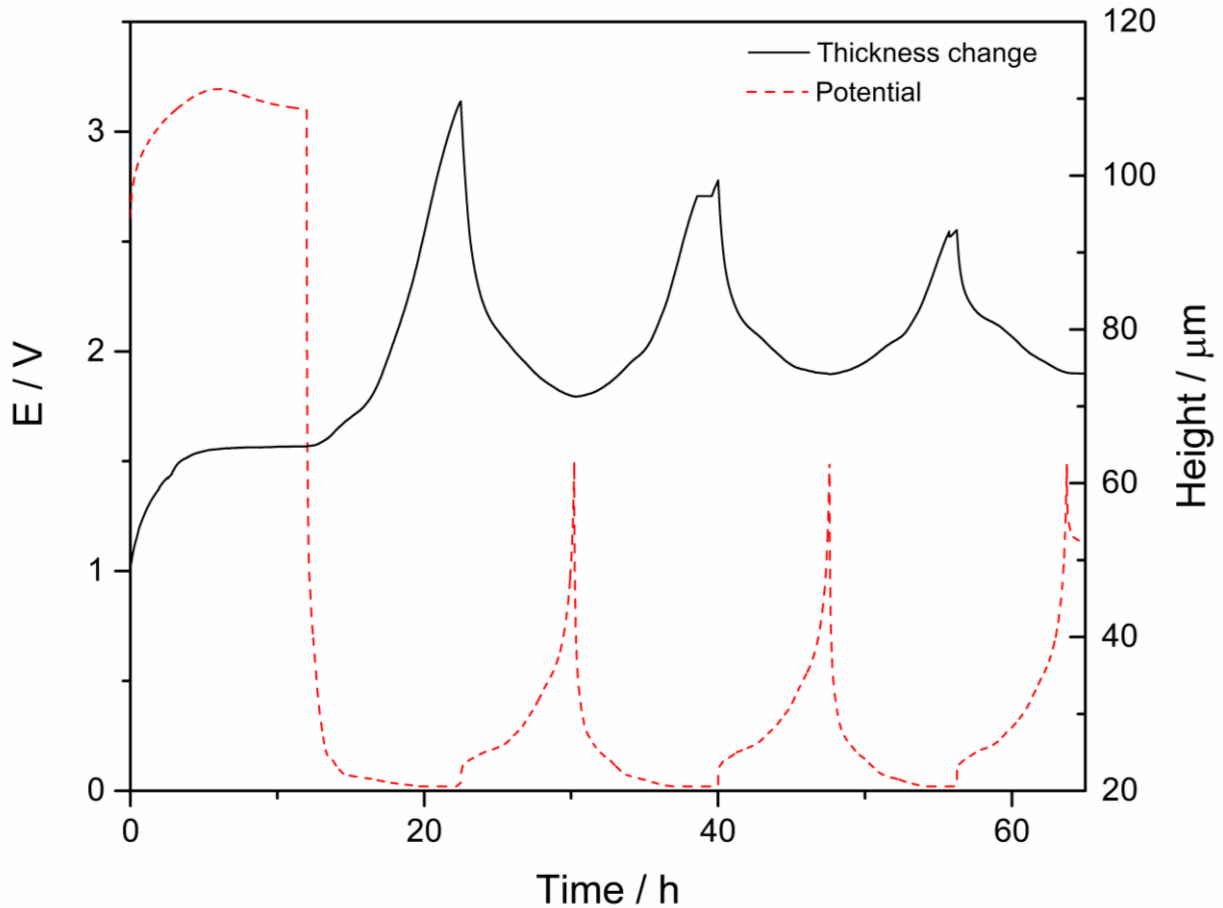


Fig 5.42 – Height change of electrode #1 according to potential.

This 30% thickness increase cannot be ascribed to the alloying/dealloying reactions, because no current is applied to the cell. Such an increase cannot be due solely to the electrode swelling by the electrolyte. Several researchers attributed this feature to problems concerning the dilatometry cell such as:

- 🔋 Electrode swelling;
- 🔋 Electrolyte creeping between the tested electrode and the current collector (piston);

- 🔦 Electrolyte degradation and subsequent gassing;
- 🔦 Electrode bending due to a high coating tension.

All these factors can randomly contribute to the final results, making a good and consistent assembly necessary. The test repetition with electrode #2 shown similar features, showing the difficulty to obtain reproducible results, but at the same time giving an idea of the order of magnitude of the thickness change. Figure 5.43 shows the comparison between the two tested electrodes in terms of height increase (A) and height increase percentage (B). During the first lithiation a thickness increase of 123% and 86% are present, respectively for electrodes #1 and #2. For the subsequent cycles these values decrease for both electrodes and their values are listed in the table 5x.

	Electrode #1		Electrode #2	
	Thickness / μm	Δh %	Thickness / μm	Δh %
<i>Start</i>	49	0%	49	0%
<i>After OCV step</i>	64.9	32.4 %	56.4	15.1 %
<i>1st lithiation</i>	109.6	123.7 %	91.9	87.6 %
<i>1st delithiation</i>	71.3	45.5 %	66.2	35.1 %
<i>2nd lithiation</i>	99.2	102.4 %	88.7	81.0 %
<i>2nd delithiation</i>	74.1	51.2 %	69.1	41.0 %
<i>3rd lithiation</i>	92.8	89.4 %	84.9	73.3 %
<i>3rd delithiation</i>	74.1	51.2 %	70.2	43.3 %

Table 5x – Summary of the results obtained from electrodes #1 and #2. The thickness values are referred only to the coating thickness (copper foil excluded).

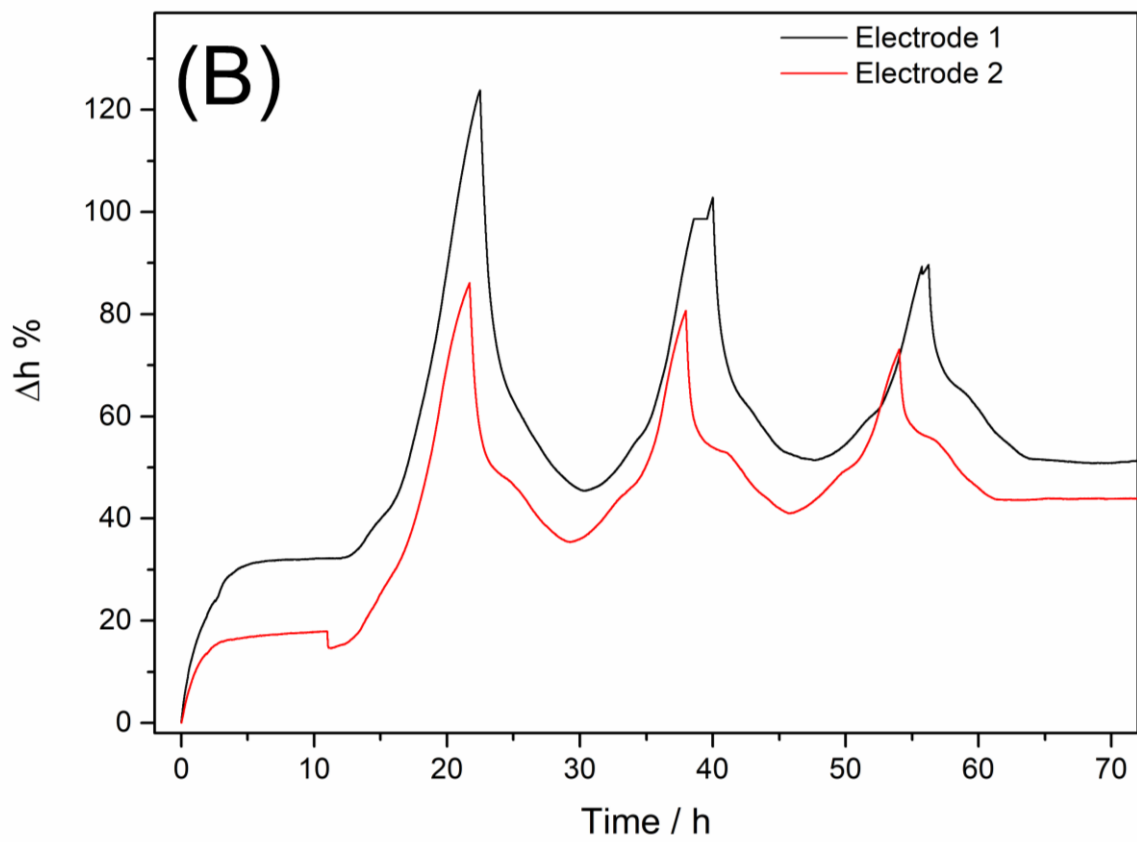
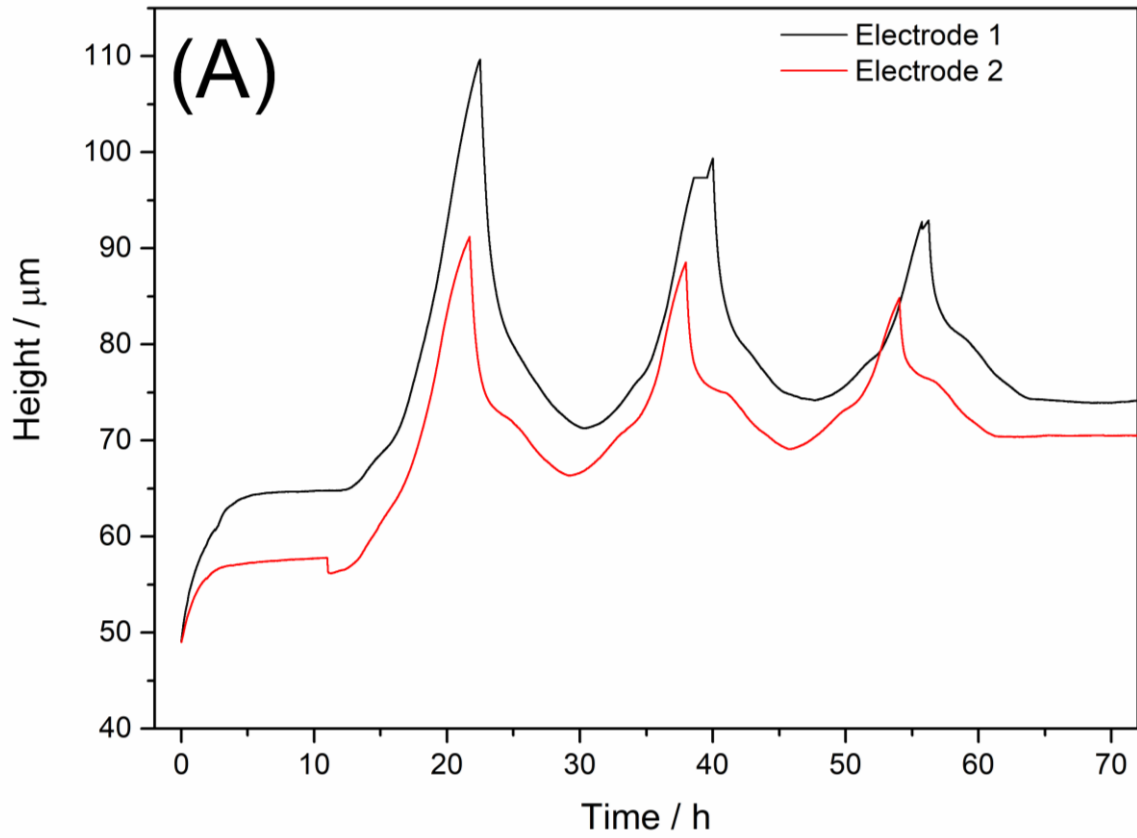


Fig 5.43 – Comparison between electrode #1 and electrode #2: (A) Height vs. Time; (B) $\Delta h \%$ vs. Time.

In both cases, at the end of the delithiation, the initial electrode thickness is never restored, reaching thickness values around the 43% of the pristine electrode thickness after 3 cycles. This is a very useful data, because it is possible to have an idea of the thickness variations of this Si@Gr composite. Post-mortem cross section SEM of Si@Gr-based electrode (Formulation G) have been carried out to evaluate the volume expansion after a long-term cycling protocol.

Fig. 5.44 shows the thickness change comparison between a pristine Si@Gr electrode (A) and a fully discharged Si@Gr-based electrode after 100 cycles (B). The pristine electrode shows an average coating thickness of 46.3 μm , while the fully discharged electrode shows an average coating thickness of 77.53 μm . The resulting 67.4% thickness change respect to the pristine electrode is a value even greater than that observed at the end of the third cycle using the ELL-CELL setup.

This further confirms that the electrode no longer recovers the initial thickness, but also that the thickness of the electrode in the delithiated state increases with the number of cycles. This could be due to a failure of the Si@Gr structure, together with a binder deterioration, which cannot longer support the silicon volume variation.

The situation that would be created in a real system is obviously different and more articulated than these created in those experiments. The presence of multiple double-coated electrodes in a closed environment such as a metallic can (e.g. 18650 format) or a coffee bag (e.g. pouch-cell format) can really give a completely different response since the expansion could be directly linked to the cell volume and the relative pressure experienced by those electrodes. Moreover, the still incomplete characterization of structural and morphological evolution of silicon-based electrodes upon cycling sets limits for the complete understanding of the obtained dilatometry results.

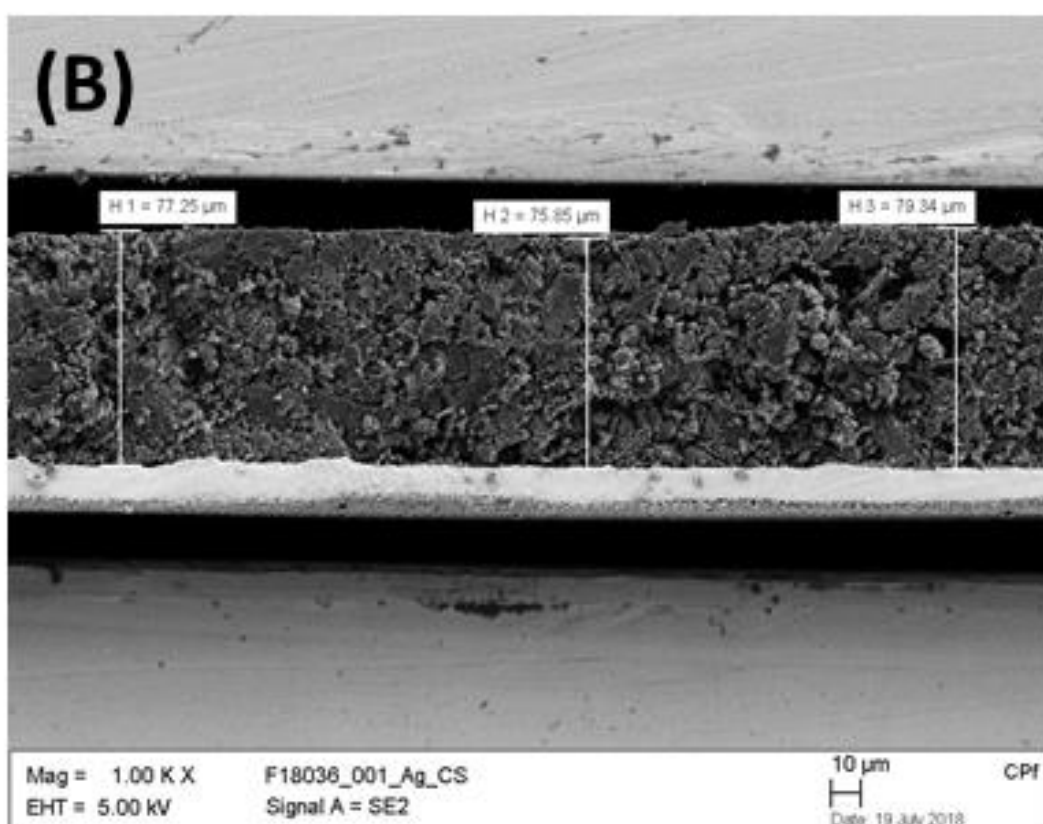
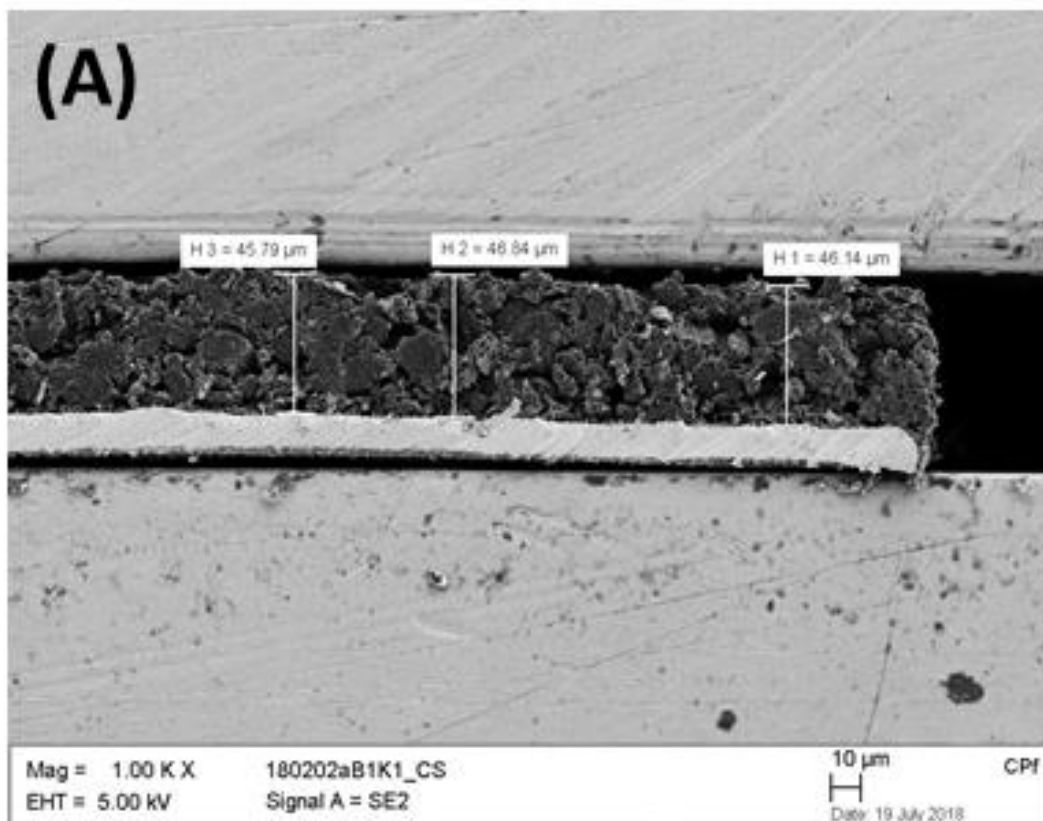


Fig 5.44 – Post-mortem cross section SEM micrographs: (A) Pristine Si@Gr-based electrode; (B) Fully discharged Si@Gr-based electrode after 100 cycles.

5.6 Conclusion

This study tried to show and get more information about the implementation of a silicon based composite in a pre-industrial lithium-ions battery manufacturing process. The process steps from slurry preparation to single-layer pouch cell assembly have been explored. The obtained results and finding are listed below.

- **SLURRY PREPARATION:** The application of dispersant such as PVP and PVA has been evaluated, but further studies on its concentration and implementation are required to make them a feasible option to obtain a good slurry homogeneity. Moreover, the use of a buffer solution to change the binder/active material interaction has not proven to be an achievable approach. The final presence of roughly 4% buffer-derived salts, in addition to the use of a relative low specific capacity material, leads to an active material content below 94%. Formulation A has shown the easiest preparation and the best results. It has shown good reproducibility in terms of rheological and mechanical properties, and the possibility of scaling up using a pilot line coater.
- **HALF-CELL FORMAT:** Due to a more uniform pressure distribution, the CR 2032-coin cell format has proven to be the most performant and reproducible cell format for the tested lithium half-cells. The capacity scattering observed with the CR 2016-coin cell format has shown to be a consequence of the lithium dendrites formation.
- **SINGLE-LAYER POUCH CELLS:** The single-layer pouch cells assembly has demonstrated the problems connected to this cell format. The needs to have a good contact between anode and cathode requires the use of a cell holder during the electrochemical tests. The difficulty in applying the same pressure to all cells seems to be a fundamental parameter when pursuing optimal performance. Different combinations and different drying methods have been evaluated, but due to an inhomogeneous pressure distribution, it is impossible to assess a meaningful correlation between these variables. Testing the same anode/cathode combinations on a different cell format (CR 2032) has shown better and more reproducible results, confirming the necessity for a different cell format or the development of a new pouch cell holder.

- **DILATOMETRY TESTS:** Because of the silicon volume change upon cycling, dilatometry measurements were performed on the Si@Gr composite. During the first charge, we reached a maximum thickness increase of 123.7% respect to the initial thickness, a lower expansion values than pure silicon ($\approx 311\%$). After the first charge, the initial thickness has never been recovered as already shown by others studies.

Chapter 6 – Vanillin-templated Fe₂O₃ nanoparticles as conversion anode material for LIBs

6.1 Introduction

The fast development of electric vehicles and portable devices requires Li-Ion batteries with higher energy densities, lower weight and better electrochemical performances [132]. Alongside the traditional carbon-based anode materials such as graphite (mass and volume capacities of 372 mAh g⁻¹ and 975 mAh cm⁻³), the research of new lithium-storage chemistries has been taken into consideration in the last decades. As already said, alloying [133] and conversion materials [44] have been deeply studied in order to make their marketing possible within few years. Conversion materials have emerged as feasible LIBs active materials because of their high capacities, low cost and relatively low environmental impact, and among them, transition metal oxides (TMOs) could be used as anode materials. Particularly, iron oxides such as Fe₂O₃ have been taken into consideration owing to its high capacity (1007 mAh g⁻¹), low toxicity, and high abundance. The use of conversion material is plagued by structural problems due to the volume change upon cycling, and low electronic conductivity. A common approach used to overcome this issue is the use of nanoparticles in order to buffer volume variations, reduce Li⁺ diffusion path length, and improve reaction kinetics [134,135]. The use of vanillin as renewable and sustainable templating agent is evaluated here. Vanillin is a cheap and water-soluble aromatic aldehyde where the presence of oxygen and functional groups make it suitable as possible capping agent for nanoparticles synthesis. Electrode processing has been optimized as well. The use of Poly(acrylic acid) (PAA)/Ethanol system has been preferred instead of the PVdF/NMP system. PAA has already shown outstanding mechanical features in mechanically-stressed anodes (e.g. Si NPs), and its solubility in water and ethanol allows to avoid the use of the toxic and expensive NMP solvent. This chapter reports the synthesis and the structural, morphological, and electrochemical characterization of vanillin-templated Fe₂O₃ nanoparticles (FeVan) as candidate material for lithium-ion battery anodes.

6.2 Experimental

6.2.1 Synthesis

A cheap and simple co-precipitation method was used. $\text{FeCl}_2 \cdot 4\text{H}_2\text{O}$ and $\text{FeCl}_3 \cdot 6\text{H}_2\text{O}$ were added to 40 mL of ultrapure H_2O in a 1:2.7 mass ratio. After the addition of 1 g of vanillin dissolved in 20 ml of H_2O , the solution pH was brought approximately to 11 by adding about 30 ml of ammonia solution (30%). The reaction was kept under stirring overnight at 70 °C. The resulting powder was collected and washed with water, ethanol and acetone at different steps. Eventually, after the complete solvent removal at 80 °C under vacuum, the resulting powder annealed at 800 °C for 8 h in Ar atmosphere (2 °C min^{-1} heating ramp) in a tubular furnace.

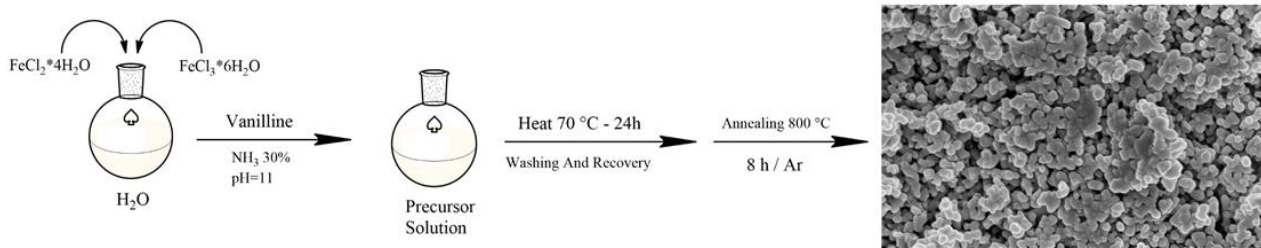


Figure 6.1 – Synthetic scheme of the FeVan nanoparticles.

6.2.2 Electrodes preparation

Electrodes slurry has been prepared by finely grounding the active material and the conductive additive (Super C65) in an agate mortar. The resulting mixture was added to a Poly(acrylic acid) (PAA) solution in ethanol and left to stir overnight.

The slurry has been spread onto a 10 μm -thick copper foil using the “Doctor Blade” technique and a wet thickness of 100 μm . The electrode foil has been dried 2h at 70 °C on a heating plate and calendared with a roll press. 9 mm-diameter circular electrodes have been cut and furtherly dried at 120 °C for 12h under vacuum before being transferred in the glovebox. The average active material mass loading was around 1.4 mg cm^{-2} .

	FeVan-PAA	
Active Material:	FeVan	70 %
Binder:	PAA ($M_w \approx 450000$)	10 %
Conductive Agent:	Super C65	20%
Solvent:	Ethanol	---

Table 6a – Electrode formulation of FeVan-PAA coating.

6.2.3 Cell Assembly and Cycling

Three-electrodes “T-shaped” cells have been assembled in an Ar-filled glovebox using metallic lithium (Sigma-Aldrich) as counter and reference electrode and Whatman GF/A glass-fiber disks as separators. A solution of LiPF₆ 1M in EC:DMC 1:1 v/v (Solvionic, France) was used as electrolyte. All the cells have been cycled with a VMP-2Z multi-channel galvanostat-potentiostat (Bio-Logic, France) in a $0.005 < E \text{ (V)} < 3$ potential window at specific currents ranging from 0.2 A g^{-1} to 10 A g^{-1} . An OCV period (12h) has been used to enable a full wetting of electrodes and separator before cycling. Electrochemical Impedance Spectroscopy (EIS) has been performed in the 200 KHz – 9 mHz frequency range with a sinusoidal amplitude of $\pm 5 \text{ mV}$ and applying a bias potential of $E = 0.8 \text{ V}$ for the first cycle and $E = 1.0 \text{ V}$ for the subsequent cycles. All the measurements have been recorded at room temperature. All potential values are given vs. Li⁺/Li redox couple.

6.3 Discussion

The synthesis of Fe₂O₃ nanoparticles has been carried out on the assumption that vanillin could act as a soft templating agent during synthesis [136], since its hydroxyl and methoxy moieties have metal-coordinating ability.

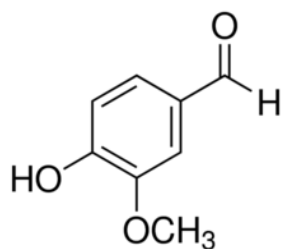


Fig 6.2 – Vanillin structure.

Beyond that, it has been reported that high pH values could favor the formation of small and spherical particles [137]. The products formed during the synthetics involving vanillin have been examined by FTIR spectroscopy.

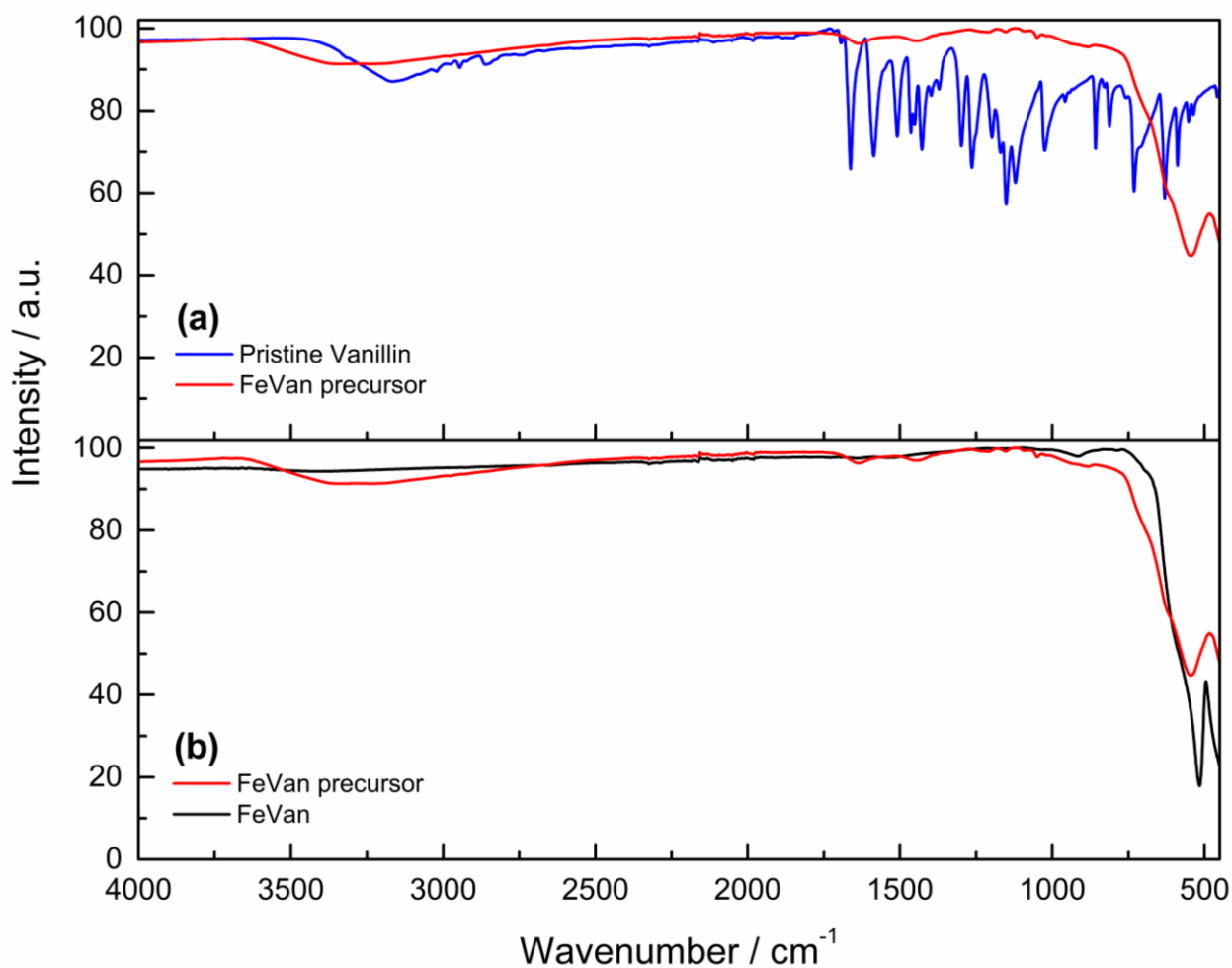


Figure 6.3 – FTIR spectroscopy analysis: (a) Pristine vanillin vs. FeVan precursor; (b) FeVan precursor vs. FeVan.

Panel (a) in Fig. 6.3 shows the normalized FTIR spectra of pristine vanillin and FeVan precursor. Pristine vanillin shows a large band centered at 3164 cm^{-1} assigned to O-H stretching vibration, while the weak bands at 2948 cm^{-1} and 2858 cm^{-1} have been assigned to the C-H stretching of the aldehyde group and the C-H bond stretching of $-\text{CH}_3$ group. The sharp peak at 1662 cm^{-1} has been assigned to the stretching of the carbonyl C=O moiety and the peaks at 1585 cm^{-1} and 1508 cm^{-1} have been assigned to the C=C aromatic bond stretching. FeVan precursor exhibits similar bands but with a much lower intensity and two features that hint an iron-vanillin interaction: a broadening of O-H band due to a possible hydrogen bonding, and a band centered at 550 cm^{-1} due to the iron oxide particles. Moving to panel (B), it is possible to observe how the final product shows no sign of functional bands due to vanillin, but instead there is an increasing and a sharpening of the band (550 cm^{-1}) due to the formation of iron oxide particles.

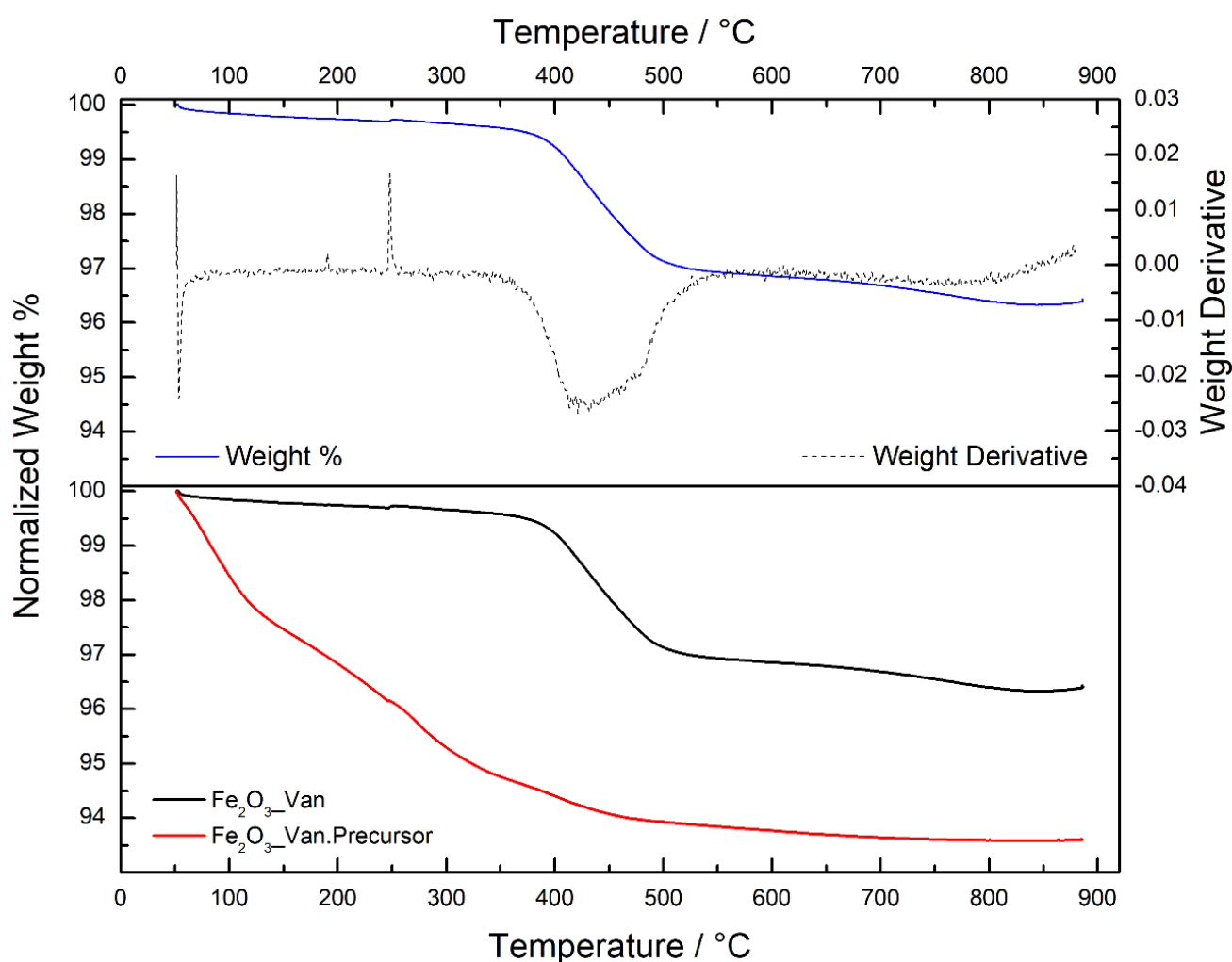


Fig 6.4 – Thermogravimetric analysis (TGA) of FeVan (upper panel), and TGA comparison with FeVan precursor (lower panel).

From the thermogravimetric analysis (TGA) in Fig. 6.4, it is possible to notice a 3.4% weight loss. Since the analysis has been carried out in oxygen atmosphere, we can assume that this loss is due to the pyrolysis of the vanillin-derived carbon obtained during the thermal annealing at 800 °C in Ar atmosphere.

X-ray diffraction pattern of the synthesized FeVan is shown in Figure 6.5. All the peaks are in good accordance with the JCPDS card no. 33-064 corresponding to the α -Fe₂O₃ phase. This Fe₂O₃ polymorph has the rhombohedral structure where the central iron atom is bound to six oxygen ligands. The absence of additional peaks suggests the presence of an α -Fe₂O₃ pure phase, whereas the peak sharpness is the signature of a good crystallinity degree. The low amount of carbon detected during TGA analysis is not visible using X-Ray diffraction.

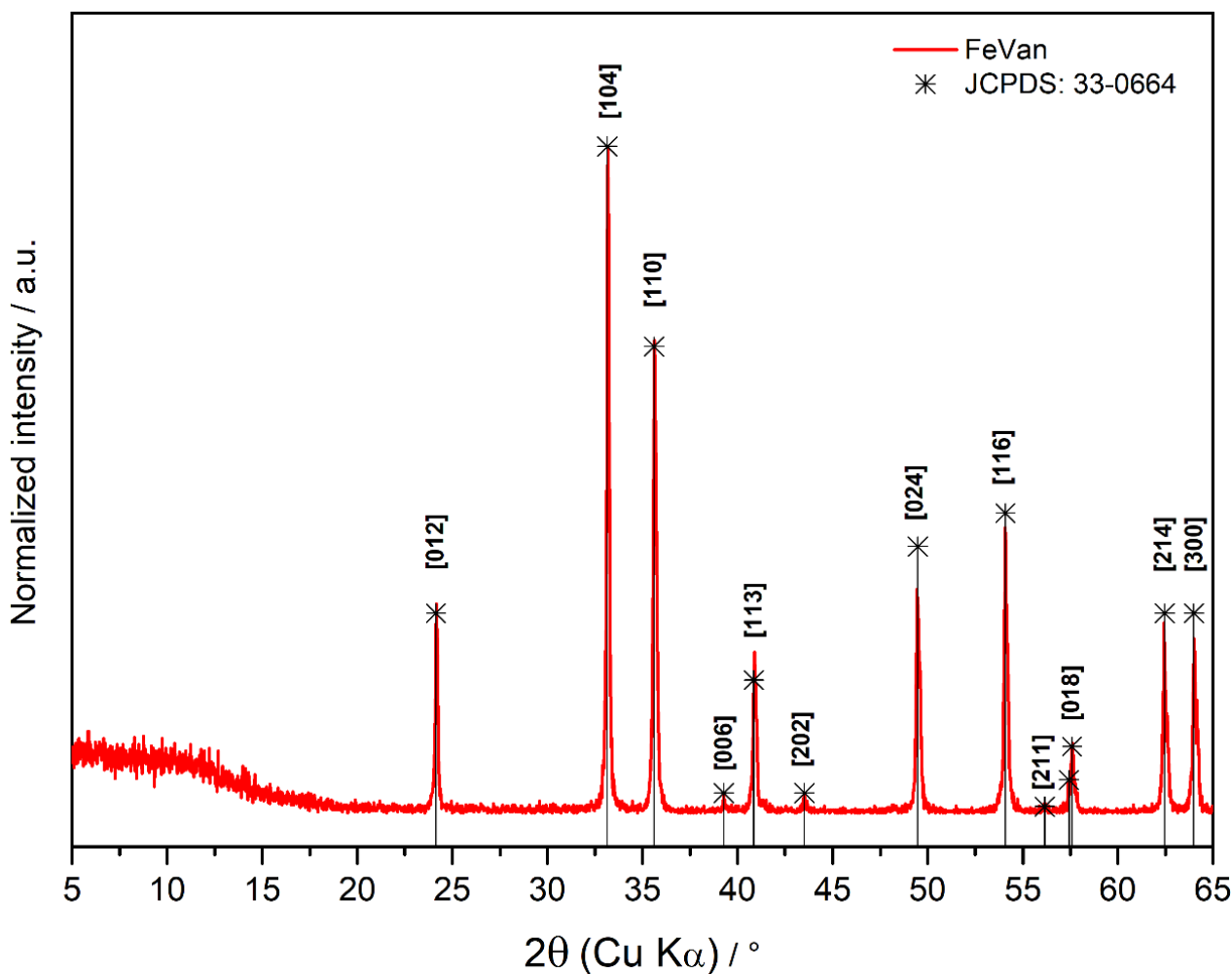


Fig 6.5 – X-Ray diffraction pattern of the FeVan powder.

In order to further confirm FeVan structure, Raman spectroscopy has been carried out. Using a 532 nm green laser as excitation source, a Raman spectrum was recorded. Comparing the obtained results with an Fe₂O₃ reference spectrum [138], it is possible to notice a good overlap of the bands. For the sake of clarity, it must be said that the shift of the bands with respect to the reference bands may be due to the instrument setup, to the synthesis, and to the annealing conditions.

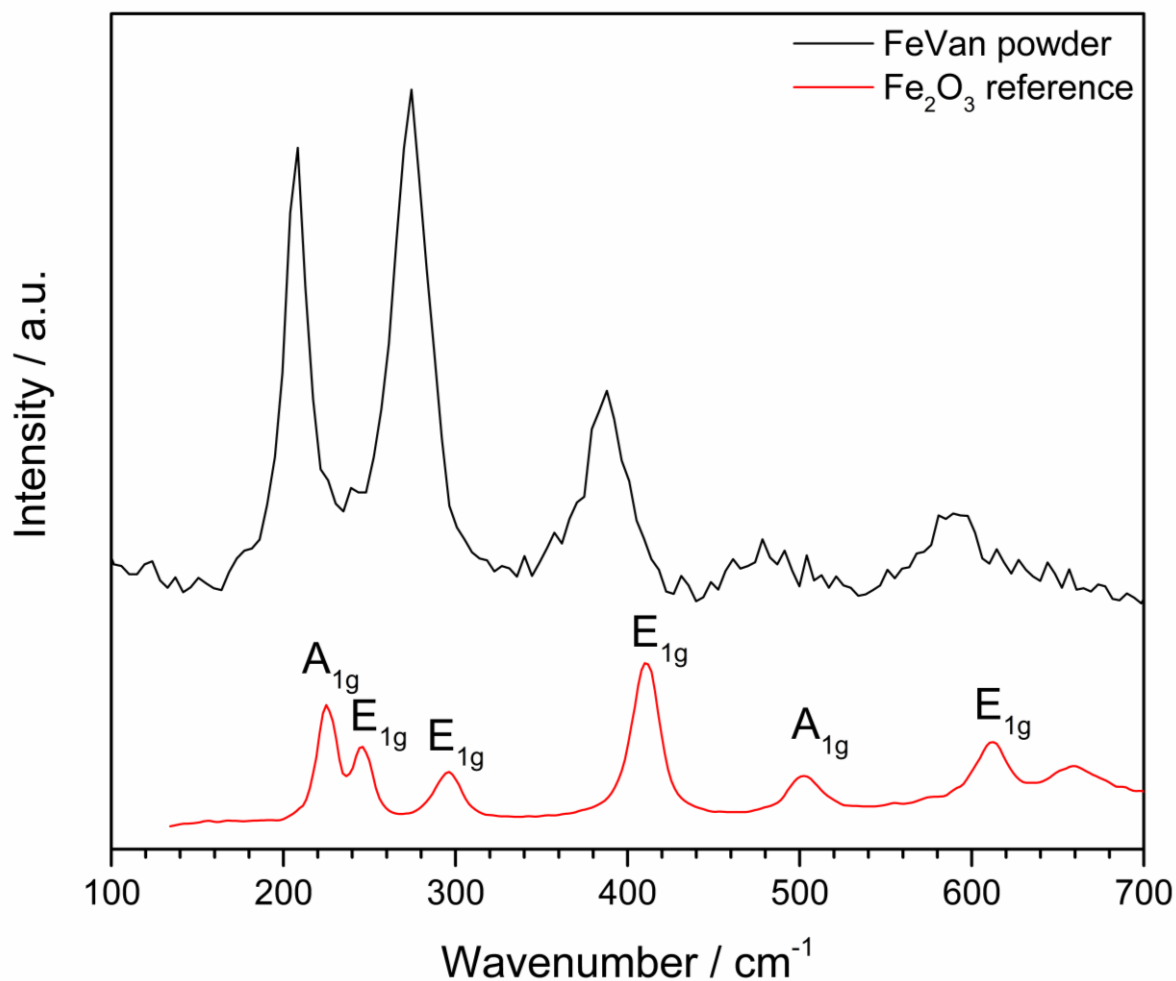


Fig. 6.6 – Raman spectra of the FeVan powder.

From the morphological point of view, it is possible to observe how the annealing process influences the FeVan particles shape. Figure 6.7 (a-b) shows the SEM micrographs of the FeVan before the thermal treatment. This precursor is made up of irregularly aggregated particles, but immediately after the annealing it is possible to notice that the final product (FeVan) is composed by regular spherical nanoparticles around 100 nm (Fig 6.7 (c-d)).

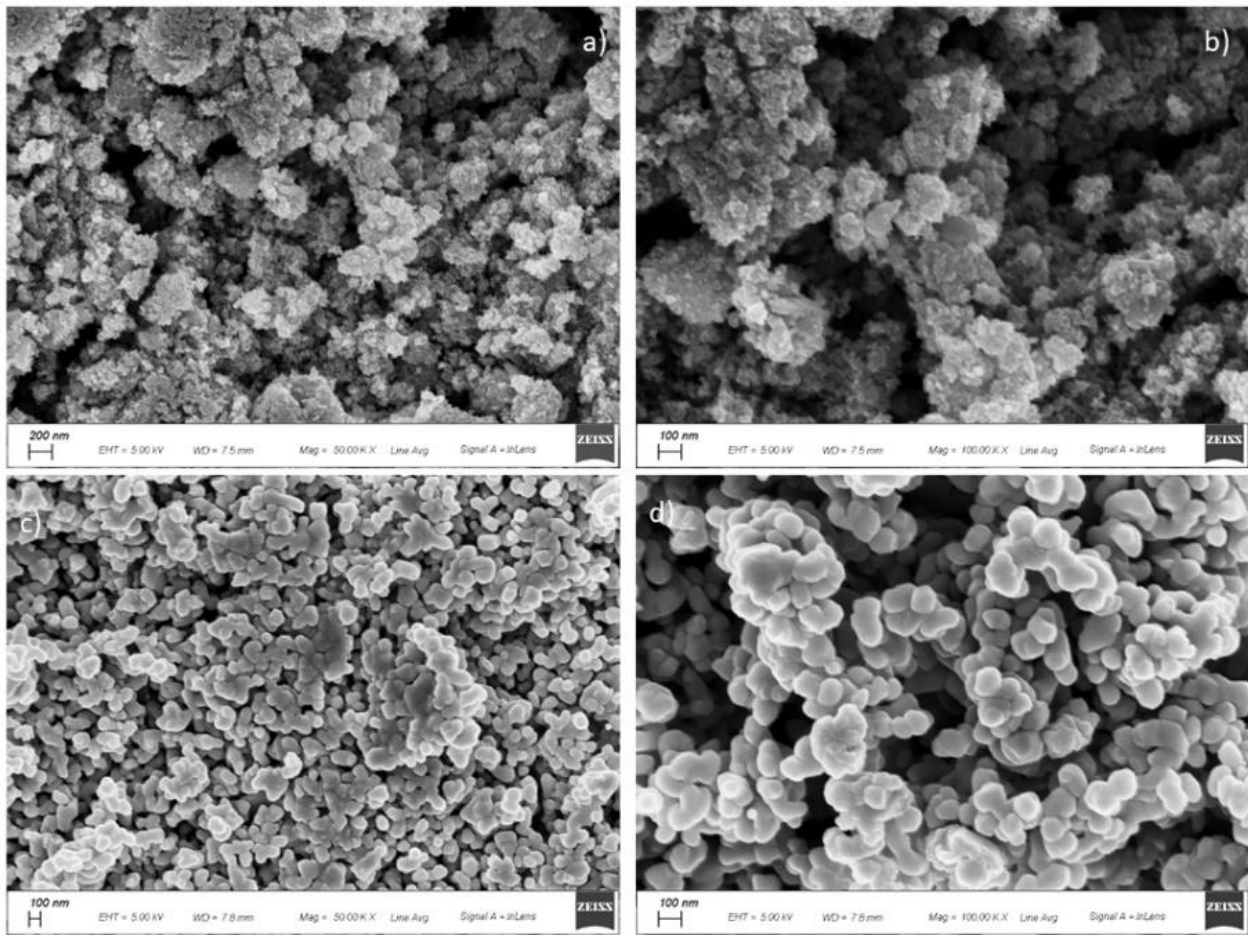
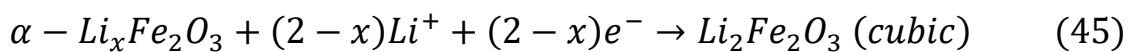
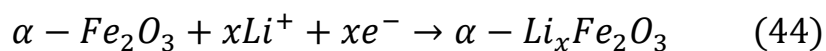
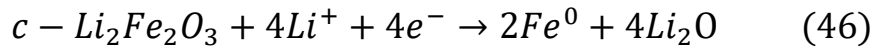


Fig. 6.7 – SEM micrographs of (a)-(b) FeVan precursor, and (c)-(d) FeVan annealed nanoparticles.

Cyclic voltammetry (CV) experiments have been performed to provide a characterization of the redox processes. Fig. 6.8 shows the results obtained of the first two cycles in a $0.005 < E \text{ (V)} < 3$ potential range at a scan rate of 0.05 mV s^{-1} . During the cathodic scan, the first cycle shows the presence of three different peaks labelled respectively as A ($E = 1.63 \text{ V}$), B ($E = 0.96 \text{ V}$) and C ($E = 0.85 \text{ V}$). Peaks A and B are assigned respectively to a preliminary $\alpha\text{-Fe}_2\text{O}_3$ lithiation (Eq. 44) and to an irreversible phase transition to a cubic $\text{Li}_2\text{Fe}_2\text{O}_3$ (Eq. 45) [139,140].



Peak C is assigned to the reduction of Fe^{+++} to Fe^0 nanoparticles with the contemporary formation of the Li_2O inorganic matrix (Eq. 46).



During the anodic step, the presence of the large peak D ($1.5 < E \text{ (V)} < 2.1$) is attributed to a two-step oxidation of Fe^0 to Fe^{++} and to Fe^{++} to Fe^{+++} [141]. From the second cycle on, the cathodic region shows only the peak E ($E = 1.0 \text{ V}$), confirming the irreversibility of the first cycle discussed in the literature [142,143]

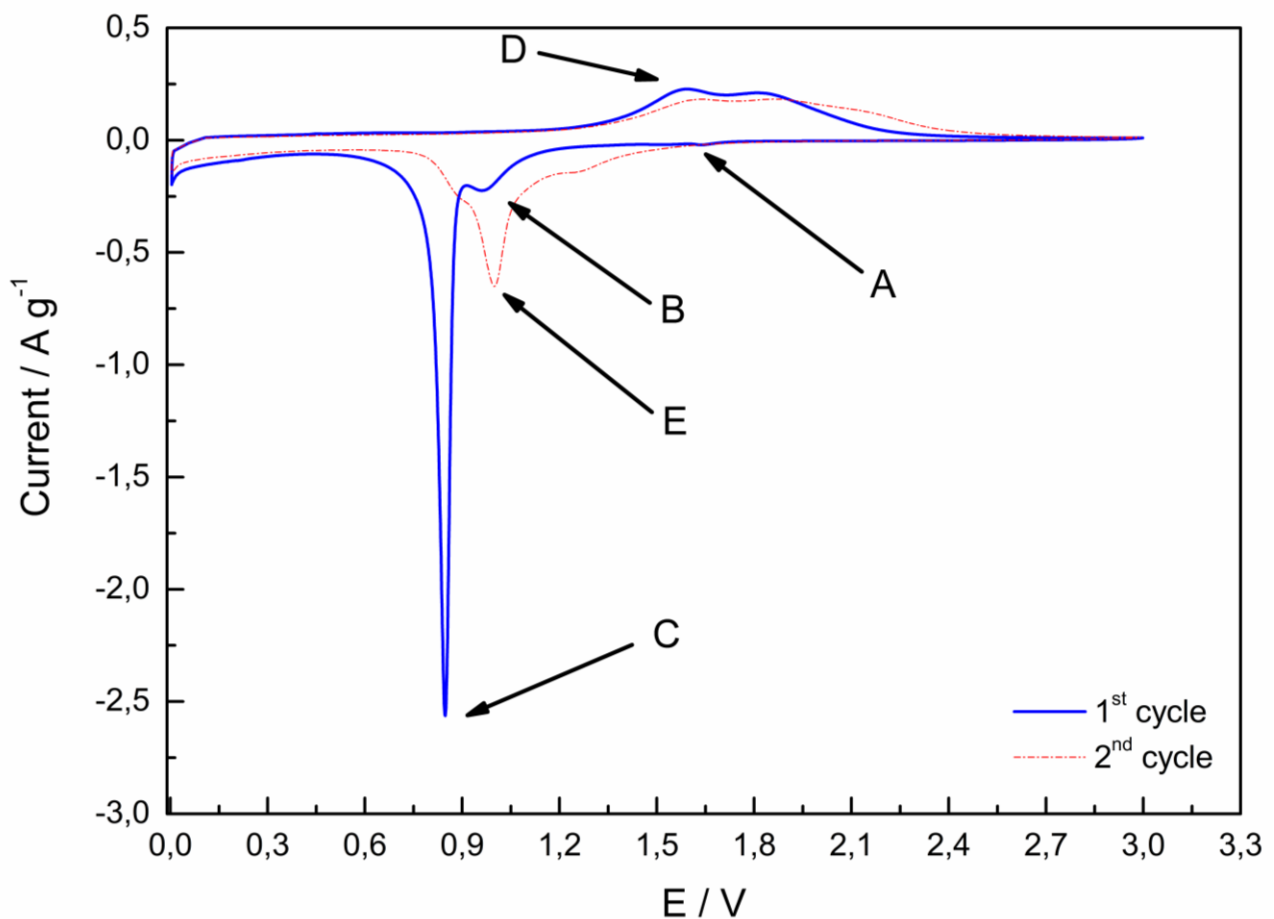


Fig. 6.8 – FeVan cyclic voltammetry experiment; Scan rate = 0.050 mV s^{-1} ; $0.005 < E \text{ (V)} < 3$ potential range.

Galvanostatic cycling tests were carried out to investigate electrochemical stability of the synthesized FeVan nanoparticles.

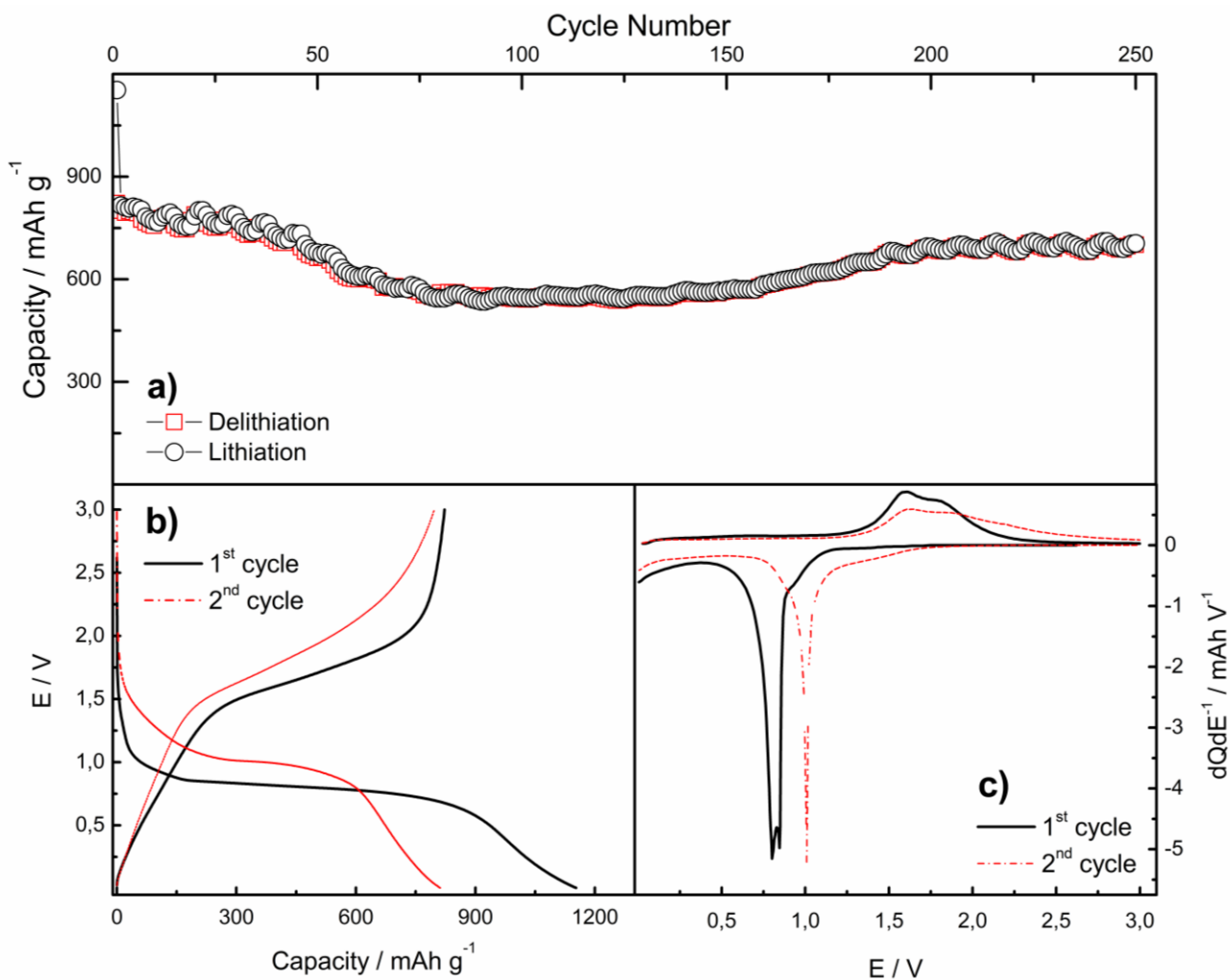


Fig. 6.9 – FeVan galvanostatic cycling test ($I = 500 \text{ mA g}^{-1}$), $0.005 < E \text{ (V)} < 3$ potential range.

Fig. 6.9a shows the cycling results obtained by cycling FeVan nanoparticles at 500 mA g^{-1} specific current for 250 cycles in the $0.005 < E \text{ (V)} < 3$ potential window. They reveal a first cycle discharge capacity of 1153 mAh g^{-1} with a relatively high coulombic efficiency of 71%. At the second cycle, a specific capacity of 815 mAh g^{-1} is observed. Taking into account this value, a capacity retention of 86.4% after 250 cycles can be calculated, together with an coulombic efficiency increasing beyond 99% during cycling.

In Figure 6.9b the galvanostatic profiles of the first two cycles are reported. During the first-cycle lithiation, it is possible to note a plateau at $E = 0.83$ V due to the Fe^0 nanoparticles/ Li_2O matrix system formation. The sloping line that reaches the 0.005 V lower cut-off potential can be assigned to the Li^+ insertion inside the conductive agent structure. During the first-cycle delithiation, the conversion mechanism-related plateau is located at high potential ($E = 1.69$ V), which is consistent with the large hysteresis frequently observed in the conversion-based materials. Figure 6.9c confirms the results already obtained with the cyclic voltammetry shown in Figure 6.8.

In order to investigate the FeVan nanoparticles capacity retention at different specific currents, a rate capability test was conducted. Specific currents ranging from 200 mA g^{-1} to 10000 mA g^{-1} have been applied. Each step of the rate capability test consisted in 5 cycles at a fixed charge/discharge rate, restoring at the end a specific current of 1000 mA g^{-1} for 100 cycles. The respective capacity values are listed in Table 6b.

Specific Current	Capacity
200 mA g^{-1}	925 mAh g^{-1}
500 mA g^{-1}	835 mAh g^{-1}
1000 mA g^{-1}	730 mAh g^{-1}
2000 mA g^{-1}	615 mAh g^{-1}
5000 mA g^{-1}	450 mAh g^{-1}
10000 mA g^{-1}	320 mAh g^{-1}
1000 mA g^{-1}	715 mAh g^{-1}

Table 6b – Rate capability experiment: summary of the capacity values at different specific currents.

The obtained results show outstanding capacity values at all current rates. Finally, when the current is restored to 1000 mA g⁻¹, a remarkable capacity value of 715 mAh g⁻¹ and a very stable cycling behavior is obtained.

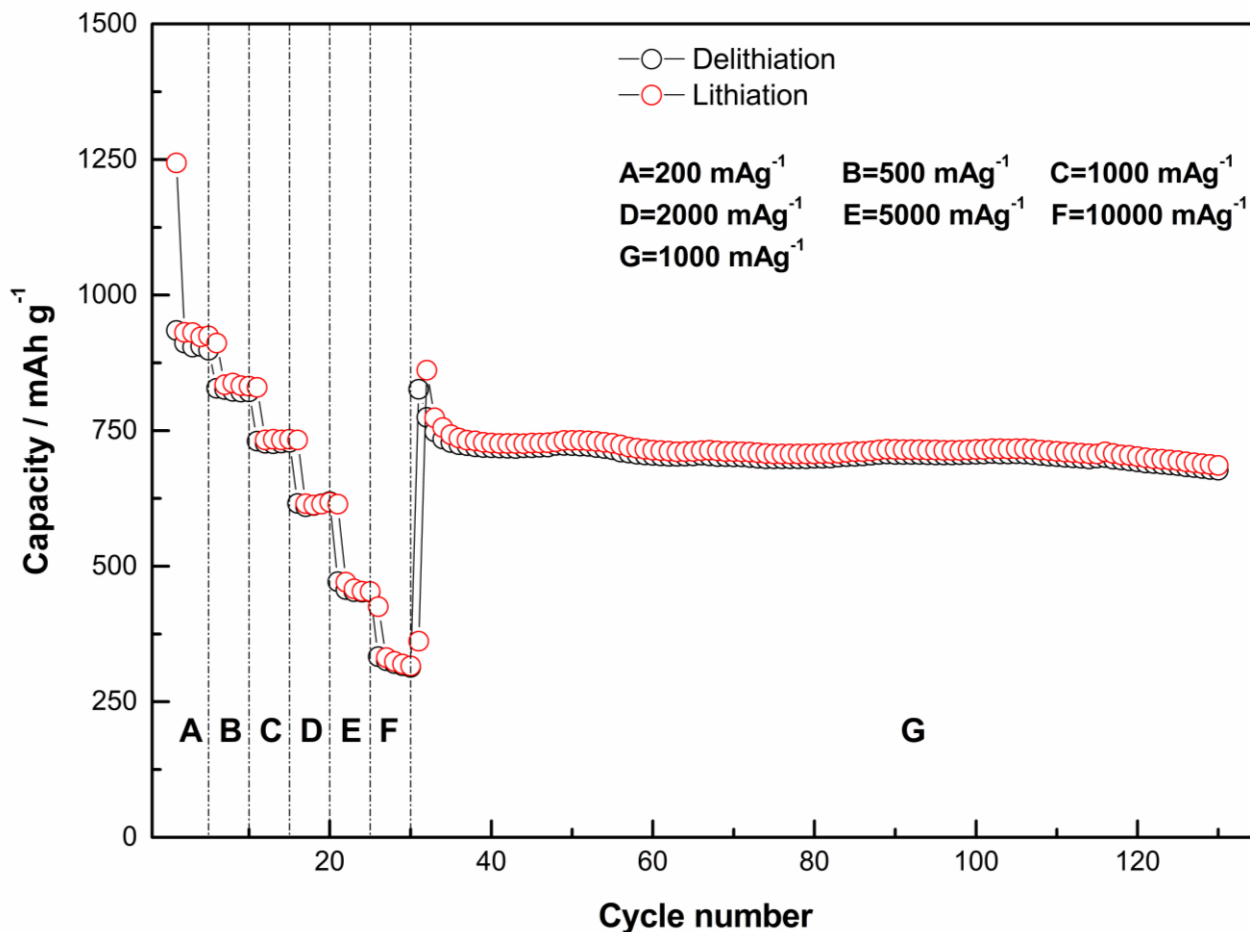


Fig. 6.10 – Rate capability experiment. Specific currents: (A) 200 mA g⁻¹; (B) 500 mA g⁻¹; (C) 1000 mA g⁻¹; (D) 2000 mA g⁻¹; (E) 5000 mA g⁻¹; (F) 10000 mA g⁻¹; (G) 1000 mA g⁻¹. 0.005 < E (V) < 3 potential range.

The outstanding performances shown by this material could be due to a synergistic interplay of the FeVan porous-structure and the stabilizing effect of the Poly(acrylic acid) (PAA) used as binder. The possibility of H-bonding with the metal nanoparticles has already demonstrate to be beneficial for the electrode mechanical stability in conversion and alloying materials [72].

Because of the good performances evidenced by the rate capability test, long-term cycling at high rates have been carried out. Figure 6.11 shows the results of this electrochemical test using a long-term cycling, overlapped to the results obtained at a reference specific current of 500 mA g⁻¹ (cell a).

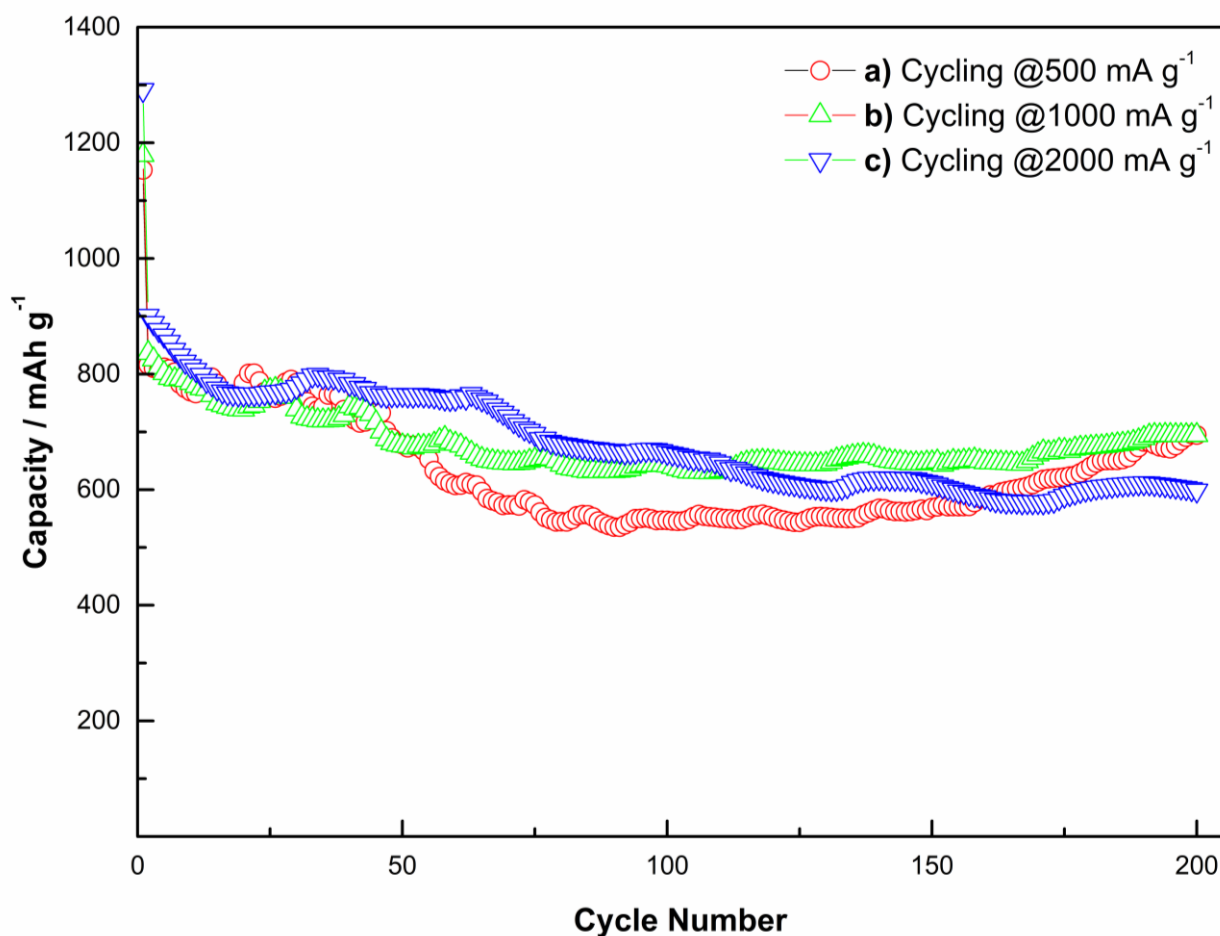


Fig. 6.11 – High-rate galvanostatic cell experiment. (a) Discharge capacity at 500 mA g^{-1} ; (b) Discharge capacity at 1000 mA g^{-1} ; (c) Discharge capacity at 2000 mA g^{-1} . $0.005 < E \text{ (V)} < 3$ potential range.

Cell **b**) shows an initial specific capacity of 1178 mAh g^{-1} with a capacity retention of 83% after 200 cycles (taking into account the 2nd cycle capacity), while cell **c**) shows an initial specific capacity of 1291 mAh g^{-1} with a capacity retention of 66.5% after 200 cycles (taking into account the 2nd cycle capacity).

Because of importance of electrode/electrolyte interfaces, electrochemical impedance spectroscopy (EIS) was carried out at different cycles with a 500 mA g^{-1} specific current. Nyquist plot (Figure 6.12, upper panels) shows a high frequency semicircle assigned to the solid electrolyte interphase (SEI), a depressed semicircle at medium frequency assigned to charge-transfer and double-layer formation processes, and a sloping line due to diffusion at low frequency ($f < 1 \text{ Hz}$).

There is a clear impedance increase in the charge-transfer region upon cycling, most likely due to electrode/electrolyte interface degradation phenomena such as aggregation and active material pulverization. In order to quantify the different resistance values, the Boukamp's software [80,104] was used for the fitting of the Nyquist plot equivalent circuit shown below:

$$R_{el}(R_{SEI}C_{SEI})(R_{ct}C_{dl})W$$

Where, R_{el} is the electrolyte bulk resistance, R_{SEI} and C_{SEI} are the resistance and the capacitance associated to the SEI layer, R_{ct} is the charge-transfer resistance, C_{dl} is the double-layer capacitance, and W represents the diffusion. It is worth noting that all the capacitive elements have been fitted using a Constant Phase element (CPE) [144] that takes into account the roughness and inhomogeneity effects. All the obtained χ^2 values were in the order of 10^{-4} - 10^{-5} .

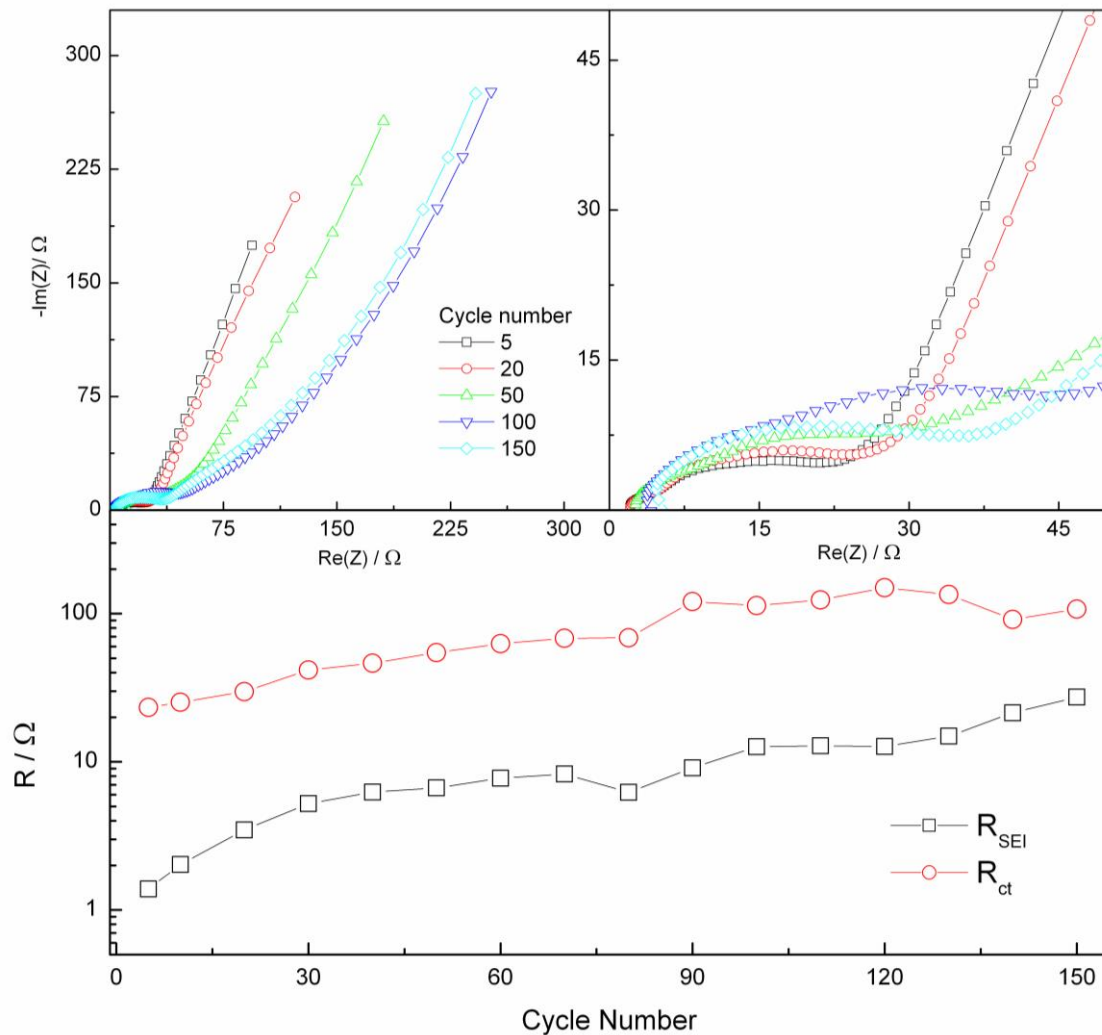


Fig. 6.12 – FeVan nanoparticles Electrochemical Impedance Spectroscopy (EIS) experiments. $200\text{ KHz} < f < 10\text{ mHz}$; $\pm 5\text{ mV}$ oscillation amplitude (upper panels); Electrochemical Impedance Spectroscopy (EIS) equivalent circuit element fit. Resistance Values vs. Cycle Number (lower panel).

The fitted resistance values associated to SEI layer (R_{SEI}) and charge-transfer processes (R_{ct}) are reported in the lower panel of Figure 6.12.

Both resistance values show an increasing trend upon cycling. The higher resistance values associated to charge-transfer processes hint a progressive electrode degradation leading to low capacities and coulombic efficiencies, which mean poor cycling performances.

6.4 Conclusion

A vanillin-templated iron oxide material was successfully synthesized. Several structural and morphological studies have shown the purity of the Fe_2O_3 nanoparticles (< 100 nm). In addition, infrared spectroscopy provided information about the iron-vanillin interaction, while thermogravimetric analysis revealed the presence of 3.4% of vanillin-derived carbon that could increase the active material overall conductivity. The electrochemical characterization revealed good capacity values of 701 mAh g^{-1} at 500 mA g^{-1} after 250 cycles together with remarkable rate capabilities. Resistance values obtained from the EIS experiments highlighted also good resistance values indicating a good SEI stability upon cycling. The obtained results, together with the use of an environmentally benign synthesis and electrode processing, enable this material to be considered as a potential candidate for the next-generation sustainable anode materials for lithium-ion batteries.

7. References

- [1] R. Socolow, S. Pacala, Stabilization Wedges: Solving the Climate Problem for the Next Half-Century with Technologies Available Today, *Science*. 305 (2004) 968–972. doi:10.1126/science.1100103.
- [2] P.G. Bruce, B. Scrosati, J.M. Tarascon, Nanomaterials for rechargeable lithium batteries, *Angew. Chemie - Int. Ed.* 47 (2008) 2930–2946. doi:10.1002/anie.200702505.
- [3] M. Winter, R.J. Brodd, What are batteries, fuel cells, and supercapacitors?, *Chem. Rev.* 104 (2004) 4245–4269. doi:10.1021/cr020730k.
- [4] J.M. Tarascon, M. Armand, Issues and challenges facing rechargeable lithium batteries, *Nature*. 414 (2001) 359–367. doi:10.1038/35104644.
- [5] H.J. Bang, S. Kim, J. Prakash, Electrochemical investigations of lithium-aluminum alloy anode in Li/polymer cells, *J. Power Sources*. 92 (2001) 45–49. doi:10.1016/S0378-7753(00)00522-X.
- [6] J. Cannarella, C.B. Arnold, The Effects of Defects on Localized Plating in Lithium-Ion Batteries, *J. Electrochem. Soc.* 162 (2015) A1365–A1373. doi:10.1149/2.1051507jes.
- [7] C. Monroe, J. Newman, Dendrite Growth in Lithium/Polymer Systems, *J. Electrochem. Soc.* 150 (2003) A1377. doi:10.1149/1.1606686.
- [8] P.C. Shi, M. Lin, H. Zheng, X.D. He, Z.M. Xue, H.F. Xiang, C.H. Chen, Effect of propylene carbonate-Li⁺solvation structures on graphite exfoliation and its application in Li-ion batteries, *Electrochim. Acta*. 247 (2017) 12–18. doi:10.1016/j.electacta.2017.06.174.
- [9] A. Ohta, H. Koshina, H. Okuno, H. Murai, Relationship between carbonaceous materials and electrolyte in secondary lithium-ion batteries, *J. Power Sources*. 54 (1995) 6–10. doi:10.1016/0378-7753(94)02031-W.
- [10] T. Ohzuku, Formation of Lithium-Graphite Intercalation Compounds in Nonaqueous Electrolytes and Their Application as a Negative Electrode for a Lithium Ion (Shuttlecock) Cell, *J. Electrochem. Soc.* 140 (1993) 2490. doi:10.1149/1.2220849.
- [11] D. Aurbach, B. Markovsky, I. Weissman, E. Levi, Y. Ein-Eli, On the correlation between

surface chemistry and performance of graphite negative electrodes for Li ion batteries, *Electrochim. Acta.* 45 (1999) 67–86. doi:10.1016/S0013-4686(99)00194-2.

- [12] S.J. An, J. Li, C. Daniel, D. Mohanty, S. Nagpure, D.L. Wood, The state of understanding of the lithium-ion-battery graphite solid electrolyte interphase (SEI) and its relationship to formation cycling, *Carbon N. Y.* 105 (2016) 52–76. doi:10.1016/j.carbon.2016.04.008.
- [13] M. Steinhauer, T. Diemant, C. Heim, R. Jürgen Behm, N. Wagner, K. Andreas Friedrich, Insights into solid electrolyte interphase formation on alternative anode materials in lithium-ion batteries, *J. Appl. Electrochem.* 47 (2017) 249–259. doi:10.1007/s10800-016-1032-3.
- [14] Y.M. Lee, J.Y. Lee, H.-T. Shim, J.K. Lee, J.-K. Park, SEI Layer Formation on Amorphous Si Thin Electrode during Precycling, *J. Electrochem. Soc.* 154 (2007) A515. doi:10.1149/1.2719644.
- [15] M. Nie, J. Demeaux, B.T. Young, D.R. Heskett, Y. Chen, A. Bose, J.C. Woicik, B.L. Lucht, Effect of Vinylene Carbonate and Fluoroethylene Carbonate on SEI Formation on Graphitic Anodes in Li-Ion Batteries, *J. Electrochem. Soc.* 162 (2015) A7008–A7014. doi:10.1149/2.0021513jes.
- [16] S.J. Rezvani, M. Ciambezi, R. Gunnella, M. Minicucci, M.A. Munioz, F. Nobili, M. Pasqualini, S. Passerini, C. Schreiner, A. Trapananti, A. Witkowska, A. Di Cicco, Local Structure and Stability of SEI in Graphite and ZFO Electrodes Probed by As K-Edge Absorption Spectroscopy, *J. Phys. Chem. C.* 120 (2016) 4287–4295. doi:10.1021/acs.jpcc.5b11798.
- [17] S.J. Rezvani, R. Gunnella, A. Witkowska, F. Mueller, M. Pasqualini, F. Nobili, S. Passerini, A. Di Cicco, Is the Solid Electrolyte Interphase an Extra-Charge Reservoir in Li-Ion Batteries?, *ACS Appl. Mater. Interfaces.* 9 (2017) 4570–4576. doi:10.1021/acsami.6b12408.
- [18] S. Goriparti, E. Miele, F. De Angelis, E. Di Fabrizio, R. Proietti Zaccaria, C. Capiglia, Review on recent progress of nanostructured anode materials for Li-ion batteries, *J. Power Sources.* 257 (2014) 421–443. doi:10.1016/j.jpowsour.2013.11.103.
- [19] L. Ji, Z. Lin, M. Alcoutlabi, X. Zhang, Recent developments in nanostructured anode materials for rechargeable lithium-ion batteries, *Energy Environ. Sci.* 4 (2011) 2682. doi:10.1039/c0ee00699h.

- [20] V. Aravindan, Y.S. Lee, S. Madhavi, Research Progress on Negative Electrodes for Practical Li-Ion Batteries: Beyond Carbonaceous Anodes, *Adv. Energy Mater.* 5 (2015). doi:10.1002/aenm.201402225.
- [21] D. Bresser, S. Passerini, B. Scrosati, Leveraging valuable synergies by combining alloying and conversion for lithium-ion anodes, *Energy Environ. Sci.* 9 (2016) 3348–3367. doi:10.1039/c6ee02346k.
- [22] Y. Domi, H. Usui, D. Iwanari, H. Sakaguchi, Effect of Mechanical Pre-Lithiation on Electrochemical Performance of Silicon Negative Electrode for Lithium-Ion Batteries, *J. Electrochem. Soc.* 164 (2017) A1651–A1654. doi:10.1149/2.1361707jes.
- [23] F. Holtstiege, P. Bärmann, R. Nölle, M. Winter, T. Placke, Pre-Lithiation Strategies for Rechargeable Energy Storage Technologies: Concepts, Promises and Challenges, *Batteries.* 4 (2018) 4. doi:10.3390/batteries4010004.
- [24] G. Gabrielli, M. Marinaro, M. Mancini, P. Axmann, M. Wohlfahrt-Mehrens, A new approach for compensating the irreversible capacity loss of high-energy Si/C|LiNi_{0.5}Mn_{1.5}O₄ lithium-ion batteries, *J. Power Sources.* 351 (2017) 35–44. doi:10.1016/j.jpowsour.2017.03.051.
- [25] M. Ashuri, Q. He, L.L. Shaw, Silicon as a potential anode material for Li-ion batteries: Where size, geometry and structure matter, *Nanoscale.* 8 (2016) 74–103. doi:10.1039/c5nr05116a.
- [26] N. Dimov, S. Kugino, M. Yoshio, Mixed silicon-graphite composites as anode material for lithium ion batteries - Influence of preparation conditions on the properties of the material, *J. Power Sources.* 136 (2004) 108–114. doi:10.1016/j.jpowsour.2004.05.012.
- [27] J.H. Lee, W.J. Kim, J.Y. Kim, S.H. Lim, S.M. Lee, Spherical silicon/graphite/carbon composites as anode material for lithium-ion batteries, *J. Power Sources.* 176 (2008) 353–358. doi:10.1016/j.jpowsour.2007.09.119.
- [28] J. Yang, Y. Wang, W. Li, L. Wang, Y. Fan, W. Jiang, W. Luo, Y. Wang, B. Kong, C. Selomulya, H.K. Liu, S.X. Dou, D. Zhao, Amorphous TiO₂ Shells: A Vital Elastic Buffering Layer on Silicon Nanoparticles for High-Performance and Safe Lithium Storage, *Adv. Mater.* 29 (2017) 1–7. doi:10.1002/adma.201700523.
- [29] M. Ashuri, Q. He, Y. Liu, K. Zhang, S. Emani, M.S. Sawicki, J.S. Shamie, L.L. Shaw, Hollow Silicon Nanospheres Encapsulated with a Thin Carbon Shell: An Electrochemical Study,

Electrochim. Acta. 215 (2016) 126–141. doi:10.1016/j.electacta.2016.08.059.

- [30] L. Chen, K. Wang, X. Xie, J. Xie, Effect of vinylene carbonate (VC) as electrolyte additive on electrochemical performance of Si film anode for lithium ion batteries, *J. Power Sources*. 174 (2007) 538–543. doi:10.1016/j.jpowsour.2007.06.149.
- [31] V. Etacheri, O. Haik, Y. Goffer, G.A. Roberts, I.C. Stefan, R. Fasching, D. Aurbach, Effect of fluoroethylene carbonate (FEC) on the performance and surface chemistry of Si-nanowire lithium battery anodes, *Langmuir*. 28 (2012) 965–976. doi:10.1021/la203712s.
- [32] W. Porcher, S. Chazelle, A. Boulineau, N. Mariage, J.P. Alper, T. Van Rompaey, J.-S. Bridel, C. Haon, Understanding Polyacrylic Acid and Lithium Polyacrylate Binder Behavior in Silicon Based Electrodes for Li-Ion Batteries, *J. Electrochem. Soc.* 164 (2017) A3633–A3640. doi:10.1149/2.0821714jes.
- [33] H. Buqa, M. Holzzapfel, F. Krumeich, C. Veit, P. Novák, Study of styrene butadiene rubber and sodium methyl cellulose as binder for negative electrodes in lithium-ion batteries, *J. Power Sources*. 161 (2006) 617–622. doi:10.1016/j.jpowsour.2006.03.073.
- [34] N. Ding, J. Xu, Y. Yao, G. Wegner, I. Lieberwirth, C. Chen, Improvement of cyclability of Si as anode for Li-ion batteries, *J. Power Sources*. 192 (2009) 644–651. doi:10.1016/j.jpowsour.2009.03.017.
- [35] X. Zuo, J. Zhu, P. Müller-Buschbaum, Y.J. Cheng, Silicon based lithium-ion battery anodes: A chronicle perspective review, *Nano Energy*. 31 (2017) 113–143. doi:10.1016/j.nanoen.2016.11.013.
- [36] M.T. McDowell, S.W. Lee, W.D. Nix, Y. Cui, Understanding the lithiation of silicon and other alloying anodes for lithium-ion batteries, *Adv. Mater.* 25 (2013) 4966–4985. doi:10.1002/adma.201301795.
- [37] M.N. Obrovac, L. Christensen, Structural Changes in Silicon Anodes during Lithium Insertion/Extraction, *Electrochem. Solid-State Lett.* 7 (2004) A93. doi:10.1149/1.1652421.
- [38] M.N. Obrovac, L. Christensen, D.B. Le, J.R. Dahn, Alloy Design for Lithium-Ion Battery Anodes, *J. Electrochem. Soc.* 154 (2007) A849. doi:10.1149/1.2752985.
- [39] V.L. Chevrier, J.W. Zwanziger, J.R. Dahn, First principles study of Li-Si crystalline phases:

Charge transfer, electronic structure, and lattice vibrations, *J. Alloys Compd.* 496 (2010) 25–36. doi:10.1016/j.jallcom.2010.01.142.

- [40] B.P.N. Nguyen, S. Chazelle, M. Cerbelaud, W. Porcher, B. Lestriez, Manufacturing of industry-relevant silicon negative composite electrodes for lithium ion-cells, *J. Power Sources.* 262 (2014) 112–122. doi:10.1016/j.jpowsour.2014.03.119.
- [41] S. Chae, M. Ko, K. Kim, K. Ahn, J. Cho, Confronting Issues of the Practical Implementation of Si Anode in High-Energy Lithium-Ion Batteries, *Joule.* 1 (2017) 47–60. doi:10.1016/j.joule.2017.07.006.
- [42] E. Radvanyi, K. Van Havenbergh, W. Porcher, S. Jouanneau, J.S. Bridel, S. Put, S. Franger, Study and modeling of the Solid Electrolyte Interphase behavior on nano-silicon anodes by Electrochemical Impedance Spectroscopy, *Electrochim. Acta.* 137 (2014) 751–757. doi:10.1016/j.electacta.2014.06.069.
- [43] H. Bin Wu, J.S. Chen, H.H. Hng, X.W. Lou, Nanostructured metal oxide-based materials as advanced anodes for lithium-ion batteries, *Nanoscale.* 4 (2012) 2526–2542. doi:10.1039/c2nr11966h.
- [44] J. Cabana, L. Monconduit, D. Larcher, M.R. Palacín, Beyond intercalation-based Li-ion batteries: The state of the art and challenges of electrode materials reacting through conversion reactions, *Adv. Mater.* 22 (2010) 170–192. doi:10.1002/adma.201000717.
- [45] K. Cao, T. Jin, L. Yang, L. Jiao, Recent progress in conversion reaction metal oxide anodes for Li-ion batteries, *Mater. Chem. Front.* (2017) 2213–2242. doi:10.1039/C7QM00175D.
- [46] M.J. Aragón, B. León, C. Pérez Vicente, J.L. Tirado, On the use of transition metal oxysalts as conversion electrodes in lithium-ion batteries, *J. Power Sources.* 189 (2009) 623–627. doi:10.1016/j.jpowsour.2008.07.046.
- [47] L. Zhang, H. Bin Wu, X.W. Lou, Iron-oxide-based advanced anode materials for lithium-ion batteries, *Adv. Energy Mater.* 4 (2014) 1–11. doi:10.1002/aenm.201300958.
- [48] X. Liu, C. Chen, Y. Zhao, B. Jia, A review on the synthesis of manganese oxide nanomaterials and their applications on lithium-ion batteries, *J. Nanomater.* 2013 (2013). doi:10.1155/2013/736375.

- [49] M. Lazzari, A Cyclable Lithium Organic Electrolyte Cell Based on Two Intercalation Electrodes, *J. Electrochem. Soc.* 127 (1980) 773. doi:10.1149/1.2129753.
- [50] B.M.S. Whittingham, *History, Evolution, and Future Status of Energy Storage*, 100 (2012).
- [51] K. Mizushima, P.C. Jones, P.J. Wiseman, J.B. Goodenough, Li_xCoO_2 ($0 < x \leq 1$): A new cathode material for batteries of high energy density, *Solid State Ionics*. 3–4 (1981) 171–174. doi:10.1016/0167-2738(81)90077-1.
- [52] L. Yunjian, L. Xinhai, G. Huajun, W. Zhixing, H. Qiyang, P. Wenjie, Y. Yong, Electrochemical performance and capacity fading reason of LiMn_2O_4 /graphite batteries stored at room temperature, *J. Power Sources*. 189 (2009) 721–725. doi:10.1016/j.jpowsour.2008.08.044.
- [53] M. Pasqualini, S. Calcaterra, F. Maroni, S.J. Rezvani, A. Di Cicco, S. Alexander, H. Rajantie, R. Tossici, F. Nobili, Electrochemical and spectroscopic characterization of an alumina-coated LiMn_2O_4 cathode with enhanced interfacial stability, *Electrochim. Acta*. 258 (2017) 175–181. doi:10.1016/j.electacta.2017.10.115.
- [54] T. Ohzuku, Y. Makimura, Layered Lithium Insertion Material of $\text{LiCo}_{1/3}\text{Ni}_{1/3}\text{Mn}_{1/3}\text{O}_2$ for Lithium-Ion Batteries, *Chem. Lett.* 30 (2001) 642–643. doi:10.1246/cl.2001.642.
- [55] H. Kobayashi, Y. Arachi, S. Emura, K. Tatsumi, Investigation on lithium de-intercalation mechanism for $\text{LiNi}_{0.45}\text{Mn}_{0.45}\text{Al}_{0.1}\text{O}_2$, *Solid State Ionics*. 178 (2007) 1101–1105. doi:10.1016/j.ssi.2007.05.003.
- [56] N. Nitta, F. Wu, J.T. Lee, G. Yushin, Li-ion battery materials: Present and future, *Mater. Today*. 18 (2015) 252–264. doi:10.1016/j.mattod.2014.10.040.
- [57] J.W. Choi, D. Aurbach, Promise and reality of post-lithium-ion batteries with high energy densities, *Nat. Rev. Mater.* 1 (2016). doi:10.1038/natrevmats.2016.13.
- [58] S.T. Myung, F. Maglia, K.J. Park, C.S. Yoon, P. Lamp, S.J. Kim, Y.K. Sun, Nickel-Rich Layered Cathode Materials for Automotive Lithium-Ion Batteries: Achievements and Perspectives, *ACS Energy Lett.* 2 (2017) 196–223. doi:10.1021/acsenergylett.6b00594.
- [59] Y. Lan, X. Wang, J. Zhang, J. Zhang, Z. Wu, Z. Zhang, Preparation and characterization of carbon-coated LiFePO_4 cathode materials for lithium-ion batteries with resorcinol-

- formaldehyde polymer as carbon precursor, *Powder Technol.* 212 (2011) 327–331. doi:10.1016/j.powtec.2011.06.005.
- [60] J.C. Bachman, S. Muy, A. Grimaud, H.H. Chang, N. Pour, S.F. Lux, O. Paschos, F. Maglia, S. Lupart, P. Lamp, L. Giordano, Y. Shao-Horn, *Inorganic Solid-State Electrolytes for Lithium Batteries: Mechanisms and Properties Governing Ion Conduction*, *Chem. Rev.* 116 (2016) 140–162. doi:10.1021/acs.chemrev.5b00563.
- [61] K. Xu, *Nonaqueous liquid electrolytes for lithium-based rechargeable batteries*, *Chem. Rev.* 104 (2004) 4303–4417. doi:10.1021/cr030203g.
- [62] A.M. Haregewoin, A.S. Wotango, B.-J. Hwang, *Electrolyte additives for lithium ion battery electrodes: progress and perspectives*, *Energy Environ. Sci.* 9 (2016) 1955–1988. doi:10.1039/C6EE00123H.
- [63] A.L. Michan, B.S. Parimalam, M. Leskes, R.N. Kerber, T. Yoon, C.P. Grey, B.L. Lucht, *Fluoroethylene carbonate and vinylene carbonate reduction: Understanding lithium-ion battery electrolyte additives and solid electrolyte interphase formation*, *Chem. Mater.* 28 (2016) 8149–8159. doi:10.1021/acs.chemmater.6b02282.
- [64] R. Jung, M. Metzger, D. Haering, S. Solchenbach, C. Marino, N. Tsiouvaras, C. Stinner, H.A. Gasteiger, *Consumption of Fluoroethylene Carbonate (FEC) on Si-C Composite Electrodes for Li-Ion Batteries*, *J. Electrochem. Soc.* 163 (2016) A1705–A1716. doi:10.1149/2.0951608jes.
- [65] Y. Shi, X. Zhou, G. Yu, *Material and Structural Design of Novel Binder Systems for High-Energy, High-Power Lithium-Ion Batteries*, *Acc. Chem. Res.* 50 (2017) 2642–2652. doi:10.1021/acs.accounts.7b00402.
- [66] J.E.S. Technol, N. Choi, S. Ha, Y. Lee, J.Y. Jang, M. Jeong, W.C. Shin, M. Ue, *Recent Progress on Polymeric Binders for Silicon Anodes in Lithium-Ion Batteries*, *J. Electrochem. Sci. Technol.* 6 (2015) 35–49. doi:10.5229/JECST.2015.6.2.35.
- [67] D.L. Wood, J. Li, C. Daniel, *Prospects for reducing the processing cost of lithium ion batteries*, *J. Power Sources.* 275 (2015) 234–242. doi:10.1016/j.jpowsour.2014.11.019.
- [68] C.C. Nguyen, T. Yoon, D.M. Seo, P. Guduru, B.L. Lucht, *Systematic Investigation of Binders for Silicon Anodes: Interactions of Binder with Silicon Particles and Electrolytes and Effects*

of Binders on Solid Electrolyte Interphase Formation, *ACS Appl. Mater. Interfaces*. 8 (2016) 12211–12220. doi:10.1021/acsami.6b03357.

- [69] J. Li, R.B. Lewis, J.R. Dahn, Sodium Carboxymethyl Cellulose - A potential binder for Si negative electrodes for Li-ion batteries, *Electrochem. Solid-State Lett.* 10 (2007) A17. doi:10.1149/1.2398725.
- [70] A. Tranchot, H. Idrissi, P.X. Thivel, L. Roué, Impact of the Slurry pH on the Expansion/Contraction Behavior of Silicon/Carbon/Carboxymethylcellulose Electrodes for Li-Ion Batteries, *J. Electrochem. Soc.* 163 (2016) A1020–A1026. doi:10.1149/2.1071606jes.
- [71] A. Toudjine, M. Morcrette, M. Courty, C. Davoisne, M. Lejeune, N. Mariage, W. Porcher, D. Larcher, Partially Oxidized Silicon Particles for Stable Aqueous Slurries and Practical Large-Scale Making of Si-Based Electrodes, *J. Electrochem. Soc.* 162 (2015) A1466–A1475. doi:10.1149/2.0301508jes.
- [72] A. Magasinski, B. Zdyrko, I. Kovalenko, B. Hertzberg, R. Burtovyy, C.F. Huebner, T.F. Fuller, I. Luzinov, G. Yushin, Toward efficient binders for Li-ion battery Si-based anodes: Polyacrylic acid, *ACS Appl. Mater. Interfaces*. 2 (2010) 3004–3010. doi:10.1021/am100871y.
- [73] Z.Y. Wu, L. Deng, J.T. Li, Q. Sen Huang, Y.Q. Lu, J. Liu, T. Zhang, L. Huang, S.G. Sun, Multiple hydrogel alginate binders for Si anodes of lithium-ion battery, *Electrochim. Acta*. 245 (2017) 371–378. doi:10.1016/j.electacta.2017.05.094.
- [74] H.K. Park, B.S. Kong, E.S. Oh, Effect of high adhesive polyvinyl alcohol binder on the anodes of lithium ion batteries, *Electrochem. Commun.* 13 (2011) 1051–1053. doi:10.1016/j.elecom.2011.06.034.
- [75] C. Wang, H. Wu, Z. Chen, M.T. Mcdowell, Y. Cui, Z. Bao, Self-healing chemistry enables the stable operation of silicon microparticle anodes for high-energy lithium-ion batteries, *Nat. Chem.* 5 (2013) 1042–1048. doi:10.1038/nchem.1802.
- [76] G. Xu, Q. bo Yan, A. Kushima, X. Zhang, J. Pan, J. Li, Conductive graphene oxide-polyacrylic acid (GOPAA) binder for lithium-sulfur battery, *Nano Energy*. 31 (2017) 568–574. doi:10.1016/j.nanoen.2016.12.002.
- [77] R.W. O'Brien, B.R. Midmore, A. Lamb, R.J. Hunter, Electroacoustic studies of moderately concentrated colloidal suspensions, *Faraday Discuss. Chem. Soc.* 90 (1990) 301–312.

doi:10.1039/DC9909000301.

- [78] D.A.H. Hanaor, M. Michelazzi, C. Leonelli, C.C. Sorrell, D.A.H. Hanaor, M. Michelazzi, C. Leonelli, C.C. Sorrell, The Effects of Carboxylic Acids on the Aqueous Dispersion and Electrophoretic Deposition of ZrO_2 , *J. Eur. Ceram. Soc.* 32 (2012) 235–244. doi:10.1016/j.jeurceramsoc.2011.08.015.
- [79] M. Amirjan, H. Khorsand, Processing and properties of Al-based powder suspension/slurry: A comparison study of aqueous binder systems, stability and film uniformity, *Powder Technol.* 254 (2014) 12–21. doi:10.1016/j.powtec.2013.12.051.
- [80] B.A. Boukamp, A package for impedance/admittance data analysis, *Solid State Ionics.* 18–19 (1986) 136–140. doi:10.1016/0167-2738(86)90100-1.
- [81] J. Zhu, L. Cao, Y. Wu, Y. Gong, Z. Liu, H.E. Hoster, Y. Zhang, S. Zhang, S. Yang, Q. Yan, P.M. Ajayan, R. Vajtai, Building 3D structures of vanadium pentoxide nanosheets and application as electrodes in supercapacitors, *Nano Lett.* 13 (2013) 5408–5413. doi:10.1021/nl402969r.
- [82] B. Alonso, J. Livage, Synthesis of Vanadium Oxide Gels from Peroxovanadic Acid Solutions : A 51 V NMR Study, *J. Solid State Chem.* 19 (1999) 16–19. doi:10.1006/jssc.1999.8283.
- [83] J. Livage, Vanadium Pentoxide Gels, *Chem. Mater.* 3 (1991) 578–593. doi:10.1021/cm00016a006.
- [84] M. Nabavi, C. Sanchez, J. Livage, Structure and properties of amorphous V_2O_5 , *Philos. Mag. Part B.* 63 (1991) 941–953. doi:10.1080/13642819108205549.
- [85] A. Moretti, S. Passerini, Bilayered Nanostructured $V_2O_5 \cdot nH_2O$ for Metal Batteries, *Adv. Energy Mater.* 6 (2016). doi:10.1002/aenm.201600868.
- [86] F. Maroni, A. Birrozzi, G. Carbonari, F. Croce, R. Tossici, S. Passerini, F. Nobili, Graphene/ V_2O_5 Cryogel Composite As a High-Energy Cathode Material For Lithium-Ion Batteries, *ChemElectroChem.* 4 (2017) 613–619. doi:10.1002/celec.201600798.
- [87] A.L. Patterson, The scherrer formula for X-ray particle size determination, *Phys. Rev.* 56 (1939) 978–982. doi:10.1103/PhysRev.56.978.
- [88] A. Moretti, M. Secchiaroli, D. Buchholz, G. Giuli, R. Marassi, S. Passerini, Exploring the Low

Voltage Behavior of V_2O_5 Aerogel as Intercalation Host for Sodium Ion Battery, *J. Electrochem. Soc.* 162 (2015) A2723–A2728. doi:10.1149/2.0711514jes.

- [89] C. Meier, S. Lüttjohann, V.G. Kravets, H. Nienhaus, A. Lorke, H. Wiggers, Raman properties of silicon nanoparticles, *Phys. E Low-Dimensional Syst. Nanostructures.* 32 (2006) 155–158. doi:10.1016/j.physe.2005.12.030.
- [90] F. Maroni, R. Raccichini, A. Birrozzi, G. Carbonari, R. Tossici, F. Croce, R. Marassi, F. Nobili, Graphene/silicon nanocomposite anode with enhanced electrochemical stability for lithium-ion battery applications, *J. Power Sources.* (2014). doi:10.1016/j.jpowsour.2014.07.064.
- [91] P. Limthongkul, Y. Il Jang, N.J. Dudney, Y.M. Chiang, Electrochemically-driven solid-state amorphization in lithium-silicon alloys and implications for lithium storage, *Acta Mater.* 51 (2003) 1103–1113. doi:10.1016/S1359-6454(02)00514-1.
- [92] L. Zhang, M. Yang, S. Zhang, Z. Wu, A. Amini, Y. Zhang, D. Wang, S. Bao, Z. Lu, N. Wang, C. Cheng, V_2O_5 -C-SnO₂ Hybrid Nanobelts as High Performance Anodes for Lithium-ion Batteries, *Sci. Rep.* 6 (2016) 33597. doi:10.1038/srep33597.
- [93] S.S. Zhang, A review on electrolyte additives for lithium-ion batteries, *J. Power Sources.* 162 (2006) 1379–1394. doi:10.1016/j.jpowsour.2006.07.074.
- [94] T. Jaumann, J. Balach, U. Langklotz, V. Sauchuk, M. Fritsch, A. Michaelis, V. Teltevskij, D. Mikhailova, S. Oswald, M. Klose, G. Stephani, R. Hauser, J. Eckert, L. Giebeler, Lifetime vs. rate capability: Understanding the role of FEC and VC in high-energy Li-ion batteries with nano-silicon anodes, *Energy Storage Mater.* 6 (2017) 26–35. doi:10.1016/j.ensm.2016.08.002.
- [95] S. Dalavi, P. Guduru, B.L. Lucht, Performance Enhancing Electrolyte Additives for Lithium Ion Batteries with Silicon Anodes, *J. Electrochem. Soc.* 159 (2012) A642. doi:10.1149/2.076205jes.
- [96] F. Maroni, G. Carbonari, F. Croce, R. Tossici, F. Nobili, Anatase TiO₂ as a Cheap and Sustainable Buffering Filler for Silicon Nanoparticles in Lithium-Ion Battery Anodes, *ChemSusChem.* (2017). doi:10.1002/cssc.201701431.
- [97] A.E. Danks, S.R. Hall, Z. Schnepf, The evolution of “sol-gel” chemistry as a technique for materials synthesis, *Mater. Horizons.* 3 (2016) 91–112. doi:10.1039/c5mh00260e.

- [98] L. Kavan, Lithium insertion into TiO₂ (anatase): Electrochemistry, Raman spectroscopy, and isotope labeling, *J. Solid State Electrochem.* 18 (2014) 2297–2306. doi:10.1007/s10008-014-2435-x.
- [99] H.C. Choi, Y.M. Jung, S. Bin Kim, Size effects in the Raman spectra of TiO₂nanoparticles, *Vib. Spectrosc.* 37 (2005) 33–38. doi:10.1016/j.vibspec.2004.05.006.
- [100] F.M. Liu, B. Ren, J.H. Wu, J.W. Yan, X.F. Xue, B.W. Mao, Z.Q. Tian, Enhanced-Raman scattering from silicon nanoparticle substrates, *Chem. Phys. Lett.* 382 (2003) 502–507. doi:10.1016/j.cplett.2003.10.102.
- [101] A. Birrozzi, F. Maroni, R. Raccichini, R. Tossici, R. Marassi, F. Nobili, Enhanced stability of SnSb/graphene anode through alternative binder and electrolyte additive for lithium ion batteries application, *J. Power Sources.* 294 (2015) 248–253. doi:10.1016/j.jpowsour.2015.06.065.
- [102] J.H. Lee, U. Paik, V.A. Hackley, Y.M. Choi, Effect of poly(acrylic acid) on adhesion strength and electrochemical performance of natural graphite negative electrode for lithium-ion batteries, *J. Power Sources.* 161 (2006) 612–616. doi:10.1016/j.jpowsour.2006.03.087.
- [103] J. Chong, S. Xun, H. Zheng, X. Song, G. Liu, P. Ridgway, J.Q. Wang, V.S. Battaglia, A comparative study of polyacrylic acid and poly(vinylidene difluoride) binders for spherical natural graphite/LiFePO₄ electrodes and cells, *J. Power Sources.* 196 (2011) 7707–7714. doi:10.1016/j.jpowsour.2011.04.043.
- [104] B.A. Boukamp, A nonlinear least squares fit procedure for analysis of immittancs data of electrochemical systems, *Solid State Ionics.* 20 (1986) 31–44. doi:10.1016/0167-2738(86)90031-7.
- [105] N.A. Kaskhedikar, J. Maier, Lithium storage in carbon nanostructures, *Adv. Mater.* 21 (2009) 2664–2680. doi:10.1002/adma.200901079.
- [106] J. Li, J.R. Dahn, An In Situ X-Ray Diffraction Study of the Reaction of Li with Crystalline Si, *J. Electrochem. Soc.* 154 (2007) A156. doi:10.1149/1.2409862.
- [107] E. Radvanyi, W. Porcher, E. De Vito, A. Montani, S. Franger, S. Jouanneau Si Larbi, Failure mechanisms of nano-silicon anodes upon cycling: An electrode porosity evolution model, *Phys. Chem. Chem. Phys.* 16 (2014) 17142–17153. doi:10.1039/c4cp02324b.

- [108] A. Casimir, H. Zhang, O. Ogoke, J.C. Amine, J. Lu, G. Wu, Silicon-based anodes for lithium-ion batteries: Effectiveness of materials synthesis and electrode preparation, *Nano Energy*. 27 (2016) 359–376. doi:10.1016/j.nanoen.2016.07.023.
- [109] B. Philippe, R. Dedryvère, J. Allouche, F. Lindgren, M. Gorgoi, H. Rensmo, D. Gonbeau, K. Edström, Nanosilicon electrodes for lithium-ion batteries: Interfacial mechanisms studied by hard and soft X-ray photoelectron spectroscopy, *Chem. Mater.* 24 (2012) 1107–1115. doi:10.1021/cm2034195.
- [110] K. Schroder, J. Alvarado, T.A. Yersak, J. Li, N. Dudney, L.J. Webb, Y.S. Meng, K.J. Stevenson, The Effect of Fluoroethylene Carbonate as an Additive on the Solid Electrolyte Interphase on Silicon Lithium-Ion Electrodes, *Chem. Mater.* 27 (2015) 5531–5542. doi:10.1021/acs.chemmater.5b01627.
- [111] M. Ko, S. Chae, J. Ma, N. Kim, H.W. Lee, Y. Cui, J. Cho, Scalable synthesis of silicon-nanolayer-embedded graphite for high-energy lithium-ion batteries, *Nat. Energy*. 1 (2016) 1–8. doi:10.1038/nenergy.2016.113.
- [112] M. Ashuri, Q. He, Y. Liu, S. Emani, L.L. Shaw, Synthesis and performance of nanostructured silicon/graphite composites with a thin carbon shell and engineered voids, *Electrochim. Acta*. 258 (2017) 274–283. doi:10.1016/j.electacta.2017.10.198.
- [113] M. Wu, X. Xiao, N. Vukmirovic, S. Xun, P.K. Das, X. Song, P. Olalde-velasco, D. Wang, A.Z. Weber, L. Wang, V.S. Battaglia, Toward an Ideal Polymer Binder Design for High-Capacity Battery Anodes, (2013).
- [114] S.F. Lux, A. Balducci, F.M. Schappacher, S. Passerini, M. Winter, Na-CMC as Possible Binder for LiFePO₄, *ECS Trans.* 25 (2010) 265–270. doi:10.1149/1.3393862.
- [115] N. Ogihara, Y. Ozawa, O. Hiruta, A self-assembled intercalated metal-organic framework electrode with outstanding area capacity for high volumetric energy asymmetric capacitors, *J. Mater. Chem. A*. 4 (2016) 3398–3405. doi:10.1039/c5ta09559j.
- [116] S.J. Harris, P. Lu, Effects of Inhomogeneities - Nanoscale to Mesoscale - on the Durability of Li-Ion Batteries, *J. Phys. Chem. C*. 117 (2013) 6481–6492. doi:10.1021/jp311431z.
- [117] M. Aslan, D. Weingarth, N. Jäckel, J.S. Atchison, I. Grobelsek, V. Presser, Polyvinylpyrrolidone as binder for castable supercapacitor electrodes with high

electrochemical performance in organic electrolytes, *J. Power Sources*. 266 (2014) 374–383. doi:10.1016/j.jpowsour.2014.05.031.

- [118] B. Lestriez, S. Bahri, I. Sandu, L. Roué, D. Guyomard, On the binding mechanism of CMC in Si negative electrodes for Li-ion batteries, *Electrochem. Commun.* 9 (2007) 2801–2806. doi:10.1016/j.elecom.2007.10.001.
- [119] D.V. Carvalho, N. Loeffler, G.T. Kim, M. Marinaro, M. Wohlfahrt-Mehrens, S. Passerini, Study of water-based lithium titanate electrode processing: The role of pH and binder molecular structure, *Polymers (Basel)*. 8 (2016). doi:10.3390/polym8080276.
- [120] D. Mazouzi, Z. Karkar, C.R. Hernandez, P.J. Manero, D. Guyomard, L. Roué, B. Lestriez, Critical roles of binders and formulation at multiscales of silicon-based composite electrodes, *J. Power Sources*. 280 (2015) 533–549. doi:10.1016/j.jpowsour.2015.01.140.
- [121] S. Lim, K.H. Ahn, M. Yamamura, Latex migration in battery slurries during drying, *Langmuir*. 29 (2013) 8233–8244. doi:10.1021/la4013685.
- [122] M. Müller, L. Pfaffmann, S. Jaiser, M. Baunach, V. Trouillet, F. Scheiba, P. Scharfer, W. Schabel, W. Bauer, Investigation of binder distribution in graphite anodes for lithium-ion batteries, *J. Power Sources*. 340 (2017) 1–5. doi:10.1016/j.jpowsour.2016.11.051.
- [123] Z. Chen, D. Chao, J. Lin, Z. Shen, Recent progress in surface coating of layered $\text{LiNi}_x\text{Co}_y\text{Mn}_z\text{O}_2$ for lithium-ion batteries, *Mater. Res. Bull.* 96 (2017) 491–502. doi:10.1016/j.materresbull.2017.05.021.
- [124] S.-U. Woo, C.S. Yoon, K. Amine, I. Belharouak, Y.-K. Sun, Significant Improvement of Electrochemical Performance of AlF_3 -Coated $\text{Li}[\text{Ni}_{0.8}\text{Co}_{0.1}\text{Mn}_{0.1}]\text{O}_2$ Cathode Materials, *J. Electrochem. Soc.* 154 (2007) A1005. doi:10.1149/1.2776160.
- [125] W. Li, J. Reimers, J. Dahn, In situ X-ray diffraction and electrochemical studies of $\text{Li}_{1-x}\text{NiO}_2$, *Solid State Ionics*. 67 (1993) 123–130. doi:10.1016/0167-2738(93)90317-V.
- [126] W. Li, J.N. Reimers, J.R. D, In situ X-ray diffraction and electrochemical studies of $\text{Li}(1-x)\text{NiO}_2$, *Solid State Ionics*. 67 (1993) 123–130.
- [127] T. Waldmann, B.I. Hogg, M. Wohlfahrt-Mehrens, Li plating as unwanted side reaction in commercial Li-ion cells – A review, *J. Power Sources*. 384 (2018) 107–124.

doi:10.1016/j.jpowsour.2018.02.063.

- [128] M. Winter, G.H. Wrodnigg, J.O. Besenhard, W. Biberacher, P. Novák, Dilatometric Investigations of Graphite Electrodes in Nonaqueous Lithium Battery Electrolytes, *J. Electrochem. Soc.* 147 (2000) 2427. doi:10.1149/1.1393548.
- [129] P.N. M. Winter, G.H. Wrodnigg, J.O. Besenhard, W. Biberacher, Dilatometric investigations of graphite electrodes in non aqueous lithium battery electrolyte.pdf, *J. Electrochem. Soc.* 147 (2000) 2427–2431.
- [130] J. Yang, Y. Xia, Suppressing the Phase Transition of the Layered Ni-Rich Oxide Cathode during High-Voltage Cycling by Introducing Low-Content Li_2MnO_3 , *ACS Appl. Mater. Interfaces.* 8 (2016) 1297–1308. doi:10.1021/acsami.5b09938.
- [131] J.L. Gómez-Cámer, C. Bünzli, M.M. Hantel, T. Poux, P. Novák, On the correlation between electrode expansion and cycling stability of graphite/Si electrodes for Li-ion batteries, *Carbon N. Y.* 105 (2016) 42–51. doi:10.1016/j.carbon.2016.04.022.
- [132] J. Li, Z. Du, R.E. Ruther, S.J. An, L.A. David, K. Hays, M. Wood, N.D. Phillip, Y. Sheng, C. Mao, S. Kalnaus, C. Daniel, D.L. Wood, Toward Low-Cost, High-Energy Density, and High-Power Density Lithium-Ion Batteries, *Jom.* 69 (2017) 1484–1496. doi:10.1007/s11837-017-2404-9.
- [133] M. N. Obrovac and V. L. Chevrier, Alloy Negative Electrodes for Li-Ion Batteries, *Chem. Rev.* (2014) 11444–11502.
- [134] H. Kim, M. Seo, M.H. Park, J. Cho, A critical size of silicon nano-anodes for lithium rechargeable batteries, *Angew. Chemie - Int. Ed.* 49 (2010) 2146–2149. doi:10.1002/anie.200906287.
- [135] D. Bresser, E. Paillard, P. Niehoff, S. Krueger, F. Mueller, M. Winter, S. Passerini, Challenges of “going nano”: Enhanced electrochemical performance of cobalt oxide nanoparticles by carbothermal reduction and in situ carbon coating, *ChemPhysChem.* 15 (2014) 2177–2185. doi:10.1002/cphc.201400092.
- [136] S. Saeed, M. Rafiq, Q.-A. Baloach, S.H.A. Naqvi, A. Tahira, H. Khain, A.A. Hullio, A.B. Mallah, M. Willander, M. Akhtar, Z.H. Ibupoto, Vanillin Assisted Synthesis of Co_3O_4 Nanostructures for the Development of Sensitive and Selective Peptone Biosensor, *Sens. Lett.*

15 (2017) 536–544. doi:10.1166/sl.2017.3850.

- [137] J. Jaramillo, B.A. Garzón, L.T. Mejía, Influence of the pH of the synthesis using sol-gel method on the structural and optical properties of TiO₂, *J. Phys. Conf. Ser.* 687 (2016) 012099. doi:10.1088/1742-6596/687/1/012099.
- [138] C. Baratto, P. Lottici, D. Bersani, Sol-gel preparation of α -Fe₂O₃ thin films: structural characterization by XAFS and Raman, *J. Sol-Gel ...* 671 (1998) 667–671. doi:10.1023/a:1008694519106.
- [139] R. Verrelli, R. Brescia, A. Scarpellini, L. Manna, B. Scrosati, J. Hassoun, A lithium ion battery exploiting a composite Fe₂O₃ anode and a high voltage Li_{1.35}Ni_{0.48}Fe_{0.1}Mn_{1.72}O₄ cathode, *RSC Adv.* 4 (2014) 61855–61862. doi:10.1039/c4ra12598c.
- [140] J.-M. Jeong, B.G. Choi, S.C. Lee, K.G. Lee, S.-J. Chang, Y.-K. Han, Y.B. Lee, H.U. Lee, S. Kwon, G. Lee, C.-S. Lee, Y.S. Huh, Hierarchical Hollow Spheres of Fe₂O₃@Polyaniline for Lithium Ion Battery Anodes, *Adv. Mater.* 25 (2013) 6250–6255. doi:10.1002/adma.201302710.
- [141] J. Morales, L. Sánchez, F. Martín, F. Berry, X. Ren, Synthesis and Characterization of Nanometric Iron and Iron-Titanium Oxides by Mechanical Milling - Electrochemical properties as anodic materials in lithium cells, *J. Electrochem. Soc.* 152 (2005) A1748. doi:10.1149/1.1972812.
- [142] Y. Chen, H. Xia, L. Lu, J. Xue, Synthesis of porous hollow Fe₃O₄ beads and their applications in lithium ion batteries, *J. Mater. Chem.* 22 (2012) 5006. doi:10.1039/c2jm15440d.
- [143] H.-S. Lim, B.-Y. Jung, Y.-K. Sun, K.-D. Suh, Hollow Fe₃O₄ microspheres as anode materials for lithium-ion batteries, *Electrochim. Acta.* 75 (2012) 123–130. doi:10.1016/j.electacta.2012.04.082.
- [144] E.B. D.J.R. Macdonald, *Impedance spectroscopy Theory, Experiment, and Applications*, John Wiley & Sons, Inc., USA, Hoboken, NJ, 2005. doi:10.1002/0471716243.